# Two Cases of Symmetry Breaking of Free Surface Flows

Hamid AIT ABDERRAHMANE

A thesis

In

The department

of

Mechanical and Industrial Engineering

Presented in Partial Fulfilment of the Requirements
For the Degree of Doctor Philosophy (Mechanical Engineering) at

Concordia University
Montreal, Quebec, Canada

November 2008

*Your file Votre référence*
*ISBN:* 978-0-494-63388-5
*Our file Notre référence*
*ISBN:* 978-0-494-63388-5

# ABSTRACT

Two Cases of Symmetry Breaking of Free Surface Flows

Hamid AIT ABDERRAHMANE, Ph.D.
Concordia University, 2008

The present thesis consists of two parts; both are devoted to two celebrated old problems in fluid dynamics. The first deals with symmetry breaking in a liquid layer flowing down an inclined plane. The second problem concerns the equilibrium and symmetry breaking of interfacial polygonal patterns generated by a system of vortices arranged on a circular ring.

The first problem dates back to Nusselt (1916) who obtained the solution for the basic flow. Since then, thin layers of liquid falling down inclined plane continues to be the subject of extensive studies for both their practical applications and theoretical value. In this thesis, the problem is approached analytically. Three new mathematical models are proposed. The first two involve three and four equations respectively. These produce linear stability results that agree fairly with past experimental outcomes and results obtained with similar models. For a deeper and qualitative analysis a lower dimension model that retains the physics is needed. Hence, a two-equation model (involving only two fundamental flow parameters namely the film thickness and flow rate) is derived. The new model taking account of the

shear stress at the free surface is shown to be superior to the existing two-equation model of Usha and Uma in *Phys Fluid* (2004).

The influence of electrical and magnetic fields on the stability of falling film of an electrically conductor fluid is also investigated. In comparison with the model of Korsunsky (*Eur.J.F.M.1999*) for higher Reynolds numbers. The proposed model takes account of the inertia terms, which are of second order with respect to a small parameter namely the long wave parameter. As shown through the chapter four of the part one, the proposed two-equation model improves significantly Korsunsky's model.

The second problem dates back to Kelvin (1867) who hypothesized atoms to be point vortices arranged in circular ring forming symmetrical polygonal patterns. Although, the atomic vortex model is long abandoned, the problem of system of point vortices has become of great interest in superfluidity and by analogy in plasma physics. Moreover, polygonal patterns, which are the signature of the presence of vortices, equally distributed in rings were also observed in several engineering problems and geophysical flows in nature. In fluid dynamics, polygonal patterns become clearly visible in swirling flows where the vortex core is hollow. The empty core can eventually support polygonal shapes (up to hexagonal). The first experimental report on the phenomenon was by Vatistas in 1990. In this thesis the phenomenon is revisited using image-processing technique that allows a deeper and more precise investigation. The dynamics of the patterns

is investigated and for the first time the transition from one pattern to another is explored in detail. The stability condition for a system of point vortices on circular ring derived first by J.J Thomson (1897) and generalized later by Havelock (1931) for $N$ point vortices including the influence of circular boundaries surrounding the equilibrium is confirmed. Frequency locking between the pattern and the disk frequencies which are suspected in the previous experiments is established and quantified. Moreover, the transition from the elliptical to the hexagonal pattern is found that it follows a "devil's staircase" scenario. Due to the similarity between the problem under the scope and other fields of physics, the present experimental results are anticipated to go beyond the field of fluid mechanics.

## ACKNOWLEDGEMENTS

I would like to thank my supervisors, Dr. G.H Vatistas and K. Siddiqui for their help and support during the preparation of my PhD. In particular Dr G.H Vatistas who is more than a supervisor; he was for me a mentor. I would also like to thank my examiners for managing to read the present manuscript. Much respect to my officemates, and hopefully still friends, Mohamed, Jomeir, and Saadi, for putting up with me for almost three years for all that serious discussion (!) and all those lunches.

# TABLE OF CONTENTS

# List of the Figures

# General Introduction

For any given problem in fluid mechanics and in physics, one of the fundamental questions is the identification and characterization of its transition from order to disorder. In fluid mechanic problems, transition towards turbulence continues to fascinate researchers and has become the one favorable subject of several well known fluid dynamics laboratories over the world. Theoretical, numerical and experimental approaches were undertaken to deepen understanding of the transition towards turbulence. One of these theoretical approaches is the determinist approach which consists of the elaboration of a low dimensional model which captures the fundamental mechanisms leading to chaos or turbulence. This determinist approach of the transition towards chaos started in 1960 with the work of Lorenz, who discovered the concept of strange attractor. This fundamental concept was elaborated after by Ruelle and Takens (1971). These two authors unified the study of irregular behaviors on one concept which nowadays is known as nonlinear dynamic or deterministic chaos. Nonlinear dynamics has become a paradigm through which problems in several fields of physics are investigated.

The two problems considered in this thesis are investigated within this paradigm. The first problem was to model the flow of a thin layer of liquid down an inclined plane, investigate and identify the bifurcations which lead to the chaotic behavior of the free surface. The second problem that deals with vortex polygonal patterns espoused by a hollow vortex core was

experimentally investigated. The equilibrium and their transition towards next equilibrium were explored. Our contributions to the research on these two problems can be considered as significant.

A thin layer of fluid flowing along an inclined plane, tackled in the first part of this thesis, dates back to Nusselt (1916); this problem continues to be the subject of extensive studies for its theoretical interests and industrial relevance. The problem is experimentally within reach; thus constituting an interesting test problem for nonlinear and bifurcations theories. Also falling film fluid down inclined planes or cylinders is found in several engineering applications such as precision coating, heat exchangers and evaporators. The free surface is the place where momentum, heat and mass transfers take place; these exchanges depend strongly on the instabilities of the free surface. Understanding their development is of primary importance. The stability of a thin film fluid flowing down an inclined plane remains the subject of numerous theoretical, numerical an experimental studies. The competition between gravity, surface tension, viscosity, and inertia makes the dynamics at the free surface complex, exhibiting generic bifurcation scenarios. The interface of a falling film of fluid undergoes a primary instability in the form of hydraulic jump (heteroclinic bifurcation) or oscillator waves (Hopf bifurcation). This initial instability is followed, more often, by secondary instabilities leading to spatiotemporal chaos through a cascade of periodic doubling or homoclinic bifurcations (solitary waves).

The experimental investigation of the problem started with Kapitza & Kapitza (1949). In order to trigger the free surface instabilities, they introduced sinusoidal perturbations with different amplitudes and frequencies at the entrance. They found that depending on the perturbations, the wave at the free surface can exhibit quasi-sinusoidal or solitary wave behaviour. The elaborate experiments revealed that the evolving flow could become chaotic downstream if the inclined plane is sufficiently long.

Analytical studies on the stability of this problem began with the work of Yih (1955) and Benjamin (1957). Using a perturbation method to reduce the Navier-Stokes equation into a well known Orr-Sommerfeld equation, the two authors found that the basic flow of Nusselt becomes unstable if $\frac{\cot\theta}{R} \leq \frac{5}{6}$ where $\theta$ is the incline angle and $R$ is Reynolds number. Linear stability which is valid only for infinitesimal perturbation gives only the stability thresholds and cut-off frequency, but it does not inform us on what happens when the amplitude of the perturbation grows becomes finite and nonlinear effects turn out to be no long negligible. To consider the nonlinear effects, weak nonlinear theories were developed and several model where proposed.

At small Reynolds numbers, Benney (1966) proposed the first single-equation model for the spatiotemporal evolution of the film fluid thickness. Afterwards, a simplified version of the Benney equation was derived and called the Kuramoto-Sivashinsky equation. Although, Benney (1966) predicted the stability threshold ($\frac{\cot\theta}{R} \leq \frac{5}{6}$), it suffers from finite-time blow up and furthermore it is valid only in narrow region around the critical

Reynolds number. Recently, some authors proposed other single-equation models; see Ooshida (1999) and Panga & Balakotaiah (2003). However, none of these two models are free from the finite-time blow up impediment, thus making the search for an accurate single-equation model representation hopeless, see Ruyer and Manneville (2004).

At relatively high Reynolds numbers, perturbation method is no longer valid; hence an ad hoc method based on the integral method was developed. Shkadov (1968) was the first who used the momentum integral method to reduce the Navier-Stokes equations into a two-equation model which involves the film thickness and flow rate. The Shkadov's model suffers from two major drawbacks. It does not predict a stability threshold nor does it foresee the oscillatory waves (Hopf bifurcation). Lee and Mei (1996), including second order terms in Navier-Stokes equation and using similar integral method, derived a two-equation model. This model exhibits a Hopf bifurcation but also fails to predict the stability threshold. Recently, following the same strategy as Lee and Mei (1996), Usha and Uma (2004), using an energy integral method instead of the momentum integral method, developed a two-equation model which predicts the stability thresholds and exhibits generic bifurcations scenarios observed during the experiments. However, this last model does not satisfy one of the boundary conditions at the free surface up to the second order, with respect to the long wave parameter, as claimed. In this thesis, this inconsistency is corrected. It shows that the correction introduced to the model of Usha and Uma (2004) is significant.

Higher dimension models, such as the four-equation models of Ruyer-Quil & Manneville (2000) and Amaouche et al (2005) can also be found in the literature. Besides the film fluid thickness and the flow rate, these models include two more terms, which are associated with the corrections to the flow rate. In this thesis, four- and three-equation models are proposed, both involving only physical quantities such as free surface and shear stress at the free surface in addition to the film fluid thickness and the flow rate. As shown, the results of the linear stability obtained with these two models agree with results obtained by more involved numerical methods, experimental results and those obtained using Ruyer-Quil & Manneville's model.

Although, these higher dimension models exhibit accurate linear stability results; they complicate the qualitative analysis of the nonlinear effects. In order to achieve such a qualitative examination Ruyer-Quil & Manneville (2000), Amaouche et al (2005) were forced to use simplified models which involve only film fluid height and the flow rate which are two-equation models.

The second part of the present thesis deals with the exploration of the vortex polygonal pattern espoused by a hollow-vortex in high swirl flows. These patterns are laboratory models of the equilibrium of a system of point vortices, equally distributed on circular ring. Indeed, the apexes of the polygonal pattern are equally distributed on a circular ring and host satellite

vortices. The problem was tackled experimentally. When the swirl is imparted to a thin liquid layer confined in a stationary cylinder, by rotating a disk near the bottom of the cylindrical container, the centrifugal force due to the rotary motion of the liquid along with gravity causes the free surface to form an inverted bell shape. Its central depression grows deeper as the disk speed increases. Eventually, the receding liquid exposes part of the disk's central surface to air whereby, the line of intersection between the surfaces of the disk, liquid, and air outlines the core shape. With the increase of the disk speed, the circular shape of the core first becomes elliptical and then acquires different polygonal equilibrium patterns, called Kelvin's stationary equilibria. This symmetry breaking was reported for the first time by Vatistas (1990), subsequently confirmed by Janssen et al. (2006).

Interest in the problem, of a system of vortices equally distributed on circular ring, arose one hundred and fifty years ago with celebrated vorticity theorems of Helmholtz (1858). This seminal work inspired several prominent scientists of the Victorian era, such as Kelvin (1867), to consider eddies as paradigms in explaining the atomic structure of matter; Kelvin (1867) remarked that "Helmholtz's vortex rings are the only true atoms". The era that began with Kelvin's (1867) "vortex atoms" ended by Einstein (1905) who rendered Ether obsolete which led to the desertion of the "vortex atoms" idea. However, the ensued impetus on the subject matter contributed significantly towards the growth of hydrodynamics, and led J. J. Thomson

(1897) to the discovery of the electron. Detailed historical accounts can be found in the fine contributions of Aref (1983) and Aref et al.(1992).

Although the vortex atom theory was deserted; the theoretical developments vis-à-vis the stability of point vortices arranged in a ring become of great interest in superfluidity and plasma physics. Indeed, arrangements of vortices within a circular ring are found in swirling superfluids, see Yarmuck et al (1979) and by analogy in electron columns, Durkin and Fajans (2000). Durkin and Fajans showed that the 2-D drift-Poisson equations describing the evolution of electron columns, under the influence of magnetic and electrical fields, are dynamically analogous to those developing in an ideal fluid. In 1883, J.J. Thomson dealt with the general situation of three, four, five, six, and seven vortices. He forecasted instability to occur for seven vortices. Havelock (1931) extended the approach to the N-vortex problem, deducing that with no boundary, the case of seven vortices was neutrally stable. The presence of confining outer or inner boundaries could destabilize the flow, while a sufficiently strong central vortex could stabilize an unstable ring.

A first experimental confirmation of this more than a century old theory on the stability of a ring is given in this thesis. Our experimental results confirmed that modes $N \leq 6$ are stable while $N \geq 7$ are unstable. Also, the stability condition given by Havelock (1931) is confirmed. This condition stipulates that for a system of $N \leq 6$ vortices, confined in circular domain, to

be stable, the vortices should be equally distributed on circular ring situated at equidistance from the center and the external boundaries. A detailed analysis of the dynamics of the system of satellites with respect to the "parent vortex" is included in the present thesis. For the first time the transition from *N-* to *N+1-gons* is thoroughly investigated. Regarding the similitude of the polygonal pattern with those found in plasma physics and rotating superfluid Helium (4He- 4 must be a superscript) below the $\lambda$ point (temperature at which normal fluid becomes superfluid), the present experimental results become very elaborative.

The first part of the thesis which is dedicated to the falling film fluid problem starts with a literature review (chapter 1). In chapter 2, we describe our attempts to develop accurate four- and three-equation models. These two models involve only physical flow parameters namely, the film thickness, flow rate, shear stress and velocity at the free surface. The accuracy of these two models is shown by comparisons of the results with experimental data and simulations obtained with more involved numerical investigation and the outcomes obtained with the four-equation model of Ruyer and Mannevile (2000). Higher dimension models are found not to allow a deeper investigation of the bifurcation scenarios. These investigations are provided in chapter 3 using a two-equation model. As indicated above, the two-equation model is an improvement of an existing model. A qualitative analysis using bifurcation theory is carried out and numerical simulations were also performed to illustrate the different bifurcation scenarios exhibited by a

falling film flow. In chapter 4, we extend the analysis to the Magnetohydrodynamics case, showing the influence of both magnetic and electrical fields on the stability of falling electrically conducting film. Here we have also improved an existing model proposed by Korsunsky (1999).

The second part of the thesis begins with an extensive but not exhaustive literature review on the problem of vortex pattern, its manifestation in different fields of physics and its presence in nature (in chapter 1). Chapter 2 is devoted to the confirmation of Kelvin's equilibria J.J Thomson (1883). Moreover, the influence of flow dynamics around the troughs and apexes were also investigated; preliminary results on the surrounding dynamics are provided. In chapter 3, we examine for the first time the transition between two subsequent polygonal patterns. The transition is investigated in absolute and relative frames of reference whereby original findings are presented.

# Chapter I: Introduction

There are a score of situations in nature and industry where a thin layer of fluid with a free surface flows down inclined or vertical walls. At the free surface, mass, momentum, and heat transfers take place. These transfers depend on the dynamics of the free surface, which can be complex. Industrial situations can be found in coating, photography, casting, evaporators, condensers and heat exchangers. On one hand, instabilities can have a beneficial effect on the industrial process and therefore are encouraged. On the other hand, they can have a negative effect and hence are to be suppressed. For example, instabilities trigger turbulence and increase heat exchange in heat exchangers. While in coating and photography industry a wavy free surface is to be avoided.

The applications mentioned above, and others, were the motivation behind the countless theoretical, numerical and experimental studies on the instabilities of the thin layer of the fluid flowing down inclined plane and vertical walls. One of the objectives of these studies is the derivation of simplified models capable of describing accurately, the flow and hence improves industrial process. The other objective is academic. Thin film flow exhibits a complex nonlinear phenomena and hydrodynamic chaos; therefore this problem can be used to better understand the bifurcation scenarios leading to the symmetry breaking.

As mentioned earlier, research on this topic started with the analytical work of Nusselt (1916), who derived the basic flow solution for the unperturbed flow. The competition between gravity and surface tension yields interfacial waves. Kapitzas & Kapitza (1949) are the first researchers who studied experimentally the stability of the interface; they reported that the free surface can undergo several types of deformations. There, the free surface deformations depend on the perturbations at the flow entrance. They reported that perturbations with small amplitude and high frequencies induce a quasi-sinusoidal wave train, while perturbations with relatively high amplitudes produce solitary waves and chaos. Several other experimental results can be found in Tailby & Portalsky (1965), Stainhorp & Allen (1965), Jones & Whitaker (1966), Strobel & Whitaker (1969), Takahama & Kato (1980), and Brauner & Maron (1982). The relatively more recent tests were conducted by Liu, Paul & Gollub (1993). These authors considered relatively small incline angles ( $4^0 < \theta < 10^0$ ) and used an optical technique which is more precise. They have shown that depending on Reynolds, Weber and incline angle, the downstream film flow can become chaotic and three dimensional.

The film flow is subjected to two kinds of instabilities; namely surface and shear mode instabilities. The surface mode instabilities are due to gravity and grow slowly. The surface modes are triggered by Reynolds number exceeding a critical value of $\frac{5}{6}\cot\theta$, where $\theta$ is the angle of inclination. This critical Reynolds number is obtained through linear stability investigations of

the problem worked out by Yih (1955) and Benjamin (1957). Performing an asymptotic examination of the Orr-Sommerfeld equation for long waves, these two authors found that the stationary solution of Nusselt becomes unstable for long wave perturbation when the Reynolds number exceeds a critical value. They also computed the critical wave number below which the film flow becomes unstable. A more sophisticated linear stability analysis, based on wave packets and pseudo-spectral method, was conducted by Brevdo et al (1999). Moreover, using collision Briggs' criteria, they have shown that the instability of the thin film flow is convective. This propriety indicates that instabilities are amplified as they are swept far downstream. Their research showed fair agreement with the experimental results obtained by Liu et. al (1993).

The second kind of instability is due to shear modes arising at high Reynolds numbers and at very small incline angles ($\approx 0.5^0$); they have finite wave number and strong amplification rate. The cause of this instability is attributed to viscosity. Debruin (1974) and Florian (1987) showed that the amplification rate of this instability can be reduced by increasing the surface tension or by reducing the incline angle. They also indicate that the critical Reynolds numbers for the shear mode instability does not vary monotonically with the surface tension and the incline angle.

Weak nonlinear stability analyses were implemented. Taking advantage of small thickness to length ratio, several researchers employed a

perturbation method and proposed one-equation models for the spatiotemporal evolution of the film thickness. The most well known equations are those of Benney (1966) and Kuramoto-Sivashinsky (1980); the latter is the simplification of the first. Benney's equation failed in capturing all the inertial effects in both the flow domain and at the free surface confining the efficacy of the model to a narrow region around the critical Reynolds number. Furthermore, Benney's equation suffers from finite-time blow up. Several others like Ooshida (1999) and Panga & Balakotaiah (2003) attempted to derive a single-equation model, which is free from a finite-time, blow up. Yet, none of these models are free from the last impediment, thus, making the search for an accurate single-equation model representation hopeless, see Ruyer and Manneville (2004).

The perturbation method is no longer valid for high Reynolds numbers. In an attempt to extend the analysis to higher Reynolds numbers, an ad hoc method, similar to the integral boundary layer approximation, was employed to reduce the number of governing equations to two. Shkadov (1968) was the first to employ this technique and reduced the governing equations to a two-equation model involving film thickness and flow rate. Unfortunately, Shkadov's model suffers from two major drawbacks. First, it predicts a stability threshold ($\frac{\cot\theta}{R} \leq 1$) that is different from the one of Yih (1955) and Benjamin (1957), and second, it does not predict periodic waves (Hopf bifurcation). To improve the approximation of Shkadov (1968), Steinhuk & Duckler (1989) included terms of second order with respect to the long wave

parameter, but they considered a uniform pressure distribution along the film thickness. This hypothesis is inconsistent with the required second order accuracy. Similar studies were conducted by Prokopiou et. al (1991). These authors assumed a hydrostatic distribution along the film thickness and used normal form theory to find analytical solutions for limit cycles and homoclinic orbits, but they did not succeed in predicting a stability threshold. Later, second order terms with respect to a long wave parameter were included by Lee and Mei (1996). They captured the Hopf bifurcations, but were unsuccessful in predicting the stability threshold. Recently, the same parabolic velocity profile used in Lee and Mei (1996) were employed along with the energy integral method by Usha and Uma (2004) and they recovered the instability threshold given by Benjamin (1957) and Yih (1955). Yet, the velocity profile used by Usha and Uma (2004), and Mei and Lee (1996) cancels the shear stress at the free surface and prevents the tangential component of the dynamic interfacial condition to be satisfied at the second order level. The flaw of the Usha and Uma model is corrected and the consistency of the approximate solution at $O(\varepsilon^2)$, is insured, where $\varepsilon$ is a wave length parameter, in all governing equations and boundary conditions. This is achieved by introducing the shear stress at the free surface as an additional variable in the velocity profile. Fortunately, the introduction of this new degree of freedom does not increase the number of modeling equation at the accuracy order considered in this thesis ($O(\varepsilon^2)$). It was shown that for the case of stationary long waves, this correction has

significant implications on the condition of occurrence of Hopf and heteroclinic bifurcations.

A Four-equation model was derived by Ruyer-Quil and Manneville (2002) using the Galerkin method with specific test functions. This model correctly predicts the condition for the onset of instability. Following the same strategy, and including the smaller inertia terms, Amaouche et al (2005) improved the accuracy of the model proposed by Ruyer-Quil and Manneville (2000) in the high Reynolds number range. It is important to note that the models of Ruyer-Quil and Manneville (2000), and Amaouche et al (2005) involve four nonlinear differential equations for the film thickness, the flow rate, as well as two corrections to the last parameter.

Despite the simplifications introduced by the long wave hypothesis, the equations that model the problem remain complex. More simplifications were made when a frame of reference moving with the perturbation celerity is considered. In this frame, the waves are stationary, their celerity and form remain unchanged. This simplification allows a qualitative analysis with the aim to examine the influence of the flow parameters on the bifurcations scenarios. Several numerical studies were reported for the case of stationary waves. These investigations have identified the existence of periodic waves and periodic doubling. Most of the studies were restricted to the case of low Reynolds numbers and have used the finite element method, Bach and Villadsen (1984), Kheshgi & Scriven (1987), and Armstrong & Brown (1994).

# Chapter II: Four-equation Model and Three-equation Model

## 1. Introduction

In this chapter, two models that consist of four and three equations respectively are proposed. The four-equation model describes the spatiotemporal evolution of the flow rate, $q(x,t)$, film thickness, $h(x,t)$, shear stress at the wall $\tau 0(x,t)$ and free-surface velocity $s(x,t)$. While the three-equation model involves the spatiotemporal evolution of the film height, shear stress at the wall and flow rate. The results of the linear stability conducted with these two models are compared with those obtained with four-equation model of Ruyer and Maneville (2000), which involves besides the flow rate and the film thickness two correcting parameters of the flow rate. Moreover, the results are also compared with the results of Brevdo et al (1999) who tackled the linear stability of a falling film of fluid numerically using the mathematically involved spectral method. The results of the linear stability are also validated using the experimental results of Liu et al (1993).

For long wave approximation, low Reynolds number and high Weber number, the Navier-Stokes equations are first simplified by neglecting terms of order higher than two with respect to the long wave parameters. These equations are reduced subsequently into four and three equations, using the integral momentum method of Karman-Polhausen. The momentum integral

method requires the presumption of a velocity profile; hence the model depends on the choice of the velocity field. Having first used polynomials of order two and three, we have crystallized a four-order polynomial that represents the velocity profile with which we found the stability threshold to be $R_c = \frac{5}{6}\cot\theta$, as in Benjamin (1957) and Yih (1955). A velocity profile in the form of a polynomial of order two and three gives the following stability threshold $R_c = \cot\theta$ and $R_c = \frac{16}{19}\cot\theta$, respectively. Note that the stability threshold is slightly different from the value ( $R_c = \frac{5}{6}\cot\theta$ ) predicted by Benjamin (1957) and Yih (1955).

This chapter is organized in the following way. First the formulation of the problem is presented in section two, followed by the presentation of our models in section three. Subsequently linear stability of four-equation and three-equation models is investigated. The effectiveness of the proposed models is shown through the comparison of our results with experimental observations given by Liu et al (1993), the theoretical results presented in Brevdo et al (1999) and those obtained with the four equation model of Ruyer and Mannevile (2000). Finally concluding remarks are given in section four.

# 2. Formulation of the problem

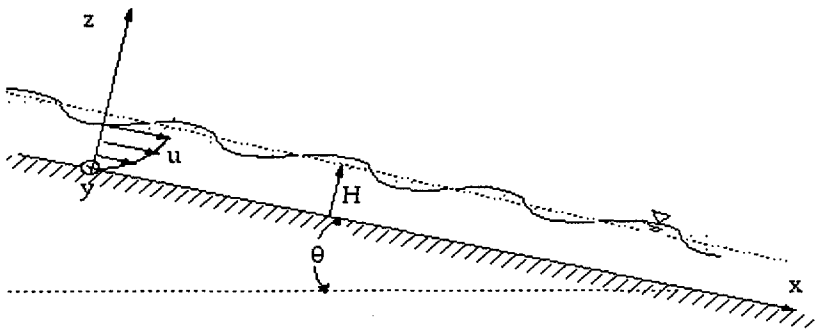


Figure 2.1 Schematic of the problem.

A two-dimensional flow of a thin layer of fluid down an inclined plane, making an angle $\theta$ with the horizontal, under the action of gravity is considered; see in figure 2-1. The fluid is assumed incompressible and Newtonian. The upper half space consists of air having a negligible density. A Cartesian coordinate system is adopted in which the x-axis is parallel to the bottom plane with the positive axis along the streamwise direction, and the z-axis normal to the incline plane directed away from the film. The gravitational acceleration is $\vec{g} = (g\sin\theta, -g\cos\theta)$. The governing equations are:

$$\nabla.\vec{V} = 0 \tag{2-1}$$

$$\frac{\partial\vec{V}}{\partial t} + \vec{V}.\nabla\vec{V} = \frac{1}{\rho}\nabla P + \nu\Delta\vec{V} + \vec{g} \tag{2-2}$$

Where $\vec{V}, P, \rho$ and $\nu$ are the velocity vector, static pressure, density, and kinematic viscosity, respectively. The boundary conditions for the problem under consideration consist of the non-slip condition between the fluid and solid wall, along with the kinematic and stress conditions imposed at the free surface.

$$\vec{V}(x,0,t) = \vec{0} \tag{2-3}$$

$$w(x,z,t)\big|_{z=H(x,t)} = \frac{\partial H(x,z,t)}{\partial t} + u(x,t)\frac{\partial H(x,z,t)}{\partial x} \tag{2-4}$$

$$(-P_1 \overline{\overline{\delta}} + 2\mu_1 \overline{\overline{D}}_1)\vec{n} = (-P_2 \overline{\overline{\delta}} + 2\mu_2 \overline{\overline{D}})\vec{n} - (\gamma div\vec{n})\vec{n} \tag{2-5}$$

Where $H(x,t)$ , $\mu$ , $\gamma$ , $\vec{n}$ , $\overline{\overline{\delta}}$ and $\overline{\overline{D}}$ represent the film depth, dynamic viscosity, surface tension coefficient, normal unit vector directed away from the film, unity tensor and deformation tensor, respectively. The subscripts (1) and (2) indicate the inner and outer regions of the fluid domain, respectively. Since air is considered inviscid, the equation (2-5) reduces to:

$$(-P\overline{\overline{\delta}} + 2\mu\overline{\overline{D}}_1)\vec{n} = (-P_a - \gamma divn)\overline{\overline{\delta}}\vec{n} \tag{2-6}$$

$P_a$ is the ambient pressure. The projection of this equation on the local frame, attached to the free surface, $(\vec{n}, \vec{t})$ provides the following two equations:

$$P - P_a = \gamma . div\vec{n} + 2\mu(\overline{\overline{D}}.\vec{n}).\vec{n} \tag{2-7}$$

$$(\overline{\overline{D}}.\vec{n}).\vec{t} = 0 \tag{2-8}$$

With $\vec{t}$ is the tangent to the free surface and $\overline{\overline{D}}$ is the deformation tensor defined as.

$$\overline{\overline{D}} = \begin{bmatrix} u_x & 0 & \frac{u_z + w_x}{2} \\ 0 & 0 & 0 \\ \frac{u_z + w_x}{2} & 0 & w_z \end{bmatrix}$$

The projection of the equations (2-7 and 2-8) in the x and z directions yields:

$$\mu\left(u_z + w_x - 2u_x H_x + (P - P_a - \gamma.(\nabla.\vec{n}))H_x\right) = 0 \tag{2-9}$$

$$\mu\left((w_x + u_z)H_x + P - P_a - \gamma.(\nabla.\vec{n})\right) = 0 \tag{2-10}$$

with

$$\vec{n} = \frac{(-H_x, 0, 1)}{\left(1 + H_x^2\right)^{\frac{1}{2}}} \tag{2-11}$$

$$\nabla.(\vec{n}) = -H_{xx}(1 + H_x^2)^{\frac{-3}{2}} \tag{2-12}$$

Subscripts, $x$ and $z$, indicate partial derivatives of the variables with respect to $x$ and $z$. For normalisation we choose the scales based on the Nusselt flow: $H_0$, $L$ and $c_0 = \frac{gH_0^2 \sin\theta}{3\nu}$ which are the initial film depth, characteristic length and Nusselt velocity, respectively. The variables are thus

normalized as follows:

$$u^* = \frac{u}{c_0}, x^* = \frac{x}{L}, z^* = \frac{z}{H_0}, w^* = \frac{wL}{H_0 c_0}, p^* = \frac{p - p_a}{\rho c_0^2}, t^* = \frac{t c_0}{L}, \quad H^* = \frac{H}{H_0}.$$

The non-dimensional equations involve now the following fundamental numbers: $R = \frac{c_0 H_0}{\nu}$, $We = \frac{\gamma}{\rho H_0 c_0^2}$, $Fr = \frac{g H_0 \cos\theta}{c_0^2} = \frac{3\cot\theta}{R}$ and $\varepsilon = \frac{H_0}{L}$ which are the Reynolds, Weber, and Froude numbers, and a long wave parameter. Note that for the problem under consideration, the last dimensionless parameter is relatively small. This hypothesis allows us to neglect the higher order terms and simplify, appreciably, the governing equations. In addition to the shallow water condition, we assume the following order of magnitude for the Reynolds and Weber numbers: $R = O(1)$ and $We = O(\varepsilon^{-2})$. The simplified governing equations in dimensionless form (subscripts are omitted henceforth) are:

$$u_t + uu_x + wu_z = -p_x + \frac{1}{R}(\varepsilon u_{xx} + \frac{1}{\varepsilon} u_{zz} + \frac{3}{\varepsilon}) \tag{2-13}$$

$$\varepsilon^2 (w_t + uw_x + ww_x) = -p_z + \frac{\varepsilon}{R}(w_{zz} - \frac{3}{\varepsilon}\cot\theta) \tag{2-14}$$

$$u_x + w_z = 0 \tag{2-15}$$

$$z = 0: \qquad u = w = 0 \tag{2-16}$$

$$z = H(x,t): \qquad w = H_t + uH_x \tag{2-17}$$

$$u_z + \varepsilon RPH + \varepsilon^2 (w_x - 2u_x H_x) + \frac{\varepsilon^3 W_e R H_{xx} H_x}{(1+\varepsilon^2 H_x)^{\frac{3}{2}}} = 0 \tag{2-18}$$

$$P + \frac{\varepsilon}{R}(u_z H_x - 2w_z) + \frac{\varepsilon^2 WeH_{xx}}{(1+\varepsilon^2 H_x^2)^{\frac{3}{2}}} = 0 \tag{2-19}$$

# 3. Models

## 3.1 Four-equation model

Within certain ranges of flow parameters, the basic solution loses its stability thus giving rise to solutions for which inertial effects are of paramount importance. The basic flow solution that corresponds to the zero order of the system of equations (2-13-2-19) assumes that $u = U(z)$, $p = P(z)$, $w = 0$, $H = H_0$, where $U(z)$ and $P(z)$ are the solutions to the problem:

$$P_z = +\frac{1}{R}(-3\cot\theta) \tag{2-20}$$

$$u_{zz} + 3 = 0 \tag{2-21}$$

$$u(0) = 0 \qquad u_z(H) = 0 \qquad p(H) = 0 \tag{2-22}$$

The basic flow solution for the velocity is then:

$$U(z) = 3(z - \frac{1}{2}z^2) \tag{2-23}$$

The solution of the problem is approximated via the integral method of Karman-Polhausen, and the following velocity profile is assumed in order to initiate the analysis.

$$u(x,z,t) = a(x,t)z + b(x,t)z^2 + c(x,t)z^3 + d(x,t)z^4 \tag{2-24}$$

From the definitions of velocity at the free surface, the flow rate, shear stress at the wall and free surface, and the following unknown coefficients $a(x,t)$ , $b(x,t)$ , $c(x,t)$ and $d(x,t)$ can be related by four equations to the previously mentioned parameters $q(x,t)$ , $\tau 0(x,t)$ , $\tau_s(x,t)$ and $s(x,t)$ .

$$a(x,t) = \tau 0(x,t)$$

$$b(x,t) = -\frac{3}{2}\frac{-h(x,t)^2\tau_s(x,t) + 3.\tau 0(x,t).h(x,t)^2 + 8.h(x,t).s(x,t) - 20.q(x,t)}{h(x,t)^2}$$

$$c(x,t) = \frac{2.(14.h(x,t).s(x,t) + 3\tau 0(x,t).h(x,t)^2 - 30.q(x,t) - 2.h(x,t)^2\tau_s(x,t)}{h(x,t)^4}$$

$$d(x,t) = -\frac{5}{2}\frac{-12.q(x,t) + \tau 0(x,t).h(x,t)^2 - h(x,t)^2\tau_s(x,t) + 6.h(x,t).s(x,t)}{h(x,t)^5}$$

Four equations are required to determine the unknown physical quantities $q(x,t)$ , $\tau_s(x,t)$ $\tau 0(x,t)$ and $h(x,t)$ . Combining the continuity equation (2-15) and the kinematic boundary condition (2-17) with Leibniz's rule yields the first equation:

$$h_t + q_x = 0 \tag{2-25}$$

Integrating equation (2-14) from a $z$-coordinate somewhere inside the film to the free surface and using the boundary condition (2-19) we obtain the pressure. Substituting the expression for the pressure into equation (2-13) and integrating over the entire film thickness with the boundary condition (2-18), we produce the second required equation. Using the method of moments with a monomial of order one and two respectively we deduce both the third and the fourth equations. The three nonlinear equations are given in appendix A.

### *3.1.1 Linear stability*

Linear analysis provides the location of the bifurcation points in the parameters space, and predicts the qualitative characteristics of developing disturbances. The four nonlinear equations (see appendix A) are linearized around the basic solution:

$$(q(x,t), h(x,t), \tau 0(x,t), s(x,t)) = (1,1,3,\frac{3}{2}) + (Q(x,t), H(x,t), \tau(x,t), S(x,t))$$

given as:

$$H_t + Q_x = 0 \tag{2-26}$$

$$-We\varepsilon^3 H_{xxxx}+\frac{\varepsilon^2}{R}(-S_{xxx}+\frac{9}{2}H_{xxx}+3H_{xxt})+\varepsilon(-\frac{15}{7}H_{xt}+\frac{8}{35}S_{xx}-\frac{1}{35}\tau_{xx}-\frac{36}{35}H_{xx}\frac{3}{R}H_{xx}.\cot\theta-H_{tt}) \\ +\frac{1}{R}(\tau_x-3H_x)=0 \tag{2-27}$$

$$\frac{1}{2}We\varepsilon^3 H_{xxxx}+\frac{\varepsilon^2}{R}(\frac{7}{10}S_{xxx}-\frac{61}{20}H_{xxx}-2H_{xxt}-\frac{1}{60}\tau_{xxx})+\varepsilon(\frac{39}{35}H_{xt}-\frac{1}{10}S_{xt}+\frac{3}{160}\tau_{xx}+\frac{1}{120}\tau_{xt}-\frac{137}{560}S_{xx}+\frac{639}{1120}H_{xx} \\ -\frac{3}{2R}H_{xx}.\cot\theta+\frac{1}{2}H_{tt})-\frac{1}{R}(S_x-3H_x)=0 \tag{2-28}$$

$$\frac{1}{3}We\varepsilon^3 H_{xxxx}+\frac{\varepsilon^2}{R}(\frac{61}{105}S_{xxx}-\frac{169}{70}H_{xxx}-\frac{11}{7}H_{xxt}-\frac{1}{70}\tau_{xxx})+\varepsilon(\frac{183}{280}H_{xt}-\frac{13}{105}S_{xt}+\frac{1}{80}\tau_{xx}+\frac{1}{140}\tau_{xt}-\frac{13}{56}S_{xx} \\ +\frac{39}{112}H_{xx}-\frac{1}{R}H_{xx}.\cot\theta+\frac{2}{7}H_{tt})-\frac{2}{R}(S_x+H_t)=0 \tag{2-29}$$

Subsequently, the perturbation quantities are expanded in the form of normal modes and the equations are rescaled in the streamwise direction in order to drop the parameter $\varepsilon$ and to be consistent with the long wave hypothesis.

$$(Q(x,t),H(x,t),\tau(x,t),S(x,t))\approx(A,B,C,D).e^{I(k.x-ct)} \tag{2.30}$$

where $A,B,C,D$ are arbitrary constants, while $c=c_r+I.c_i$ and $k=k_r+I.k_i$ are the complex angular frequency and complex wave number, respectively. Then, the four linear partial differential equations (2-26-2-29) are transformed into four algebraic equations with the four constants $A,B,C,D$. The condition for a nontrivial solution for the algebraic system leads to the

dispersion equation, which relates the angular frequency $c$ to the wave number $k$. The last equation is a polynomial of seventh order and is given in appendix B. In the frame of long waves (the wave number $k$ is very small), the angular frequency can be expanded as: $c = a_1 k + a_2 k^2 + a_3 k^3 + O(k^4)$. Substituting this series of angular frequency into the dispersion equation and solving for the coefficients $a_1, a_2$, yields $a_1 = 3$ which is the angular frequency of the long waves and $a_2 = \frac{1}{5}(6.R - 5\cot\theta).I$, where $I$ is the pure imaginary complex number. At the marginal stability condition, the imaginary part of the angular frequency is null; hence, the imaginary coefficient $a_2$ should be null. This condition leads to the stability threshold $R_c = \frac{5}{6}\cot\theta$, which is already given in Benjamin (1957) and Yih (1995). Note that the latter condition is independent from the Weber number, which is expected because the curvature of the free surface is small (long wave approximation). Separating the real and the imaginary parts of the dispersion equation, we obtain two equations which can be solved for $k_r$. In the spatial and temporal marginal stability conditions ( $c_i = 0$ and $k_i = 0$ ) the variation of the cut-off wave number $k_r$ with the Reynolds number for different value of the Kapitza number ( $Ka = \frac{\gamma}{\rho g^{1/3} \nu^{4/3}}$ ) , is shown in the figure 2-2. The critical wave number is compared to the results given in Nguyen & Balakotaiah (2000) for $Ka = 100$. The present results are seen to be nearer to those given by the solution of the Orr-Sommerfeld equation.

The cut-off frequency ( $\frac{c_r}{2\pi}$ ), which separates the stable from the unstable region is also calculated and compared to the experimental results in the figures 2-3 and 2-4. A good agreement with experimental results is amply evident. The angular frequency for the marginal stability conditions is compared to the experimental results in figures 2-5. Once more, the agreement between the numerical and experimental results is good.

The accuracy of the proposed model is further verified using the formalism of absolute-convective stability based on the Briggs' collision criteria. Solutions have been obtained by Brevdo et al (1999). Using Fourier-Laplace transformation, they reduced the linearized Navier-Stokes around the parabolic profile to an inhomogeneous Orr-Sommerfeld equation with inhomogeneous boundary conditions. The resulting boundary value problem is solved using the spectral method. The temporal growth rate and angular frequency as a function of the wave number are represented in the figure 2-6 and 2-7. These are found to be similar to figure 2 in Brevdo (1999). As in Brevdo, we consider $R = 40$ , $We = 41.46$ , $\theta = 4.6^o$ . For a given growth rate, $c_i$ , the solution of the dispersion relation is displayed in the $(k_r, k_i)$ plane as the oscillation frequency, $c_r$ , is varied. Like in Brevdo et al (1999), we show through figures 2-7 and 2-8 the solution curves when the growth rate is decreased from $c_i = 0.02$ to $c_i = 0$ . No pinching of the spatial branches is observed, which, according to the collision criteria implies that the film flowing down an inclined plane is absolutely stable and convectively unstable, see Huerre and Monkewitz (1998). The results hold true for Reynolds numbers up to $R = 100$ .

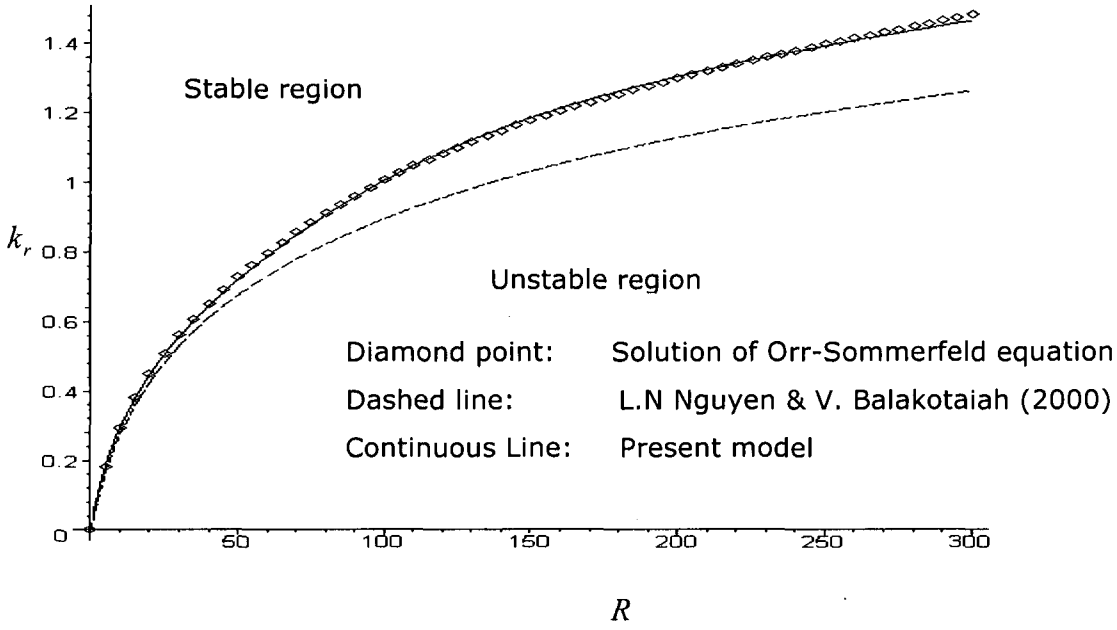


Figure2-2: Critical wave number in the case of vertical plane. Kapitza number=100.

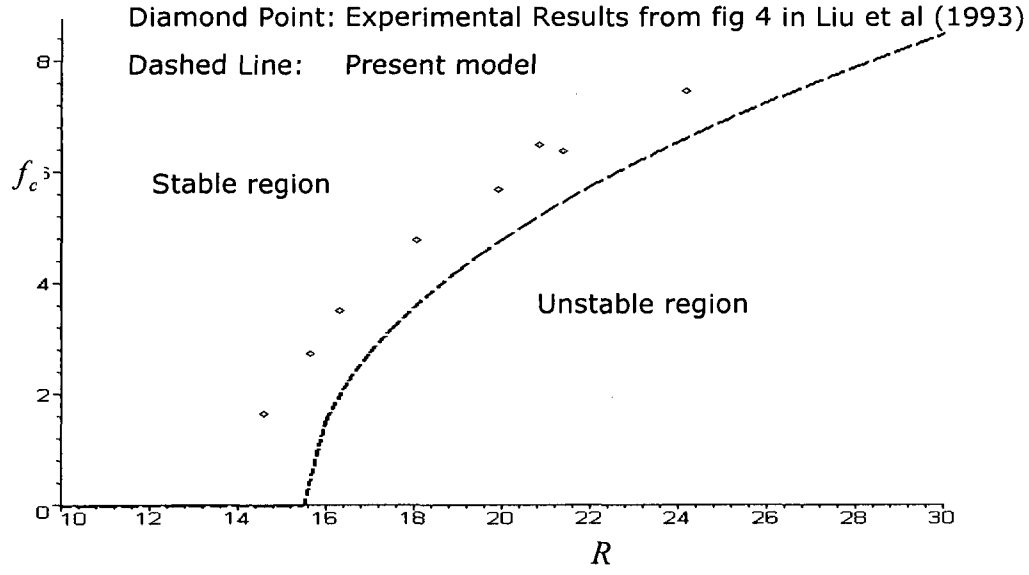


Figure 2-3- Cutoff frequency $\theta = 5.6$, $\nu = 5.02.10^{-6} m^2 s^{-1}$, $\rho = 1130.kg.m^{-3}$,

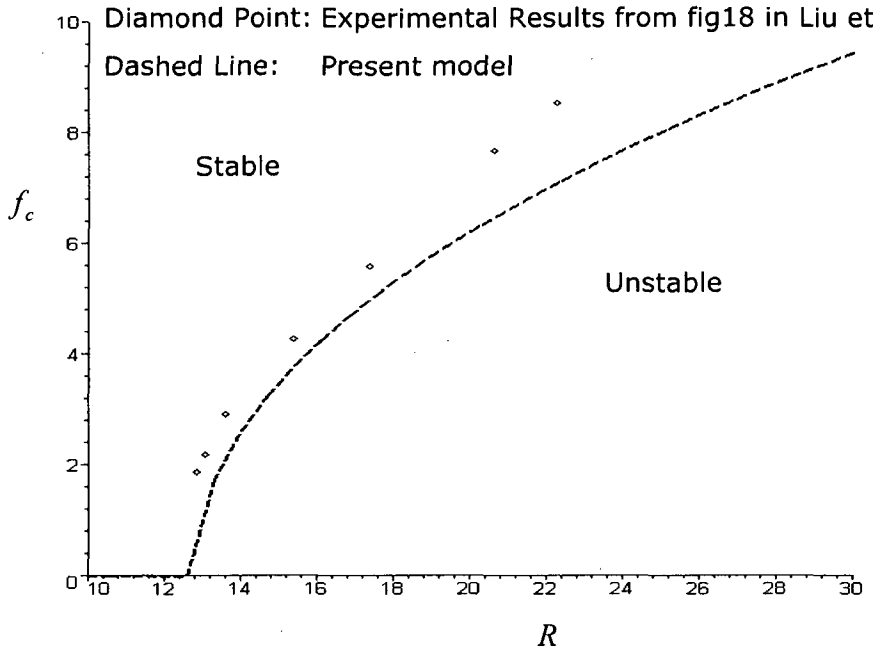


Figure2- 4- Cutoff frequency $\theta = 4.6$ , $\nu = 5.02.10^{-6} m^2 s^{-1}$ , $\rho = 1130.kg.m^{-3}$ , $\sigma = 69.10^{-3} N.m^{-1}$

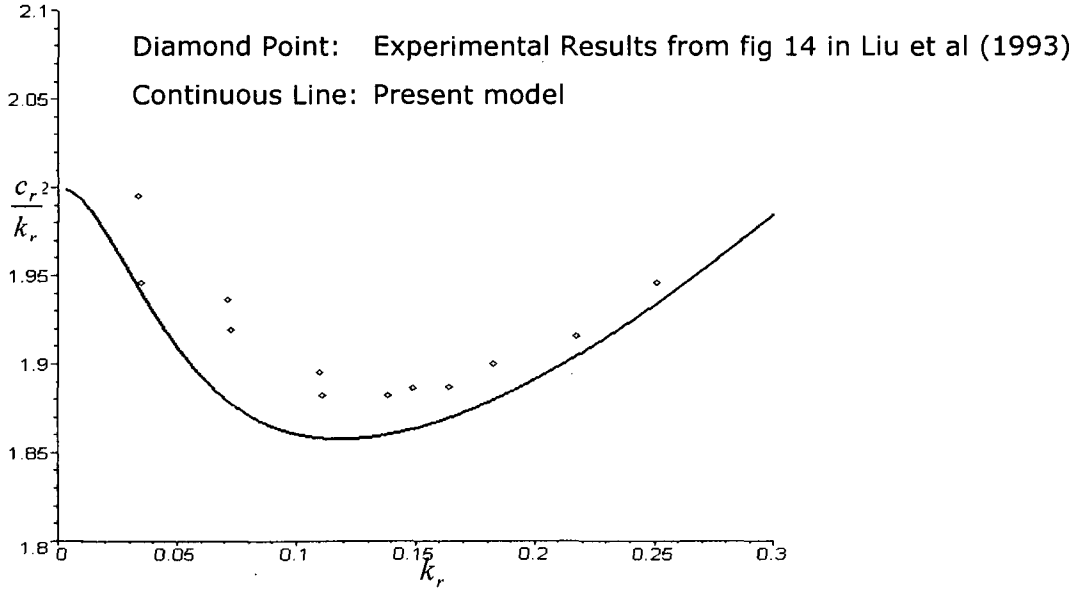


Figure 2-5 Phase velocity $\frac{c_r}{k_r}$ as function of wave number $k_r$. $\nu = 5.02.10^{-6} m^2 s^{-1}$ , $\rho = 1130.kg.m^{-3}$ $\sigma = 69.10^{-3} N.m^{-1}$

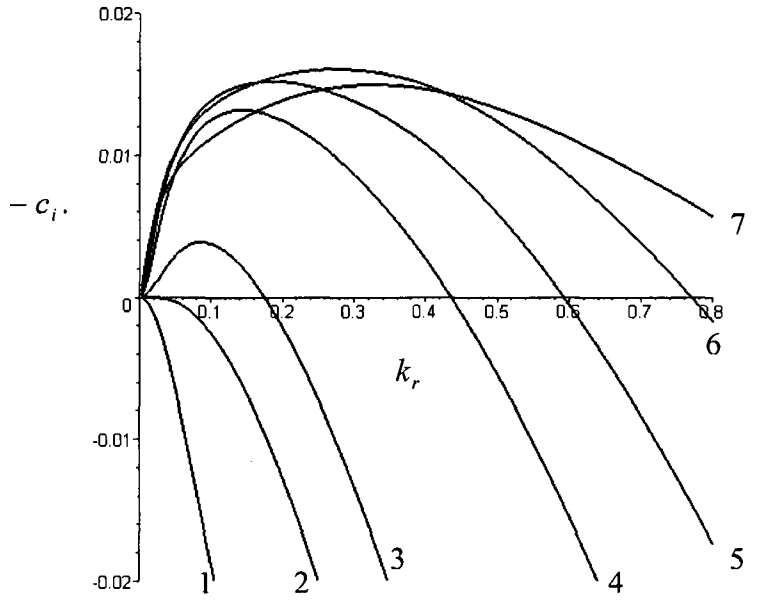


Figure 2- 6 : Temporal growth rate $-c_i$ function of the wave number $k_r$ :
$\theta = 4.6$ , $\nu = 5.02.10^{-6} m^2 s^{-1}$ , $\rho = 1130.kg.m^{-3}$ , $\sigma = 69.10^{-3} N.m^{-1}$. (1) : R=10, $W_e$=104.4.

(2) : $R_c$, $W_e$=77.88. (3): R=20, $W_e$=65.8. (4): R=40,$W_e$=41.46. (5): R=60,$W_e$=31.6. (6): R=100, $W_e$=22.5. (7) R=200, $W_e$=14.18

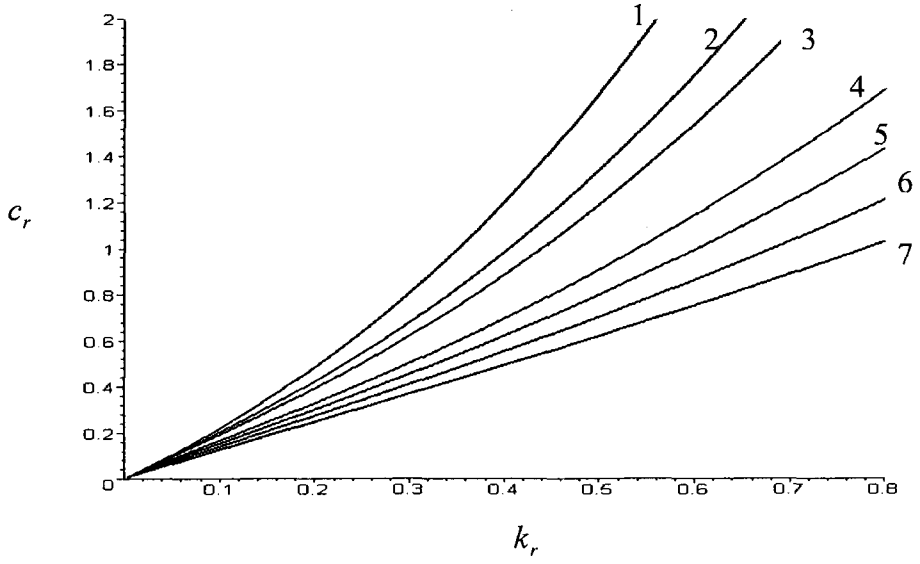


Figure 2-7: Angular frequency $c_r$ function of the frequency $k_r$

$\theta = 4.6$ , $\nu = 5.02.10^{-6} m^2 s^{-1}$ , $\rho = 1130.kg.m^{-3}$ , $\sigma = 69.10^{-3} N.m^{-1}$. (1) : R=10, $W_e$=104.4. (2) : $R_c$, $W_e$=77.88. (3): R=20, $W_e$=65.8. (4): R=40,$W_e$=41.46. (5): R=60,$W_e$=31.6. (6): R=100, $W_e$=22.5. (7) R=200, $W_e$=14.18

The resemblance between figure 2-8(a, b), 2-9(a, b) and figures 3(a, b, c, d) in Brevdo, is clear. The agreement between our results and those given by Brevdo et al is further verified when a reference frame, moving at speeds $V = 1.15$ and $V = 1.16$ with respect to the laboratory frame, is considered. The similitude between the results shown in the figures 2-10, 2-11, 2-12 and 2-13 and those displayed in the figures 5 and 6 given by Brevdo is encouraging. Figure 2-12a shows the three solution branches noted by (1), (2) and (3) for $c_i = 0.01$. The solution (1) is located in the positive $k_i$ half plan. When the growth rate $c_i$ decreases to $c_i = 0.0079$ (see figure 2-12b) the collision of the solution branches (1) and (3) run into the point marked by $k_I$. When the spatial growth rate is decreased, further, to $c_i = 0.0078$, the collision is found between branches (1) and (2) (see figure 2-13b). This collision point is denoted by $k_{II}$. The same similitude is found among figure 2-10a, 2-10b, 2-11a and 2-11b with figure 6 in Brevdo et al.

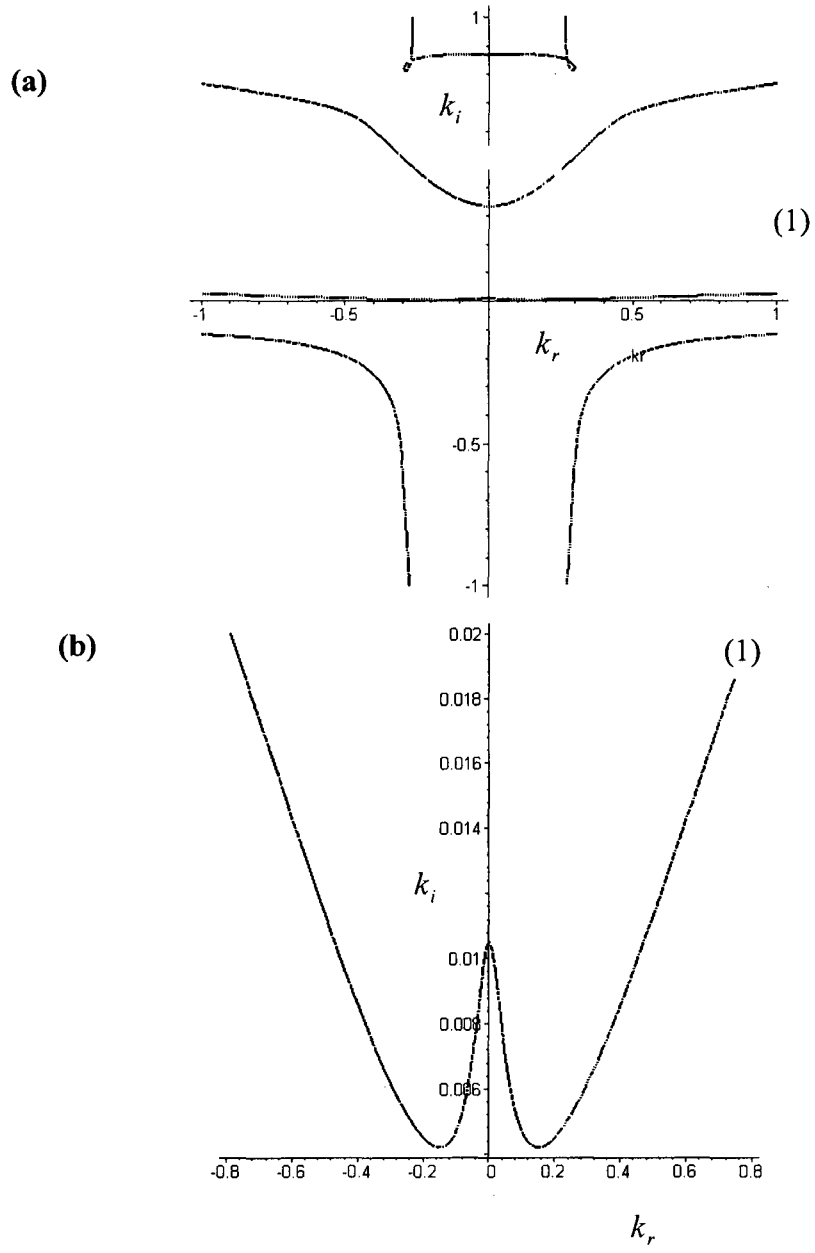


Figure 2-8 a Image of different branches when the growth rate is $c_i = 0.02$

b – Close view on the curve (1) R=40

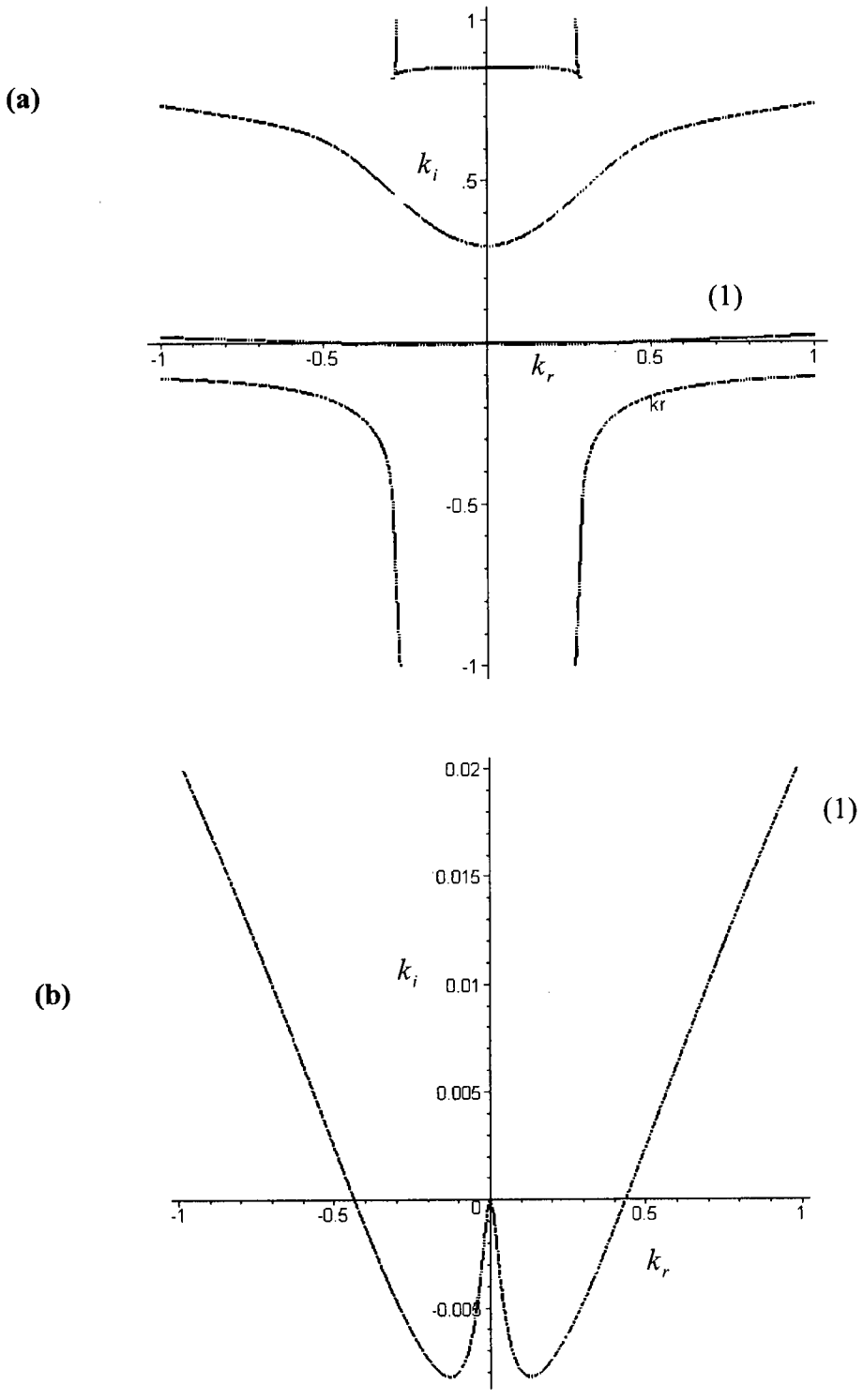


Figure 2-9 a Image of different branches when the growth rate is $c_i = 0$

b – Close view on the curve (1) R=40

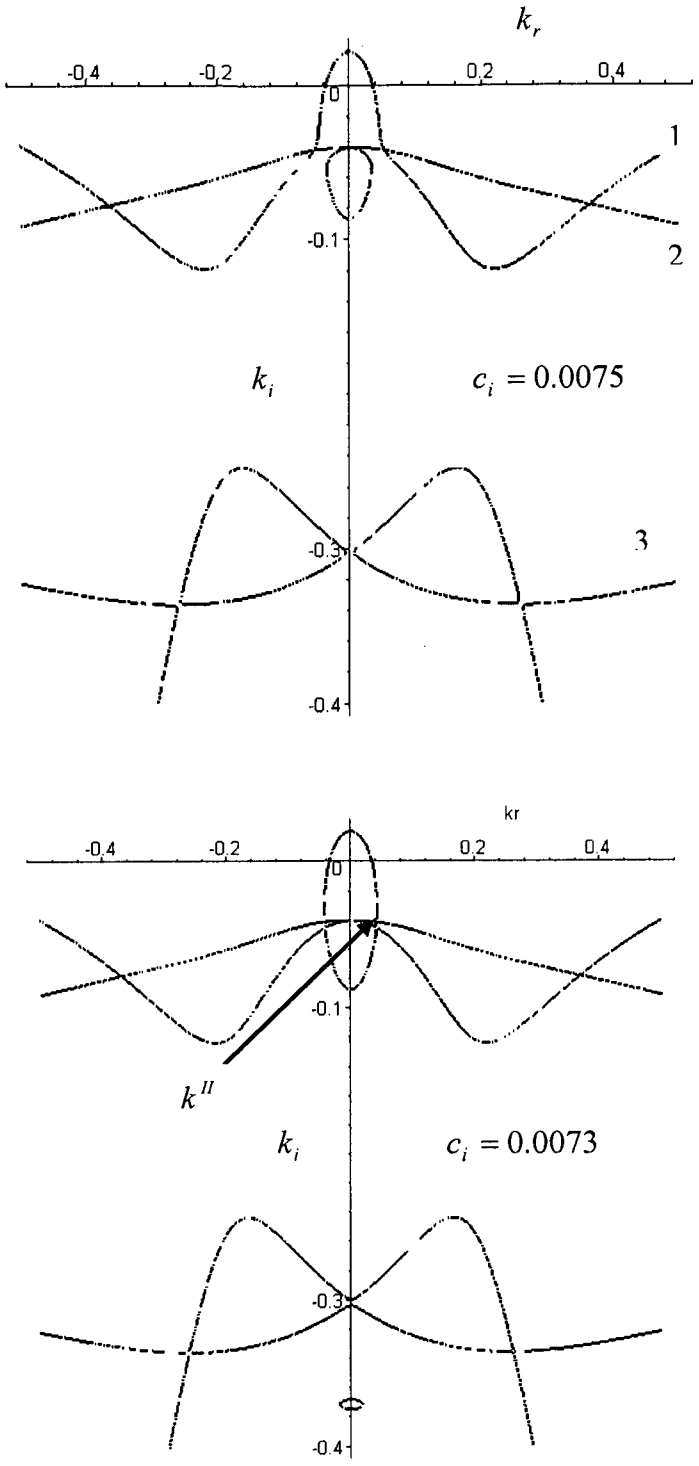


Figure 2-10 Pinching process in the complex wave number plane $(k_i, k_r)$ for V=1.15

$R = 200\ We = 14.18 : \theta = 4.6, \nu = 5.02.10^{-6} m^2 s^{-1}, \rho = 1130.kg.m^{-3}, \sigma = 69.10^{-3} N.m^{-1}$.

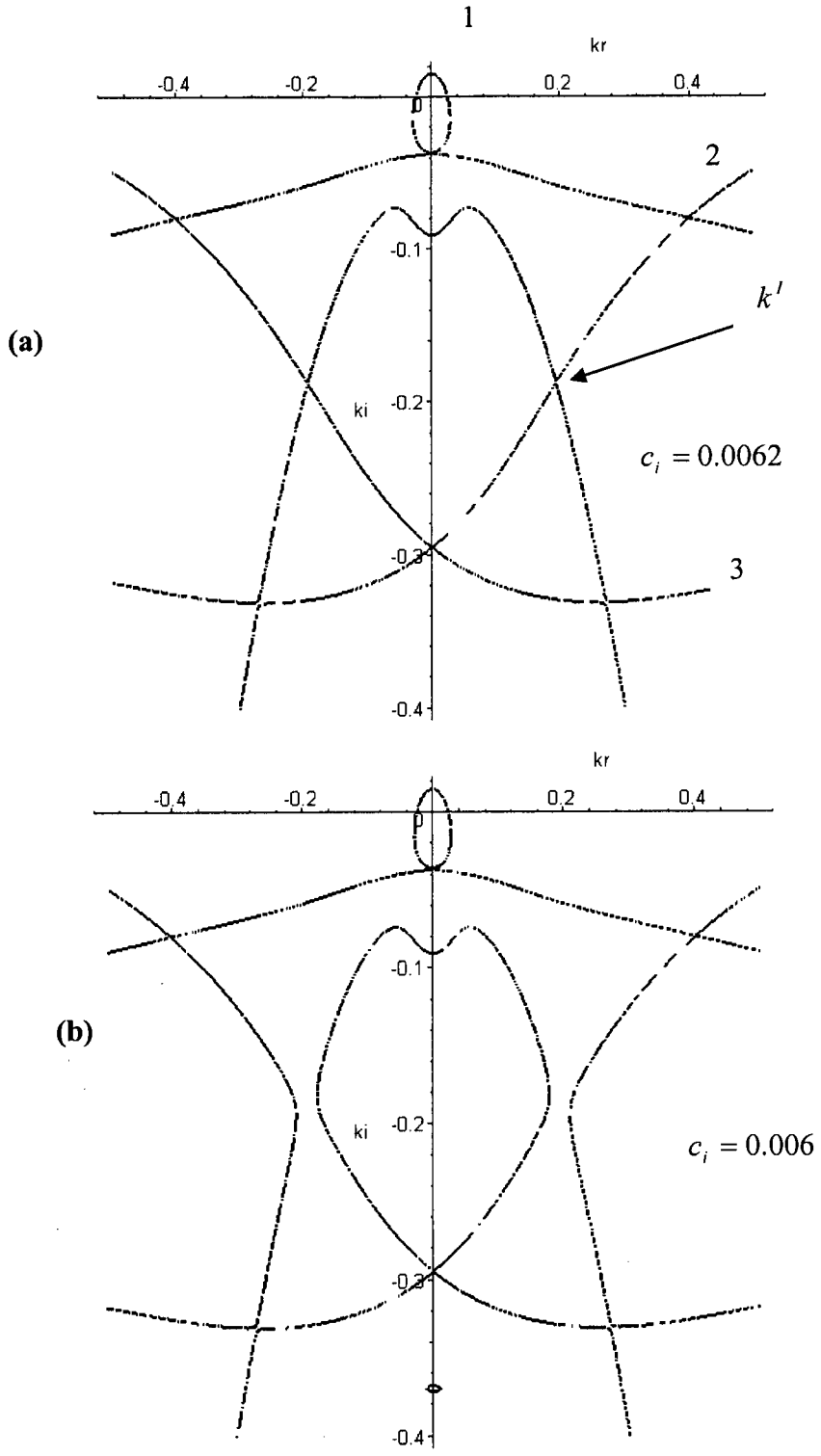


Figure 2-11 Pinching process in the complex wave number plane $(k_i, k_r)$ for V=1.15 $R = 200$ $We = 14.18 : \theta = 4.6, \nu = 5.02.10^{-6} m^2 s^{-1}, \rho = 1130.kg.m^{-3}$, $\sigma = 69.10^{-3} N.m^{-1}$.

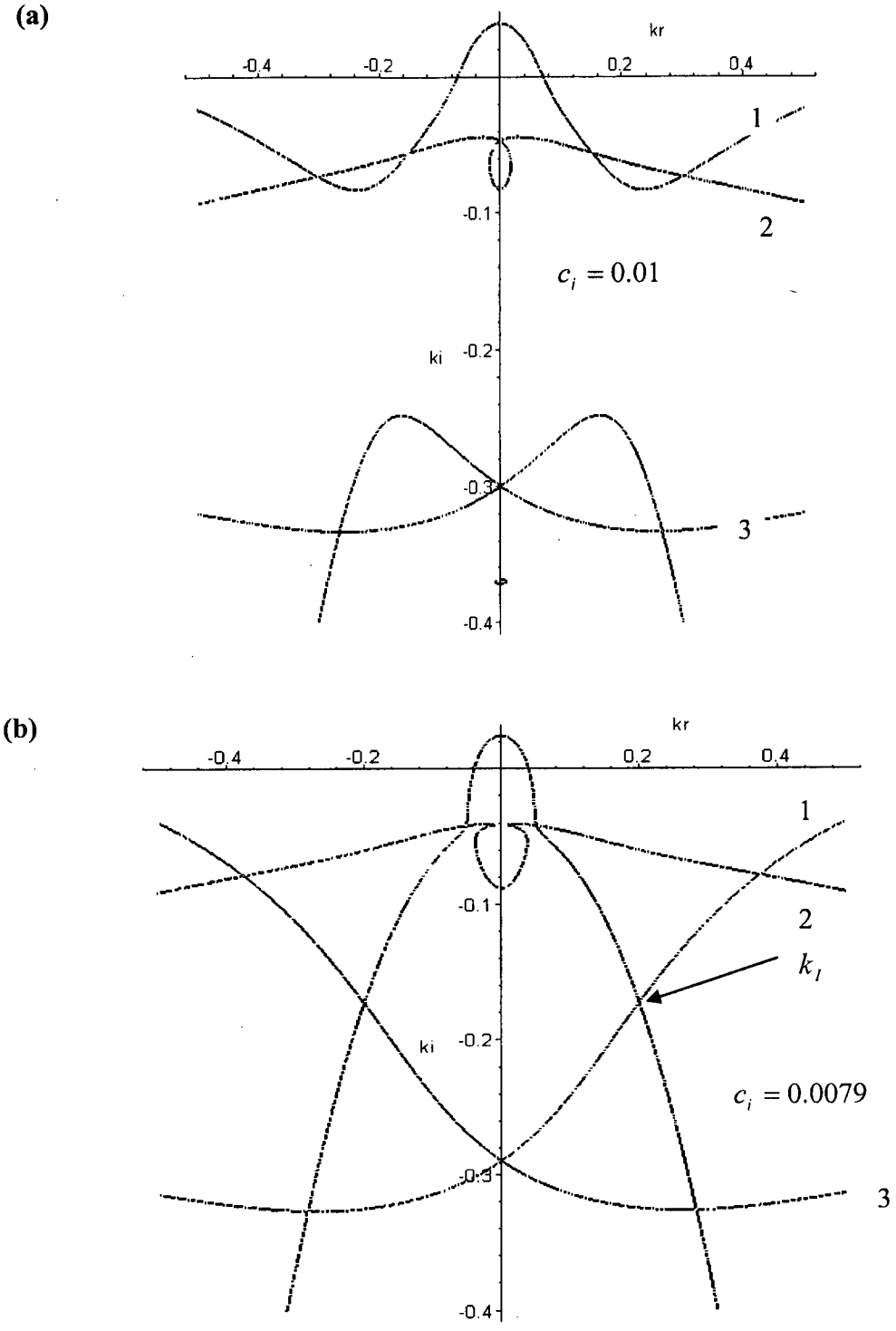


Figure 2-12 Pinching process in the complex wave number plane $(k_i, k_r)$ for V=1.16

$R = 200$ $We = 14.18$ : $\theta = 4.6$, $\nu = 5.02.10^{-6} m^2 s^{-1}$, $\rho = 1130.kg.m^{-3}$, $\sigma = 69.10^{-3} N.m^{-1}$.

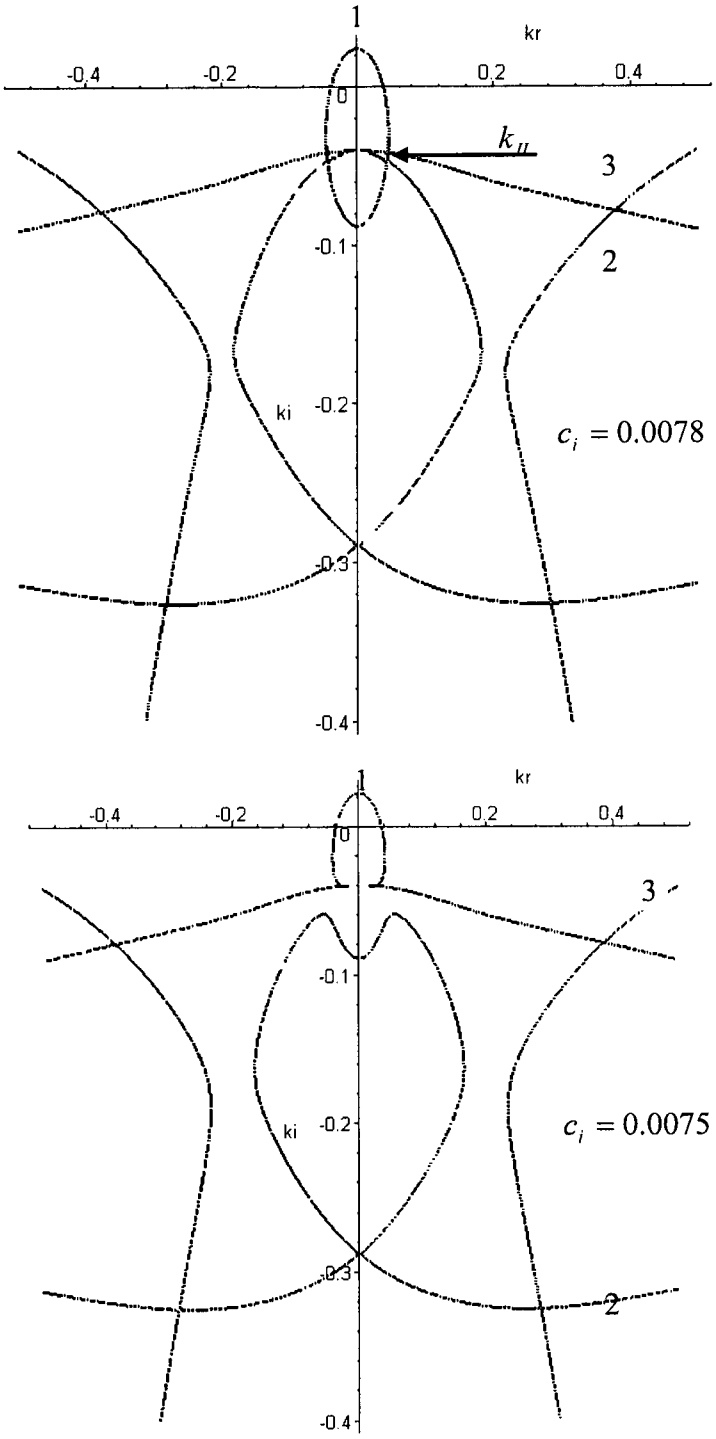


Figure 2-13: Pinching process in the complex wave number plane $(k_i, k_r)$ for V=1.16

$R = 200$ $We = 14.18 : \theta = 4.6, \nu = 5.02.10^{-6} m^2 s^{-1}, \rho = 1130.kg.m^{-3}$, $\sigma = 69.10^{-3} N.m^{-1}$.

The positions of the two saddle points or collision points are recovered with remarkable precision. The results are summarized in the following table.

| | Collision points | $V = 1.15$ | $V = 1.16$ |
|---|---|---|---|
| | | $c_i$ | $c_i$ |
| Brevdo & al | I | 0.0062 | 0.0079 |
| Present model | I | 0.0061 | 0.007889 |
| Brevdo & al | II | 0.0073 | 0.0078 |
| Present model | II | 0.00732 | 0.00779 |

It was shown above that in the range of moderate Reynolds and high Weber numbers respectively, the instability of a liquid film flowing down an inclined plane is convective, which means that the perturbations are swept downstream. Therefore, studying spatial instabilities is more appropriate than temporal. In figures 2-14 and 2-15 the spatial growth rate and angular frequency are calculated and represented for the same values of the incline angle, Reynolds number, and Weber number considered in Brevdo et al. There are no noticeable differences between our results with those presented in the figure 9 in Brevdo et al. Furthermore, the spatial growth rate calculated is compared to the experimental results in figure 16. Here again, there is fair agreement.

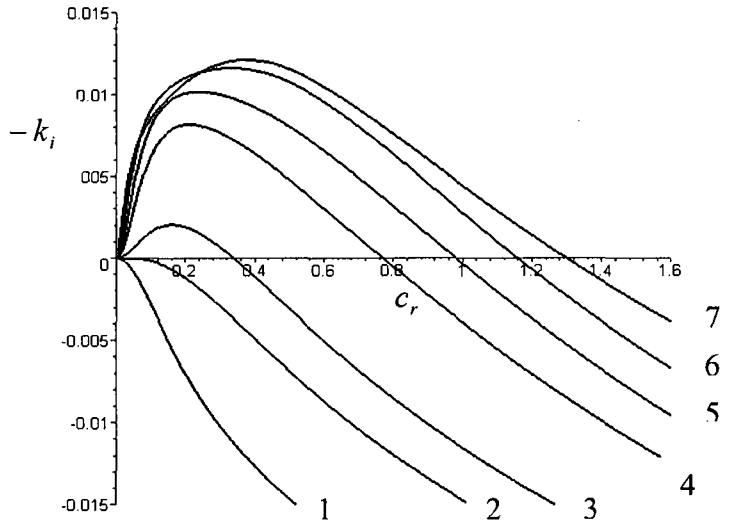


Figure 2-14: Spatial growth rate $-k_i$ function of the frequency $c_r$ :

$\theta = 4.6$ , $\nu = 5.02.10^{-6} m^2 s^{-1}$ , $\rho = 1130.kg.m^{-3}$ , $\sigma = 69.10^{-3} N.m^{-1}$ . (1) : R=10, $W_e$=104.4. (2) : $R_c$, $W_e$=77.88. (3): R=20, $W_e$=65.8. (4): R=40,$W_e$=41.46. (5): R=60,$W_e$=31.6. (6): R=100, $W_e$=22.5. (7) R=200, $W_e$=14.18

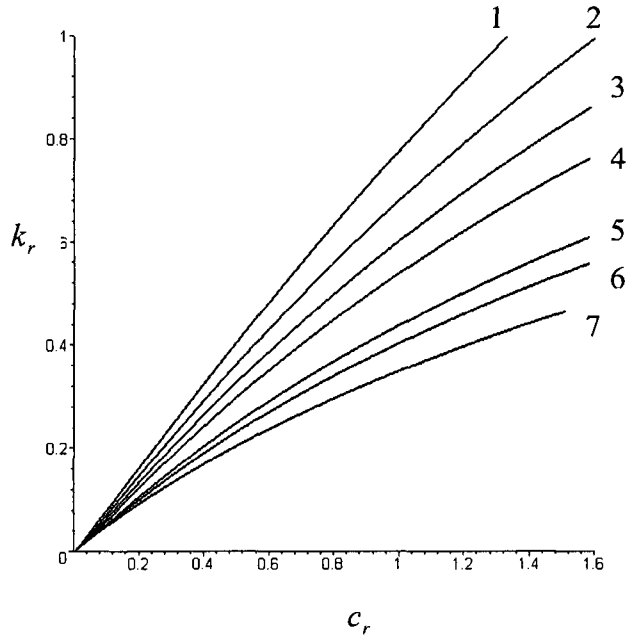


Figure 2-15: Wave number $k_r$ function of the frequency $c_r$ :

$\theta = 4.6$ , $\nu = 5.02.10^{-6} m^2 s^{-1}$ , $\rho = 1130.kg.m^{-3}$ , $\sigma = 69.10^{-3} N.m^{-1}$ . (1) : R=10, $W_e$=104.4. (2) : $R_c$, We=77.88. (3): R=20, $W_e$=65.8. (4): R=40,We=41.46. (5): R=60, $W_e$=31.6. (6): R=100, $W_e$=22.5. (7) R=200, $W_e$=14.18

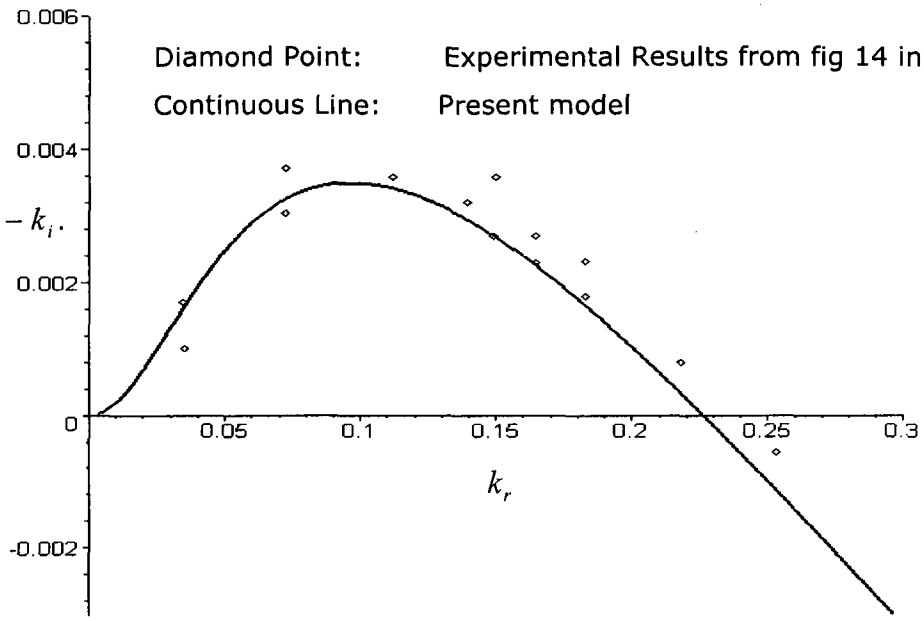


Figure 2-16 Spatial growth rate $-k_i$ as function of wave number $k_r$
$\theta = 4.6$ , $\nu = 5.02.10^{-6} m^2 s^{-1}$ , $\rho = 1130.kg.m^{-3}$ , $\sigma = 69.10^{-3} N.m^{-1}$

### *3.1.2 Conclusion*

Four nonlinear differential equations are proposed to describe the motion of a liquid film flowing down an inclined plane. The formulation involves four equations that portray the development, flow rate, film thickness, shear stress, and velocity on the free surface. The results obtained were found to follow closely those calculated solving the Orr-Sommerfeld equation numerically. The model was further validated using past experimental observations and the outcome of more encompassing linear analyses.

## 3.2. Three-equation model equation

In the following sub section, a three-equation model, one dimension less than the one described in the sub section above, is proposed. In the same way, as before, we use the integral method and similar velocity profile (2-24). Using the cross derivative of the pressure, we relate the coefficient $c(x,t)$ to the coefficient $a(x,t)$ in the velocity profile, hence, reducing the number of equations from four to three. The three-equation model involves only measurable physical quantities: the film depth, flow rate, and wall shear stress. The momentum integral method is used to reduce the Navier-Stokes equations. The adequacy of the proposed model is shown by comparing the present linear stability results with the four-equation model of Ruyer and Manneville (2000) as well as with the numerical solutions of the linear

dynamics of wave packets by Brevdo et al (1999). Moreover, the present solutions compare well with the experiment measurements of Liu et al (993).

Cross differentiating the pressure, and eliminating it from $x-$ and $z-$ momentum equations (2-1) and (2-2), yields the two following equations.

$$p_{xz} = \frac{\partial\left(-\left(u_t + uu_x + wu_z\right) + \frac{1}{R}\left(\varepsilon u_{xx} + \frac{1}{\varepsilon}u_{zz} + \frac{3}{\varepsilon}\right)\right)}{\partial z}$$

$$p_{zx} = \frac{\partial\left(-\left(\varepsilon^2\left(w_t + uw_x + ww_x\right)\right) + \frac{\varepsilon}{R}\left(w_{zz} - \frac{3}{\varepsilon}\cot\theta\right)\right)}{\partial x}$$

Using equation (2-8) and the continuity equation (2-3), we deduce the vertical component, $w$ of the velocity field. Substituting the two velocity components in the two cross derivative equations of pressure above and evaluating the obtained equation at $z=0$, we acquire the following relation between the coefficients $c(x,t)$ and $a(x,t)$.

$$c(x,t) = -\frac{1}{3}.\varepsilon^2\frac{\partial^2 a(x,t)}{\partial x^2} + \frac{R.\varepsilon}{6}\frac{\partial a(x,t)}{\partial t} + O(\varepsilon^3) \qquad (2\text{-}31)$$

From the definitions of the flow rate $q(x,t)$, shear stress at the wall $\tau 0(x,t)$, and shear stress at the free surface $\tau_s(x,t)$, the unknown

coefficients $a(x,t)$ , $b(x,t)$ , and $d(x,t)$ can be related to the film height $h(x,t)$ and the physical quantities $q(x,t)$ $\tau 0(x,t)$ and $\tau_s(x,t)$ by the three following expressions:

$$a(x,t) = \tau 0(x,t)$$

$$b(x,t) = -\frac{3}{14}\frac{h(x,t)^2\tau_s(x,t) + 9.\tau 0(x,t).h(x,t)^2 + 2.c(x,t).h(x,t)^4 - 20.q(x,t)}{h(x,t)^3}$$

$$d(x,t) = \frac{5}{28}\frac{-12.q(x,t) + 4.\tau 0(x,t).h(x,t)^2 - 3.c(x,t).h(x,t)^4 + 2.h(x,t)^2\tau_s(x,t)}{h(x,t)^5}$$

Since $\tau_s(x,t)$ is given by the equation (3-6), only three equations are required to determine the unknown physical quantities $q(x,t)$ , $\tau 0(x,t)$ and $h(x,t)$ . Combining the continuity equation (2-3) and the kinematic boundary condition (2-5) along with Leibniz rule we obtain

$$h_t + q_x = 0 \tag{2.32}$$

Integrating equation (2-2) along the z-coordinate from somewhere in the film to the free surface and using the boundary condition (2-7) to find the constant of integration we find pressure to be.

$$p = \int_z^{h(x,t)} (-\varepsilon^2(w_t + uw_x + ww_x). + \frac{\varepsilon}{R}(w_{zz} - \frac{3}{\varepsilon}\cot\theta))dz + cst$$

$$p = -\varepsilon^2.We.h_{xx} + \frac{\varepsilon\left(-a_x(h+z) - b_x.(h^2+z^2) - c_x.(h^3+z^3) - d_x.(h^4+z^4)\right)}{R} + \frac{3.\cot(\theta)(h-z)}{R}$$

Substituting the pressure, $p$, into equation (2-1) and using the method of moments with a monomial of first and second order with the boundary condition (2-6), we deduce both the second and the third equations.

$$\int_0^{h(x,t)} z.(u_t + uu_x + wu)dz = \int_0^{h(x,t)} z.\left(-p_x + \frac{1}{R}(\varepsilon u_{xx} + \frac{1}{\varepsilon}u_{zz} + \frac{3}{\varepsilon})\right)dz$$

$$\int_0^{h(x,t)} z^2.(u_t + uu_x + wu)dz = \int_0^{h(x,t)} z^2.\left(-p_x + \frac{1}{R}(\varepsilon u_{xx} + \frac{1}{\varepsilon}u_{zz} + \frac{3}{\varepsilon})\right)dz$$

These two nonlinear equations are given in appendix C. Note that the long wave parameter $\varepsilon$ is not a supplementary parameter, one can get rid of it by rescaling the equations.

### *3.2.1 Linear stability*

The system of three nonlinear equations (see appendix C) is linearized around the basic solution:

$$(q(x,t), h(x,t), \tau 0(x,t)) = (1,1,3) + (Q(x,t), H(x,t), \tau(x,t))$$

and leads to:

$$H_t + Q_x = 0 \qquad (2\text{-}33)$$

$$\frac{1}{2}H_{xxxx}.We.\varepsilon^3+\left(-\frac{67}{14}\frac{H_{xx}}{R}-\frac{137.R}{94080}\tau_{xxt}-\frac{13}{84.R}\tau_{xxx}-\frac{R}{1680}\tau_{xtt}-\frac{47}{14.R}H_{xxt}\right).\varepsilon^2+ \tag{2-34}$$
$$\left(\frac{1503}{784}H_{xt}+\frac{1227}{980}H_{xx}-\frac{3}{2.R}H_{xx}.\cot(\theta)+\frac{5}{7}H_{tt}+\frac{279}{3920}\tau_{xx}+\frac{1}{42}\tau_{xt}\right).\varepsilon+\frac{81}{14.R}H_x+\frac{3}{14.R}\tau_x+\frac{15}{7.R}H_t=0$$

$$-\frac{1}{3}H_{xxxx}.We.\varepsilon^3+\left(\frac{883}{245}\frac{H_{xx}}{R}+\frac{13.R}{9408}\tau_{xxt}+\frac{169}{1470R}\tau_{xxx}+\frac{13.R}{17640}\tau_{xtt}+\frac{124}{49.R}H_{xxt}\right).\varepsilon^2 \tag{2-35}$$
$$+\left(-\frac{733}{490}H_{xt}-\frac{195}{197}H_{xx}+\frac{1}{.R}H_{xx}.\cot(\theta)-\frac{27}{49}H_{tt}-\frac{61}{980}\tau_{xx}-\frac{16}{735}\tau_{xt}\right).\varepsilon-\frac{39}{7.R}H_x-\frac{3}{7.R}\tau_x-\frac{16}{7.R}H_t=0$$

Note that equation (2-11) was used to eliminate $q(x,t)$ from the two linearized equations (2-12) and (2-13). The perturbation quantities are expanded in the form of normal modes and the equations are rescaled in the streamwise direction in order to drop the parameter $\varepsilon$.

$$(H(x,t),\tau(x,t))\approx(A,B).e^{i(k.x-ct)}$$

Where $A$ and $B$ are arbitrary constants, while $c=c_r+i.c_i$ and $k=k_r+i.k_i$ are the complex angular frequency and complex wave number, respectively. Subsequently, the two linear partial differential equations (2-12) and (2-13) are transformed into two algebraic equations with two constants $A$ and $B$. The condition for a nontrivial solution for the algebraic system leads to the dispersion equation, which relates the angular frequency $c$ to the wave number $k$. The dispersion equation is a polynomial of sixth order and it is given in appendix B. In the frame of long waves ( $k\to 0$ ), the angular frequency can be expanded as: $c=a_1k+a_2k^2+a_3k^3$. Thus, solving the dispersion equation for $a_1,a_2$, yields $a_1=3$ which is the angular frequency of

the long waves and $a_2 = \frac{1}{5}(6.R - 5\cot\theta).i$. At the marginal stability condition, the imaginary coefficient $a_2$ should be null; this condition leads to the stability threshold $R_c = \frac{5}{6}\cot\theta$, given in Yih (1955) and Benjamin (1957). Note that the latter condition is independent from the Weber number, which is expected because the curvature of the free surface is small. Separating the real and the imaginary parts of the dispersion equation, we obtain two equations for four unknowns, $k_r$ , $k_i$ , $\omega_i$ and $\omega_r$ . The marginal stability conditions for both spatial and temporal formulation are ensured for $c_i = 0$ and $k_i = 0$. In order to compare our results with those given by Brevdo et al (1999) and those obtained with the model of Ruyer and Manneville (2000) the transformation $(c, R, We) \rightarrow (\frac{3}{2}c, \frac{2}{3}R, \frac{9}{2}\frac{We}{R})$ is performed. Then the two previous equation that resulted from the dispersion equation are solved for $k_r$ and $c_r$. The results are presented in the form of a cut-off frequency that separates the stable region from the unstable one. The results are compared to the experimental results provided by Liu et al (1993) and to those obtained with the dispersion equation given by Ruyer and Manneville (2002), given in the figures 2-16 and 2-17 for two different angles of $\theta$. Our results are in excellent agreement with the ones obtained with the four-equation model of Ruyer and Manneville (2002). It is worth noting that the same discrepancy with experimental results of Liu et al (1993) is observed in Brevdo et al (1999) (see figure 12 in Brevdo et al (1999)).

Diamond Point: Experimental Results from fig 4 in Liu et al (1993)
Dashed Line: Present model
Doted Line: Four equation model of Ruyer and Manneville (2000)

Stable region

Stable region

$f_c(Hz)$

Unstable region

$R$

R

Figure 2-17- Cutoff frequency $\theta = 5.6$, $\nu = 5.02.10^{-6} m^2 s^{-1}$, $\rho = 1130.kg.m^{-3}$ $\sigma = 69.10^{-3} N.m^{-1}$

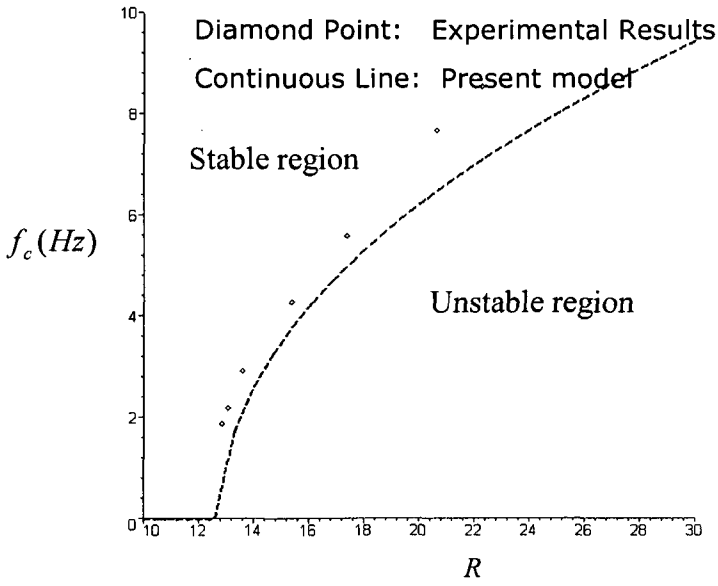


Figure 2-18 Cutoff frequency $\theta = 4.6$, $\nu = 5.02.10^{-6} m^2 s^{-1}$, $\rho = 1130.kg.m^{-3}$,

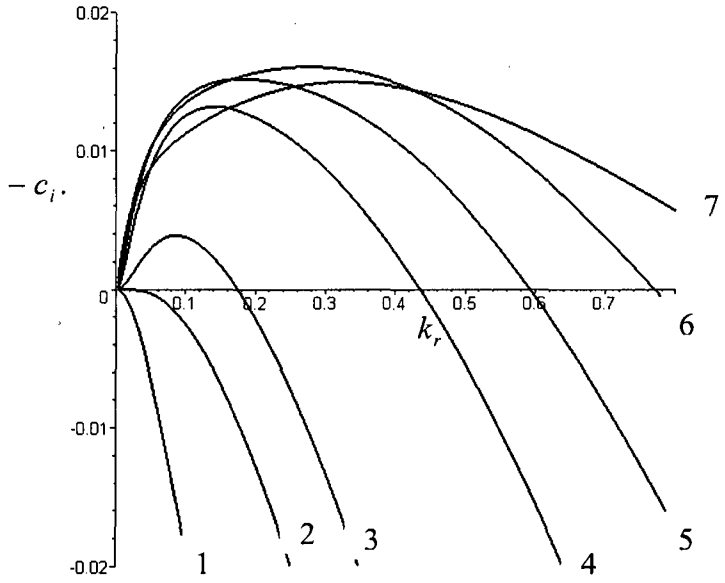


Figure 2-19 : Temporal growth rate $-c_i$ function of the wave number $k_r$ :

$\theta = 4.6$ , $\nu = 5.02.10^{-6} m^2 s^{-1}$ , $\rho = 1130.kg.m^{-3}$ , $\sigma = 69.10^{-3} N.m^{-1}$. (1) : R=10, $W_e$=104.4. (2) : $R_c$, $W_e$=77.88 (3): R=20, $W_e$=65.8. (4): R=40,$W_e$=41.46. (5): R=60,$W_e$=31.6. (6): R=100, $W_e$=22.5.

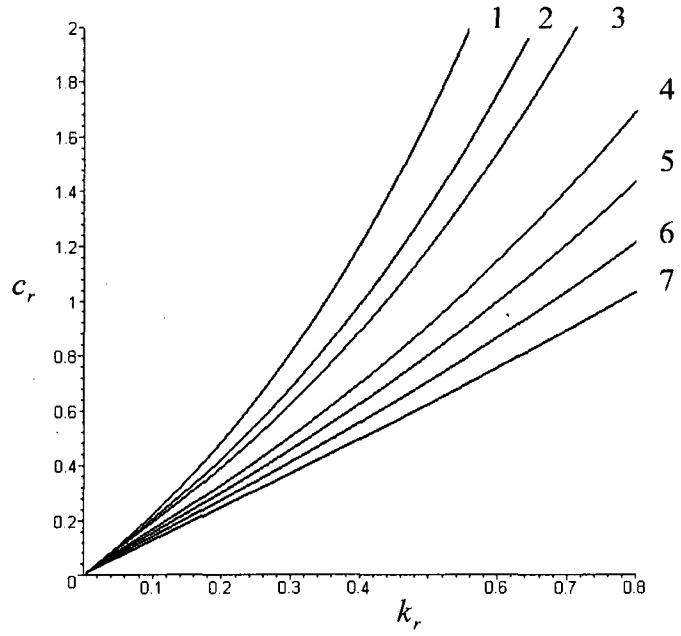


Figure 2-20: Angular frequency $c_r$ function of the frequency $k_r$ :

$\theta = 4.6$ , $\nu = 5.02.10^{-6} m^2 s^{-1}$ , $\rho = 1130.kg.m^{-3}$ , $\sigma = 69.10^{-3} N.m^{-1}$. (1) : R=10, $W_e$=104.4. (2) : $R_c$, $W_e$=77.88. (3): R=20, $W_e$=65.8. (4): R=40,$W_e$=41.46. (5): R=60,$W_e$=31.6. (6): R=100, $W_e$=22.5.

wave number are calculated and represented in the figure 2-18 and 2-19. These are found to be similar to figure 2 in Brevdo et al (1999). The comparison of our results for the temporal growth rate with the model of Ruyer and Manneville for two values of the Reynolds number shows a good agreement between the two models, see figures 2-20 and 2-21. In figure 2-21 the curves coincide very well. As in Brevdo et al (1999) we have displayed in figures 2-22 and 2-23 the numerical solutions of the dispersion equation in the $(k_r, k_i)$ plane, for $R = 40$, $We = 41.46$, $\theta = 4.6^o$ and given growth rate $c_i$, while the oscillation frequency, $c_r$, is varied. As in Brevdo et al (1999) we show through figures 2-22 and 2-23 the motion of the solution curves when the growth rate is decreased from $c_i = 0.02$ to $c_i = 0$. No pinching of the spatial branches occurs; according to the collision criteria, the film flowing down an inclined plane is absolutely stable and convectively unstable, see Huerre and Monkewitz (1998). In figure 2-22 and 2-23 our results are also compared to those obtained with the four-equation model of Ruyer and Manneville (2002). The resemblance between figure 2-22(a, b), 2-23(a, b) and figures 3(a, b, c, d) in Brevdo et al (1999) is clear, and the agreement with the results in Ruyer and Manneville (2002) is again evident.

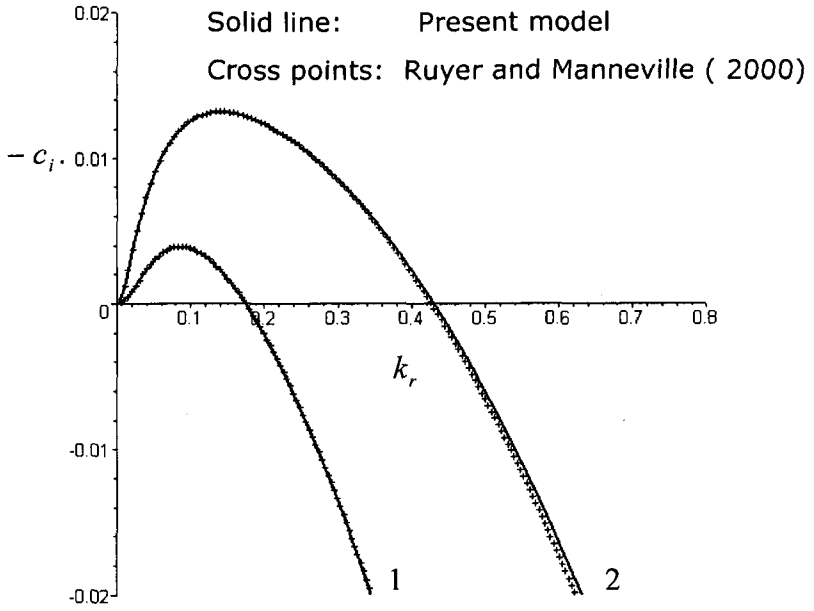


Figure 2-21 : Temporal growth rate $-c_i$ function of the wave number $k_r$ :

$\theta = 4.6$ , $\nu = 5.02.10^{-6} m^2 s^{-1}$ , $\rho = 1130.kg.m^{-3}$ , $\sigma = 69.10^{-3} N.m^{-1}$ . R=20, $W_e$=65.8. (1): R=40,$W_e$=41.46. (2).

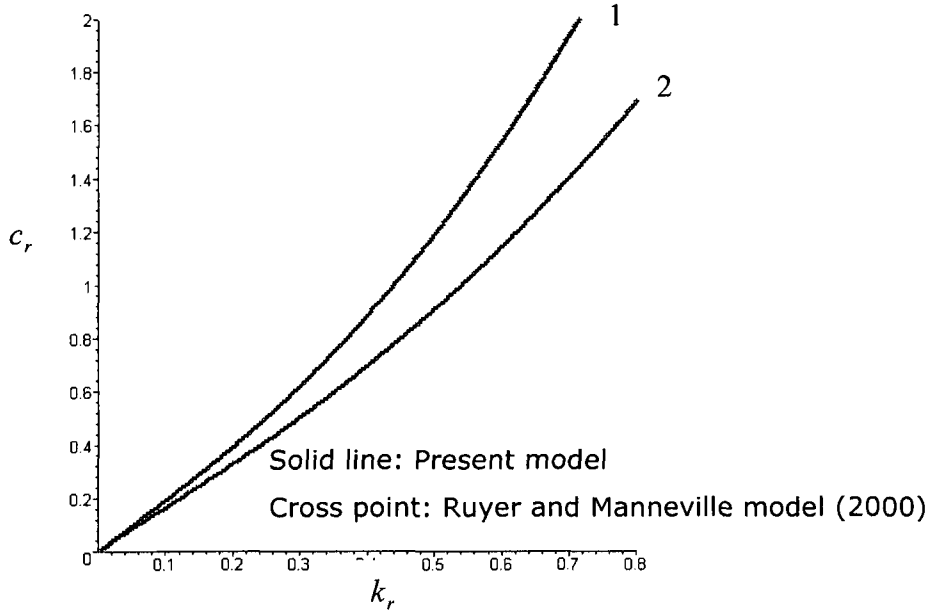


Figure 2-22: Angular frequency $c_r$ function of the frequency $k_r$ :

$\theta = 4.6$ , $\nu = 5.02.10^{-6} m^2 s^{-1}$ , $\rho = 1130.kg.m^{-3}$ , $\sigma = 69.10^{-3} N.m^{-1}$ . R=20, $W_e$=65.8. (1): R=40,$W_e$=41.46. (2).

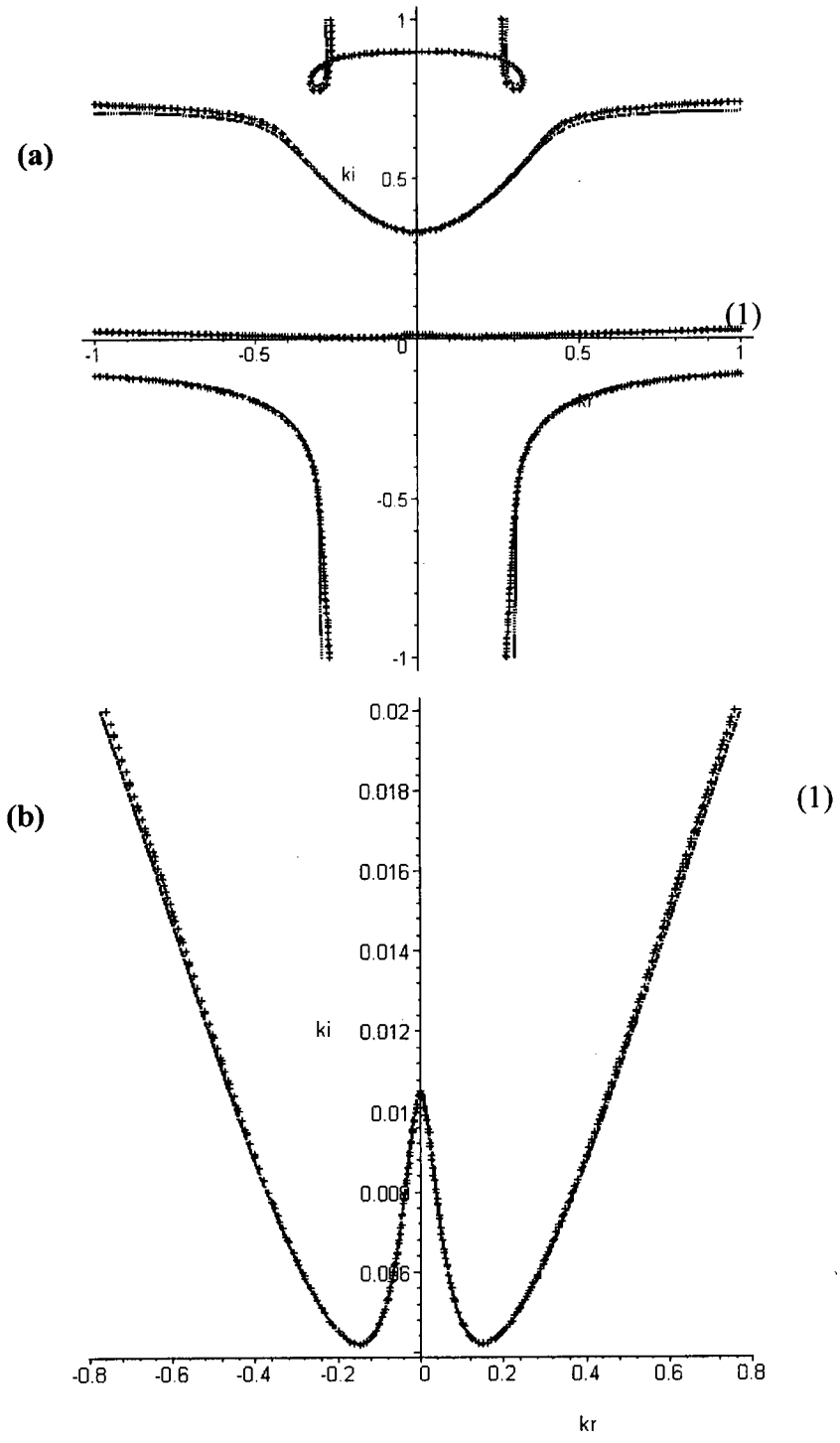


Figure 2-23 a - Image of different branches in $(k_r, k_i)$ plan when the growth rate is $c_i = 0.02$ , b – Close view on the curve (1) R=40

Solid line: Present model

Cross points: Ruyer and Manneville ( 2000)

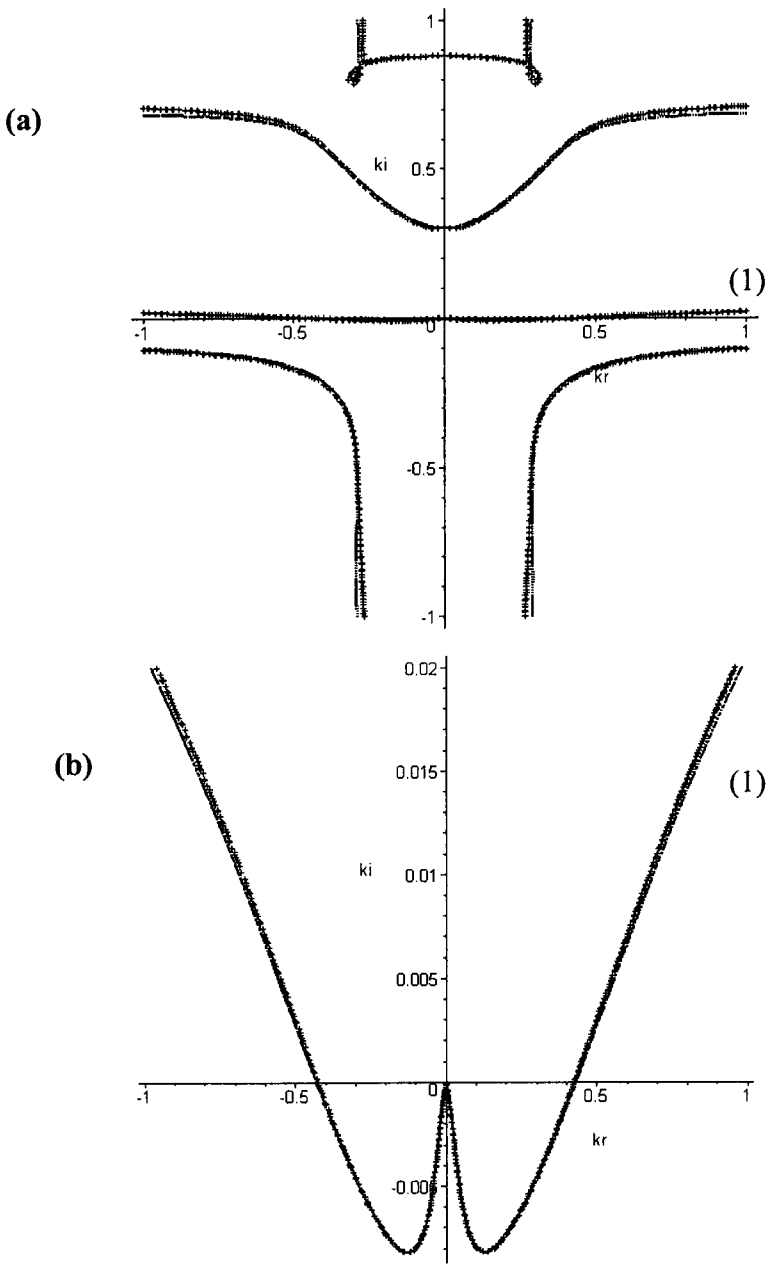


Figure 2.24 a - Image of different branches when the growth rate is $c_i = 0$

b – Close view on the curve (1) R=40

Since the perturbations are swept down (convective instability), studying spatial instabilities is more appropriate than temporal ones. In figures 2-24 and 2-25 we present the spatial growth rate and the angular frequency for the same values of the incline angle, Reynolds, and Weber considered by Brevdo et al (1999). There are no noticeable differences between our results with those presented in figure 9 in Brevdo et al (1999). Furthermore, the spatial growth rate and the angular frequency are calculated and compared to the experimental results and with those obtained from the model proposed by Ruyer and Manneville (2002) see figure 3-26 and figures 3-27. Here again, the agreement with the four-equation model of Ruyer and Manneville is very good, and fairly good with experimental data.

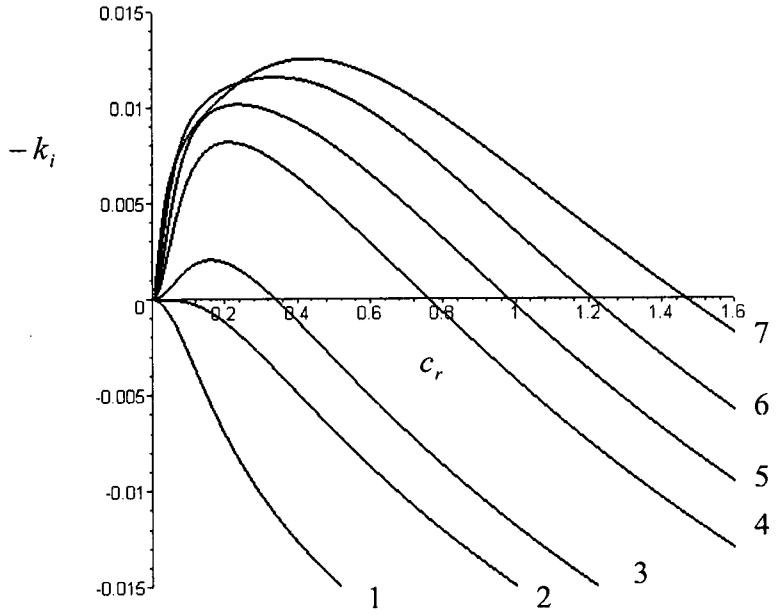


Figure 2-25 : Spatial growth rate $-k_i$ function of the frequency $c_r$ :

$\theta = 4.6$ , $\nu = 5.02.10^{-6} m^2 s^{-1}$ , $\rho = 1130.kg.m^{-3}$ , $\sigma = 69.10^{-3} N.m^{-1}$. (1) : R=10, $W_e$=104.4. (2) : $R_c$, $W_e$=77.88. (3): R=20, $W_e$=65.8. (4): R=40,$W_e$=41.46. (5): R=60,$W_e$=31.6. (6): R=100, $W_e$=22.5. (7) R=200, $W_e$=14.18

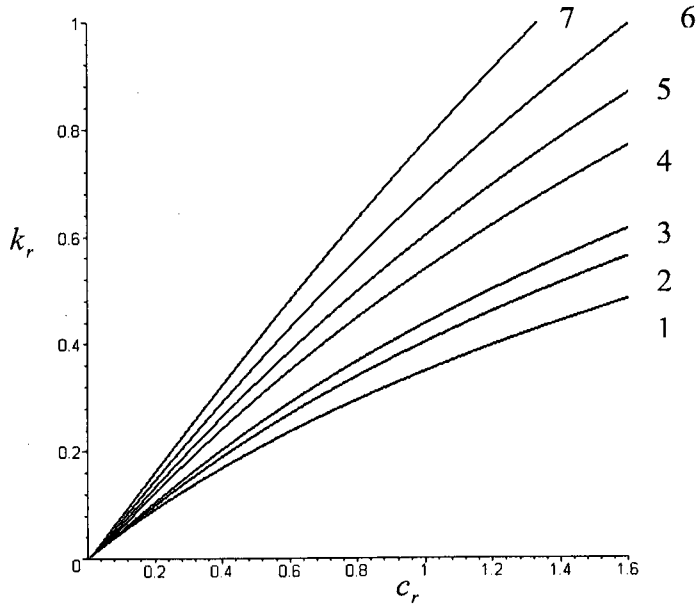


Figure 2-26 : Wave number $k_r$ function of the frequency $c_r$ :

$\theta = 4.6$ , $\nu = 5.02.10^{-6} m^2 s^{-1}$ , $\rho = 1130.kg.m^{-3}$ , $\sigma = 69.10^{-3} N.m^{-1}$. (1) : R=10, $W_e$=104.4. (2) : $R_c$, We=77.88. (3): R=20, $W_e$=65.8. (4): R=40,We=41.46. (5): R=60, $W_e$=31.6. (6): R=100, $W_e$=22.5. (7) R=200, $W_e$=14.18

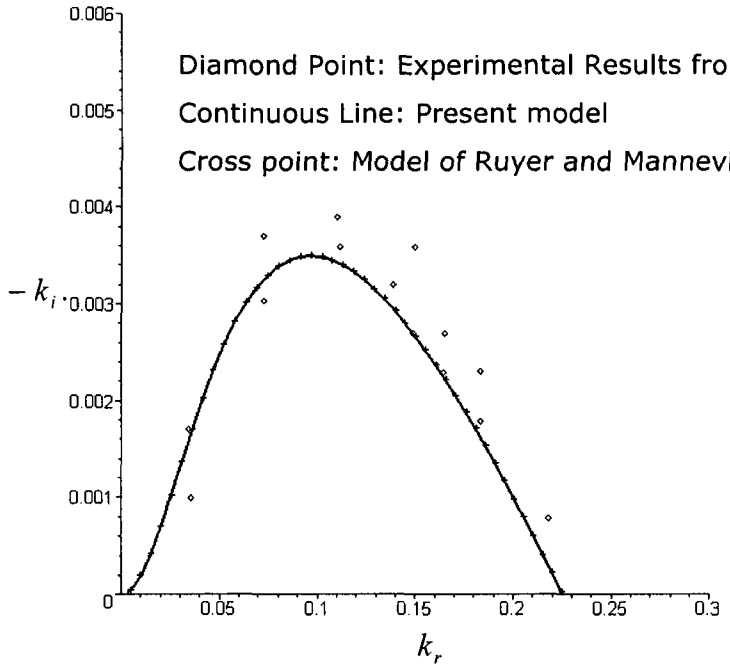


Figure 2-27 Spatial growth rate $-k_i$ as function of wave number $k_r$

$\theta = 4.6$ , $\nu = 5.02.10^{-6} m^2 s^{-1}$ , $\rho = 1130.kg.m^{-3}$ , $\sigma = 69.10^{-3} N.m^{-1}$

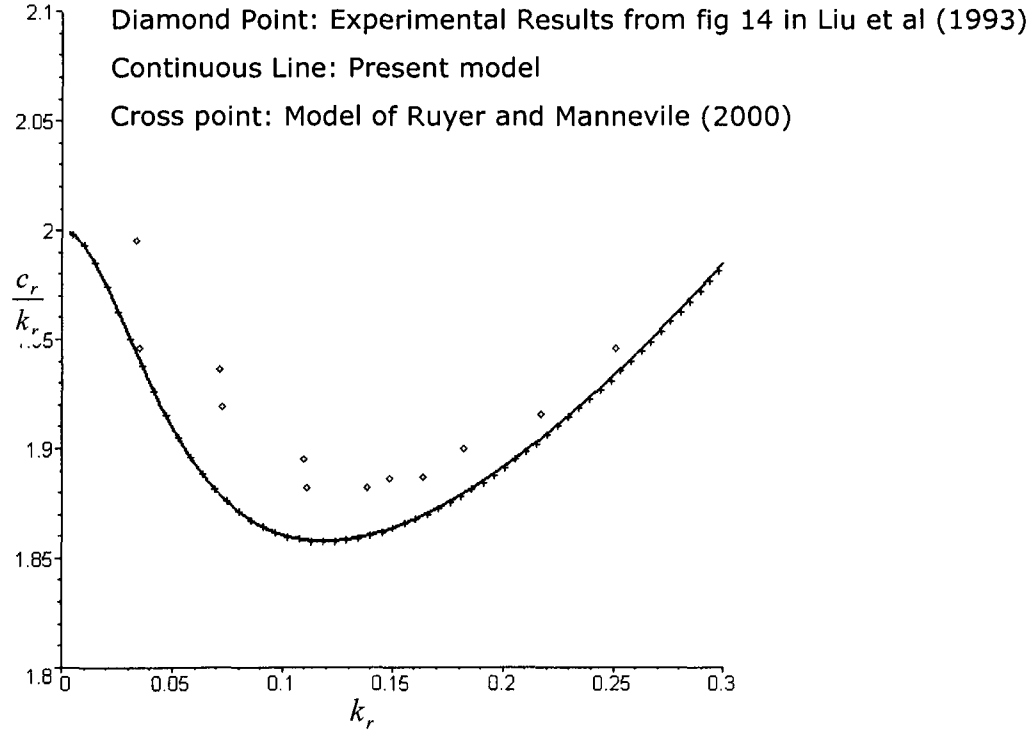


Figure 2-28 Phase velocity $\frac{c_r}{k_r}$ as function of wave number $k_r$.

$\theta = 4.6$ , $\nu = 5.02.10^{-6} m^2 s^{-1}$ , $\rho = 1130.kg.m^{-3}$ , $\sigma = 69.10^{-3} N.m^{-1}$

### 3.2.2 Conclusion

In the frame of long wave approximation, the Navier-Stokes equations, accurate up to second order with respect to the long wave parameter, are reduced with the momentum integral method into three equations which involve three measurable quantities: the flow rate, film thickness, and shear stress. This model predicts the stability threshold, $R_c = \frac{5}{6}\cot\theta$, and linear stability results are in perfect agreement with the outcome of more encompassing linear analyses of Brevdo et al (1999). Furthermore, our results agree very well with those obtained with the four-equation model of Ruyer and Manneville (2002). Similar to the named contributions, the measured cut-off frequency, spatial growth rate and phase velocity are satisfactory recovered.

# Chapter III: Two-equation Model

Our contribution depicted in this chapter consists of the improvement of the two-equation model of Usha and Uma (2004). The two authors have claimed that their model is accurate up to the second order with respect to the long wave parameter (ratio between film height and wave length). However a close examination of their model indicates that, although it is of second order, they have neglected the variation of shear stress at the free surface. In this chapter, this inconsistency is corrected by including the shear stress in the velocity profile. This third degree of freedom, besides the flow rate and film thickness in the equations, induce significant differences in the occurring conditions of the bifurcations (symmetry breaking), as well as on the wave profiles.

## 1. The Model

As before, let us consider the two-dimension flow of the thin liquid layer down an inclined plane, see Figure 2.1. The air above the film fluid is considered to have a negligible density. The governing equations, accurate up to the second order in dimensionless form, are given as follow

$$u_t + uu_x + wu_z = -p_x + \frac{1}{R}(\varepsilon u_{xx} + \frac{1}{\varepsilon}u_{zz} + \frac{3}{\varepsilon}) \tag{3-1}$$

$$\varepsilon^2(w_t + uw_x + ww_x) = -p_z + \frac{\varepsilon}{R}(w_{zz} - \frac{3}{\varepsilon}\cot\theta) \tag{3-2}$$

$$u_x + w_z = 0 \tag{3-3}$$

$$z=0: \qquad u=w=0 \tag{3-4}$$

$$z=H(x,t): \qquad w=H_t+uH_x \tag{3-5}$$

$$u_z+\varepsilon RPH_x+\varepsilon^2(w_x-2u_xH_x)+\varepsilon^3W_eRH_{xx}H_x=0 \tag{3-6}$$

$$P+\frac{\varepsilon}{R}(u_zH_x-2w_z)+\varepsilon^2W_eH_{xx}=0 \tag{3-7}$$

Subscripts, $x$ and $z$, indicate partial derivatives of the variables with respect to $x$ and $z$, respectively. For normalisation, the scales based on the Nusselt flow are used; which are: $H_0$, $L$ and $c_0$. Initial film is represented by $H_0$, $L$ is the characteristic length and $c_0$ is the Nusselt velocity, which is defined by $c_0=\frac{gH_0^2\sin\theta}{3\nu}$. The non-dimensional equations now involve the following dimensionless parameters: $R=\frac{c_0H_0}{\nu}$, $We=\frac{\gamma}{\rho H_0c_0^2}$, $Fr=\frac{gH_0\cos\theta}{c_0^2}=\frac{3\cot\theta}{R}$ and $\varepsilon=\frac{H_0}{L}$ which are the Reynolds, Weber, Froude numbers and a long wave parameter. Note that for the problem under consideration, the last dimensionless parameter, $\varepsilon$, is relatively small. In addition, the equations (3-1-3-7), we have assumed that the Reynolds number is relatively high $R=O(\varepsilon^{-1})$. For most fluids, such as water and mercury, the corresponding Weber number is $We=O(1)$. In a certain range of flow parameters the basic solution, corresponding to the zero order solution of the system (3-1-3-7), loses its stability and gives rise to solutions for which inertial effects are important. In order to initiate the analysis via the energy integral method and momentum integral method, Usha and Uma (2004) and Lee and Mei (1996) considered a

parabolic velocity profile similar to the basic solution of Nusselt (1916). This parabolic velocity profile leads to $\tau(x,H,t)=\left.\frac{du}{dz}\right|_{z=H}=0$ while the remaining terms in equation (3-6) are not null, which is inconsistent with the second order accuracy with respect to the long wave parameter $\varepsilon$ . To remedy this inconsistency, the following velocity profile is assumed

$$u(x,z,t)=a(x,t)z+b(x,t)z^2 \tag{3-9}$$

From the definitions of the flow rate, $Q(x,t)$, shear stress at the free surface, $\tau_s(x,t)$, and unknown coefficients $a(x,t)$ and $b(x,t)$ can be related by the following two equations.

$$a(x,t)=-\frac{1}{2}\frac{H(x,t)^2\tau_s(x,t)-6Q(x,t)}{H(x,t)^2} \tag{3-10}$$

$$b(x,t)=\frac{3}{4}\frac{-2Q(x,t)+H(x,t)^2\tau_s(x,t)}{H(x,t)^3} \tag{3-11}$$

Hence, three equations are required to determine the unknown physical quantities $Q(x,t)$ , $\tau_s(x,t)$ and $H(x,t)$ . The equation (3-6) can be rewritten explicitly in term of variables $Q(x,t)$ and $H(x,t)$,as:

$$\tau_s(x,t) = \varepsilon^2 \left(\frac{3Q_x.H_x}{H} - \frac{3QH_x^{\ 2}}{H^2} + Q_{xx} - \frac{3}{2}\frac{QH_{xx}}{H}\right) + O(\varepsilon^4) \tag{3-12}$$

Then, only two equations are required to describe the problem of thin film flow over an inclined plane. The first equation is obtained by combining the continuity equation (3-3) and the kinematic boundary condition (3-5) along with Leibniz rule.

$$H_t + Q_x = 0 \tag{3-13}$$

Integrating the equation (3-2) for pressure and using the boundary condition (3-7) to eliminate the constant. The pressure is derived with respect to $x$ and substituted in equation (3-1). The latter equation is multiplied by the velocity profile (3-9) and averaged over the film depth in the normal direction. Finally the shear stress $\tau_s(x,t)$, given by (3-12), is substituted in the last equation and the second equation is obtained.

$$\int_0^H u\left(\frac{\partial u}{\partial t} + u\frac{\partial u}{\partial x} + w\frac{\partial u}{\partial z} + \frac{\partial p}{\partial x} - \frac{3}{\varepsilon.R} - \frac{\varepsilon}{R}\frac{\partial^2 u}{\partial^2 x} - \frac{1}{\varepsilon.R}\frac{\partial^2 u}{\partial^2 z}\right)dz = \sum_{i=1}^{5} t_i = 0 \tag{3-14}$$

where,

$$t_1=\int_0^H u(\frac{\partial u}{\partial t}+u\frac{\partial u}{\partial x}+w\frac{\partial u}{\partial z})dz=\frac{6}{5}\frac{QQ_t}{H}-\frac{69}{40}\frac{H_tQ^2}{H^2}+\frac{333}{280}\frac{Q^2Q_x}{H^2}-\frac{54}{35}\frac{H_xQ^3}{H^3}+$$

$$\varepsilon^2\left(\begin{array}{l}\frac{3}{40}H_xQ_xQ_t-\frac{3}{20}\frac{QH_x^2Q_t}{H}+\frac{3}{40}QH_{xt}Q_x-\frac{7}{20}QH_tQ_{xx}+\frac{6}{5}\frac{H_x^2H_tQ^2}{H^2}+\frac{3}{40}QH_xQ_{xt}+\frac{1}{40}HQQ_{xxt}-\frac{9}{8}\frac{QH_tH_xQ_x}{H}\\ \quad+\frac{1}{40}HQ_{xx}Q_t+\frac{9}{16}\frac{H_{xx}H_tQ^2}{H}-\frac{3}{20}\frac{H_xH_{xt}Q^2}{H}-\frac{3}{40}QQ_{xx}Q_t-\frac{3}{80}H_{xxt}Q^2\end{array}\right)$$

$$t2=\int_0^H u\frac{\partial p}{\partial x}dz=\frac{3q\cot(\theta)h_x}{R}+\varepsilon\left(-\frac{27}{10}\frac{QQ_{xx}}{H.R}+\frac{129}{20}\frac{QH_xQ_x}{R.H^2}-\frac{123}{20}\frac{H_x^2Q^2}{R.H^3}+\frac{129}{40}\frac{H_{xx}Q^2}{R.H^2}\right)$$

$$+\varepsilon^2\left(\begin{array}{l}\frac{23}{112}\frac{H_x^3q^3}{H^3}-\frac{113}{112}\frac{Q_xH_x^2Q^2}{H^2}+\frac{107}{280}QQ_tH_{xx}-\frac{9}{35}\frac{QH_tH_xQ_x}{H}-\frac{95}{224}\frac{Q^2H_xQ_{xx}}{H}-QWeH_{xxx}-\frac{1}{3}Q^2Q_{xxx}-\frac{333}{448}\frac{H_xH_{xx}Q^3}{H^2}\\ +\frac{241}{448}\frac{H_{xxx}Q^3}{H}+\frac{107}{280}QH_tQ_{xx}+\frac{107}{280}QH_{xt}Q_x-\frac{123}{140}\frac{H_{xx}H_tQ^2}{H}+\frac{107}{280}Q^2H_{xxt}-\frac{33}{140}HQQ_{xxt}+\frac{1}{3}QQ_xQ_{xx}-\frac{39}{70}\frac{H_x^2H_tQ^2}{H^2}\\ +\frac{73}{112}\frac{QH_xQ_x^2}{H}+\frac{533}{448}\frac{Q_xQ^2H_{xx}}{H}-\frac{9}{35}\frac{H_xH_{xt}Q^2}{H}+\frac{87}{140}\frac{QH_x^2Q_t}{H}-\frac{33}{140}QH_xQ_{xt}\end{array}\right)$$

$$t_3=-\frac{3}{\varepsilon.R}\int_0^H u.dz=\frac{-3Q}{\varepsilon R}$$

$$t4=-\frac{\varepsilon}{R}\int_0^H u\frac{\partial^2u}{\partial^2x}=\left(\frac{69}{40}\frac{H_{xx}Q^2}{R.H^2}-\frac{6}{5}\frac{QQ_{xx}}{H.R}+\frac{69}{20}\frac{QH_xQ_x}{R.H^2}-\frac{63}{20}\frac{H_x^2Q^2}{R.H^3}\right)$$

$$t5=-\frac{1}{\varepsilon.R}\int_0^H u\frac{\partial^2u}{\partial^2z}=\frac{3Q^2}{\varepsilon RH^3}-\frac{\varepsilon}{R}\left(-\frac{9}{2}\frac{Q_xQ.H_x}{R.H^2}+\frac{9}{2}\frac{H_x^2Q^2}{R.H_3^2}+\frac{9}{4}\frac{H_{xx}Q^2}{R.H^2}-\frac{3}{2}\frac{QQ_{xx}}{R.H}\right)$$

Comparing the above terms with the corresponding ones given in Usha and Uma (2004), our model includes additional second order terms in, $t_1$. At this stage, the spatial-temporal evolution of film fluid falling down an inclined plane is described with two fundamental nonlinear equations (3-13-3-14). In the following, the dynamics of the stationary waves, which are analytically tractable in contrast with non-stationary, are explored.

## 2. Dynamic system formulation of stationary waves

Stationary waves are the waves that travel with constant celerity and keep their shape constant. Equations (3-13) and (3-14) are rescaled and rewritten in the moving frame of reference by introducing a new phase variable $\xi = \varepsilon^{-1}(x - c.t)$. Hence, from equation (3-13) the flow rate can be given as:

$$Q = c(H-1)+1 \tag{3-15}$$

Substituting this expression for the flow rate into equation (3-14), we obtain one nonlinear equation for the film height.

$$D_3 H_{\xi\xi\xi} + D_2 H_{\xi\xi} + D_1 H_{\xi} + D_0 = 0 \tag{3-16}$$

$$D_3 = \left(c(H-1)+1\right)\left(-WeH^3 + \frac{797cH^3(1-c)}{3360} + \frac{41c^2H^4}{1344} + \frac{187H^2(c-1)^2}{448}\right)$$

$$D_2 = \left[\left(\frac{495H(c-1)^3}{448} - \frac{8cH^2(c-1)^2}{7} - \frac{1485}{448}cH(c-1) - \frac{25H^3c^2(c-1)}{192}\right)H_{\xi} + \frac{9H}{5R}\left(c(H-1)+1\right)\left(cH+4(1-c)\right)\right]H_{\xi\xi}$$

$$D_1 = \left(\frac{54(c-3)^3}{35} + \frac{6c^3H^3}{35} - \frac{162c(c-1)}{35} + \frac{3.H^3\cot\theta}{R}\left(c(H-1)+1\right)\right)H_{\xi}$$

$$D_0 = \left(\frac{4cH}{7}(c-1)^2 + \frac{23}{560}c^3H^3 - \frac{11(c-1)^3}{16}\right)H_{\xi}^3 + \left(\frac{3(cH+8(c-1))(c(H-1)+1)}{5R}\right)H_{\xi}^2 - \frac{3(H-1)(c(H-1))(H^2+H-c+1)}{R}$$

In order to apply dynamics system and bifurcation theory to investigate the complex dynamics exhibited by the film fluid falling down, we transform the equation (3-16) into a third order dynamic system. Introducing the phase variables, $H$, $H_\xi$ and $H_{\xi\xi}$, the equation (3-16) can be rewritten in the form :

$$\frac{d\mathbf{H}}{d\xi} = F(\mathbf{H}) \tag{3-17}$$

$$\mathbf{H} = (H, H_\xi, H_{\xi\xi})$$

$$F(\mathbf{H}) = (H_\xi, H_{\xi\xi}, f / D_3)^T$$

$$D_3 = \left(c(H-1)+1\right)\left(-WeH^3 + \frac{797cH^3(1-c)}{3360} + \frac{41c^2H^4}{1344} + \frac{187H^2(c-1)^2}{448}\right) \tag{3-18}$$

$$f = \frac{-D_2 H_{\xi\xi} - D_1 H_\xi - D_0}{D_3} \tag{3-19}$$

The dynamic system is of third order and it is nonlinear; therefore all the conditions for exhibiting dynamic chaos are met.

# 3. Linear stability

In this section linear analysis is conducted; it consists of the investigation of the evolution of small perturbation $h$ superposed to the basic flow $H = 1$ . Hence, substituting $H = 1 + h(\xi)$ in the equations (3-16) and neglecting nonlinear terms we obtain:

$$\left(\frac{187}{448}-We-\frac{251}{420}c+\frac{59}{280}c^2\right)h_{\xi\xi\xi\xi}+\left(\frac{36}{5}\frac{1}{R}-\frac{27}{5}\frac{c}{R}\right)h_{\xi\xi}+\left(+\frac{102}{35}c+\frac{3}{R}\cot(\theta)-\frac{54}{35}-\frac{6}{5}c^2\right)h_{\xi}$$
$$-\frac{9}{R}h+\frac{3ch}{R}=0 \qquad (3\text{-}20)$$

We look for the solution of the equation (3-20) in wave like form: $h(\xi)=e^{-ik\xi}$ where $k$ is the wave number, which can be considered a complex number $k=k_r+i\,k_i$, where $k_r$ and $k_i$ are the wave number and spatial growth rate of the perturbation. Similarly, the wave's celerity in (3-20) can also be written as $c=c_r+i.c_i$, where $c_r$ and $c_i$ are the wave celerity and temporal growth rate of the perturbation, respectively. Therefore equation (3-20) becomes:

$$-ik^3\left(\frac{187}{448}-We-\frac{251}{420}c+\frac{59}{280}c^2\right)+\left(\frac{36}{5}\frac{1}{R}-\frac{27}{5}\frac{c}{R}\right)k^2-i\left(\frac{102}{35}c+\frac{3}{R}\cot(\theta)-\frac{54}{35}-\frac{6}{5}c^2\right)k$$
$$-\frac{9}{R}+\frac{3c}{R}=0 \qquad (3\text{-}21)$$

At the marginal stability condition the spatial and temporal growth rates of the perturbation are null ($k_i=0$ and $c_i=0$). Separating the real part from the imaginary part in equation (3.21), we deduce the critical wave celerity and marginal stability conditions. The critical wave celerity is given as:

$$c=\frac{3\left(4k^2+5\right)}{9k^2+5} \qquad (3\text{-}22)$$

For the long wave perturbation ( $k \to 0$ ) the critical celerity can be expanded in terms of series:

$$c = 3 - 3k^2 + \frac{27}{5}k^4 + O(k^6) \tag{3-23}$$

The marginal stability curve is given by the following equation,

$$\frac{R}{\cot(\theta)} = \frac{5}{6} + \left(\frac{46055}{16128} + \frac{25}{108}W_e\right)k^2 + O(k^4) \tag{3-24}$$

The stability threshold predicted by the present model for the long waves ( $k \to 0$ ) is $\frac{5}{6}$ which corresponds to the value given by Benjamin (1957) and Yih (1955). The correction introduced (the shear stress) is of the second order; its effect is of order of magnitude three ( $O(k^3)$ ) with respect to the long wave parameter, $k$. The neutral stability curve is similar to the one obtained by Usha and Uma (2004), see Figure 3-1. Moreover, the wave celerity of the neutrally stable waves provided by the present model is compared with the one observed experimentally and the one obtained by Usha and Uma (2004), see Figure 3-2.

The linear stability results also agree with those obtained using the models of Amaouche et al (2005), and Nguyen and Balakotaiah (2000). Indeed, as shown in Figures 3-3 and 3-4, the neutral stability curves (evolution of the critical wave number with the Reynolds number) obtained with the present two-equation model shows a good agreement with the three-equation model proposed by Nguyen and Balakotaiah (2000) and the simplified two-equation model obtained by Amaouche et al (2005).

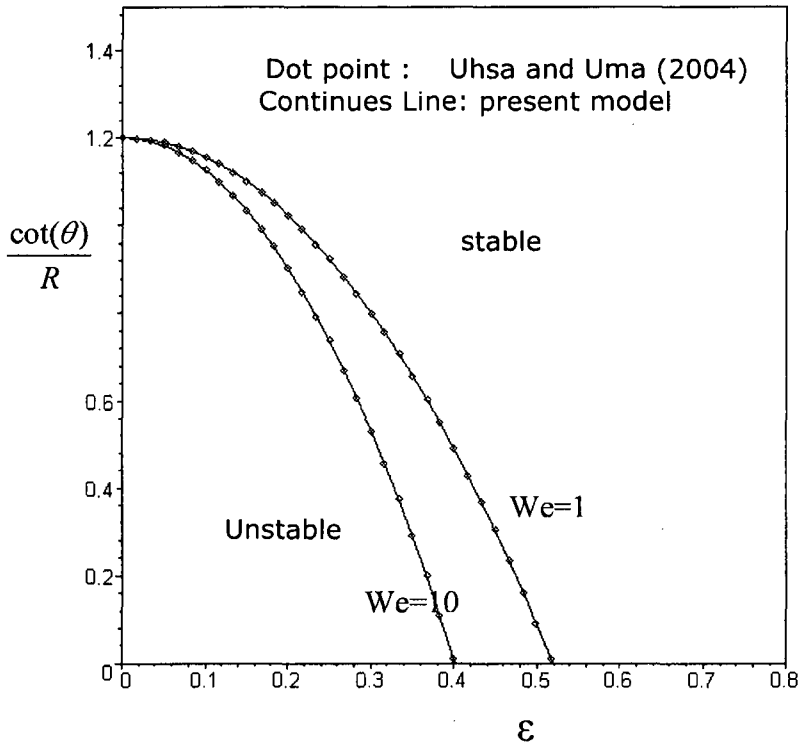


Figure 3-1: Neutral stability curves for two value of a Weber number

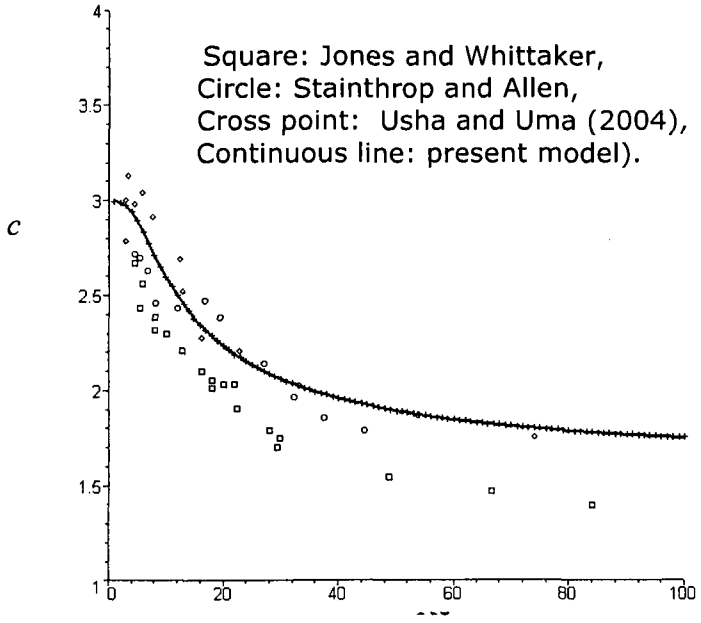


Figure 3-2 Dimensionless wave speed for vertically falling water film experimental results.

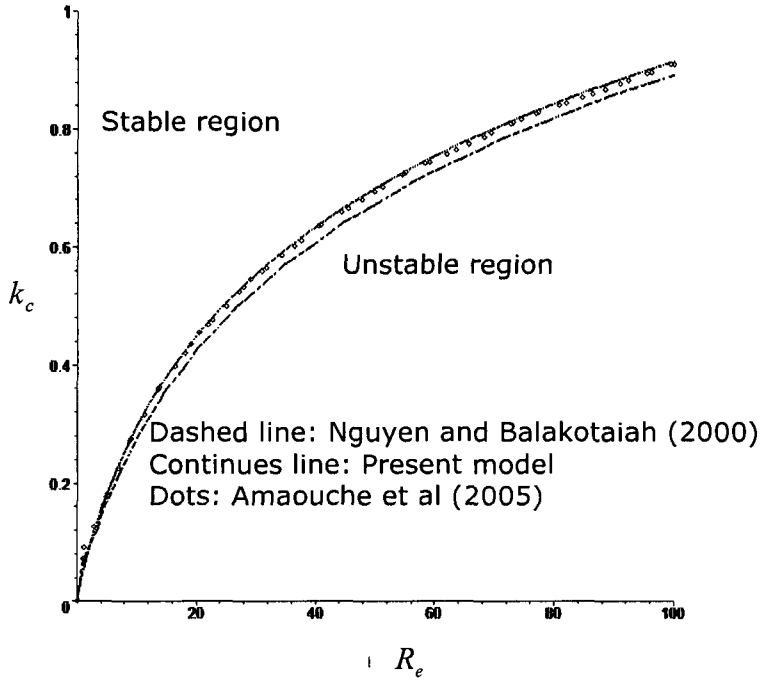


Figure 3-4: Critical wavenumber against Reynolds Number

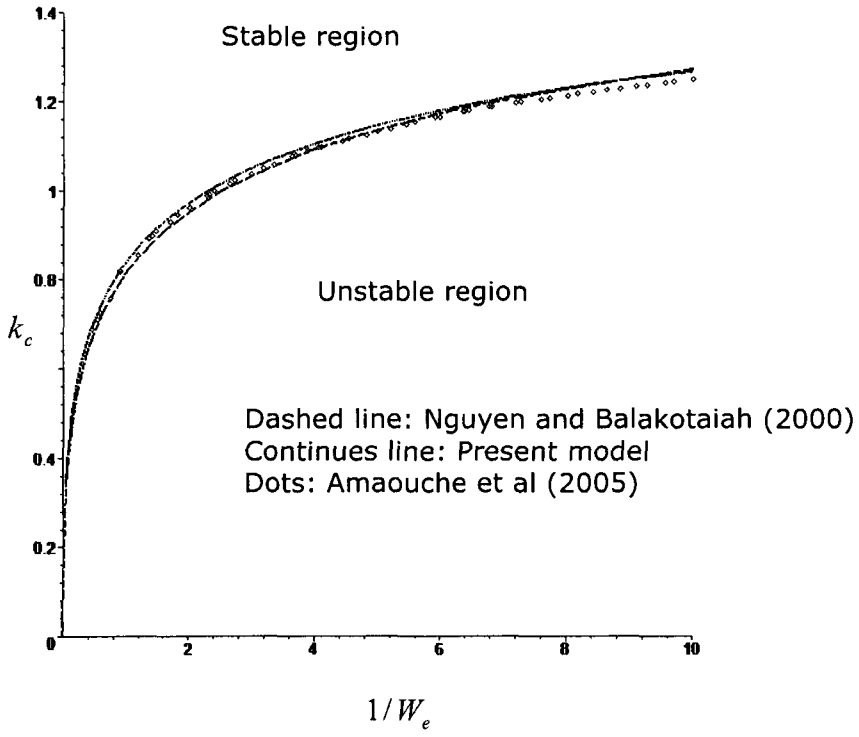


Figure 3-5: Critical wavenumber against the inverse of the Weber number

When the amplitude of the small perturbations exceeds a certain value the nonlinear terms are not longer small; and the linear stability analysis is not longer valid. The influence of the nonlinear terms will influence the stability of the stationary solution of the fixed point of the dynamic system.

## 4. Fixed points

The fixed points of the dynamic system (3-17) are by definition the constant solution in the phase space. The constant solutions are those that make the term $D_0$ equal to zero in equation (3-16). The dynamic system posses two fixed points or two stationary solutions. The first fixed point corresponds to the unperturbed solution $H_1 = 1$, and the second one is $H_2 = \frac{1}{2}(4c-3)^{\frac{1}{2}} - \frac{1}{2}$, which exists only for $c > 1$. This second stationary solution can be considered an asymptotic limit for a propagating wave. It is worth noticing that at $c = 3$ the two fixed points coincide, suggesting a possible exchange of their stability (transcritical bifurcation). This bifurcation occurs if on both sides of this critical value, $c = 3$, one of the fixed points is stable while the other one is unstable. For a given flow parameters, the existence of the unstable and stable stationary solution implies a possible transition from the unstable to the stable solution. This transition is depicted in the phase space with a heteroclinic orbit, connecting the two fixed points. Examples of heteroclinic bifurcations will be shown later through numerical simulations of the dynamic system. According to the dynamic system (3-17), the

heteroclinic bifurcation can only occur if there is no singular height intruded between the two fixed points. The singular height cancels the denominator $D_3$ in (3-16).

### 4.1 Stability and bifurcations of the stationary solutions.

Before discussing the stability properties of the two fixed points, we examine first the singularities of the dynamic system (3-17). The singularities correspond to the film height that zeros the denominator $D_3$ , given in equation (3-18). The singular heights are given by the two following equations:

$$H_s^1 = \frac{1594c(c-1)+6720We+4\sqrt{15046c^2(c-1)^2+1338960cW_e(c-1)+2822400{W_e}^2}}{410c^2} \quad (3\text{-}25)$$

$$H_s^1 = \frac{1594c(c-1)+6720We+4\sqrt{15046c^2(c-1)^2+1338960cW_e(c-1)+2822400{W_e}^2}}{410c^2} \quad (3\text{-}26)$$

The singular heights depend on the Weber number and wave celerity, $c$. The singular height prevents heteroclinic connection between the two fixed points. In figure 3-6, we show the variation of singular heights and the two stationary solutions with the wave celerity $c$ for three values of Weber number, $W_e$. Figure 3-6 shows that for a given value of the Weber number there is a range of wave celerity $c$ where the fixed points are not separated with a singular plane. Certainly for a Weber number value of 0.02, the heteroclinic bifurcation is possible for values of celerity, $c$, ranging from 1 to

9, see Figure 3-6a. At slightly higher Weber numbers (0.65) the range where heteroclinic bifurcations are possible shrinks to the interval [1, 3], see Figure 3-6b. For a Weber number equal to 2, the range where heteroclinic bifurcations are possible expands to the interval [1, 8.5]. (see Figure3-6c).

This dependency can also be shown in the $(W_e, c)$ plane, where the region bounded by the two curves $D_3^1(c, We, H_1) = 0$ and $D_3^2(c, We, H_2) = 0$, are the regions where no singular height is inserted between the two fixed points. These two curves are defined respectively by the following two equations,

$$We = \frac{59}{280}.c^2 - \frac{251}{420}.c + \frac{187}{448} \tag{3-28}$$

$$We = \frac{41(-3+4.c)^{(5/2)}}{43008} - \frac{187}{896} + \frac{5993.c}{13440} - \frac{1131.c^2}{4480} + \frac{415.(-3+4.c)^{(3/2)}}{7168} - \frac{625\sqrt{-3+4.c}}{14336} \tag{3-29}$$

The regions where heteroclinic bifurcations are possible, are shown in Figure 3-7. This figure shows that the areas where heteroclinic bifurcation are possible is underestimated by the Usha and Uma (2004) model. Outside these regions other kinds of bifurcation such as Hopf, homoclinic, and cascades of period doubling bifurcations can occur. These bifurcations are investigated through the analysis of the local stability of the fixed points. Each bifurcation is a qualitative change of the flow, which occurs when the real part of eigenvalues of the Jacobian matrix of the dynamic system (3.17) become null, when the control parameter is varied. In order to investigate

the bifurcation issued from the two fixed points we linearize the system (3.17) around the fixed points.

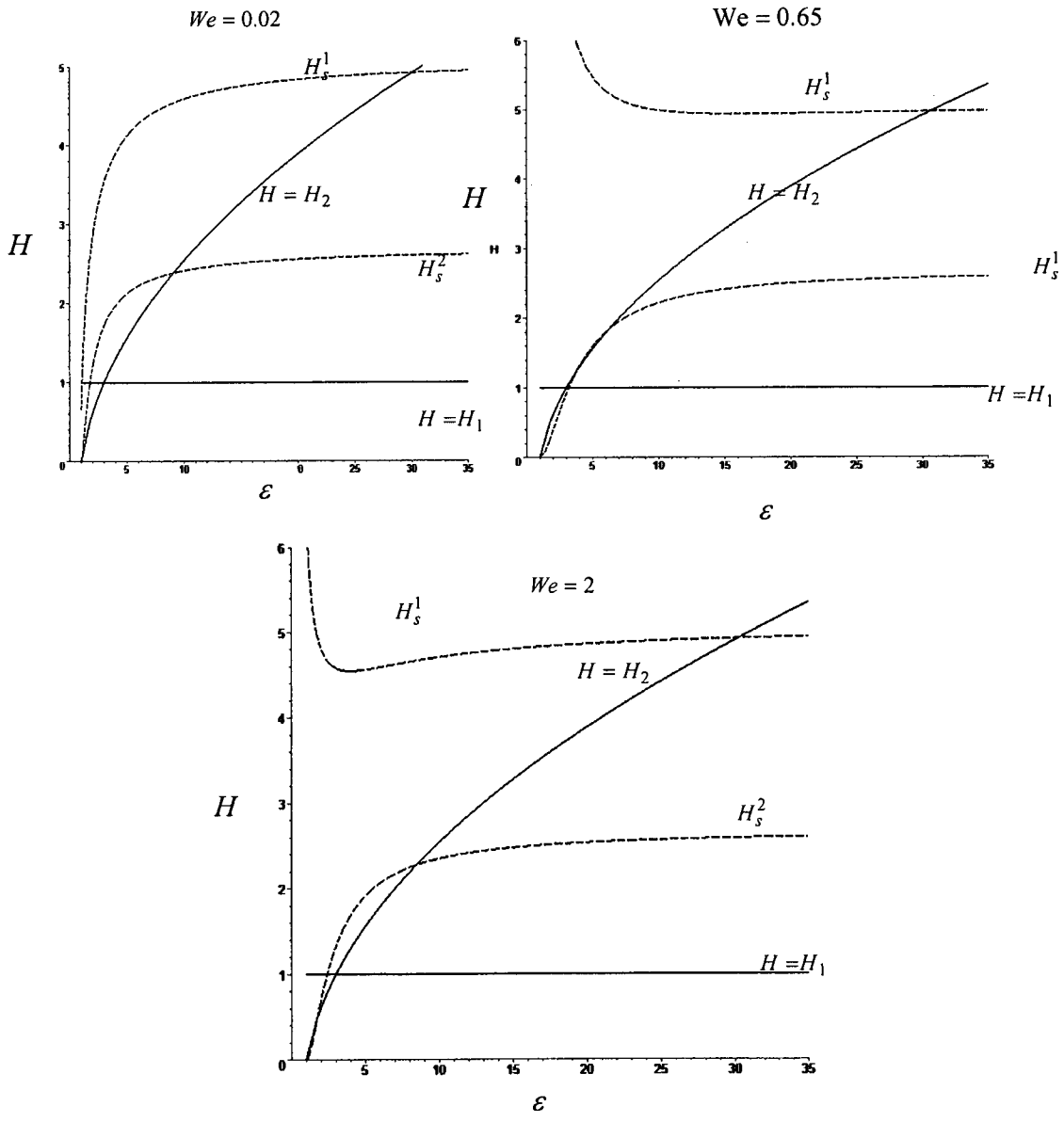


Figure 3-6: Singulars heights and fixed points. Continuous line: fixed solution. Dashed line: singular plane

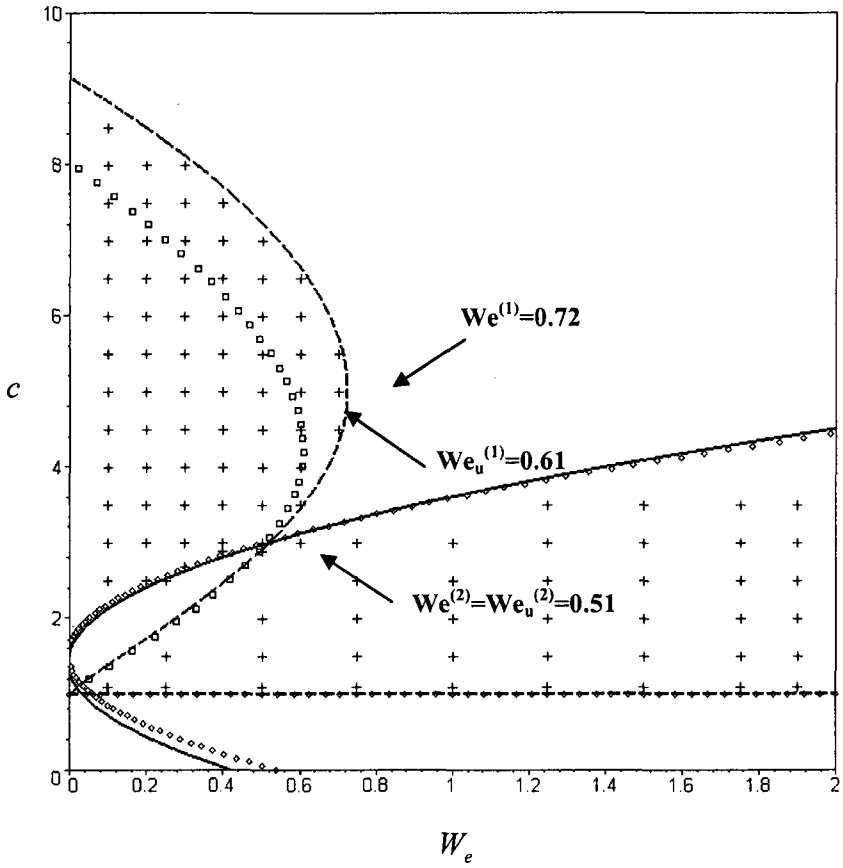


Figure 3-7 ; Regions (+) are regions where heteroclinic orbits are possible
We: value from the present model
$We_u$: Value from the model in Usha and Uma (2004)

To achieve this we consider $H = H^* + h(\xi)$, where $H^*$ indicates one of the two fixed points $H_1$ and $H_2$. The linearized system describing the evolution of the small perturbation $h(\xi)$ is give by:

$$\frac{dh}{d\xi} = Jh \tag{3.30}$$

Where $J$ is the Jacobian matrix:

$$J = \begin{bmatrix} 0 & 1 & 0 \\ 0 & 0 & 1 \\ -\beta_3 & -\beta_2 & -\beta_1 \end{bmatrix} \tag{3.31}$$

The characteristic equation of the Jacobian matrix is:

$$\det(J - \lambda I) = 0 \qquad \text{or} \quad \lambda^3 + \beta_1\lambda^2 + \beta_2\lambda + \beta_3 = 0 \tag{3.32}$$

Where the $\beta$ coefficients are given by the following expressions:

$$\beta_3 = -\frac{\left(\frac{9H^2(c-1)}{R}\right) + (6c(1+H(c-1))) - \frac{12H^3}{R}}{\left(-WeH^3 + \frac{797cH^3(1-c)}{3360} + \frac{41c^2H^4}{1344} + \frac{187H^2(c-1)^2}{448}\right)(c(H-1)+1)} \tag{3.31}$$

$$\beta_2 = -\frac{\frac{3H^3\cot\theta(1+c(H-1))}{R} + \frac{6}{35}(1+c(H-1))(-9(c-1)^2 + Hc(c((H+1)-1)))}{\left(-WeH^3 + \frac{797cH^3(1-c)}{3360} + \frac{41c^2H^4}{1344} + \frac{187H^2(c-1)^2}{448}\right)(c(H-1)+1)} \tag{3.32}$$

$$\beta_1 = \frac{-\frac{9H(1+c(H-1))(cH-4(c+1))}{5R}}{\left(-WeH^3 + \frac{797cH^3(1-c)}{3360} + \frac{41c^2H^4}{1344} + \frac{187H^2(c-1)^2}{448}\right)(c(H-1)+1)} \tag{3.33}$$

The analytical solutions of the characteristic equations are too lengthy to be given here. However, at high Reynolds number the eigenvalues of the Jacobian can be set as:

$$\begin{aligned} \lambda_1 &= -\frac{\beta_3}{\beta_2} + O(R^{-2}) \\ \lambda_{2,3} &= \frac{\beta_3 - \beta_1\beta_2}{2\beta_2} \pm i\sqrt{\beta_2} + O(R^{-2}) \end{aligned} \tag{3.34}$$

### *4.1.1 Transcritical bifurcation*

In Equation 3-34, the coefficient $\beta_3$ monitors the crossing of the real eigenvalue of the imaginary axis. At the critical value $c = 3$ the coefficient $\beta_3$ becomes null for the two fixed points and the Jacobian matrix is singular. At this critical value, the bifurcation is transcritical and the two fixed points collapse and exchange their stability. Indeed, for the given problem, the fixed point $H_1$ is stable while $H_2$ is instable for $c < 3$, and for $c > 3$ the fixed point $H_2$ is stable and $H_1$ is unstable. When the critical value $c = 3$ is crossed, one of the fixed points losses its stability in favor of the other one.

*4.1.2 Hopf bifurcation.*

In the case when two complex conjugate eigenvalues cross the imaginary axes and the other real eigenvalue is negative, the occurring bifurcation is of the Hopf type. At this bifurcation point the Jacobian remains non-singular and periodic trajectory centered at the fixed point appears. According to the equations (3-20) we deduce the conditions for the Hopf bifurcation as follows:

$$\begin{aligned} &\beta_1 > 0 \\ &\beta_2 > 0 \\ &\beta_1\beta_2 = \beta_3 \end{aligned} \tag{3.35}$$

The condition $\beta_1\beta_2 = \beta_3$ represents the Hopf threshold that is located between the critical curve $c = 3$ and the curve $\beta_2 = 0$. The influence of the flow parameters on the Hopf bifurcation is shown in Figure 3-7. Figure 3-7 illustrates the influence of the Weber number on the Hopf bifurcation threshold ( $\beta_1\beta_2 = \beta_3$ ) represented by curves $C_1$ for $H_1$ and $C_2$ for $H_2$. The region where the two fixed points are stable are located between the curve $c = 3$ and the curves $C_1$ and $C_2$.

Figures 3-8 indicates that when the Weber number is high the Hopf bifurcation thresholds lies between the curves $c = 3$ and $\beta_2 = 0$. As the Weber number decreases the Hopf bifurcation threshold approaches the curve $\beta_2 = 0$ until the threshold stands outside the curve $\beta_2 = 0$. This suggests that there is a minimum Weber number that triggers the Hopf bifurcation. For a

given value of $\frac{\cot\theta}{R}$ this minimum Weber number is obtained by solving simultaneously $\beta_1\beta_2 = \beta_3$ and $\beta_2 = 0$ . Since, for $\beta_3 \neq 0$ the problem is equivalent to zeros, $\beta's$ denominator will be $D_3^1 = 0$ and $D_3^2 = 0$, respectively for $H_1$ and $H_2$ . The elimination of the celerity, $c$ , between these two equations allows us to express the minimum Weber as function of $\frac{\cot\theta}{R}$. This necessary minimum Weber number that triggers the Hopf bifurcation is shown in Figure 3-9. Note that the present model predicts a higher minimum Weber, which is required to destabilize the second stationary solution $H_2$ via Hopf Bifurcation, than the one predicted in Usha and Uma (2004). However, the difference is relatively small for the first stationary solution, $H_1$.

Besides the singular curves, $D_3^1$ and $D_3^2$ , the Hopf and transcritical bifurcations thresholds are indicated respectively by $C_H$ and $C_T$. There is also another important curve which separates saddle spirals from saddle node points. This curve designate by $C_B$ corresponds to the coalescence of the two complex conjugate eigenvalues on the real axis and its expression is obtained by rewriting the characteristic equation (3-18) in the form:

$$(\lambda - a)^2 (\lambda - b) = 0 \tag{3-36}$$

with both $a$ and $b$ being real. Hence, the corresponding expression of the curve $C_B$ separating saddle, spirals, and saddle nodes is given as:

$$4(\beta_1^2 - 3\beta_2)(\beta_2^2 - 3\beta_1\beta_3) - (\beta_1\beta_2 - 9\beta_3)^2 = 0 \tag{3-37}$$

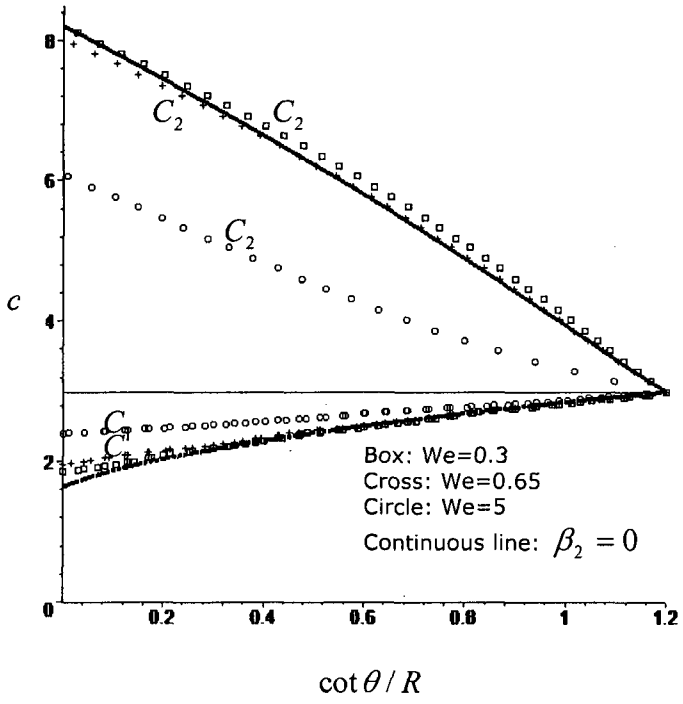


Figure 3-8: Influence of Weber number $W_e$ on Hopf bifurcation threshold.

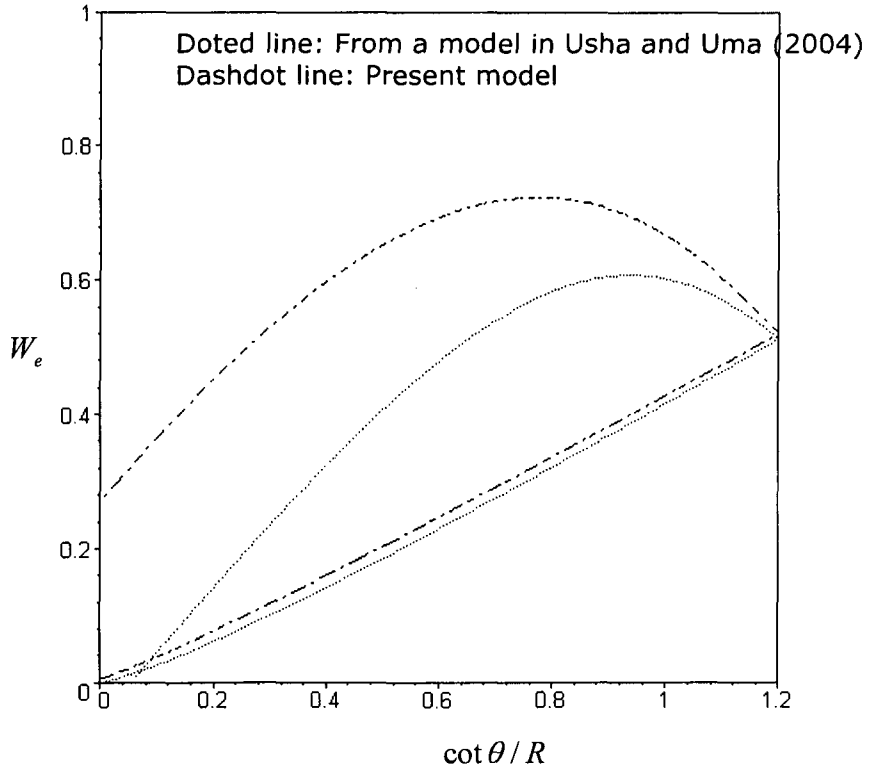


Figure 3-9; Minimum Weber required to Hopf bifurcation to occur

In order to attain a deep insight into the effect of the various parameters on the bifurcations scenarios and their corresponding attractors, qualitative analysis of the properties of the eigenvalues in the parameters plane is conducted. This qualitative analysis helps the anticipations of the numerical solutions. According to the equations (3-35) and (3-37) we notice that the distribution of the eigenvalues depends on the $We$, $R$, $c$ and $\frac{\cot\theta}{R}$. A typical value for Weber and Reynolds are chosen to illustrate their effects on the distribution of the eigenvalues in $(c, \frac{\cot\theta}{R})$ plane. In figure 3-10, we displays the distributions of the eigenvalues of the Jacobian evaluated, first, at the fixed point $H_1$ and $H_2$ for $We = 1$ and $R = 10$.

Figure 3-10 shows that in regions delimited by the transcritical curve $C_T$ and the Hopf bifurcation thresholds $C_{H1}$, the first stationary solution $H_1$ is stable whereas the second stationary solution $H_2$ is unstable. Since there is no singular plane inserted between the two fixed points a heteroclinic orbit connecting $H_2$ and $H_1$ is possible. Decreasing the value of the control parameter $c$ (wave celerity) bellow the Hopf bifurcation threshold the first stationary solution (the horizontal free surface) may undergo a bifurcation to limit cycle (periodic solution). Decreasing further the control parameter $c$ while remaining above curve $C_{B1}$, the limit cycle may also undergo complex bifurcations to complex orbits such as cascade of periodic doubling and homoclinic bifurcation. In Figure 3-10 we also draw the curve $C_S$, where the

sum of real eignenvalues and the real parts of the complex ones vanish. This curve is given by the following equation:

$$2\beta_1^3 + \beta_3 + \beta_1\beta_2 = 0 \tag{3-38}$$

According to the first theorem of Shilnikov, crossing the curve $C_S$ may lead to homoclinic chaos. Indeed, the Shilnikov theorem stipulates that in the case of saddle spiral fixed point, when the magnitude of the real eignenvalue is higher than the magnitude of the real part of the complex eignenvalues there is homoclinic orbits at this fixed points. The homoclinic orbit spiral out (or in) on the unstable (stable) manifold spanned by the two eigenvectors corresponding to the two complex conjugate eignenvalues and come back into (or out off) the fixed point along the stable (unstable) direction of the eigenvectors corresponding to the real eignenvalues which is transverse to unstable manifold. Figure 3-10 shows that homoclinic chaos can occur in the whole region delimited by the curve $C_{B1}$ and $C_{H1}$ since the curve $C_S$ do not intersect the curve $C_{B1}$. Increasing the value of the control parameter $c$, the fixed point $H_1$ loses its stability when $c$ cross the curve $C_T$ and it might bifurcate to $H_2$ if the wave celerity does not cross the singular curve $D_2$. Between the curve $D_2$ and the Hopf bifurcation threshold $C_{B2}$ the second stationary solution is stable. It loses its stability when the value of the control parameter crosses the bifurcation threshold.

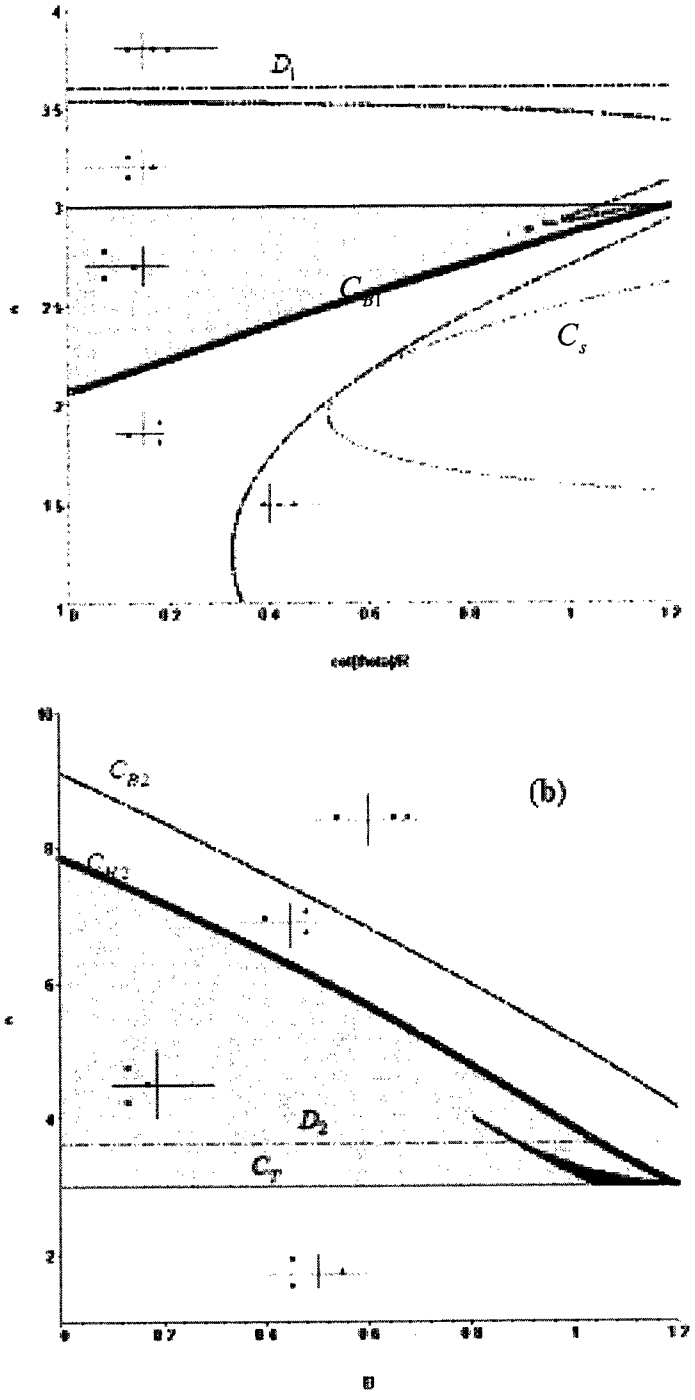


Figure 3-10: Distribution of the eigenvalues for We=1,R=10
a) H=H1, b) H=H2

At this time the second stationary solution undergoes a Hopf bifurcation into limit cycle. In the region surrounded by the curves $C_{H2}$ and $C_{B2}$ the second stationary solution might undergo a cascade of Hopf bifurcations. When the control parameter crosses the curve $C_{B2}$ the unstable spiral node becomes an unstable saddle node. The figures 3-11-3-13 display the effects of the Reynolds and Weber numbers on the eignenvalue positions. Figure 3-11-3-13 show that the curves $C_{B1}$, $C_{B2}$, $C_{H1}$ and $C_{H2}$ strongly depend on the Reynolds number; the regions delimited by these curves shrink reducing the routes toward chaos through Hopf bifurcation to small values of $\frac{\cot\theta}{R}$. Figure 3-11-3-13 also depict the influence of the Weber number $W_e$; they show that increasing the Weber number reduces the area of stability region of the two fixed points, delimited by the curves $C_T$, $C_{H1}$ and $C_{H2}$. However, an increase in the value of the Weber number augments the regions inserted between $C_{H1}$, $C_{B1}$ and $C_{H2}$, $C_{B2}$. Hence, the Weber number increases the possibilities of the bifurcation to chaos through Hopf bifurcation. An increase of Weber number influences also singular curves $D_1$ and $D_2$; we notice that augmenting the Weber number multiplies the possibilities of heteroclinic connections from the stable solution toward the unstable one.

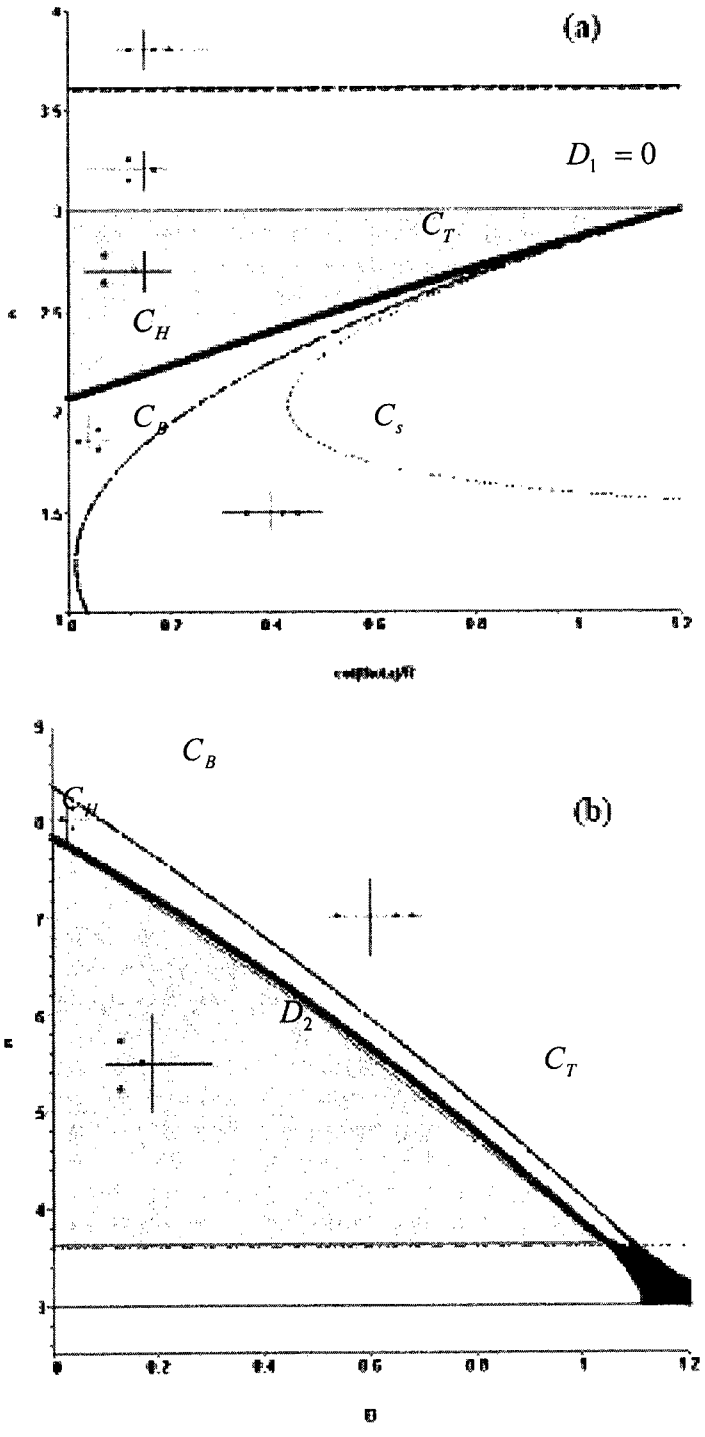


Figure 3-11: Distribution of the eigenvalues for We=1,R=100
a) H=H1 b) H=H2

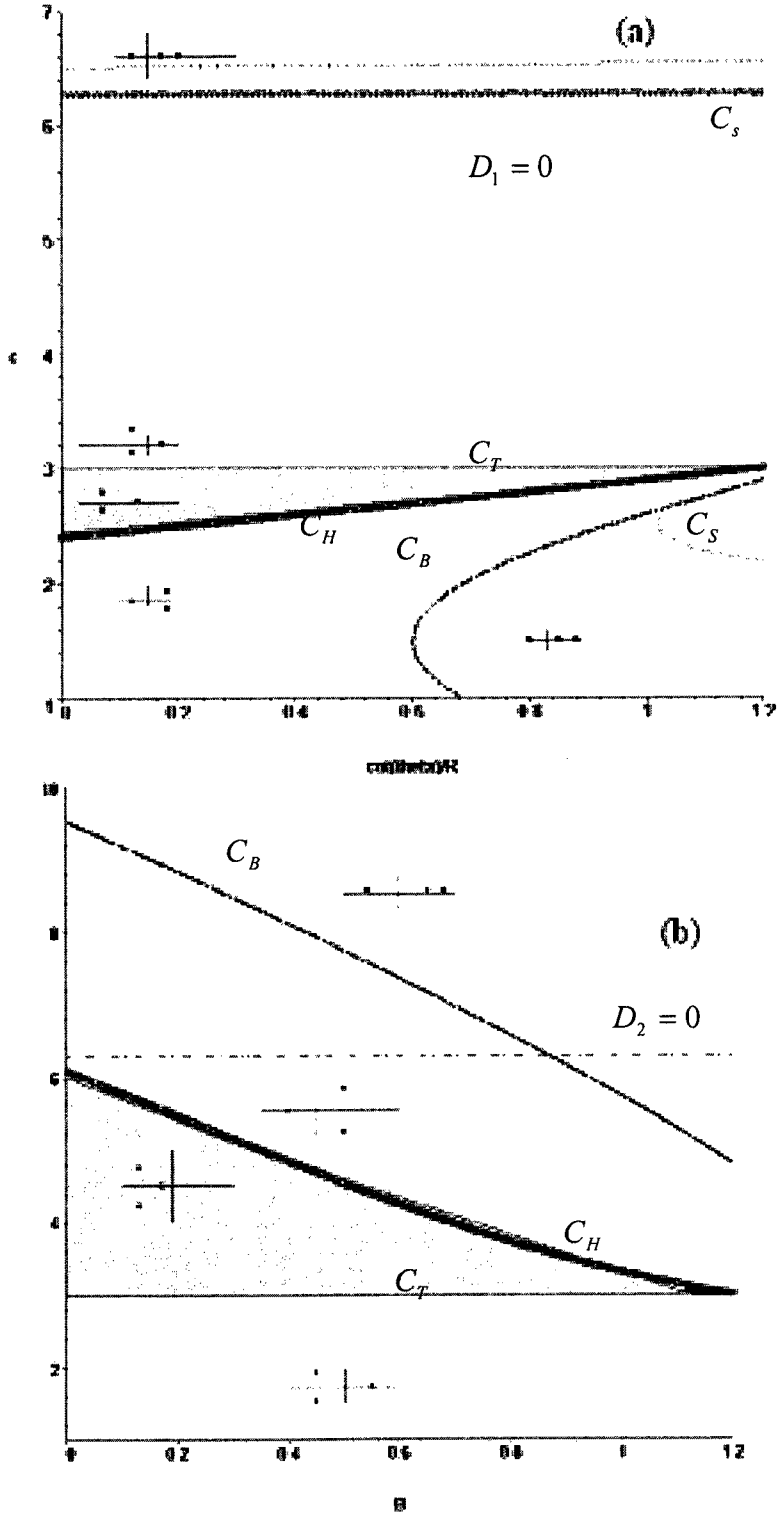


Figure 3-12: Distribution of the eigenvalues for We=5,R=10
a) H=H1 b)=H2

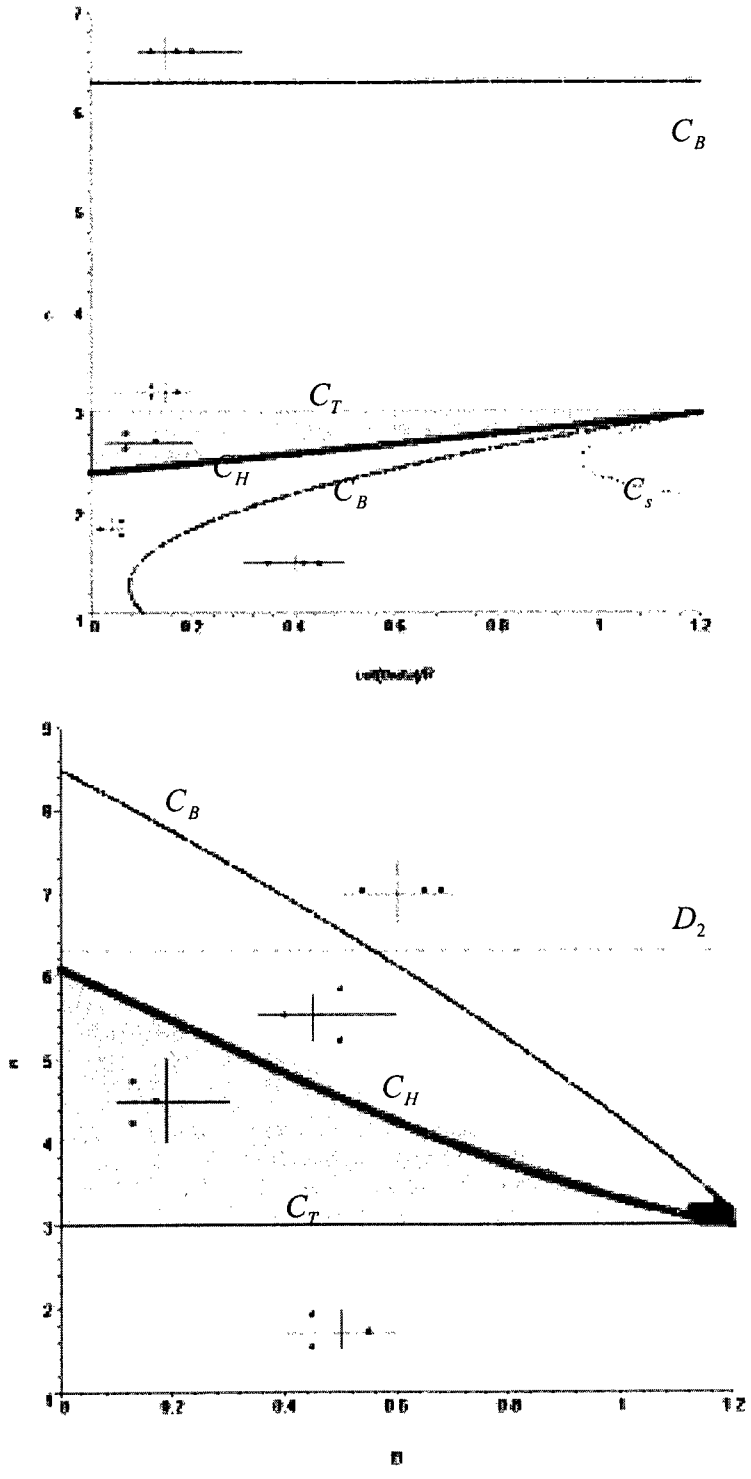


Figure 3-13: Distribution of the eigenvalues for We=5,R=100
a) H=H1 b) H=H2

# 5. Numerical Simulations

## 5.1 Illustration Bifurcation scenarios.

In light of the qualitative analysis performed in the previous subsection, a non exhaustive but rather qualitative illustration of the heteroclinic, homoclinic and Hopf bifurcations mentioned above is presented in this subsection. The dynamic system (3-17) is integrated using ODE 15s available in MATLAB, this integrator handles stiff problems. As pointed out above the bifurcation scenarios depend on Weber $W_e$, Reynolds $R$ numbers $\frac{\cot\theta}{R}$ and $c$, and are displayed through numerical simulation. We have reported above that when the critical curve $c=3$ is crossed the two fixed points of the dynamic system (17) interchange their stability properties.

For the following flow conditions: $R=100$, $We=1$, $\frac{\cot\theta}{R}=0.4$ and $c=3.3$, the first stationary solution ($H_1$) is unstable while the second stationary solution ($H_2$) is stable. Since there is no singular height intruded between these two fixed points, a heteroclinic orbit issued from $H_1$ towards $H_2$ can be found. The heteroclinic orbit and the wave profile of the free surface are shown in the figure 3-14. Similarly, when the celerity is $c=2.5$, the two fixed points interchange their stability and the heteroclinic orbit will now be issued from the unstable fixed point ($H_2$) towards ($H_1$), see Figure 3-15. Seen in Figures 3-14-3-15, the wave profile is a hydraulic jump.

The fixed points can also undergo Hopf bifurcations that lead to limit cycles in phase space or to an oscillatory motion of the free surface. For the

flow conditions defined by $R=10, We=1, \frac{\cot\theta}{R}$ and $c=2$, the first stationary solution $H_1$ is located in the unstable region between the curve $C_{H1}$ and $C_{B1}$. This point is near the Hopf bifurcation threshold. The numerical simulations corresponding to these flow conditions are displayed in the Figure 3-16. Figure 3-16 shows a limit cycle in the phase plane and periodic wave profile on the free surface.

Keeping the same flow condition but gradually lowering the value of the control parameter $c$ from 2 to 1.92, the period of limit cycle augments incrementally and the wavelength increases until a second limit cycle takes places and the period of the traveling wave doubles, see Figure 3-17. Decreasing further the value of the control parameter, the solution in phase portrait and the wave profile remains similar until the critical value is crossed and the second period doubling appears, see Figure 3-18 at $c=1.917$. According to Feigenbaum's scenarios, decreasing further the value of the control parameter leads to a cascade of periodic doubling until full chaos takes place, see Figure 3-19 where the dynamics portrayed approach chaos.

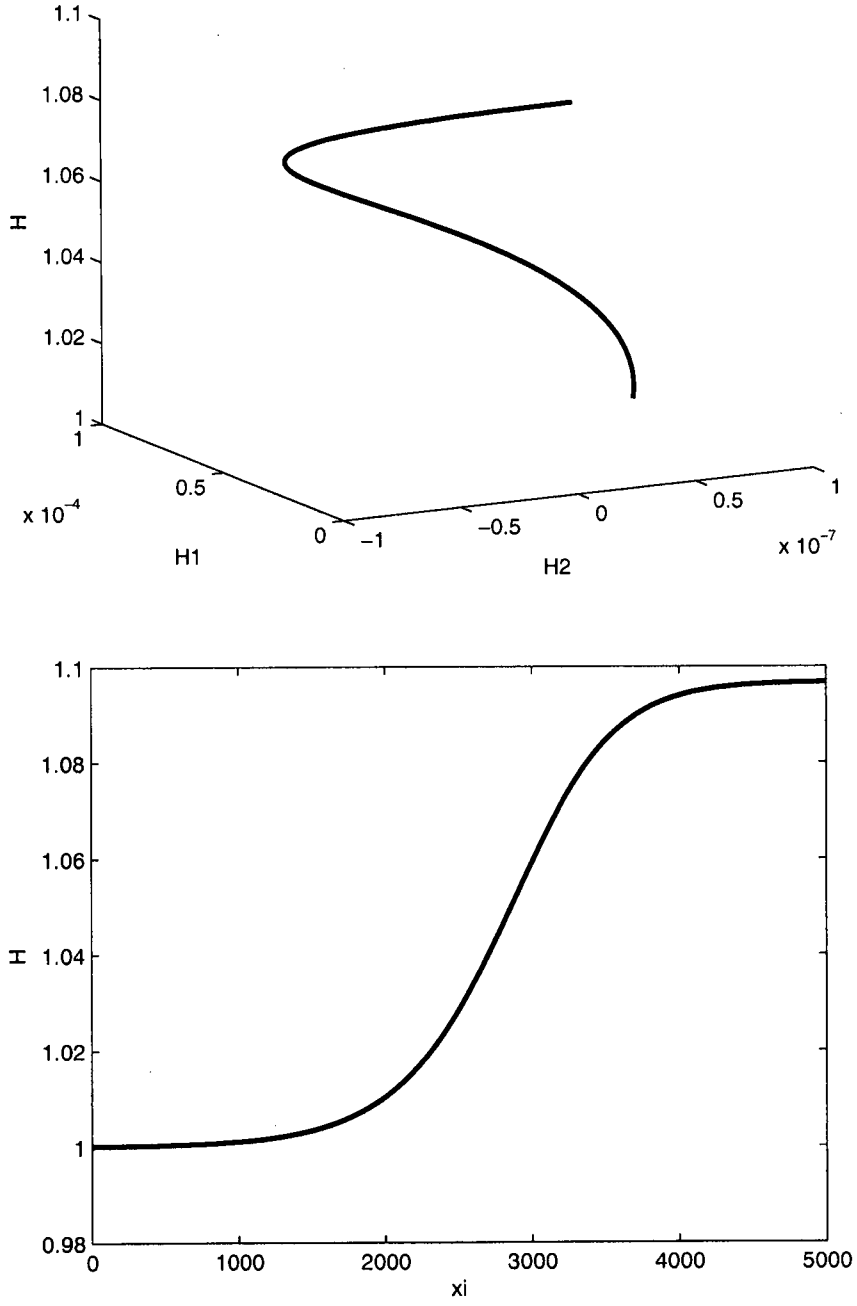


Fig 3-14: Heteroclinic orbit H1toward H1 R=100;B=0.4*R;We=1;c=3.3
a) phase trajectory b) wave profile

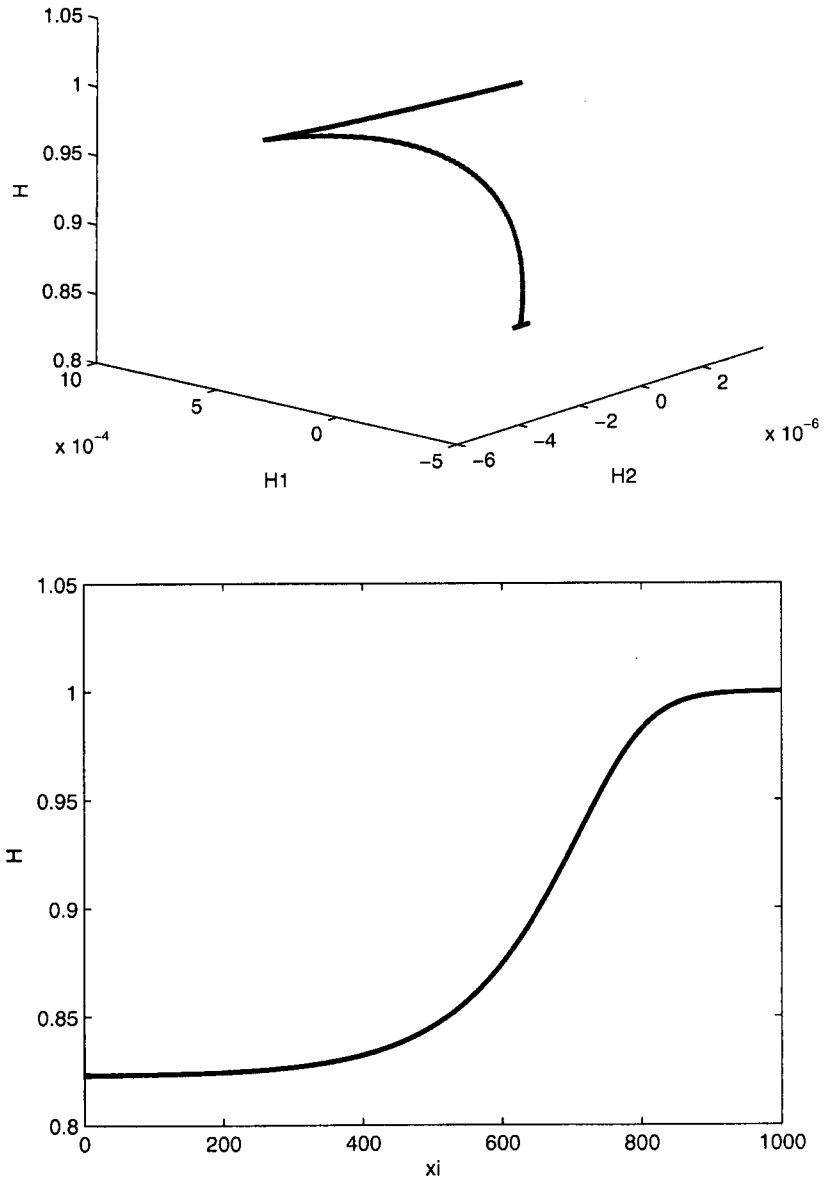


Figure 3-15 : Heteroclinic orbit H2 toward H1 R=100;B=0.4*R;We=1,c=2.5
a) phase trajectory b) wave profile

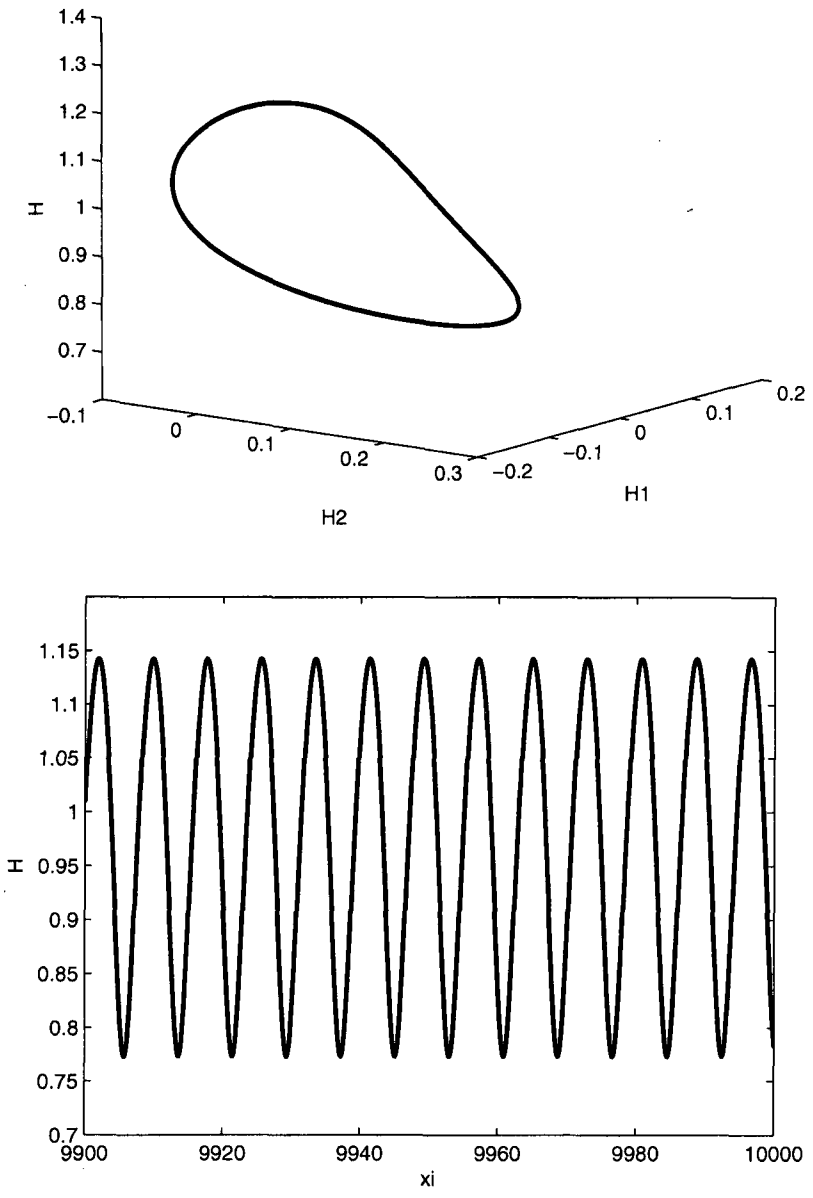


Figure 3-16: Periodic wave R=10;B=0*R;We=1;c=2
a) limit cycle b) wave profile

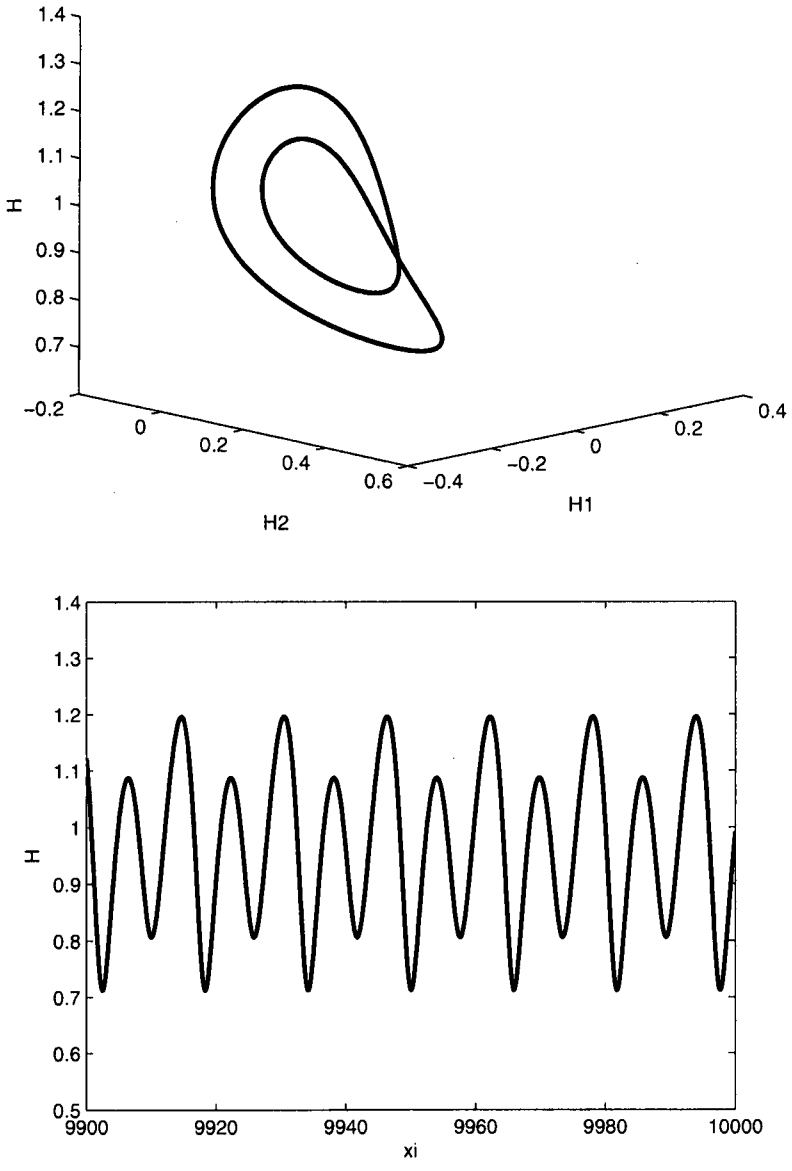


Figure 3-17: Periodic wave R=10;B=0*R;We=1;c=1.92
a) limit cycle b) wave profile

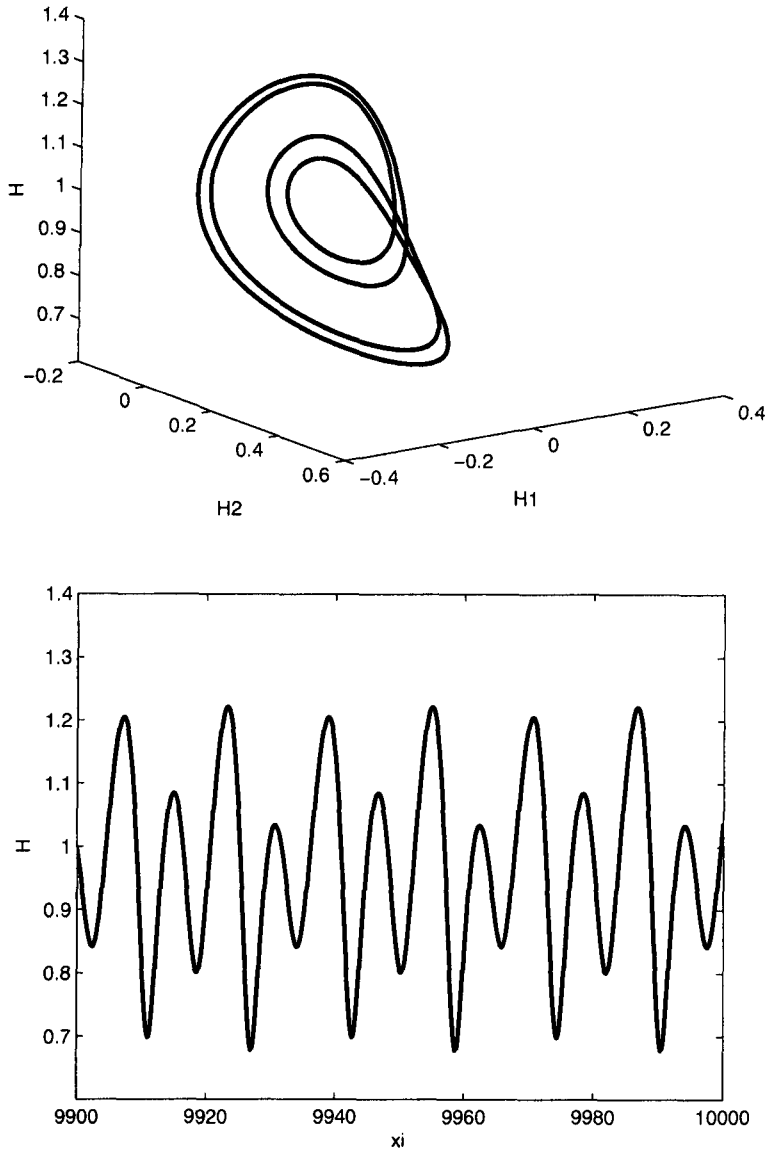


Figure 3-18: Periodic wave R=10;B=0*R;We=1;c=1.917
a) limit cycle b) wave profile

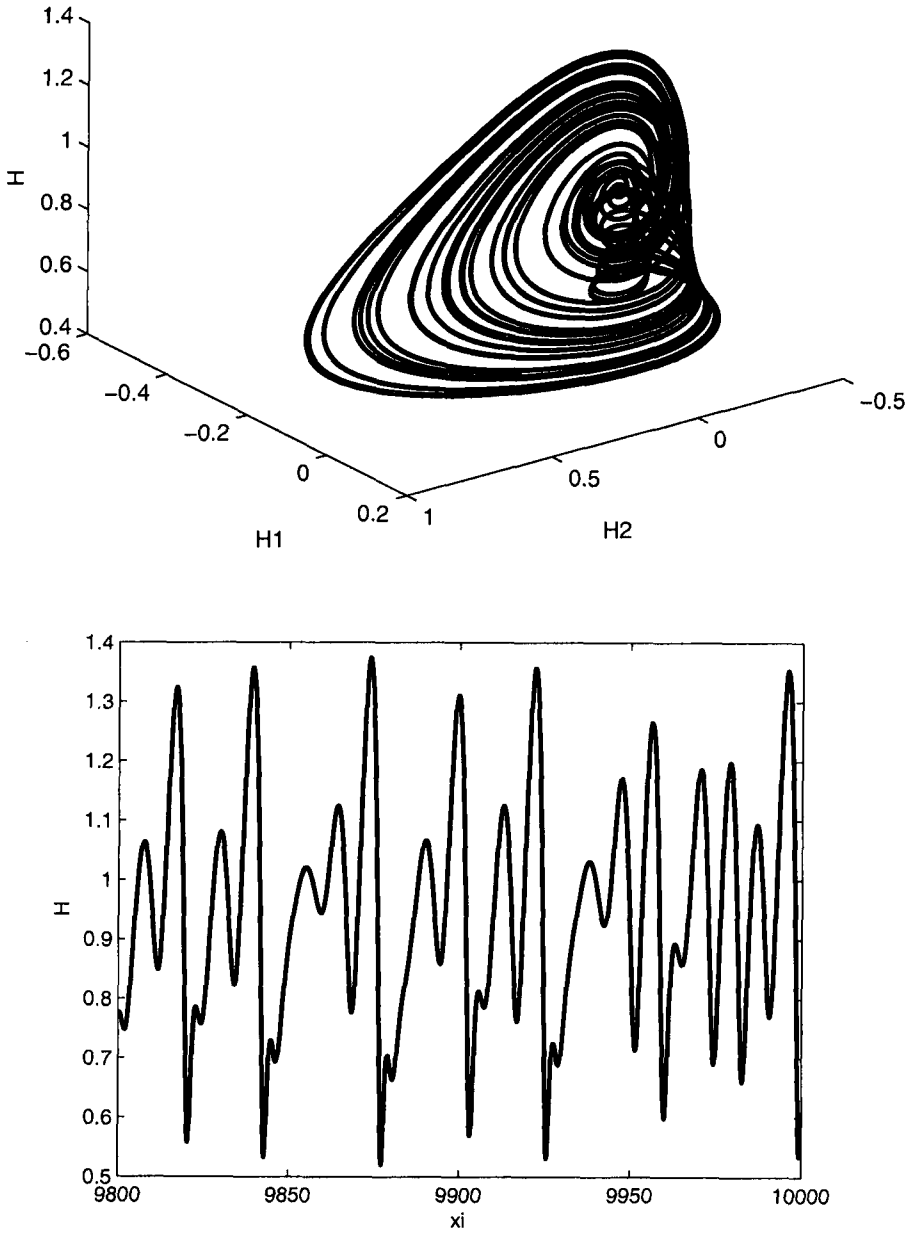


Figure 3-19: Periodic wave R=10;B=0*R;We=1;c=1.87
a) limit cycle b) wave profile

As pointed out through the qualitative analysis the film flowing down an inclined plane can undergo several complex bifurcation scenarios. The complexities of the bifurcation scenarios are summarized in figure 3-20 through bifurcation diagrams for some particular value of the flow parameters. The bifurcation diagrams show the evolution of the maximum height of the film $H_m$ with the control parameter $c$ (wave celerity) for various parameter values of the parameter $\frac{\cot\theta}{R}$. In figure 3-20a we observed a continuous increase of the period of the limit cycle until it becomes a homoclinic orbit, (see figure 3-25 c). Figure 3-20b shows a series of period doubling followed by a homoclinic orbit at the value of the control parameter equal to 2.44. In figure 3-20c homoclinic orbits with multiple humps follows a periodic doubling. In figure 3-20d the bifurcation diagram indicates that the free surface undergoes a series of periodic doubling, later leading to chaos, as depicted in figures 3-16 to 3-19.

## 5.2 Numerical implication of the correction

### *5.2.1 Transcritical bifurcation*

Above we have shown the implication of the correction introduced to the model of Usha and Uma (2004) on the occurring conditions of the bifurcations. In this subsection, we will portray its implication through numerical simulations. The wave profiles obtained using our model is compared to the ones obtained using the model of Usha and Uma (2004). In figure 3-21, we compare a wave profile issued after heteroclinic bifurcation or hydraulic jumps obtained with the two models. It can be noticed that the

correction does not affect the heteroclinic bifurcation from $H_1$ toward $H_2$, the two wave profiles coincide. However, the wave profiles issued from $H_2$ toward $H_1$ through heteroclinic bifurcations are different. Figure 3-21b shows that the shear stress (which is the added to ensure accuracy up to the second order) smoothens slightly the hydraulic jump $H_2$ toward $H_1$.

*5.2.2 Hopf bifurcation.*

In figure 3-22a, we display the periodic waves issued after the Hopf bifurcation from the first stationary solution $H_1$ for a value of the control parameter $c = 1.95$. We observe that the periodic waves predicted by the model of Usha and Uma have a larger amplitude and their period is almost double that of the one predicted by our model. The current model predicts periodic waves while the model of Usha and Uma predicts a flat free surface, see figure 3-22b. Here again the effect of shear stress is significant on the periodic waves issued from the stationary solutions.

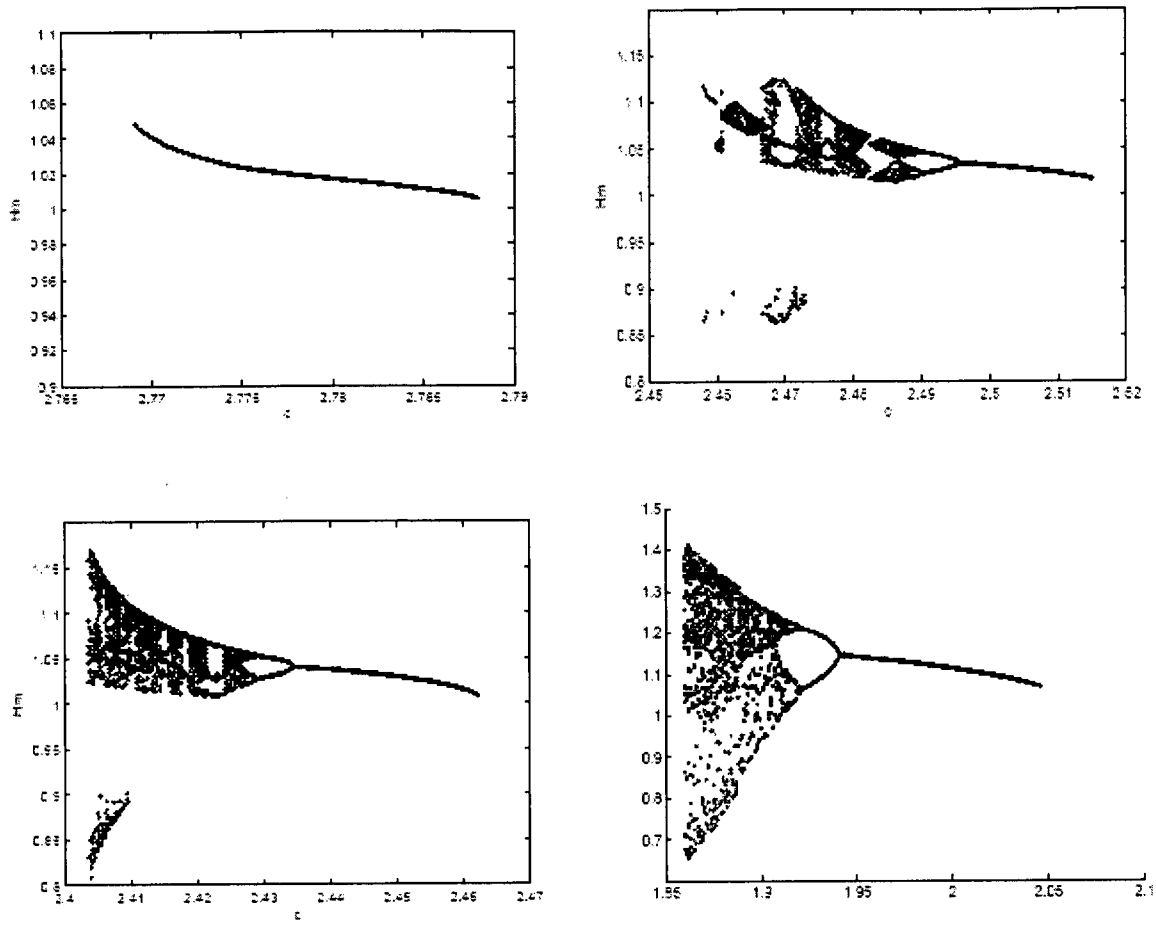

Figure 3-20: Bifurcation diagrams from the stationary solution H1
a) R=1/0.075;B=0.9*R;We=1; b) R=1/0.075;B=0.55*R;We=1;
c) R=1/0.075;B=0.48*R;We=1;d) R=1/0.075;B=0*R;We=1;

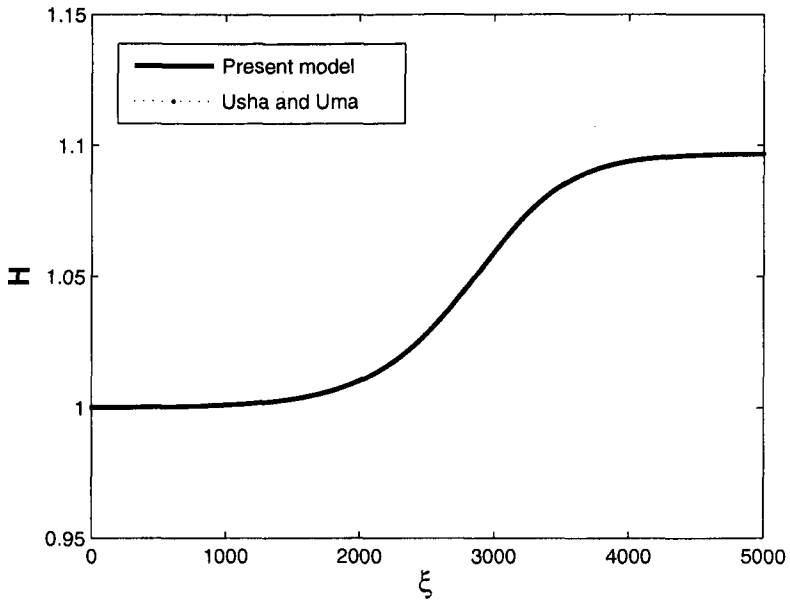


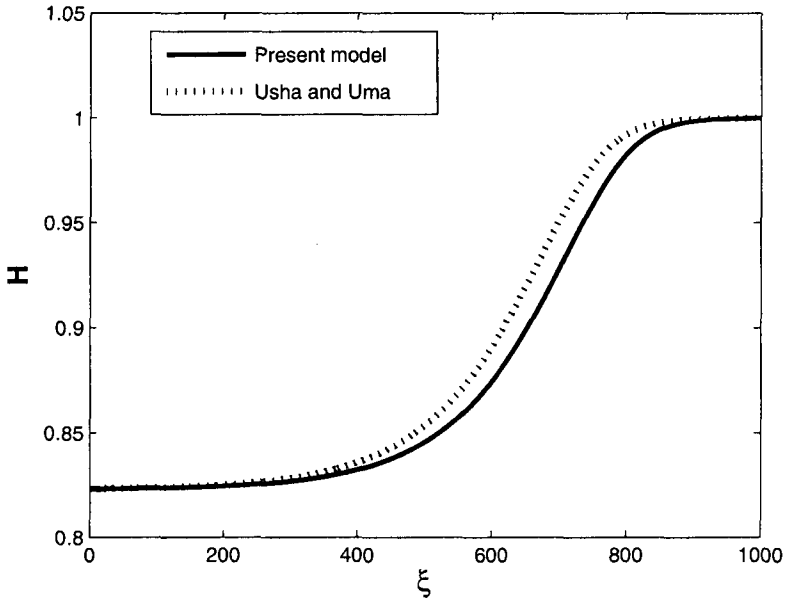


Figure 3-21: a) Wave profile during heteroclinic orbit from H1 toward H2
$R = 100 \quad \cot\theta = 0.4R \quad We = 1 \quad c = 3.3$

b) Wave profile during heteroclinic orbit from H2 toward H1
$R = 100 \quad \cot\theta = 0.4R \quad We = 1 \quad c = 2{,}5$

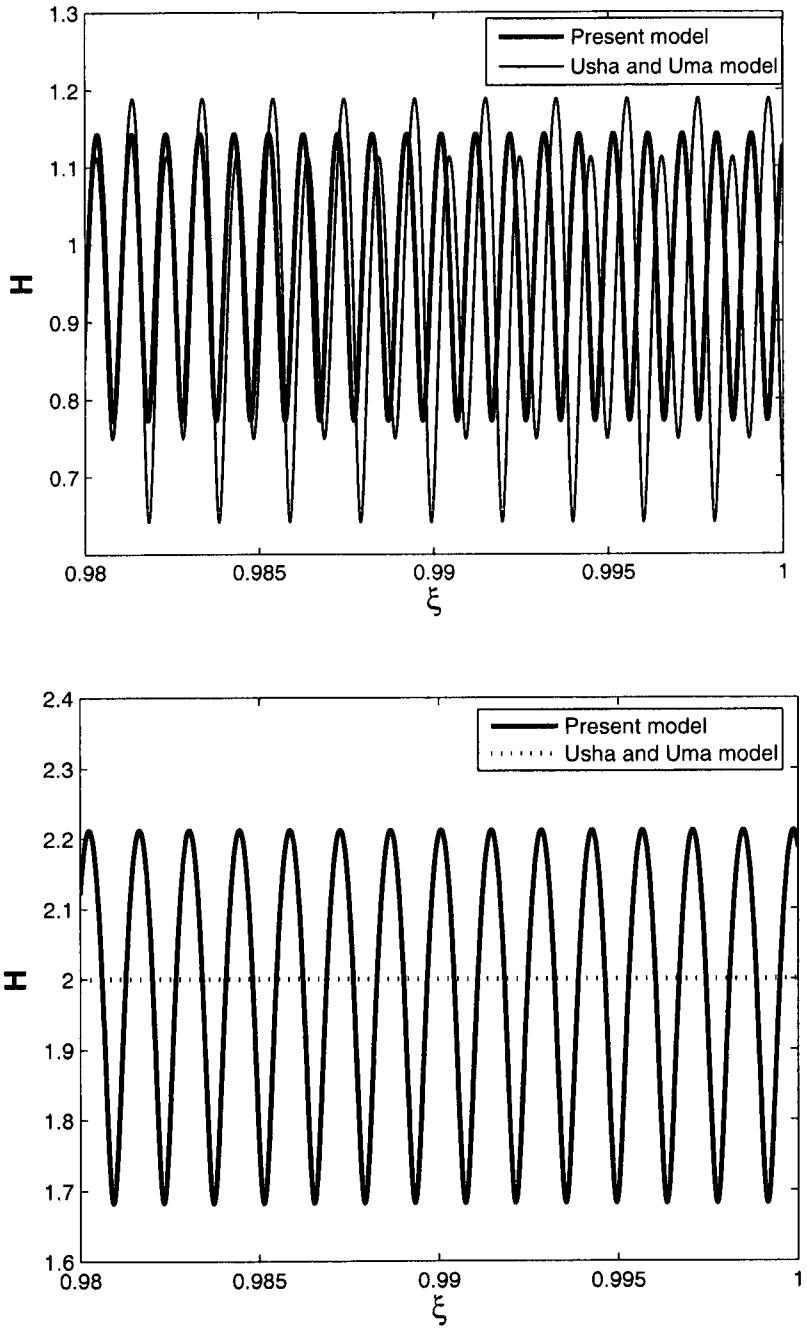


Figure 3-22: a) Wave profile after Hopf bifurcation from H1
$R = 1/0.075 \quad \cot\theta = 0 \quad We = 1 \quad c = 1.95$

b) Wave profile during heteroclinic orbit from H2
$R = 1/0.075 \quad \cot\theta = 0 \quad We = 5 \quad c = 7$

From this last observation, we can infer that the shear stress triggers Hopf bifurcations, in particular, from the second stationary solutions. Let us consider the first fixed point $H_1$ and decrease the value of the control parameter to $c = 1.93$. The numerical simulations using the model of Usha and Uma predicts a cascade of periodic doubling, while our model predicts just one periodic doubling, see the phase portraits and wave profiles displayed in figure 3-23. Here we observe that the shear stress inhibits the cascade of the symmetry breaking from the first stationary solution. Similar trends hold when the value of the control parameter was further decreased. At the value of the control parameter of $c = 1.92$ our model predicts a second periodic doubling while the model of Usha and Uma predicts more periodic doubling than the precedent case, see figures 3-24. According to the results displayed in figures 3-22, 3-23 and 3-24, we can conclude that the model of Usha and Uma (2004) anticipates the symmetry breaking or the route to chaos through periodic doubling scenarios. In figure 3-25, we show the wave profile after a homoclinic bifurcation; the train of solitary waves predicted with our model and the model of Usha and Uma are similar; the amplitude of the solitary waves is identical, while their period is slightly different. The period of the solitary waves predicted with the model of Usha and Uma is slightly higher than the one predicted with the present formulation. The difference between the two models occurs also at the beginning of the solitary waves; our model predicts a smoother bifurcation, see figure 3-25c.

As a conclusion to this subsection, the shear stress introduced in the velocity profile, to ensure the consistency of the model up to the second

order with respect to the long wave parameter, influences the bifurcation scenarios. It renders the hydraulic jump smoother and it triggers a Hopf bifurcation scenario from the second stationary solution. However, the shear stress inhibits symmetry breaking through a periodic doubling cascade of the first stationary solutions. As shown in the figure 3-26, the shear stress triggers the Hopf bifurcation from the second stationary solution.

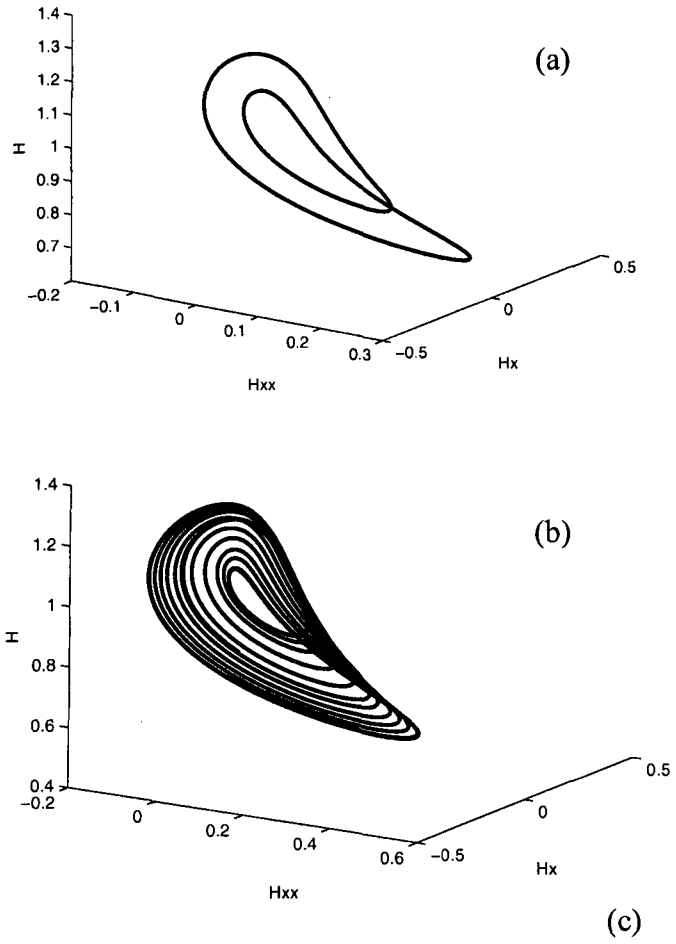


Figure 3-23: Phase trajectory from H1, $R = 1/0.075$ $\cot\theta = 0$ $We = 1$ $c = 1.93$
a) Present model b) Usha and Uma model
c) Wave profile after periodic doubling from H1

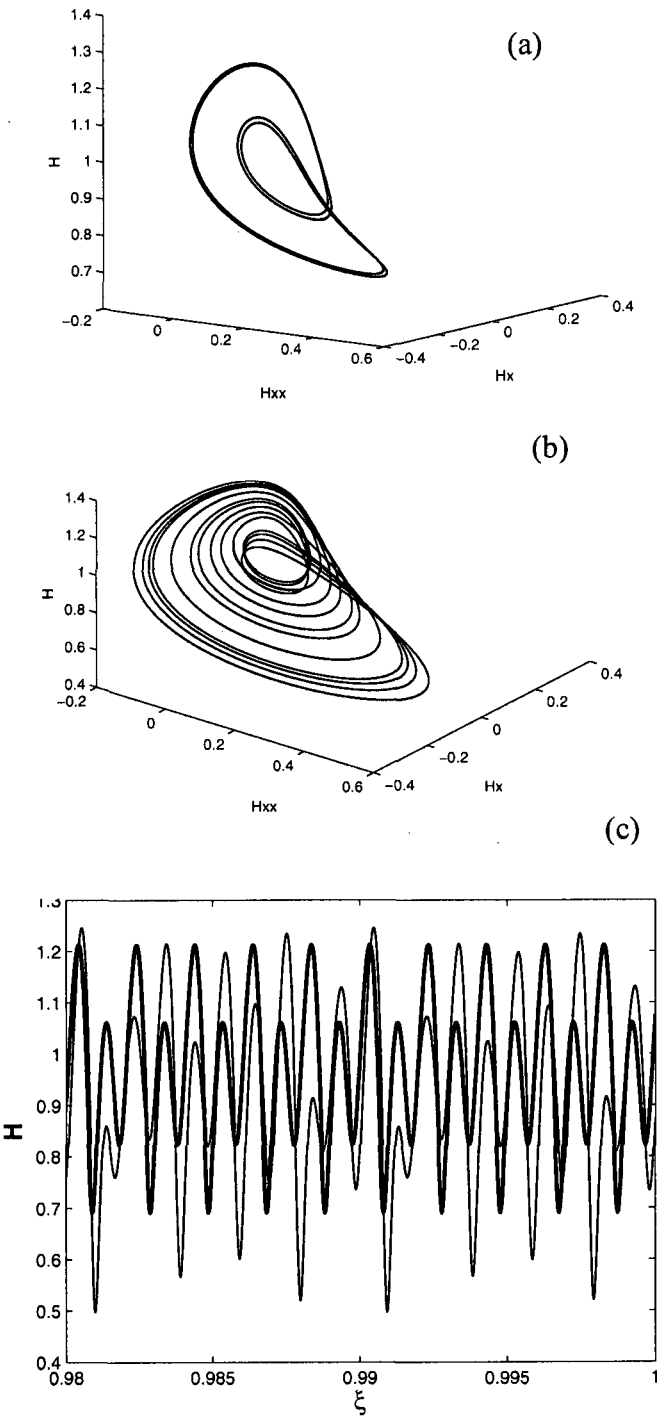


Figure 3-24: Phase trajectory from H1, $R = 1/0.075$ $\cot\theta = 0$ $We = 1$ $c = 1.92$
a ) Present model b) Usha and Uma model
c) Wave profile after periodic doubling from H1

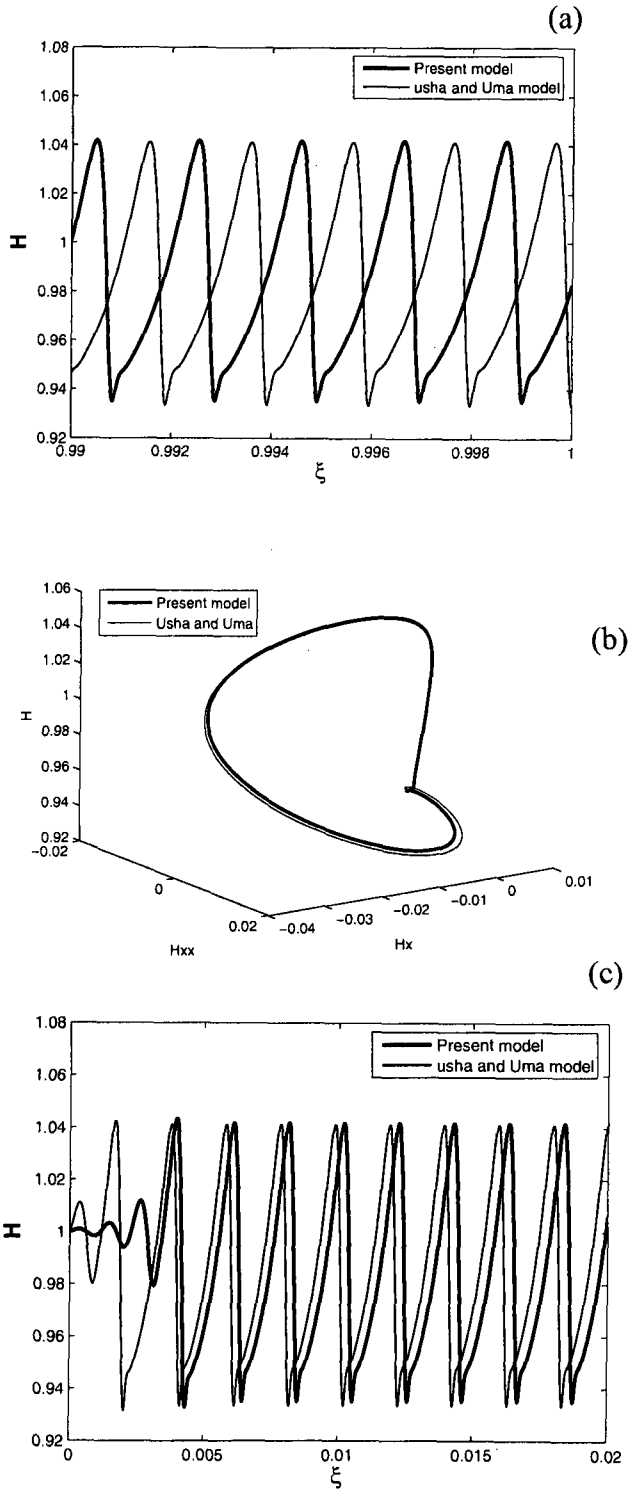


Figure 3-25: a) Phase trajectory from H1, $R = 1/0.075$ $\cot\theta = 0.9R$ $We = 1$ $c = 2.7699$
b)Wave profile after homoclinic bifurcation from H1
c) Wave profilebeginning of the homoclinic bifurcation from H1

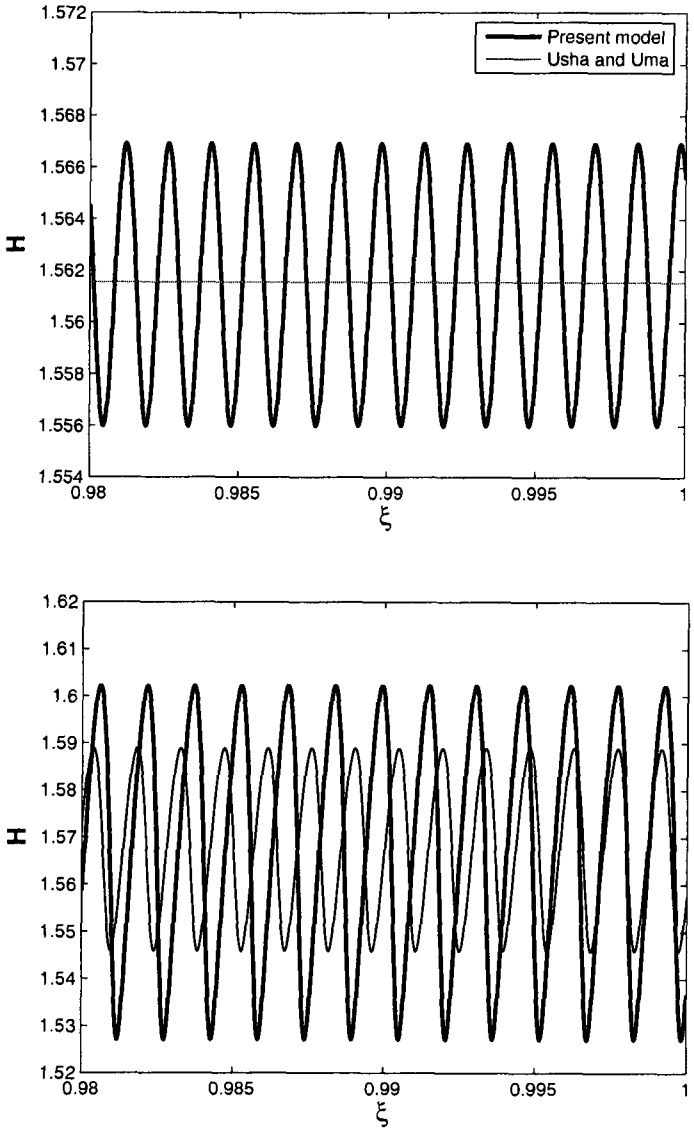


Figure 3-26: Wave profile from $H_2$

a) $c = 5 \quad R = 1/0.075 \quad \cot\theta = 0.75 \quad We = 1$

b) $c = 5.03 \; R = 1/0.075 \quad \cot\theta = 0.755 \quad We = 1$

# 6. Conclusion

The implication of the correction introduced to the two-equation model of Usha and Uma for the thin film fluid flowing down inclined plane is shown through qualitative and numerical analysis. The impact of the corrections is shown through its influence on the bifurcation scenarios. We have shown that the shear stress at the free surface influences the occurrence conditions of the two generic bifurcations namely the heteroclinic and Hopf bifurcations. We have also shown through the numerical simulation that the shear stress does not have the same effect on the solutions issued from the two stationary solutions. While its effect is insignificant on the hydraulic jump issued from the first stationary solution, it is found that the shear smoothness the hydraulic jump from the second towards the first stationary solution. We found that the shear stress has opposite effects on the symmetry breaking through Hopf bifurcation. While it inhibits the symmetry breaking through a cascade of periodic doubling from the first stationary solution, it triggers and enhances such bifurcation from the second bifurcation. We have also shown that the shear stress slightly delays the symmetry breaking through homoclinic bifurcations.

# Chapter IV: Effect of magnetic and electrical fields on falling film stability

## 1. Introduction

The interaction of a thin layer liquid metal, moving under the influence of an electromagnetic field, is of practical importance to several technological applications such as the casting industry, and in nuclear reactors. In the casting industry, magnetic fields are used in electromagnetic braking while in belt strip casting they serve as a damping mechanism, Löfgren and Åkerstedt (1998). In fusion devices, flow of a thin layer of liquid metal is employed against erosion and thermal loads of the reactor's walls, Narula et al (2005). The reliability and efficacy of the protection depend on the stability of the flowing liquid-metal layer under extreme conditions characterized by a strong surrounding magnetic field, high heat fluxes, and a significant amount of evaporation. The magnetic field has three components that vary in space and time. The flow of the liquid-metal film is three-dimensional and the fusion environment has a complex geometry, which renders the analytical approach to this problem difficult if not impossible. For design purposes, numerical and experimental means are preferred to the analytical approaches. As a result, researchers have developed over the past years solvers, which simulate liquid wall protections in nearly operating conditions. An overview of progress made in this direction is summarized in Morely (2004). Experiments have also been conducted to better understand the effect of magnetic fields on the

film thickness and its stability, see for example Narula et al (2005), Feng-Chen Li, and Akimi Serizawa (2004).

A better grasp of the mechanisms that lead to layer instability requires a detailed examination of the individual effect of the three components of the magnetic field. Most of the studies in the field have focused on the major cause of instability which is the toroidal (spanwise) component of the magnetic field. The contribution of this component on the thin liquid metal layer response, initiated by Aitov et al (1988), has been the concern of several subsequent analytical studies. A strong toriodal magnetic field makes the flow variation in the spanwise direction relatively insignificant thus rendering the problem to be two-dimensional. The toroidal component of the magnetic field strongly affects the main flow and its stability. Although the surface normal and the longitudinal components are less important in comparison with the transverse components, it nevertheless exerts a significant influence on the stability of the metal layer. Our interest focuses on the effect of the normal magnetic field component on the stability of the metal layer and the possibility of controlling the film stability via a transverse electrical field. In order to simplify the analysis, we omit the contributions of the spanwise magnetic field component.

Pioneering work on the stability of electrically conducting thin films of fluid moving down an inclined plane, under the action of gravity an a magnetic field, was carried out by Hsieh (1965), and Ladikov (1966). Their studies showed that a surface normal magnetic field stabilizes the flow.

Korsunsky (1999) investigated the long wave development on the free surface under the influence of electromagnetic fields at high and low Reynolds numbers. He found that the combination of electrical and magnetic fields could either stabilize or destabilize the flow.

At a high Reynolds number, other terms such as inertia, viscous and forcing terms, although of small magnitude, contribute significantly to the dynamic evolution of the problem, and hence affect greatly its stability characteristics. The second order terms, with respect to long-wave parameter $\varepsilon$ (ratio of the film height to the wave length), are incorporated in the analysis of Korsunsky (1999) for flow at high Reynolds numbers, (see equation (39-40) in Korsunsky (1999)). The model (equations (44)) obtained by Korsunsky (1999) is similar to the Shkadov's (1968) formulation for the pure hydrodynamic case, which is known to overestimate the cut-off wave-number that separates the stable from unstable regions. Moreover, similarly to Shkadov's model, it does not predict the Hopf bifurcation, which leads to stationary periodic waves at the free surface. Consequently, Korsunsky's formulation suffers from the same drawback. Incorporating second order terms, we remedy the weakness of Korsunsky's approach. We also show that the proposed model reduces to a model similar to the one proposed by Lee and Mei (1996) for the pure hydrodynamic case, which features both a Hopf bifurcation and a hydraulic jump. It is worth mentioning that the hydraulic jump, in a metal layer flowing under the influence of a spatially varying

magnetic field, has already been observed experimentally by Narula et al (2005).

The present chapter is organized as follows. In section 2, we recall the formulation of the problem and, similarly to Korsunsky, we use the momentum integral approach of Karman-Polhausen to reduce the Magnetohydrodynamics equations into two coupled spatiotemporal evolution equations for the film depth and flow rate. In section 3 we perform the linear stability analysis. The two spatiotemporal evolution equations for the film depth and the flow rate are linearized around the basic flow solution. We show the effects of magnetic and electrical fields on the linear stability conditions and we compare our results with those obtained with Korsunsky's model. In section four, we tackle the influence of the electrical and magnetic field on the occurring conditions of the transcritical and Hopf bifurcations. This investigation was conducted in frame of reference moving with the celerity of the perturbation. In section five some concluding remarks are given.

## 2. Formulation of the problem

We consider a flow of a thin layer of liquid metal under the combined effects of gravity, and constant and uniform electrical and magnetic fields. The fluid is assumed an incompressible, electrically conducting, Newtonian fluid. The metal liquid flows down an inclined plane that makes an angle, $\theta$, with the

horizontal, and assumed it to be an electrical insulator. As depicted in Figure 4-1, the magnetic and electric fields are, respectively, normal and transvers to the plane of flow ( $\vec{B}(0,0,B)$ and $\vec{E}(0,E,0)$ ), where $\varphi$ is the incline angle of the magnetic field. In this study we consider, $\varphi=\frac{\pi}{2}$.

For almost all electrically conducting liquid metals in both laboratory and operating conditions within the fusion power reactors, the magnetic Reynolds number is small i.e. $R_m=\mu_0.\sigma.L.c_0<<1$, where $\mu_0$, $\sigma$ and $c_o$ are the electrical conductivity, magnetic permeability of the fluid, and the characteristic velocity, respectively. Under these conditions, the perturbations of the electromagnetic fields due to the fluid motion can be neglected.

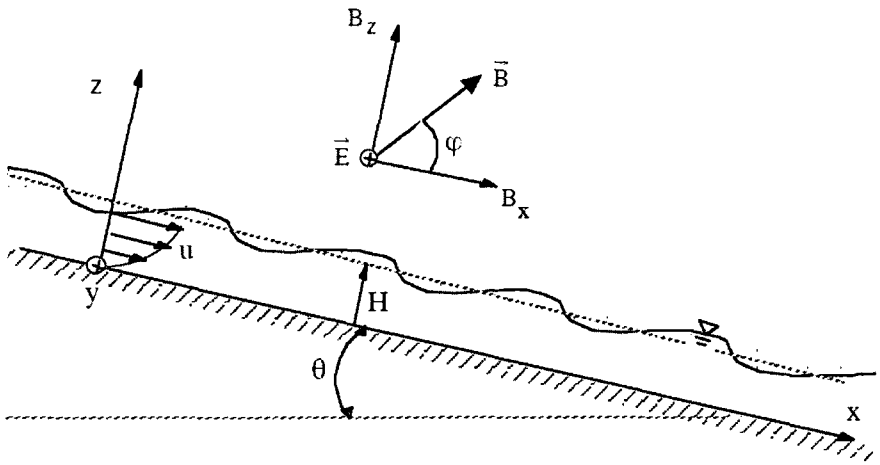


Figure 4-1 . Schematic of the problem.

The flow is supposed to be two-dimensional, described by Magnetohydrodynamics evolution equations along with the associated boundary conditions:

$$\nabla.\vec{V} = 0 \tag{4-1}$$

$$\frac{\partial \vec{V}}{\partial t} + \vec{V}.\nabla\vec{V} = \frac{1}{\rho}\nabla P + \nu\Delta\vec{V} + \vec{g} + \frac{\mu_0\sigma}{\rho}(\vec{E} + \mu_0\vec{V} \wedge \vec{H}_0) \wedge \vec{H}_0 \tag{4-2}$$

$$\vec{E} = \vec{E}_0 - \nabla\phi \tag{4-3}$$

$$\Delta\phi = \vec{H}_0.(\nabla \wedge \vec{V}) \tag{4-4}$$

$$\vec{V}(X,0,t) = \vec{0} \tag{4-5}$$

$$z = H(x,t) \quad w = \frac{\partial H}{\partial t} + u\frac{\partial H}{\partial x} \tag{4-6}$$

$$(-P\overline{\overline{\delta}} + 2\mu\overline{\overline{D}})\vec{n} = (-P_a - T div.\vec{n})\overline{\overline{\delta}}.\vec{n} \tag{4-7}$$

Where $P_a$ and $P$ are the atmospheric and fluid pressures, $\mu$ is the dynamic viscosity of a fluid, $\overline{\overline{D}}$ is the deformation tensor and $T$ is the surface tension coefficient. The projection of equations (5-6) and (5-7) in Cartesian coordinate leads to:

$$\mu\left(u_z + w_x - 2u_x H_x + (P - P_a - T(\nabla.\vec{n}))H_x\right) = 0 \tag{4-8}$$

$$\mu\left((w_x + u_z)H_x + P - P_a - T(\nabla.\vec{n})\right) = 0 \tag{4-9}$$

with,

$$\vec{n} = \frac{\left(-H_x,0,1\right)}{\left(1+H_x^2\right)^{\frac{1}{2}}} \tag{4-10}$$

$$\nabla.(\vec{n}) = -H_x(1+H_x^2)^{\frac{-3}{2}} \tag{4-11}$$

The governing equations are rewritten in dimensionless form using the following dimensionless quantities:

$$u^* = \frac{u}{c_0}, \quad x^* = \frac{x}{L}, \quad z^* = \frac{z}{d}, \quad w^* = \frac{wL}{dc_0}, \quad p^* = \frac{p - p_a}{\rho c_0^2}, \quad t^* = \frac{tc_0}{L}, \quad H^* = \frac{H}{d}$$

Where $c_0 = \frac{gd^2 \sin\theta}{3\nu}$ is the Nusselt velocity, and $L$ and $d$ are the characteristic length in stream and normal directions. In the following equations, subscripts are skipped.

$$u_t + uu_x + wu_z = -p_x + \frac{1}{R}(\varepsilon u_{xx} + \frac{1}{\varepsilon}u_{zz} + \frac{H_a^2 \sin 2\varphi}{2}w + \frac{3}{\varepsilon} + \frac{\alpha H_a^2 \sin\varphi}{\varepsilon} - \frac{H_a^2 \sin^2\varphi}{\varepsilon}u) \tag{4-12}$$

$$\varepsilon^2(w_t + uw_x + ww_z) = -p_z + \frac{\varepsilon}{R}(w_{zz} + \frac{H_a^2 \sin 2\varphi}{2\varepsilon}u - H_a^2 \cos^2\varphi w - \frac{3}{\varepsilon}\cot g\theta - \frac{\alpha H_a^2 \cos\varphi}{\varepsilon}) \tag{4-13}$$

$$u_x + w_z = 0 \tag{4-14}$$

$$z = 0: \qquad u = w = 0 \tag{4-15}$$

$$z = H(x,t): \qquad w = H_t + uH_x \tag{4-16}$$

$$u_z(1 - \varepsilon^2 H_x^2) + \varepsilon^2(w_x - 4u_x H_x) = 0 \tag{4-17}$$

$$p = 2\frac{\varepsilon}{R}w_z - \varepsilon^2 WeH_{xx} \tag{4-18}$$

The subscript indicates derivatives with respect to the stream-wise and normal coordinates. Furthermore, $u$ , $w$ and $p$ indicate the streamwise components, normal velocity components, and the static pressure, respectively. Equations (4-12-4-18) involve the following fundamental parameters: $R=\frac{c_0 d}{\nu}$ , $We=\frac{\gamma}{\rho.d.c_0^2}$ , $H_a=\mu_0 H_0\sqrt{\frac{\sigma}{\mu.}}$ and $\alpha=\frac{E_0}{\mu H_0 c_0}$ , which are Reynolds, Weber, and Hartman numbers, and the dimensionless number measuring the influence of the electrical field. Parameters $d$ , $\mu$ , $\nu$ , $\rho$ , $H_0$ $E_0$ and $\gamma$ are, respectively, the initial film thickness, dynamics viscosity, kinematics viscosity, density, intensity of the magnetic field, intensity of the electrical field and surface tension coefficient. In the dimensionless equations given above, we considered high velocity flow, where the order of magnitude of the Reynolds number is $R=O(\varepsilon^{-1})$ ( $\varepsilon=\frac{d}{L}$, in this study is equivalent to the wave number). The Reynolds number is related to the Weber number, which for most of the liquid metals a high Reynolds number corresponds to a small Weber number, $We=O(1)$.

# 3. Linear stability

Similar to Korsunsky (1999), the solution for the unperturbed flow that corresponds to the solution of the zero order with respect to $\varepsilon$ of the governing system equations (4-12-4-18) is given by:

$$U_S = D(1 - \frac{\cosh[(z-1)H_a \sin\varphi]}{\cosh(H_a \sin\varphi)}) \qquad \text{with} \qquad D = \frac{\alpha}{\sin\varphi} + \frac{3}{H_a^2 \sin^2\varphi}.$$

In a certain range of values of both the flow and electromagnetic parameters, the basic solution looses its stability and undergoes bifurcation in favour of other stable solutions. The approximate solution to the problem is obtained, using the integral method of Karman-Polhausen, which requires the presumption of a velocity profile. The following profile has been chosen for this study:

$$u(x,Z,t) = A(x,t).f_1(Z) + B(x,t).f_2(Z) \tag{4-19}$$

$$f_1(Z) = D.(1 - \frac{\cosh[(Z-1)H_a \sin\varphi]}{\cosh(H \sin\varphi)}), \qquad f_2(Z) = \sinh(Ha \sin\varphi.Z)$$

with $Z = \frac{z}{H(x,t)}$

Using the definitions for the flow rate and shear stress at the free surface, the unknown coefficients $A(x,t)$ and $B(x,t)$ are related to the flow rate, $Q(x,t)$, the layer thickness, $H(x,t)$, and the shear stress at the interface, $\tau(x,H,t)$, as shown in the following.

$$A(x,t)=\frac{Q(x,t)}{H(x,t)d(1-\dfrac{\tanh(Ha\sin(\varphi))}{Ha\sin(\varphi)})}-\frac{\tau(x,t)H(x,t)[\cosh(Ha\sin(\varphi))-1]}{Ha^2\sin(\varphi)^2 d(1-\dfrac{\tanh(Ha\sin(\varphi))}{Ha\sin(\varphi)})\cosh(Ha\sin(\varphi))}$$

$$B(x,t)=\frac{\tau(x,t)H(x,t)}{Ha\sin(\varphi)\cosh(Ha\sin(\varphi))}$$

Hence, three independent equations are then needed to determine the spatial-temporal evolutions of the fundamental variables $Q(x,t)$ , $H(x,t)$ and $\tau(x,t)$. Fortunately, the shear stress at the free surface is of order two with respect to the long wave parameter, $\varepsilon$ . Indeed, equation (4-17) can be rewritten in the following form:

$$\tau(x,t)=\varepsilon^2(4.u_xH_x-w_x)+O(\varepsilon^4) \tag{4-20}$$

Therefore, the shear stress $\tau(x,t)$ can be expanded in terms of a series with respect to $\varepsilon$ , ( $\tau(x,t)=\varepsilon^2\tau_1(x,t)+O(\varepsilon^4)$ ). As a result, the shear stress could be expressed as a function of $Q(x,t)$ and $H(x,t)$ :

$$\tau(x,t)=\frac{\varepsilon^2 D}{H(x,t)^2 Q_0 N\cosh(N)}\left[\begin{array}{c}[2NH(x,t)Q_xHx-2NH_x^2Q(x,t)-NQH(x,t)H_x^2](\cosh(N)-1)+\\ Q_x^2H(x,t)^2N\cosh(N)(1-\dfrac{\tanh(N)}{N})\end{array}\right] \tag{4-21}$$

Therefore, the flow rate and the film height are the dependent variables and only two equations are needed to completely describe the problem. The

first equation is derived from continuity (4-14), and the kinematics condition at the free surface (4-16):

$$\frac{\partial H(x,t)}{\partial t}+\frac{\partial Q(x,t)}{\partial x}=0 \tag{4-22}$$

The second equation is obtained as follows. First, the pressure is obtained by integrating equation (4-13) in the normal direction from a given point in the fluid to the free surface. The condition (4-18) at the free surface is used to determine the constant of integration. Second, the expression for pressure is differentiated with respect to $x$ along with equation (4-21), and the result is incorporated in equation (4-12). Averaging the latter over the film depth in the normal direction, we obtain the second equation. This second equation, which is a nonlinear functional of $Q(x,t), H(x,t)$ and their derivatives, is too lengthy to be given here. Out of convenience, we state it in its general form:

$$G(Q(x,t), H(x,t))=0 \tag{4-23}$$

As a means of verification, we argue that when the Hartman number $H_a$ and the coefficient $\alpha$ tend to zero the model should reduce to the pure hydrodynamics case. In the limit, equations (4-22-4-23) reduce to the pure hydrodynamic model:

$$\frac{\partial q}{\partial x}+\frac{\partial h}{\partial t}=0 \tag{4-24-a}$$

$$\left(\frac{219R}{280}h_{xxxt}+\left(-W_eR+\frac{153R}{280}\right)h_{xxxx}+\frac{11R}{40}h_{xxtt}\right)\varepsilon^3+\left(5h_{xxt}+\frac{27}{4}hxxx\right)\varepsilon^2$$
$$+\left(-Rh_{tt}+\left(3\cot\theta-\frac{6R}{5}\right)h_{xx}-\frac{12R}{5}h_{xt}\right)\varepsilon-3h_t-9h_x=0 \tag{4-24-b}$$

Comparing the equation above with the corresponding of Lee and Mei (1996) (Equations 3.1 and 3.2) we notice a slight difference in the second and third order terms. It is worth noting that our equation is more accurate than those given in Lee and Mei (1996). The reason being, the velocity profile used in Lee and Mei (1996) does not exactly satisfy the tangential dynamic condition at the free surface up to the second order with respect to the long wave parameter. However, the velocity profile deduced from equation (4-19) does. The velocity deduced from (4-19) is given as follow.

$$u(x,z,t)=a(x,t)z+b(x,t)z^2$$

where $$a(x,t)=-\frac{1}{2}\frac{h(x,t)^2\tau(x,t)-6q(x,t)}{h(x,t)^2}$$

and

$$b(x,t)=\frac{3}{4}\frac{-2q(x,t)+h(x,t)^2\tau(x,t)}{h(x,t)^3}$$

This profile reduces to the velocity profile of Lee and Mei when the shear stress is neglected. Therefore the slight difference between our pure hydrodynamic model, deduced from equation (4-22 and 4-23) and the corresponding equations in Lee and Mei (1996) is expected since the shear stress at the free surface is of second order. In contrast, the hydrodynamic model deduced from eq. (44) in Korsunsky (1999) corresponds to the Shkadov's model given by the following equations.

$$\frac{\partial q}{\partial x}+\frac{\partial h}{\partial t}=0 \tag{4-25-a}$$

$$\frac{\partial q}{\partial t}=\frac{3}{R}\left(h(x,t)-\frac{q(x,t)}{h(x,t)^2}-h(x,t)\frac{\partial h(x,t)}{\partial x}\cot\theta\right)+\frac{6}{5}\frac{q(x,t)^2\frac{\partial H(x,t)}{\partial x}}{h(x,t)^2}$$
$$-\frac{12}{5}\frac{q(x,t)\frac{\partial q(x,t)}{\partial x}}{h(x,t)}+Weh(x,t)\frac{\partial^3 h(x,t)}{\partial^3 x} \tag{4-25-b}$$

It is worth noting that differentiating equation (4-25-b) with respect to the longitudinal coordinate $x$ and using the equation (4-25-a) we find that Shkadov's model is included in our hydrodynamics model.

First we explore the influence of the electromagnetic parameters on the evolution of small disturbances, $h(x,t)$, added to initial film thickness. Using equation (4-20), the linearized form of equation (4-23) is given by:

$$\left(C_1.h_{xxxx} + C_2.h_{xxtt} + C_3.h_{xxxt}\right).\varepsilon^3 + \left(C_4.h_{xxt} + C_5.h_{xxx}\right).\varepsilon^2 + \left(C_6.h_{tt} + C_7.h_{xt} + C_8 h_{xx}\right)\varepsilon + C_{10}.h_x + C_9.h_t = 0$$

(4-26)

The coefficients $C_i$ depends on the hydrodynamic and electromagnetic parameters as well as the wave celerity (these coefficients are too lengthy to be given in this paper). We seek a solution of equation (4-26) in the wave like form: $h(x,t) = e^{i.(x-c.t)}$ where $c = c_r + i.c_i$ is a complex phase velocity. The dispersion equation rewritten in terms of the imaginary and the real parts is given by:

$$\varepsilon^3\left(C_1 - C_3.c_r - C_2.c_i^2 + C_2.c_r^2\right) - \varepsilon^2.C_4.c_i + \varepsilon\left(C_6.c_i^2 - C8 - C6.c_r^2 + C7.c_r\right) + C9.c_i +$$
$$i\left(\varepsilon^3\left(C_1 - C_3.c_r - C_2.c_i^2 + C_2.c_r^2\right) - \varepsilon^2.C_4.c_i + \varepsilon\left(C_6.c_i^2 - C_7 - C_7 c_r^2 + C_7.c_r\right)\right) = 0$$

The dispersion equation at marginal stability conditions ($c_i = 0$) reduces into:

$$\left(-c_r^2.C6 - C8 + c_r.C_7\right).\varepsilon + i\left(\left(c_r.C_4 - C5\right)\varepsilon^2 - c_r.C_9 + C_{10}\right) + O(\varepsilon^3) = 0 \qquad (4\text{-}27)$$

Therefore the imaginary and the real part should be null. From the imaginary part the celerity of the neutrally stable wave is:

$$c_r = \frac{C_{10}}{C_9} + O(\varepsilon^2)$$

Substituting the expression for $c_r$ into the real part of (4-27) we deduce the critical Reynolds number for the onset of the long wave instability, corresponding to a small wave number, $\varepsilon$.

$$R_c = \frac{C_{10} C_7}{C_9} - C_8 - \frac{C_6 C_{10}^2}{C_9^2} + O(\varepsilon^2)$$

The influence of the magnetic and electrical fields on the critical Reynolds number is displayed in Figure. 4-2 and Figure. 4-3. Figure 4-2 corresponds to the case where the electrical field is directed towards the interior of the fluid and the magnetic field is normal to the flow. The same figure shows that magnetic field pushes the critical Reynolds number up while the electrical field pulls it down. This result confirms the stabilization and destabilization effects of the magnetic and electrical field, respectively. Figure 4-3 indicates that when the direction of the electrical field is reversed it stabilizes the flow. It indicated also that an increase in electric field intensity raises the value of the critical Reynolds number. The maximum stability condition is obtained when the parameter, $D = \alpha + \frac{3}{H_a^2}$, is zero.

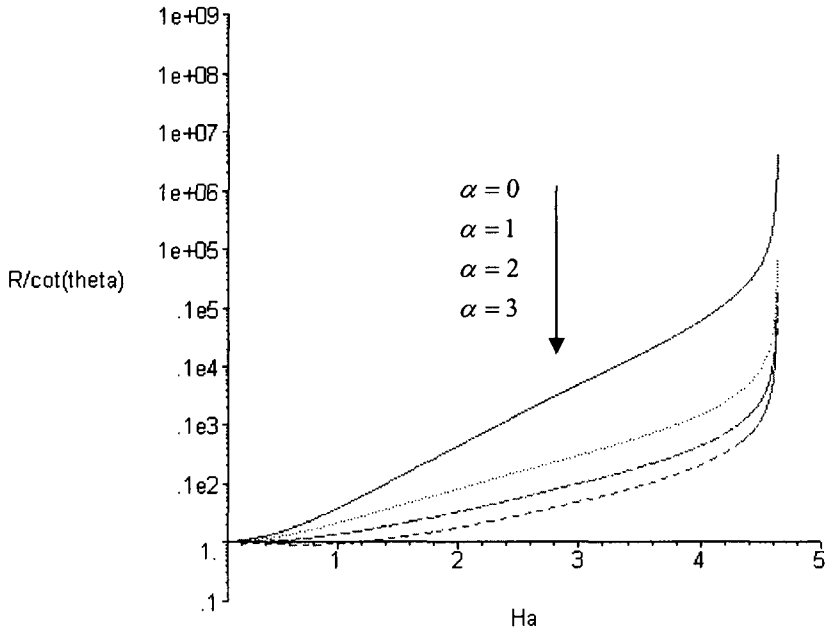


Figure 4-2: Critical Reynolds number versus Hartman number for different intensity of the electrical field directed towards the fluid interior while the magnetic field is normal to the flow
The continuous line : Korsunsky model, The dots : Present model

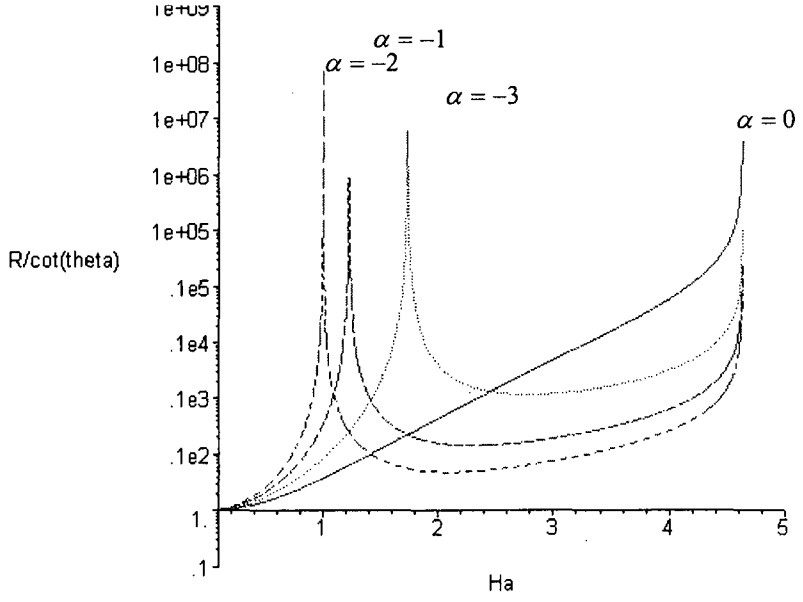


Figure 4-3: Critical Reynolds number versus Hartman number for different intensity of the electric field directed towards fluid exterior while the magnetic field is normal to the flow
The continuous line : Korsunsky model, The dots : Present model

As shown in the Figure 4-2 and Figure 4-3, the critical Reynolds number predicted by Korsunky (1999) is identical to the one predicted by our model. The latter result is expected, because the critical Reynolds number involves only a term of first order with respect to $\varepsilon$, (see eq (26)); at this order, the terms in equations (4-24-b and 4-25-b) are identical. This allows us to conclude that the corresponding magneto-hydrodynamics terms are indeed similar. Figure 4-2 and Figure 4-3 show that relatively weak intensity normal magnetic field ( $H_a$ around 4.5) can completely stabilize the liquid layer flow.

The improvement introduced to Korsunsky's model is shown through the variation of the cut-off wave-number with the Reynolds number. This curve separates the stable region from the unstable. These neutral stability curves are shown in Figure 4-4, 4-5 and 4-6. As expected, the Korsunsky's model overestimates the cut-off wave numbers and predicts a smaller area for stability.

Moreover, Korsunsky's approach does predict some of the important effects of the electrical and magnetic fields on the cut-off wave number. Our model predicts an asymptotic limit for the wave number when the Reynolds number tends to high values while the model of Korsunky's predicts a quasi linear variation with the Reynolds number. Figure 4-4 suggests that in the absence of the electrical field the cut-off wave numbers, predicted by the two models, coincides at $H_a = 3$ . This implies that at higher magnetic field intensities, the contribution of the second order terms become smaller.

Figure 4-5 shows the destabilizing effect of the electrical field when it is oriented toward the fluid interior. For a fixed intensity of the magnetic field, $H_a = 0.5$, an increase in the intensity of the electrical field reduces the area of the stability region. Figure 4-6 shows the stabilizing effect of the electrical field when its direction is reversed. It is worth noticing that Korsunsky's model predicts a larger effect of the electrical field on the stable region than the present model (see Figure 4-5 and Figure 4-6).

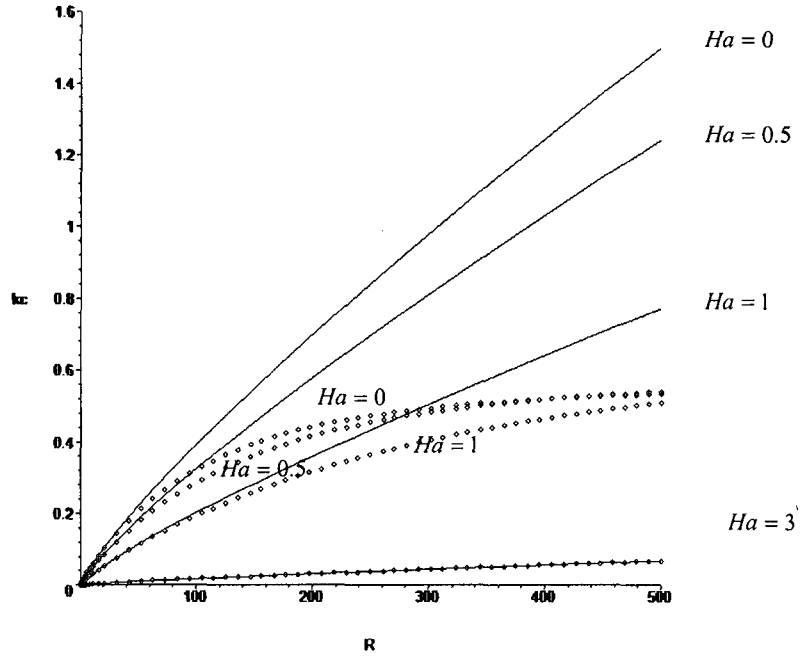


Figure 4-4 Cut-off wave-number versus Reynolds number in the absence of the electrical field. The magnetic field is normal to the direction of the flow. The continuous line : Korsunsky model, The dots : Present model

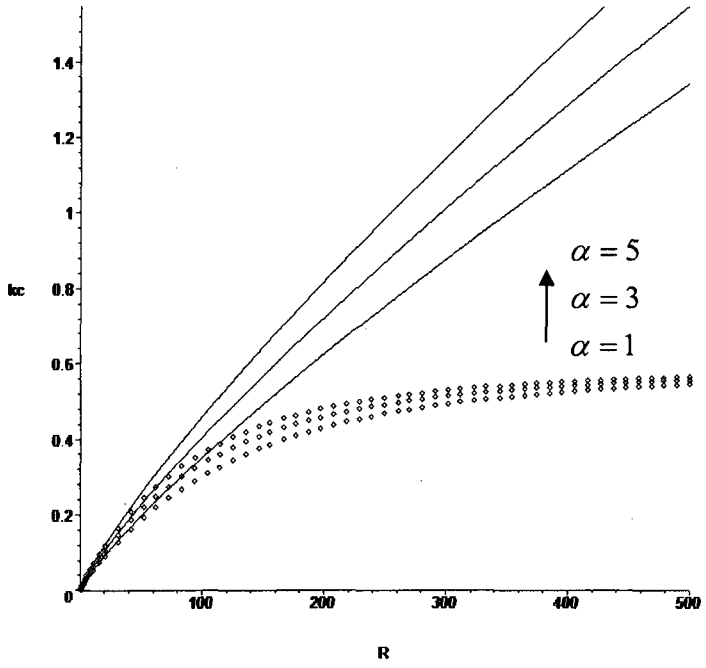


Figure 4-5 Influence of the intensity of the electrical field on the evolution of the cut-off wave-number versus Reynolds number. The magnetic field is normal to the direction of the flow, the electrical field is directed towards the fluid interior : The continuous line : Korsunsky model, The dots : Present model

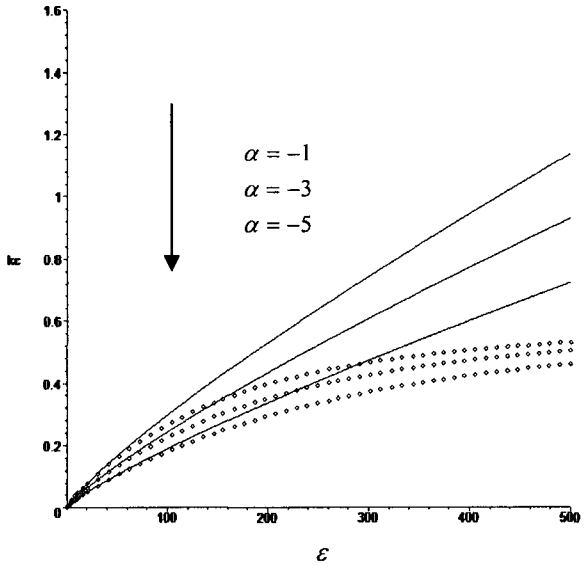


Figure 4-6 Influence of the intensity of the electrical field on the evolution of the cut-off wave-number versus Reynolds number. The magnetic field is normal to the direction of the flow, the electrical field is directed towards the fluid exterior : The continuous line : Korsunsky model, The dots : Present model

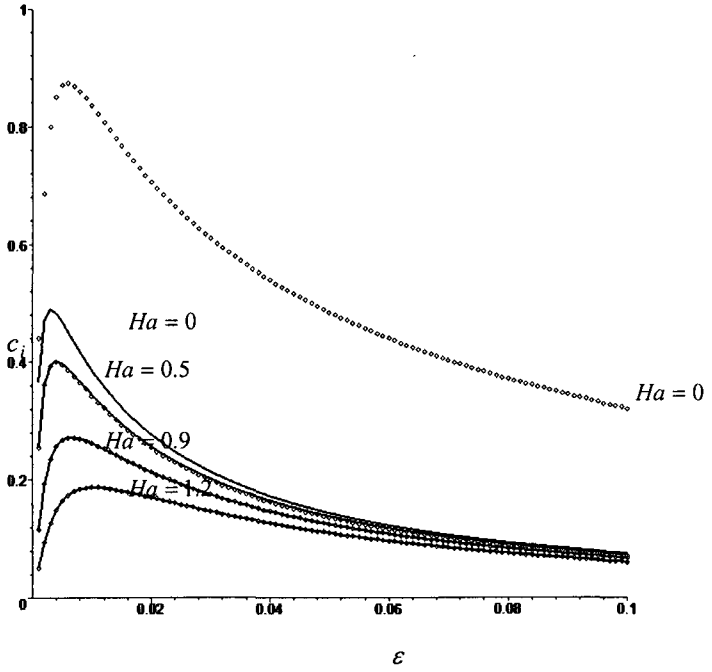


Figure 4-7 Effects of normal magnetic fields on the growth rate of the instability for vertically falling waves . (No electrical field is applied $\alpha = 0$ ) (For mercury at $20^0$C: R=500 $\gamma = 0.472\, N/m^2$ ; $\rho = 13516.2 \quad kg.m^{-3}$ $\nu = 0.1147.10^{-6} m^2.s^{-1}$ ) The continuous line : Korsunsky model, The dots : Present model

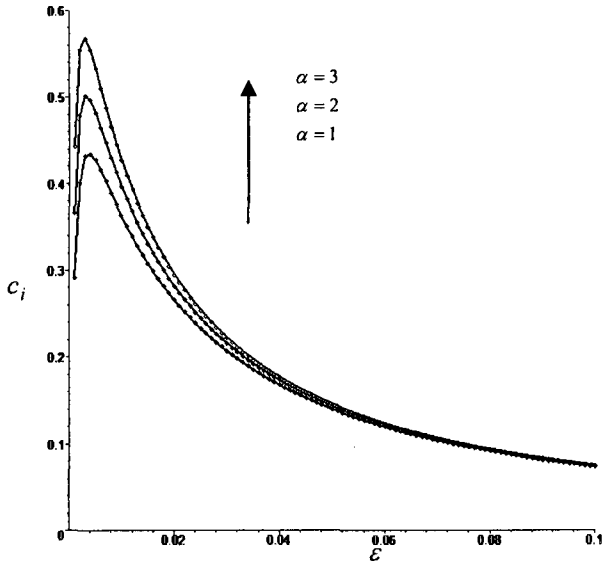


Figure 4-8 Effects of the electrical field directed towards the interior of the fluid on the grow rate of the instability for vertically falling liquid the magnetic field is normal to the flow $Ha = 0.5$ $\alpha = 1; \alpha = 2; \alpha = 3$ (For mercury at 20$^0$C: R=500, $\gamma = 0.472\ N/m^2$ ; $\rho = 13516.2\quad kg.m^{-3}$ $\nu = 0.1147.10^{-6} m^2.s^{-1}$ ) The continuous line : Korsunsky model, The dots : Present model

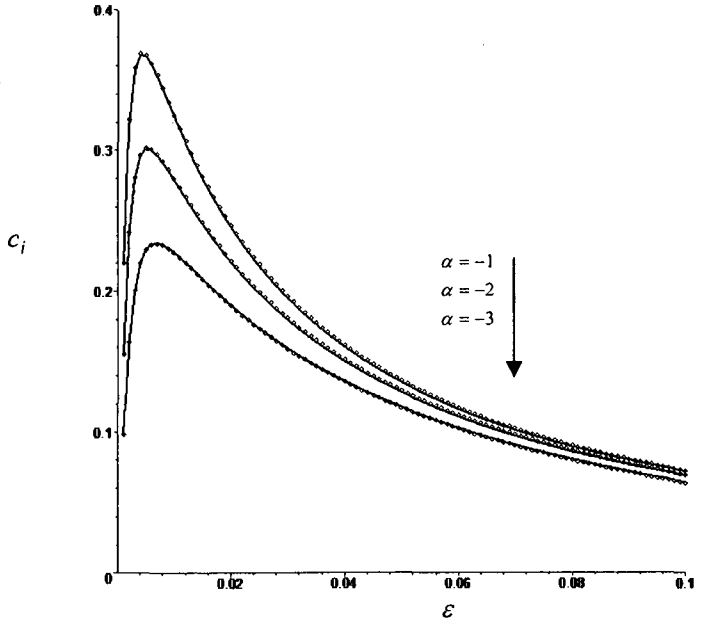


Figure 4-9 Effects of the electrical field directed towards the interior of the fluid on the growth rate of the instability for vertically falling liquid the magetic field id normal to the flow $Ha = 0.5$ $\alpha = -1; \alpha = -2; \alpha = -3$ (For mercury at 20$^0$C: R=500, $\gamma = 0.472\ N/m^2$ ; $\rho = 13516.2\quad kg.m^{-3}$ $\nu = 0.1147.10^{-6} m^2.s^{-1}$ ) The continuous line : Korsunsky model, The dots : Present model

In Figure 4-7, 4-8 and 4-9 we illustrate the effects of the electrical and magnetic fields on the growth rate of the waves at the free surface. Figure. 4-7 indicates that there is a substantial difference between the growth rates predicted by the two hydrodynamics models, equations (4-24-b, and 4-25-b). Indeed, the additional terms introduced in our model are almost all due to inertia, which tends to destabilize the flow. However, the application of the magnetic field reduces the growth rate of the perturbation and also restrains the effect of the additional inertia terms. This leads to the parity of the perturbation growth rate predicted by our model and that of Korsunsky's.

The Figure 4-8 and Figure 4-9 show the influence of the electrical field on the growth rate of the perturbation at the liquid metal free surface. The electrical field enhances the perturbation growth when it is directed toward the fluid interior, while reduces it when it is oriented toward the fluid exterior. For very high Reynolds numbers, similar qualitative effects are noticed; however, the wave-number corresponding to the maximum growth rate shifts to smaller numbers while the growth rate of higher waver-number perturbations become almost null.

# 4 Stability and bifurcation of the stationary solutions

Particular attention is devoted to the important case of stationary waves which are propagating with a constant phase velocity, $c$. For convenience we introduce the phase variable $\xi = \varepsilon^{-1}(x - ct)$ to change the stream-wise scale factor. Then, from equation (4-24), the local flow rate can be related to the film

height by: $Q = c(H-1)+1$. Substituting this into equation (4-25) gives a single evolution equation which governs the film depth evolution form:

$$D_3 H_{\xi\xi\xi} + D_2 H_{\xi\xi} + D_1 H_{\xi} + D_0 = 0 \tag{4-28}$$

This single equation can be written in the form of three order dynamic system as follow:

$$\frac{d\tilde{H}}{d\xi} = F(\tilde{H})$$
$$\tilde{H} = (H, H_{\xi}, H_{\xi\xi}) \tag{4-29}$$
$$F = (H_{\xi}, H_{\xi\xi}, \frac{-D_2 H_{\xi\xi} - D_1 H_{\xi} - D_0}{D_3})$$

To verify our calculation, we determine the coefficients of (4-28) when $H_a \to 0$ and $\alpha \to 0$. These coefficients corresponding to pure hydrodynamics are given as the following.

$$D_3 = (-\frac{11}{280}c^2H^2 + \frac{87}{280}c(c-1)H + W_e H - \frac{153}{280}(c-1)^2)$$
$$D_2 = (-\frac{1}{8}c(c-1) + \frac{54}{35H}(c-1)^2 - \frac{3}{20}c^2 H)H_{\xi} + \frac{1}{R}(-\frac{7}{4}c + \frac{27}{4H}(c-1))$$
$$D_1 = (-\frac{27}{35H^2}(c-1)^2 - \frac{1}{28}c^2)H_{\xi}{}^2 + \frac{9}{2RH^2}(1-c)H_{\xi} - \frac{1}{5}c^2$$
$$+\frac{6}{5H^2}(c-1)^2 - \frac{3\cot g\theta}{R}H$$
$$D_0 = \frac{3}{RH^2}(H-1)(H^2+H+1-c)$$

It is worth noting that magnetic and the electrical fields do not affect the form of the linear and nonlinear equations in comparison with those obtained in the pure hydrodynamics case. The some of the above coefficients are slightly different from those obtained by Lee and Mei in (1996).

$$u(x,t)=\left(-\frac{3}{2}\frac{Q(x,t)}{H(x,t)^3}+\frac{3}{4}\frac{\varepsilon^2\tau(x,t)}{H(x,t)}\right)z^2+\left(\frac{3Q(x,t)}{H(x,t)^2}-\frac{1}{2}\varepsilon^2\tau(x,t)\right)z$$

The differences come from the fact that the hydrodynamic velocity profile deduced from (4-19) satisfies the boundary condition (eq 2.17 in Korsunski (1999)) up to the second order with respect to the shallow parameter while the velocity profile used in Korsunski (1999) cancels the shear stress, so that the claimed second order accuracy in Lee and Mei in (1996) is not satisfied. Equation (4-28) expressed as a dynamic system has two fixed points, denoted by $H_1$ and $H_2$. The first is naturally the basic flow solution $H_1=1$ while the second one depends on the wave phase celerity, $Ha$ and $\alpha$. We found that as the intensity of the magnetic field increases the range of the celerity where the second stationary solutions exist becomes narrower while the application of an electrical field enlarges it.

The stability of the two stationary solutions, $H_1$ and $H_2$, is investigated through the eigenvalues of the Jacobian matrix $J$ of the dynamical system (4-29).

$$J = \begin{pmatrix} 0 & 1 & 0 \\ 0 & 0 & 1 \\ -\beta_3 & -\beta_2 & -\beta_1 \end{pmatrix}$$

The $\beta$ coefficients are functions of the hydrodynamic and electromagnetic parameters. There are two generic bifurcations, occurring when one real eigenvalue or two complex conjugate eigenvalues cross the imaginary axis. The first one corresponds to transcritical bifurcation and the second one is Hopf bifurcation. In the case of the transcritical bifurcation, the two fixed points can exchange their stability and be connected by heteroclinic orbits in the phase space. The Hopf bifurcation gives rise to periodic motion, which is characterized by a periodic trajectory limit cycle in the phase space.

### 4.2.1 Transcritical bifurcation

The effect of the electromagnetic parameters on the conditions of existence of heteroclinic orbits is considered next. Heteroclinic orbits exist if there are no singular film heights between the two fixed points ( singular heights are the solution of $D_3 = 0$ ). The results of the application of the magnetic field and the electrical field are show in comparison with the results of the purely hydrodynamic case see figure 4-10.

The regions where heteroclinic transitions exist are the regions indicated with a symbol "+". Figure 4-11 shows that the magnetic field shrinks the regions where heteroclinic orbits are possible. In other word the magnetic field

has a stabilizing effect. However, an increase in the intensity of the electrical field enlarges the concerned region, which means that the electrical field encourages the trancritical bifurcation, see figure 4-12. It is worth noting that the influence of the electrical field is less important than the magnetic field. The condition of the exchange of stability is checked. Indeed, below the critical wave (where $H_2 = H_1$) the fixed point $H_1$ is stable whereas $H_2$ is unstable and while above the critical celerity the stability properties are inverted.

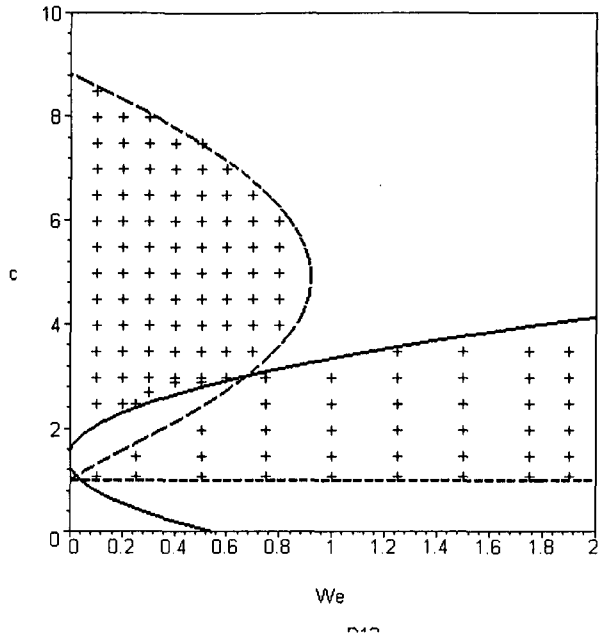


Figure 4-10 "+" deigns regions where heteroclinc orbits are possible for hydrodynamics case in this region one stationary solution is stable and the other is unstable

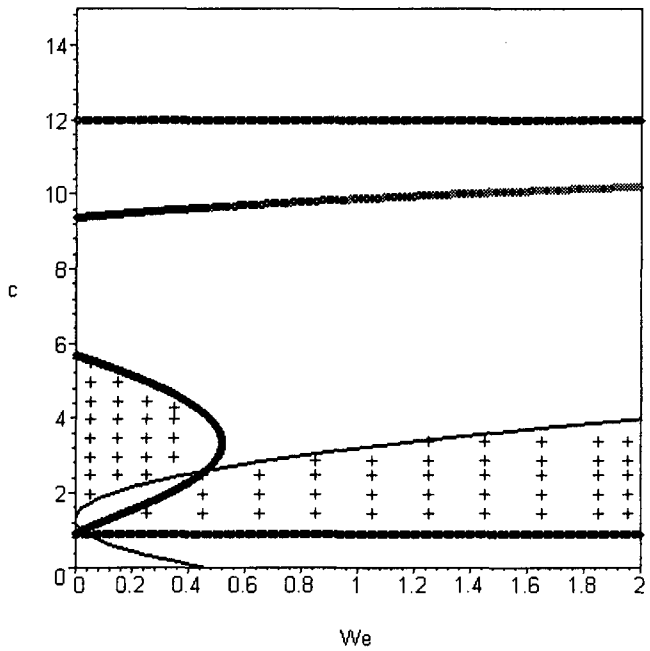


Figure 4-11 "+" deigns regions where heteroclinc orbits are possible for MHD case in this region one stationary solution is stable and the other is unstable
Ha=0.5, alpha=0, phi=Pi/2

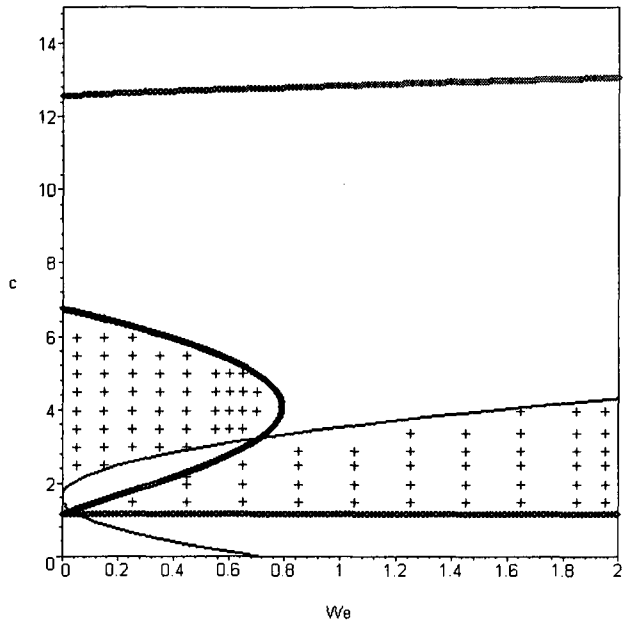


Figure 4-12 "+" deigns regions where heteroclinc orbits are possible for MHD case in this region one stationary solution is stable and the other is unstable Ha=0.5, alpha=3, phi=Pi/2

### 4.2.2 Hopf bifurcation

The Hopf bifurcation appears when the pair of purely imaginary eigenvalues of the Jacobian matrix crosses the imaginary axes. This condition corresponds to the following equations:

$$\beta_1.\beta_2 = D_1\beta_3 \tag{4-30}$$

$$\beta_1 > 0 \tag{4-31}$$

$$\beta_2 > 0 \tag{4-32}$$

We can verify that the inequality (4-31) is contained in (4-32). The curves $\beta_2 = 0$ circumscribe the region containing the curve of the Hopf

bifurcation threshold. The curves $\beta_2 = 0$ are shown for the two fixed points on figures (4-13, 4-14, and 4-15). Comparing once more the results with and without electromagnetic fields, we notice that the magnetic field reduces the region where the Hopf bifurcation is possible, while the electrical field extend this region.

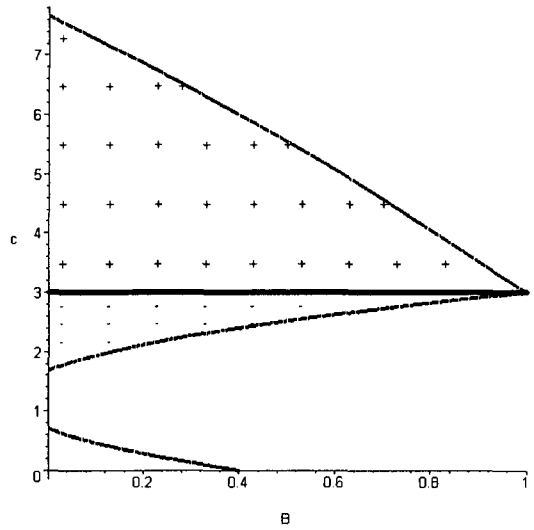


Figure 4-13 "+" deigns Regions where Hopf bifurcation is possible from $H_2$ "-" deigns Regions where Hopf bifurcation is possible from $H_1$, Hydrodynamic case

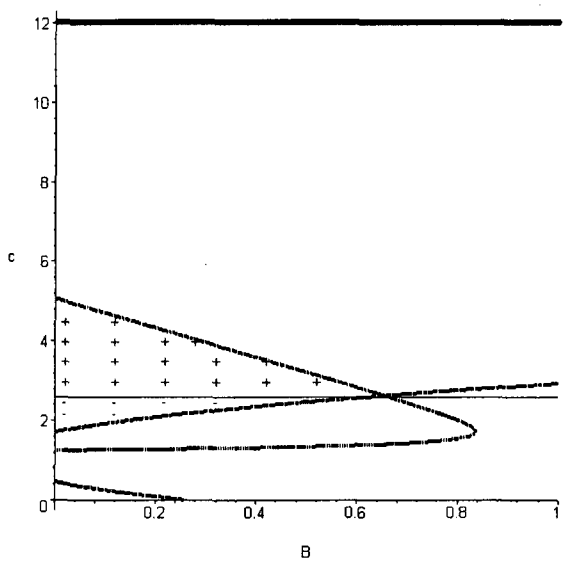


Figure 4-14 "+" deigns Regions where Hopf bifurcation is possible from $H_2$ "-" deigns Regions where Hopf bifurcation is possible from $H_1$
Magnetohydrodynamics case $Ha = 0.5 \quad \alpha = 0$

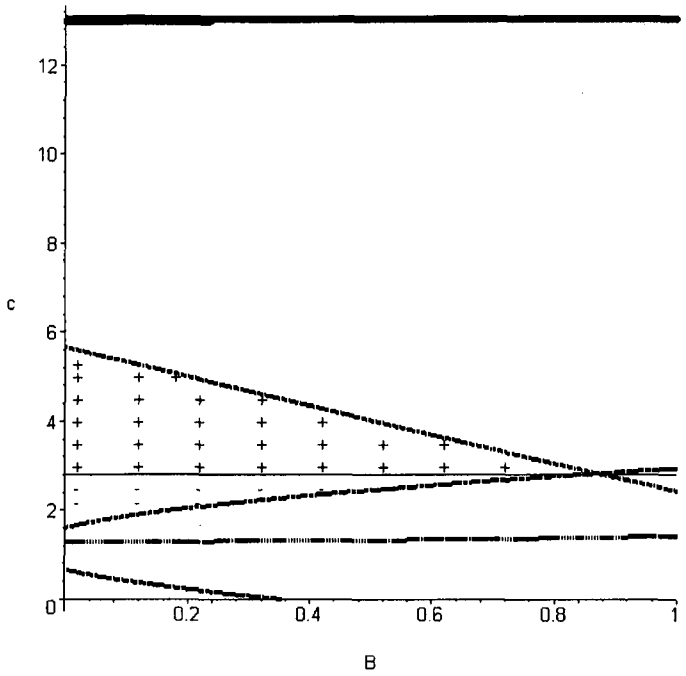


Figure 4-15 "+" deigns Regions where Hopf bifurcation is possible from $H_2$
"-" deigns Regions where Hopf bifurcation is possible from $H_1$
Magnetohydrodynamics case $Ha = 0.5 \quad \alpha = 1$

# 5. Conclusion

In this chapter we have incorporated a second order term with respect to the long wave parameter in the Korsunsky's model for high Reynolds numbers. We have shown that the Korsunsky model predicts a smaller stability region than the one predicted by our model. Moreover, it foresees larger effects of the electromagnetic field on the stability. We have shown that Korsunsky's model is similar to the Shkadov's model in the pure hydrodynamics case. Therefore, the Korsunsky's model suffers from similar drawbacks as Shkadov's, namely, they do not features Hopf bifurcation which leads to periodic waves at the free surface. The paper shows the control possibilities on liquid metal flow instabilities via a transverse electrical field. The electrical and magnetic fields together can control the free surface dynamics at the level where the heat transfer is maximum and the liquid layer is kept at a safe protecting thickness. Furthermore, the effect of the electromagnetic fields on the Hopf and transcritical bifurcations is depicted.

# Chapter 5: Introduction

## 1 Historical background

One hundred and fifty years ago, Helmholtz (1858) published his celebrated vorticity theorems. This seminal work inspired several prominent scientists of the Victorian era to consider eddies as paradigms in explaining the atomic structure of matter. The leading archetype involved ensembles of ring vortices grown within the illusive frictionless fluid aether. In 1878, Mayer performed an experiment with the aim of showing how atoms might be organized inside molecules. He placed a number of equally magnetized needles on floating corks in water, with their north poles pointing away from the free surface. Holding a strong magnet with its south pole above the water interface, he noticed that two magnetized needles ordered themselves opposite to each other forming a dumbbell-like configuration (analogous to the atomic orbital of the p-type). More than two needles organized themselves on the vertices of regular polygons; see figure 5-1.

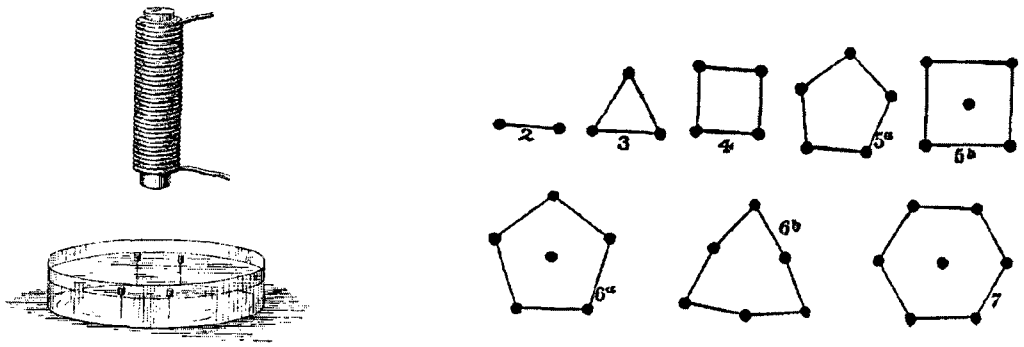


Figure 5-1: The experiment of Mayer (1878), (the picture is from J.J. Thomson (1907))

Kelvin (1867) having previously mentioned that "Helmholtz's vortex rings are the only true atoms", considered Mayer's outcome to be in accordance with the vortex atom theory. The era that began with Kelvin's (1867) "vortex atoms" and ended with Sommerfeld's (1919) "Atombau" marks the first out of four periods in the quest for building a vortex atomic theory of matter. Einstein's (1905) work on special relativity rendered the aether obsolete, which led to the desertion of the idea. The ensued impetus on the subject matter however, contributed significantly towards the growth of hydrodynamics, and perhaps led J. J. Thomson (1897) to the discovery of the electron. Detailed historical accounts can be found in the fine contributions of Aref (1983) and Aref et al. (1992).

## 2. Polygonal patterns in several fields

In addition to Alfred Mayer's (1878) magnetic needles experiments, where patterns higher than pentagon (N=5) turned out to be unstable. There are other experiments where polygonal patterns were observed. For instance, Gregory et al. (1955) revealed the presence of disturbance vortices (N = 6) around the main vortex obtained with a rotating disk tests in air as working fluid. Yarmchuk et al. (1979) observed regular vortex patterns in rotating liquid helium. Although the stability of the regular polygonal patterns was not investigated, the authors showed photographs with several N-gon vortex patterns, see figure 5-2.

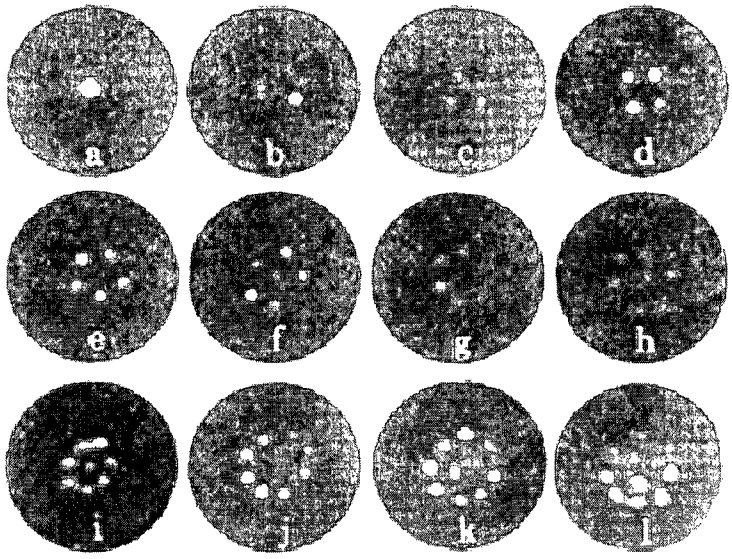


Figure 5-2 : System of point vortices in liquid helium(Yarmchuk et al.(1979)).

It has been known for over forty years that in theory the two-dimensional (2-D) drift-Poisson equations describing a magnetized electron column are analogous to those of an Eulerian flow. The last implies that plasma diocotron waves must be equivalent to liquid free surface ripples first analyzed by Kelvin (1880). This idea remained in hibernation until the 1990s where Driscoll and Fine (1990) attempted to demonstrate the equivalency of the two phenomena through experiments in electron plasmas using a Malmberg-Penning Trap. Afterwards, several papers were reported on the similarity, providing also the conditions under which the analogy is realizable; see for example Peurrung et al. (1992), Peurrung and Fajans (1992-1993). Fine et al. (1995), reported first stable 2-D plasma vortex patterns.

Dissipation in this type of high vacuum experimental configuration is relatively small thus approaching adequately the inviscid flow assumption. Their stability characteristics were thoroughly investigated, in an improved apparatus, by Durking and Fajans (2000). In fact the last investigators exploiting the analogy between the 2-D drift-Poisson equations of strongly magnetized plasmas and those of inviscid flow, confirm indirectly Havelock's (1931) main stability characteristics, see figures 5-3 and 5-4.

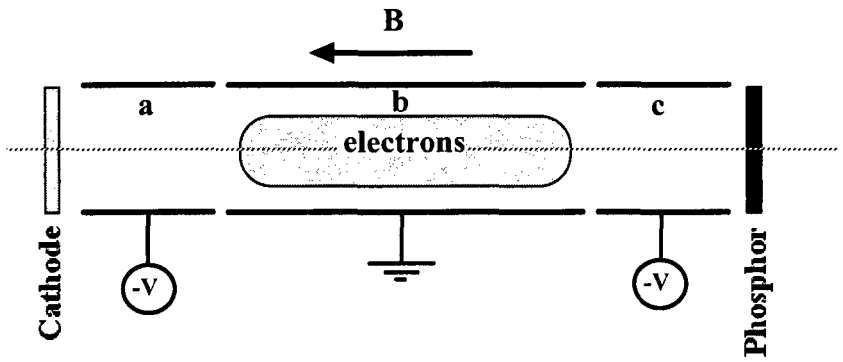


Figure 5-3: Schematic of the Malmberg-Penning trap (D. Durkin and J. Fajans (2000))

Polygonal patterns are also observed routinely in nature. Near the polar region, the Earth's surface is like a rotating disk while the atmosphere above has an "interface". Vettin (1857) employed a rotating dish within a container filled with water, having a centrally located cylindrical cup filled with ice to simulate the Earth's polar circulation. His sketches show clearly the expected polygonal structures. The equilibria are also evident in Mason's (1971) polar circulation graphs. Furthermore O'Caroll and Gutro (2002) from the Goddard Space Center presented two pictures of Antarctic Polar weather patterns, which resemble closely the mixed 2 and 3, and 4 and 5 states.

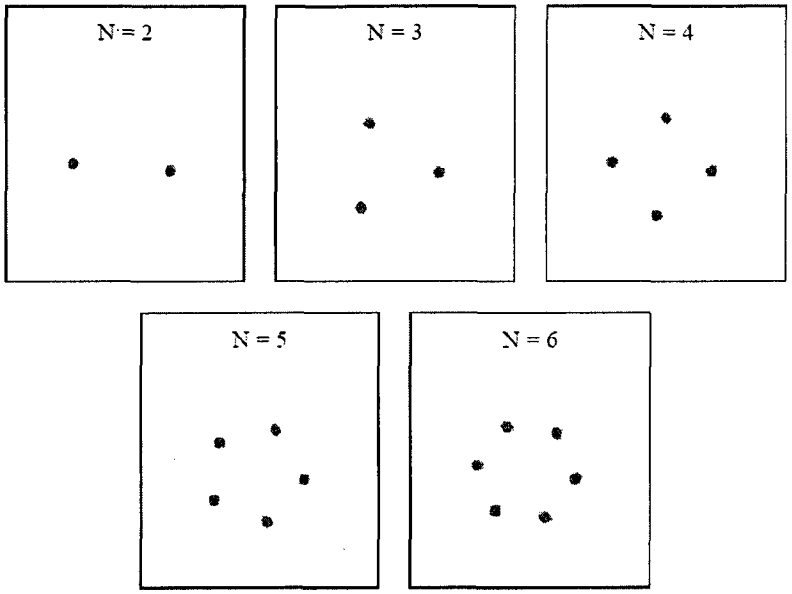


Figure 5-4: The stable electron columns observed in the Malmberg-Penning Trap for $N < 7$states ( Fig. 4.2, Durkin, D.R. 1998).

Due to the similarity between the laboratory and polar vortices, Williams et. al. (2003) was able to shed light to several fundamental phenomena associate with polar circulation by examining it in a scaled down experimental prototype. Using a rotating platform he included the Coriolis force which did not substantially alter the qualitative fundamental nature of the evolved vortex polygons. Modes of N = 2, 3, and mixed states 4 and 5 were clearly evident in his experiments, while his theoretical developments yielded patterns up to N = 5. Upon completion of his investigations he remarked that at first a teacup seems hardly the place to perform groundbreaking experiments, however Williams (2004) concluded that: "It turns out that there is a very intimate connection between the fluid dynamics

of a freshly stirred cup of tea, and those of an atmosphere on a rotating planet".

Saturn's polar images from Voyager spacecraft show a hexagonal cloud feature, Godfrey (1988). Rational explanations vis-à-vis its cause included magnetic interactions similar to the aurora borealis and fluid instability, Allison et al. (1990), see figures 5-5. The recent Cassini's infrared spectrometric data revealed that the pattern propagates deep into the planet's atmosphere (about 75 kilometers) thus making the latter a more reasonable explanation. The convective rolls in the radial-zenith plane that produce the longitudinal bands (rings) and are clearly visible in images of this and other planets are due to instability (spherical counterpart of Taylor-Göertler's vortices), Sawatzki-Zierep (1970), figures 5-6.

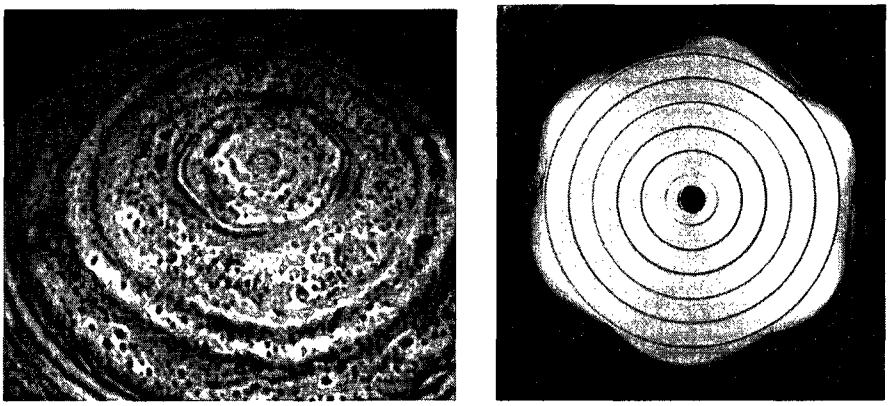

Figure 5-5: Left: Saturn's Hexagon [Image credit: NASA/JPL/Space Science Institute/University of Arizona]. See also Godfrey, A. D. 1988. Hexagonal feature around Saturn's north pole. *Icarus* , **76**(2), 335-356.
Right:typical hexagonal pattern from our experiments [Vatistas G H *et al* 2008 *Phys. Rev. Lett.* **100**(17) 174503].

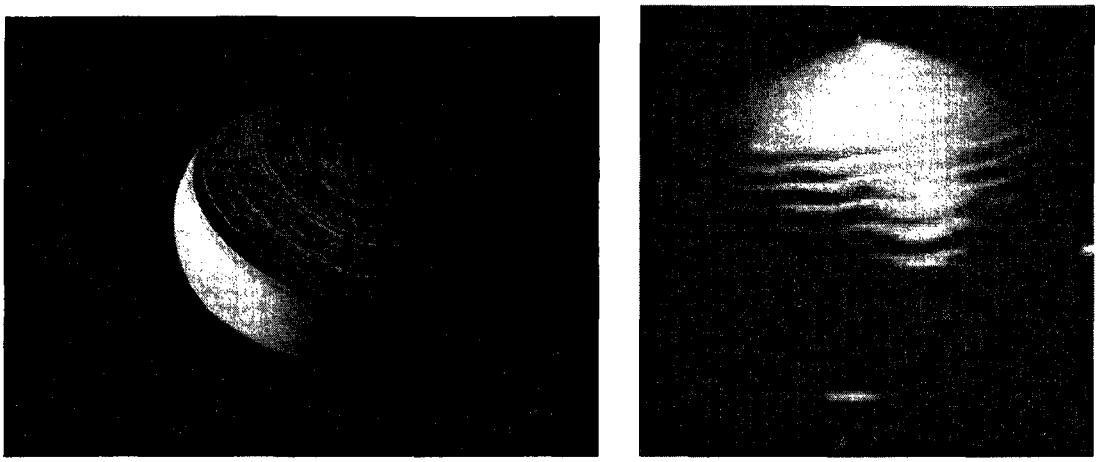

Figure 5-6: **Left:** Saturn's rings [Image credit: NASA/JPL/Space Science Institute/University of Arizona]. **Right:** image of the Sawatzki-Zierep (1970) laboratory experiments [1970. Acta Mech. **9**, 13-35].

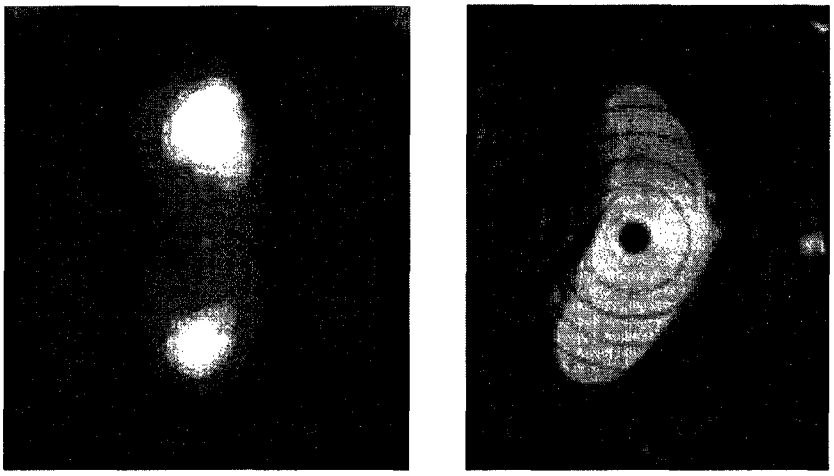

VENUS

Figure 5-7 Left: double vortex storm in Venus' North Pole cloud layer [Taylor, F. W. 2006. Venus before Venus Express. Planetary and Space Science, 54(13-14), 1249-1262]. Right: our mixed polygonal shape (unpublished).

Near the Pole, Kelvin's patterns could modulate the bands thus producing the intriguing hexagonal ribbon, Polvani & Dritschel (1993). The strong vortex in Saturn's South Pole (Sánchez-Lavega et al. (2006)), and the double vortex storm ($N$ = 2) in Venus' South Pole Suomi & Limaye (1978) and Taylor (2006),( figure 5-7) could also be of the same nature. It is interesting to note that the atmospheres of all the mentioned planets consist predominately from low viscosity gasses (Saturn 96.0% $H_2$, Venus 96.5% $CO_2$, and Earth 78.08% $N_2$).

Due to the established propensity of vortices to spawn satellite vortices these types of whirls should also be present in other high Rossby number atmospheric eddies such as hurricanes and tornadoes. Indeed these intense vortices are known to possess features such as waves, multiple vortices, and spiral bands that occur inside the core, Davies-Jones (1986) and Bluestein & Pazmany (2002). In fact these characteristics may even intensify the destructive power of these violent swirls, Maxworthy (1972). The work of Lewis & Hawkins (1982) has also revealed polygonal formations in the eye wall of hurricanes. Satellite images, given in their figures 5-8 (a) and (b) providing a top view of Hurricanes "Betsy" and "Anita", unveil hexagonal ($N$ = 6), and rectangular ($N$ = 4), core structures respectively.

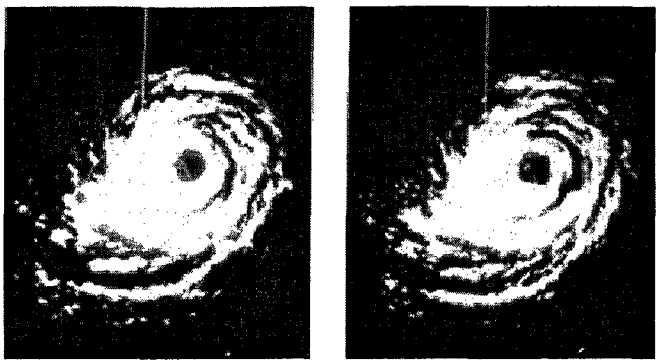

(a) (b)

Figure 5-8: Polygonal patterns in the eye wall of hurricanes from Lewis and Hawkins (1982)

Polygonal patterns are also observed in optics; when beams of light with curled wave fronts focus strongly on rings, they form toroidal optical traps called optical vortices. Periodically modulating an optical vortex's phase could generate regular N-polygonal pattern geometries (Curtis and Grier (2003a and 2003b)); see Figure. 5-9.

Many astrophysical problems have been viewed in the past as paradigms of fluid motion, see for example Fridman et al. (1985) and Lin & Roberts (1981). But, how could insignificant (in the grand scheme of things) laboratory experiments like the present (Vatistas (1990a)) reveal important characteristics of a grand celestial design? According to Fridman et al. (1985) the evolution of instabilities in the gaseous galactic disk, resulting in the formation of spiral density waves is essentially controlled by hydrodynamics.

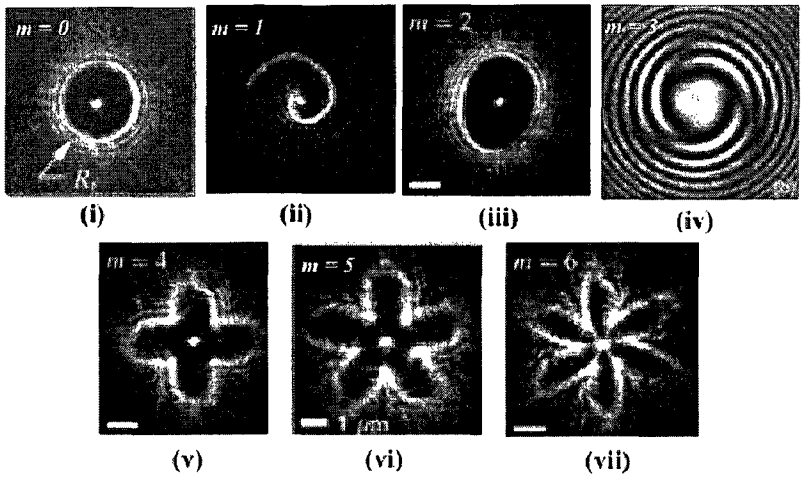


Figure 5-9: Polygonal pattern's in optical vortices. (i), Curtis, J. E. and Grier, D. G. Structure of Optical Vortices. Phys. Rev. Lett, 90(13), 133901, 4 April (2003), (ii) Alonzo, C. A., Rodrigo, P. J. and Glüsckstad, J., Optics Express 13(5) 1749 (March 7, 2005) (iii), (v)-(vii), Curtis, J. E. and Grier, D. G. Modulated optical vortices. Optics Letters 28, 872-874 (2003), (iv) Soskin, M. S., Gorshkov, N. and Vasnetsov, M. V. Topological charge and angular momentum of light beams carrying optical vortices. Phys. Rev. A 56(5), 4064 - 4075 (1997).

Therefore, by analogy the hydraulic simulations can indeed uncover some of the most essential characteristics of the grand design. The shallow water hydraulics and two-dimensional compressible gas flows are similar, Landau & Lifshitz (1987). Surprisingly, some of the dominant qualities of the phenomena may yet be common even if the similitude between the two is not (in the formal sense) complete. Exploiting the last well-known analogy, Fridman et al. (1985) used a stationary dish with a rotating ring/conical cup-like device to study the role of centrifugal instability in the development of the spiral structure of spiral galaxies. In 1993 Lauer et al. (1993) reported that Andromeda galaxy (M31) possesses a double nucleus. Lauer and colleagues attributed the reason of the manifestation a cataclysmic collision of two venerable galaxies. Based on our experience with the hydraulic

analogue, vortex instability may also be a reasonable alternative cause for this effect. Elmegreen et al. (1991) reported three-arm spirals of 18 galaxies where they show clearly the NGC 598 galaxy to have a three-arm spiral; the inner core with three dark spots (nuclei) arranged on the tips of an equilateral triangle, see figure 5-10.

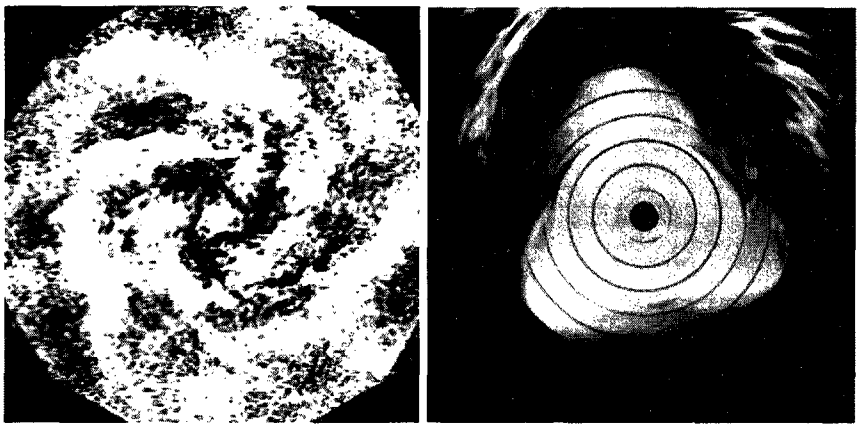

(a) (b)

Figure 5-10: (a) NGC 598 Galaxy image [Elmegreen *et al* 1992]. (b) expérimental image [Vatistas G H *et al* 2008 *Phys. Rev. Lett.* 100(17) 174503].

## 3. Analogies and Pattern's stability

Employed judiciously, classical analogy is a powerful method of scientific inquiry that has been used in many physical areas. Although often the topology for the similarity may not be strictly complete, some of the most rudimentary commonalities between two similar systems are indeed preserved. The latter enables us to predict the fundamental behaviour of a

phenomenon by studying its duality, encourages cross-fertilization between specializations, or even to go beyond the bounds of normal experience. Furthermore, because the length and time scales between the two phenomena may be different, a simile can be used as a means to magnify or shrink the problem, and accelerate or retard the dynamics of an event. The theoretical developments vis-à-vis the stability of point vortices arranged in a ring has its foundation in the similarity among point vortices and the gravitating N-body problem, whereby the vortex strength is replaced by the mass. Helmholz (1858) examined the planar motion of two point vortices. Kirchhoff (1877) provided the equations for the N-vortex case in Hamiltonian form. Gröbli (1877), Kelvin (1878), and Poincare (1893) considered the case of three vortices. In 1883 J.J. Thomson (1883) dealt with the situation of three, four, five, six, and seven vortices. He forecasted instability to occur for seven vortices. Havelock (1931) generalized the approach to the N-vortex problem, showing that with no boundary, the case of seven vortices was neutrally stable. The presence of confining outer or inner boundaries could destabilize the flow, while a sufficiently strong central vortex could stabilize the ring. Dhanak (1992) proved theoretically that vortex systems with small but finite cores possess the same stability characteristics with the N = 7 being unstable to only one normal mode of disturbance. Dritschel (1985) had concluded earlier that the N = 7 was unstable to two displacement type of modes. All the linear analytical approaches of the past were partial and thus dubious for the case of seven point vortices. Recently, based on the nonlinear Kirchhoff equation, Kurakin & Yudovich (2002) confirmed that the $N \leq 6$ and

$N \geq 8$ states are stable, and unstable, respectively. Furthermore, they also proved the seven-vortex array to be, in theory, stable.

The stability of the N-gon patterns were investigated by Fine et al.(1995), and Durkin and Fajans (2002) in the framework of electron columns confined in a Malmberg–Penning trap using static, magnetic and electric fields to confine electrons. They found that the life time of N-gons with $N \leq 6$ is around one thousand times higher than the time of bulk rotation. It become three hundred for N=7 and becomes almost equal when $N \geq 8$.

## 4. The fundamental nature of the phenomenon

The previously mentioned mathematical vortex models and experiments are idealizations of the present experiments when the liquid height is low. Nevertheless, there are countless examples in physics and technology where utopian approaches yield important deductions. All of the previously mentioned theories declared which vortex configurations were stable. None of them elaborated on the conditions of how the pattern transforms from a specific equilibrium to the next. The past experimental studies of Vatistas (1990a), Vatistas et al. (1992-1994) and (2001) conducted in a cylindrical tank have shown irrefutably that, under prevailing conditions, the free surface of a liquid vortex fosters Kelvin's (1880) standing waves. The rotary motion imparted to water by the disk, see figure. 5-11(a), generates a centrifugal force field that pushes the liquid towards the wall of the container. The receding liquid exposes part of the surface of the disk to air, whereby, the line of intersection between the surfaces of the solid disk,

liquid, and air outlines the core shape. In order to make the patterns visible, the liquid was colored with a blue water-soluble dye. Under shallow water conditions and for very low rotational disk speeds it is expected that the liquid (water) vortex core remains circular (N = 0). Increasing its rotation, the vortex flow will transfer into another state characterized by a precession of the circular core (N = 1). A further increase of disk speed ($w_d$) yielded a cores with elliptical (N=2, dumbbell-like configuration), triangular (N = 3), square (N = 4), pentagonal (N=5), and hexagonal (N=6) cross-sections. However, no heptagonal shape was able to form. Since the interval of endurance of the stationary states decreases with N, if N =7 exists in theory it must be critically stable.

The stability of the pattern N=7 is a special case and was the subject of several numerical and experimental studies. For instance, the numerical studies of Ganesh & Lee (2002) on strongly ionized plasmas arrived at the conclusion that since the turn over time is approximately 180 rotations, N = 7 is unstable. On the contrary, Durking & Fajans (2000) point out that the N = 7 equilibrium is marginally stable (with no boundary), having a lifetime equal to 300 rotations. The previous authors are basing their conclusion on rather debatable grounds; that this time is sufficient for point vortex dynamics to evolve. Like in the previous theoretical studies, the experimental designation, whether the N = 7 is stable or not, still remains open. Nevertheless, as the disk speed increases well beyond N = 6 a continuous amplification of dynamic noise eventually wipes out the sharp spectral peaks.

For higher liquid elevations, in addition to the previously described azimuth waves, the flow also develops axial waves that propagate up the free surface.

The equilibrium polygons were found to be exceptionally stable. When disturbed by a momentarily applied external disturbance to the flow, the patterns remerged after a short period of time in their original form. Both quasi-static and sudden increase to the final disk speed produced the same equilibrium pattern. The latter indicated that the phenomenon is not particularly sensitive to initial conditions. Between neighboring states, mixed-mode time dependent equilibria were found to exist. For example between the N = 3 and N = 4 band the core consists of both waves. Because the two have different phase speeds the core appears to be non-stationary. A careful study has shown that a very small degree of hysterisis does exist, Vatistas et a. (2001). The interval of endurance for both the equilibria and their transition increases with the wave number N, see Figures 5-12.

In previous experiments, visual inspection using a dye revealed that the patterns were present even if the core was flooded. Recent higher fidelity images shown in Figures 5-13 confirm the old observation. Near the core, a "circular" dry spot exists. However the region where the apexes of the polygon are located is flooded with water. The light coloring at the polygon tips indicates a free surface depression. The latter is due to the local centrifugal force generated by the satellite vortices orbiting the central vortex. In their experiments with ethylene glycol, Jansson et al. (2006) clearly described the presence of "... spiraling vortices on top of the polygon structure".

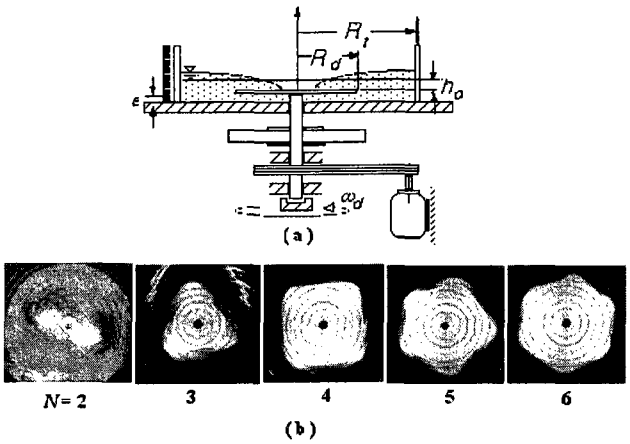


Figure 5-11. (a) Schematic of the experimental apparatus. The present experiments were conducted using tap water in a 284 mm diameter stationary cylindrical container with a 252 mm diameter circular disk spinning near the bottom. A variable-speed electrical motor drives the disk. The initial water level was measured using a ruler attached to the side of the tank. Three different initial liquid heights: 20, 25 and 30 mm were used in the present experiments. (b) Typical equilibria of $N$ = 2, 3, 4, 5, and 6. [Vatistas G H *et al* 2008 *Phys. Rev. Lett.* **100**(17) 174503].

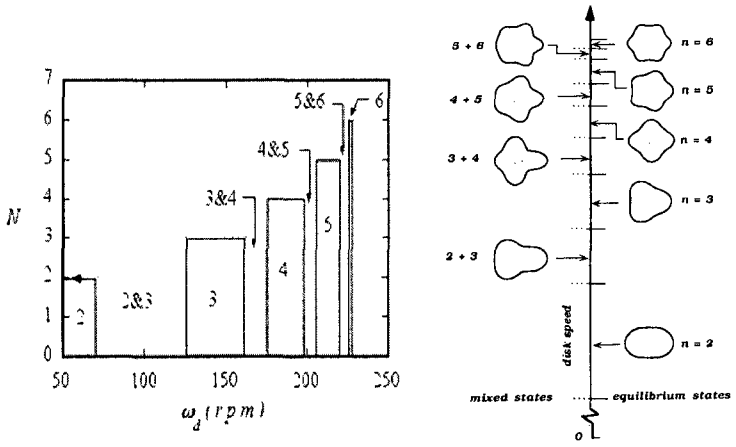


Figure 5-12. a) A typical equilibrium and mixed mode gaps spectrum for ho = 25 mm. The bandwidth of both the equilibrium and mixed modes become narrower with the wave number $N$. [Vatistas G H *et al* 2008 *Phys. Rev. Lett.* 100(17) 174503].
b) Polygonal structure spectra for water. The various shapes shown were obtained by either a pure or superimposed harmonic wave equations.

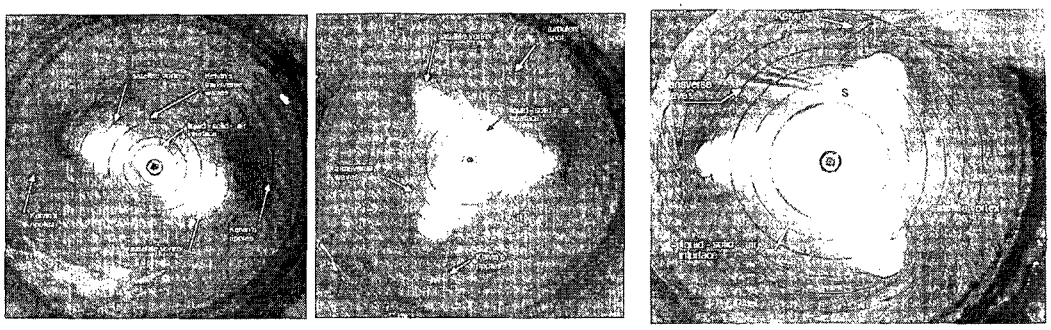

a b c

Figure 5-13 The centrifugal force imparted to the fluid by the disk compels the liquid outwards. The retreating liquid exposes the structure of the core. Every vortex with an interface develops a free-surface depression near the axis of rotation. In the corners of the polygonal core shapes satellite vortices exist. Each satellite vortex possesses a dimple. The last is very evident in (a) and (b) where the faded color polygon tips indicating a free surface depression due to the satellite vortex. Since the parent vortex is stronger, the central portion is dry. When the rotation intensifies both parent and satellite vortices become stronger. The receding water develops lobes in the place where the secondary vortices existed, and thus forms the propeller-like dry pattern shown in (c). A turbulent patch similar to Emmons in boundary layers appears in (b).

The numerical simulations and experiments of Miraghaie et al. (2003) for N = 3, in shallow depth, show indisputably the presence of three vortices located at the apexes of the regular triangle. When the rotation intensifies both parent and satellite vortices become stronger. Furthermore, the theoretical developments of Ganesh & Lee (2002), in ionized plasmas, show the tips of the polygons to be occupied by vortices/holes (holes are areas on no vorticity). The receding water develops lobes in the place where the secondary vortices existed, and thus forms the dry polygonal central pattern shown in Figure 5-14 (b). Due to the added radial thrust, a free surface upwelling near the cylindrical wall, where these vortices are positioned, is noticeable. Hence, these vortex core pattern formations can be viewed as a result of stationary waves of wave number N traveling around an otherwise

circular path, Kelvin (1880), or as an integral number N of satellite vortices, gyrating in unison about the parent vortex, J. J. Thomson (1883). In other words, it displays a vortex-wave duality. Burbea and Landau (1982) refer to the former undulations as Kelvin waves. In plasma, the patterns can be regarded as columns of charges (Durking & Fajans (2000)), or diocotron waves, Mitchell & Driscoll (1994).

The phenomenology of vortices developed in higher viscosity liquids such as Shell oil 10W is considerably richer than that of water, where a vortex core with more than N = 6 could be formed, Figure 5-14. Although these bear many similarities to water, their evolution however, exhibits a radically different behaviour. In the case of water, the equilibria emerge in succession, one after the other, by increasing the disk rotation and are nearly the same during ascending and descending sequences. In the case of oil, the order of flow patterns during the spin-up and spin-down sequences are completely different, see for example Figure 5-15.

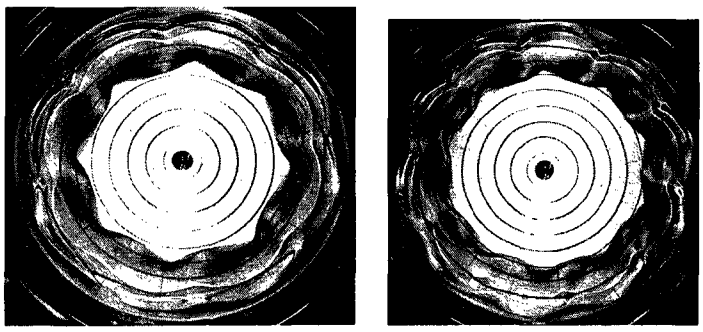

$N = 8$ $N = 10$

Figure 5-14: Typical octagonal and decagonal vortex cores using oil [Reference Vatistas et al (1994) Experiments in fluids].

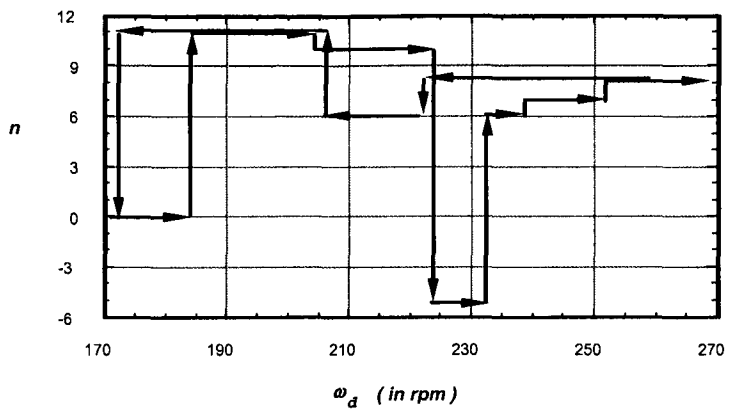


Figure 5-15: Spectra of oil core shapes during quasi-static ascending and descending sequences. [Reference Vatistas et al (1994) Experiments in fluids].

There are no fixed rotational speeds at which transformation from one wave pattern into another takes place. Given the initial liquid level, the shape of the final pattern depended on the time history of the spin up or spin-down process. There were times where, although we started the disk rotation for the same amount of oil from rest, different equilibria emerged!

# 5.Outline

Although whirls as paradigms in explaining the atomic make-up of matter was eventually abandoned, it nevertheless contributed significantly to the growth of hydrodynamics and led J.J. Thomson (1897) to the discovery of electrons. The theoretical developments vis-à-vis the stability of point vortices arranged in a ring become real for theories of vortices in helium and electron columns in plasma physics. The similarity between the polygonal patterns studied in the present experiment and those observed in several field of physics and in nature, render the present study of capital importance.

Furthermore, the outcomes are not restricted to fluid mechanics, but go beyond. Recently, the present experiments were used to corroborate the core analytical deductions of J.J. Thomson's, in relation to the stability of a ring of N-vortices. This is developed in chapter 2, of this part, of the present thesis.

All previously mentioned theoretical and experimental works dealt with the stability of the polygonal configurations. However none of them elaborated on the conditions in which the equlibria endure, or how different stationary configurations evolve from one equilibrium (mode) to the next. In Vatistas et al.(2008), we observed that the transition from one equilibrium mode to the next occurs through mixed modes and that the bandwidth of the transition interval shrinks with the increase in mode number. However, no systematic investigation has been conducted. Hence, the underlying physical mechanism(s) that leads to the transition from one stable state to the other is unknown. To the best of authors' knowledge, this is the first investigation of the transition mechanism from one mode to the next. The knowledge of the transition mechanism through sequential equilibrium states is vital for the overall understanding of the vortex ring dynamics. In addition, due to the wide range of applications of this phenomenon, it is expected that the present results will have significant implications in fluid dynamics, superfluidity and plasma physics. The transition mechanism is tackled in chapter three. Conclusions and perspectives of the present study are depicted in chapter four.

# Chapter 6: Confirmation of Kelvin's equilibria

## 1. Introduction

### 1.1 Outline

Several swirling flows in nature and technology are modeled as two-dimensional incompressible and inviscid. Although a satisfactory theory on the vortex formation is missing, vortices are present and they influence the flow dynamics where they appear. In most studies dealing with vortex flow dynamics, strong vortices are inserted in a low diffuse vorticity background. When these strong vortices are enough close to each other, they merge, and when they are too far apart to merge, they settle in equilibrium patterns termed "vortex crystals", see Aref (1983).

Some swirling flows encountered in nature and technology are reproduced, at smaller scales in laboratories, using vertical stationary or rotating cylinders driven by the rotation of one or both endwalls. When the water height is low and the swirl is imparted to the fluid is high, the vortex-core becomes hollow and undergoes several instabilities that manifest as spectacular polygonal shapes. This phenomenon was reported for the first time by Vatistas (1990). He observed the phenomena on the vortex-core of a hollow vortex generated with a rotating disc near the bottom of a cylindrical container. The observations of Vatistas (1990), and his conjecture on the

existence of satellite vortices at the apex of the polygonal shape, was recently confirmed, see figure 6-1 (Jansson et al (2006)).

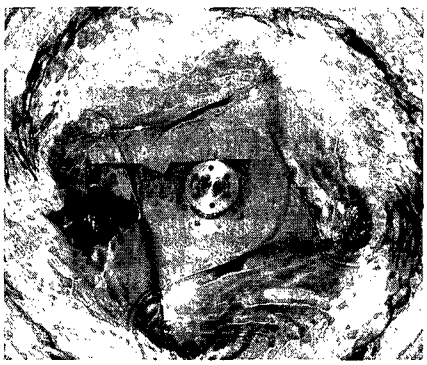

Figure 6-1 Satellite vortices at the apexes (image from Jansson et al (2006)).

Similar vortex pattern or vortex equilibrium was observed in swirling liquid helium and electrons columns in plasma physics. However, the vortex equilibrium observed in the present experiments offer more possibilities to gain insights into vortex equilibrium states. Indeed, the present experiment is accessible, offers more control possibilities, and the sequences occur in relatively long time intervals in comparison with the time duration of the experiments realized in plasma columns. The relatively long time duration of the phenomenon allows the utilization of flow visualization as a technique for an in depth investigation of the stationary states and pattern dynamics during transitions between two subsequent equilibria.

In this chapter the experiment conducted by Vatistas (1990) on the symmetry breaking of the hollow-core vortex patterns is revisited using an

image-processing technique. As shown below, this experimental method allows more possibilities in conducting more detailed investigations on this interesting phenomena. Novel results were found. First, it was discovered that in shallow water conditions the patterns rotate at constant frequency, which is one-third the frequency of the rotating disc. Although a frequency locking is suspected by Vatistas (1990) and Jansson et al (2006), it is the first time that the frequency locking is confirmed and quantified. Second, it was revealed that the apexes of the polygonal shapes hosting the satellite vortices are equally distributed on a circular ring, for which the radius is half the radius of the circular cylindrical walls that confine the swirling flow. This result confirms for the first time the analytical finding of Havelock (1931) on the stability condition of a system of point vortices. Third, the flow dynamics around the apexes (wave peaks) and the sides (wave troughs) of the polygonal shapes were investigated for the first time. An intriguing, robust, flow dynamic pattern lock-in, having a frequency of about one-third the frequency of the rotating disk, was observed. This particular property, at the apexes, gives rise to the query whether the route towards turbulence in shallow water swirling flows unfolds through a period tripling cascade.

## 1.2 Survey on Swirling Flows

Swirling flows are subject to several instabilities which they manifest in several forms such as traveling waves on the vortex core, secondary vortices around the main vortex, and vortex breakdown. These types of instability are of primary importance in geophysics flows. Indeed, at the scale of the oceans

and atmospheres these waves are known to play a major factor in controlling weather systems, Schar & Davies (1990). Such instabilities in the rotation of Earth's outer core are suspected to be responsible of the Earth's magnetic field Hollerbach (1996). The swirling flow instabilities manage the transfer of energy and mass from one scale to another and from one location to another. For instance, polar vortex instability leads to the enhancement of mixing within the vortex core, which has been found to be crucial to the weakening of the ozone layer, (M. McIntyre (1989). In engineering, the instability of the swirling jet exhausted from aircraft turbine engine leads to vortex breakdown, thus enhancing the transfer of pollutants to the atmosphere. Furthermore, deformations of the vortex-core produce unwanted vibrations and noise in the intakes of liquid pumps and draft tubes in water turbines; see, Escudier (1987) and Enauss (1987).

Similar experimental configurations to the present (stationary cylinder with a rotating bottom), have been used to shed light into vortex instabilities and vortex breakdown. Swirling flow generated in closed or open, stationary, cylindrical container by rotating one or both of its endwalls, offer more possibilities for the control of the swirl and external turbulence around the vortex-core than the ones offered by a vortex tube; see Keller and Escudier (1980). Several experimental and numerical studies were also conducted in closed containers where one endwall is rotating. These studies show that the aspect ratio (ratio of the height of the working fluid to the radii of the container) and the Reynolds number are the fundamental parameters that

control the vortex instability and breakdown, see Vogel (1968) and Escudier (1984), Daube and Sorensen (1989). Similar studies were also performed in open cylindrical containers. Spohn and his collaborators (1993) showed that a free surface has a determining effect on the conditions and on the form of the vortex breakdown. Recently, the problem of swirling flow induced in a stationary cylinder by rotating the bottom endwall was studied from the angle of symmetry breaking. Hirsa et al (2002) reported that when the ratio of the water height to the radius of the cylinder is equal to 2, and the geometrical imperfections of the experimental setup are reduced to their minimal, the symmetry breaking turns into an azimuthal rotating wave with a wave number equal to four. However, when the ratio of the water height to the radius of the cylinder is equal to 0.25, Miraghaie et. al (2003) showed that the symmetry breaking of the swirling flow with a free surface turns into an azimuthal rotating wave with a wave number of three. They found that the rotating speed of these waves is 0.62 times the rotating speed of the bottom endwall of the cylinder.

In the above-mentioned two experiments, swirl imparted to the fluid is so small that the free surface is considered flat, and accordingly the vortex core is flooded. However, when the swirl becomes stronger the pressure drops in the central core thus forming a hollow vortex. The hollow core, which is circular in the beginning, supports the subsequent polygonal shapes until hexagonal is reached at high swirl. The ability to see the polygonal

shapes allows the use of visualization and images processing techniques in order to identify their dynamic behavior.

The instability of the hollow-core vortex manifests as a symmetry breaking of the cylindrical core into helical traveling waves when the vortex core is long. These helical waves were investigated theoretically for the first time by Kelvin (1880) and they are well known as Kelvin modes. In shallow water conditions and when the vortex-core in flooded the swirling flow instabilities manifest as azimuthal rotating waves. Lopez et al (2004) investigated numerically and experimentally in a stationary open cylinder driven by the constant rotation of the bottom. The waves were found to be the result of the instability of the interface between the inner body-rotation and the shear layer swirling flow. It was shown that when high swirl is imparted to the fluid, the circular shear layer tends to roll up and the vorticity further concentrates more and more in the rolled-up region until it ends up in concentrated vortices having forms of stable dipoles, tripoles, quadripoles and more, see Poncet and Chauve (2007).

# 2. Experimental setup and measurement technique

## 2. 1 Experimental setup

The present experiments were conducted in a cylindrical Plexiglas container. The internal diameter of the cylinder is 284 mm and its height is 500 mm. The cylinder is attached to a steel table through flanges. A 252, 270 and 282 mm diameter circular disk is placed 20 mm above the bottom of the

cylinder. The disk is connected through a vertical shaft to an electric motor (see figure 6-2). A flywheel is connected to the vertical shaft in order to increase the constancy of the disk rotation. The disk rotated in the counterclockwise direction, and an electronic controller regulates its speed. Water was used as the working fluid. The experiments were conducted at four different water heights which were 20, 25, and 30 mm of water above the rotating disk. For each water depth, the disk speed varied from 1.9 to 4.28 Hz.

The rotation of the circular disc at the bottom of the tank introduces angular momentum into the liquid. The synergetic action of centrifugal and gravitational forces together with buoyancy cause the free surface to acquire the shape of an inverted "bell". For high disk speed values the hollow bell-like central portion of the vortex touches the surface of the disk forming a dry spot. The line intersection between the liquid and the surface of the disk, outlines the core shape. By increasing the disk speed different polygonal imprints begin to appear.

A CCD camera (JAI CV-M2) with the resolution of 1600 × 1200 pixels was placed above the cylinder to image the hollow-core vortex formed on the disk. The camera was connected to a PC equipped with a digital frame grabber (DVR express) that acquire 8-bit images at a rate of 30 frames per second. To avoid a blurring effect, the shutter speed of the camera was set to 1/500 sec. At each water height and each disk speed, 5000 images were acquired. A circular neon lamp surrounding the cylindrical tank was is used to

ensure uniform lighting. In order to increase the visibility of the patterns, water soluble blue dye was mixed into the water prior to the experiments.

### 2.2 Measurement technique

A typical image obtained during the experiments is shown in figure 6-3(a). Due to the dark color of water, the interface between the liquid and disk, i.e., the edges of the patterns, are clearly visible. An image processing algorithm has been developed in order to accurately detect the edges of the patterns. This algorithm has been implemented in a code within the Matlab environment. The algorithm allows the automatic processing of the image sequences acquired by the CCD camera for each case. The details of the algorithm are described below.

The first step is the image segmentation, that is, the conversion of the original 8-bit gray-scale image into a binary image, using a suitable threshold to extract the polygonal contours. The setting of a proper threshold is very crucial for the image segmentation. If the fluid in the vicinity of the pattern's contour has uniform or narrow banded gray-scale values, the selection of the proper threshold is straightforward. However, in the present experiments, due to difference in the frequency of neon light and the camera frame rate, the overall gray-scale values varied from image to image within a given run. Therefore, before selecting the proper threshold, the image intensities were equalized in each experimental run. For this purpose, the brightest image of a given test was selected and the gray-scale histograms of all other images were matched with gray-scale histogram of the selected image (Gonzales and Wood 2004).

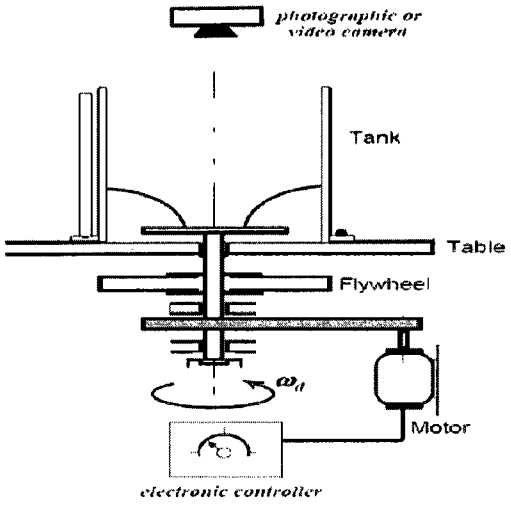


Figure 6-2 : Schematic of the experimental apparatus

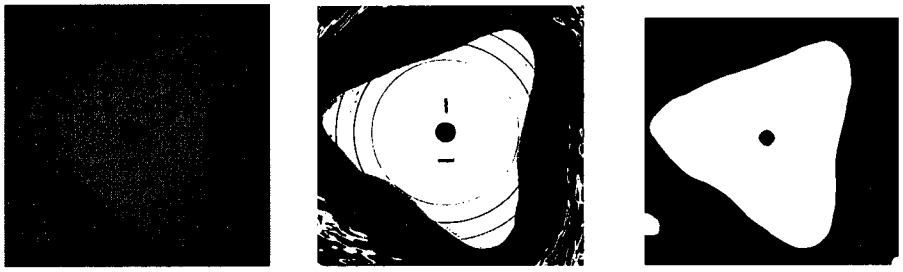

(a) Original image (b) Binary image (c) Filtered binary image

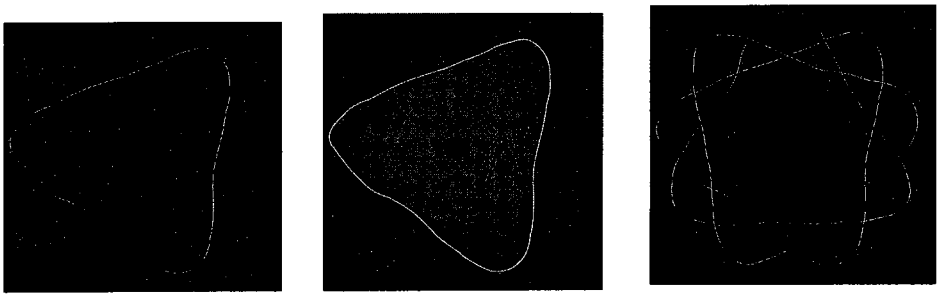

(d) Pattern boundaries (e) verification (f) Pattern superposition

Figure 6-3: Summary of the image processing technique

The quantity of the threshold for image segmentation was selected based on the gray-scale value associated with the peak in the histogram of the selected image and it was applied to all subsequent images in a given run. In the image segmentation process, all the pixels with gray-scale values higher than or equal to the threshold were assigned 1's (i.e. bright portions) and the pixels with gray-scale values lower than the threshold (i.e. dark portions) were assigned 0's. The binary image obtained after applying the threshold to image in figure 6-3(a) is shown in figure 6-3(b). To filter the noise from the images, a low-pass Gaussian filter was applied next. The binary image (figure 6-3(b)) after noise filtering is shown in figure 6-3(c). In the next step, the boundaries of the pattern were extracted using the standard edge detection procedure. The pattern contours obtained from the edge recognition procedure were then filtered using a zero-phase filter to ensure that the contours had no phase distortion. The pattern contour that corresponds to the binary image in figure 6-3(c) is shown in figure 6-3(d). In order to demonstrate the accuracy of the developed algorithm, the detected pattern contour superimposed into the original image is shown in figure 6-3(d). The figure shows that the present scheme correctly detects the boundaries of the pattern. The accuracy of the given algorithm was estimated by randomly selecting 30 images from each experimental set. In each image, the difference between the actual edge and that detected by the algorithm was recorded. The results show that the difference between the actual and detected boundaries is within 2 pixels, in almost 90% of the pattern contours. In the remaining 10% of the regions, the difference between the

actual and detected boundaries is on average 6 %, with the maximum difference of 8 %. A sample of detected patterns for different cases is shown in figure 6-3(f). The rotating speed of the disc was also measured using the image processing technique. Prior to the experiments, two small black strips were marked on the rotating discs, which are clearly visible in each image (see figure 6-3a). These strips were used to measure the disk speed through image analysis. For this purpose, another algorithm was developed. A region of interest comprised of the middle portion of the disk such that the marks remain within the region of interest throughout the disk rotation in the entire dataset was selected. The images were segmented using the same threshold as described earlier. All segmented images show a black portion at the center of the disk and two black strips. A reference image was then chosen and the subsequent images were individually superimposed into the reference image, until the black strips of the subsequent image coincides with the black strips of the reference image. The frame number of this subsequent image, in reference to the original, was recorded. Knowing the number of rotations and time difference between each image (i.e. 1/30 sec), the speed of the disk was determined for each case.

## 3. Results and discussion

The frequency spectra of the patterns for different cases were computed from the sequence of the detected patterns. Three consecutively sensed patterns are shown in figure 6-3(f) as a sample. To compute the frequency spectra, the time series of the radial distance of the pattern edge

from the disk center was extracted at each value of $\theta$ (i.e. $\theta$ = $0^0$ to 360°). The spectrum was computed for each time series and then averaged. The spectra of the patterns for different initial water heights ( $h_0$ ) are given in figure 6-4 (a-c). The plots show that for a given mode, the most energetic peak ( $f_m$ ) is related to the frequency of the pattern ( $f_p$ ) by $f_p = \frac{f_m}{N}$ where, $N$ is the number of apexes of the given polygon. As expected, $f_p$ increases with the disk frequency ( $f_d$ ). The spectra, in figure 6-4, normalized by the disk speed ( $f_d$ ) shows that the spectral peaks for all curves occur at the same normalized frequency of 1/3. That is, the frequency of the pattern is equal to 1/3 of the disk frequency, irrespective of the mode or water height. Marques et al. (2003) numerically investigated the flow in a rotating cylinder with the counter-rotating top lid under shallow water conditions. Their results show four and five wave number rotating wave with a frequency equal to 1/3 of the cylinder's speed. Despite the differences in the induction mechanism, the result remains the same. This indicates that the 1/3 locking of the rotating pattern/mode could be a general inherent feature of shallow, swirling water flows.

Further investigations with different flow generation methods will be required in order to confirm the validity of this general conclusion. The influence of the initial water height on the frequency of the pattern is investigated in figure 6-5. The plot shows that the height influences the frequency of the pattern. It has been observed that for a given mode, speed

increases with the water height. However, the increased rate in $f_p$ decreases with an increase in $h_0$. The results show that changing the given mode $h_0$ also influences the pattern evolution. When the water layer is shallow, lower modes do not occur. Whereas, when the water layer is relatively thick, the higher modes do not materialize. For example, at $h_0$ = 20 mm, the mode N= 2 does not occur. At $h_0$ = 25 mm, mode N= 6 does not occur. But, at $h_0$ = 30 mm, modes N= 5 and 6 do not occur.

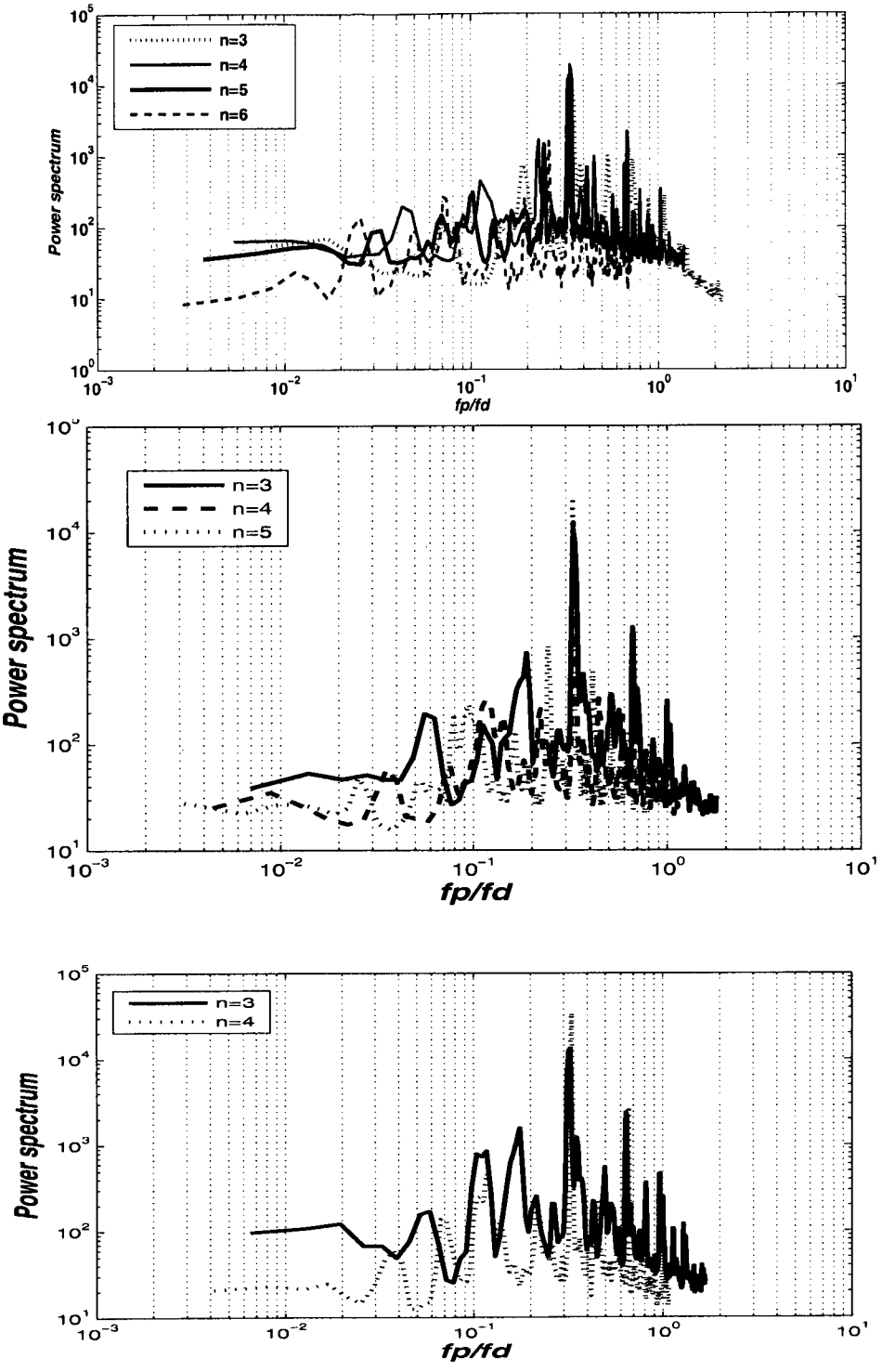


Figure 6-4: Power spectrums for $h_0$=20, 25 and 30 mm respectively

The results in figure 6-5 point out that after a certain water height, the frequency of the pattern remains unchanged by increasing the water height. However, with an increase in water height, the occurrence of the modes decreases and it is expected that after a certain threshold height, no modes will occur. Similarly, if the water layer is too shallow, no modes will occur. This means that a given pattern exist only for a certain range of water heights. Hence, the disk speed and the initial height of water determines the existence of a given pattern, the combined effect of these two parameters can be lumped into one dimensionless number, i.e. the Froude number, defined as $Fr = R_d f_d / 2\pi\sqrt{gh_0}$, where, $f_d$, $R_d$ and $g$ are the disk frequency, disk radius, and gravity, respectively.

From the sequences of the pattern contours for all modes, the radius of the pattern apexes and the base are recorded and then averaged. Here the base is defined as the valley between the two apexes. The values of the apex radius ($R_{\max}$) and base radius ($R_{\min}$) for all cases are shown in Table 6-1. The results show that except for the N = 2 (elliptical pattern), the apex radius is almost the same for all other modes (N = 3 to 6). However, the base radius changed with N. Maximum value occurs for N = 6 decreasing monotonically to a minimum value for N = 2. The apex and base radii normalized by the tank radius ($R_t$) are also presented in Table 6-1.

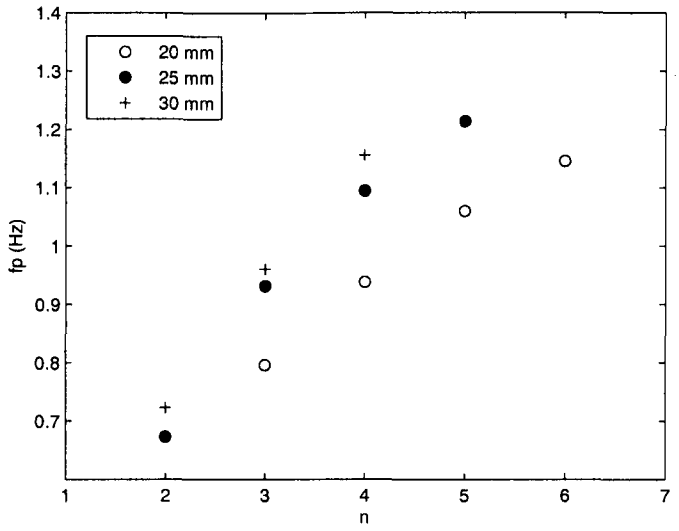


Figure 6-5: Influence of water height on the frequency of the pattern

| H=20 | $R_{max}$ | $\frac{R_{max}}{R_t}$ | $R_{min}$ | $\frac{R_{min}}{R_t}$ |
|---|---|---|---|---|
| 6 | 71.6 | 0.50 | 54.6 | 0.38 |
| 5 | 73.3 | 0.51 | 45.9 | 0.32 |
| 4 | 71.9 | 0.51 | 37.1 | 0.26 |
| 3 | 70.3 | 0.49 | 34.3 | 0.24 |
| H=25 | | | | |
| 5 | 70.3 | 0.5 | 46.8 | 0.33 |
| 4 | 70.5 | 0.5 | 42.2 | 0.3 |
| 3 | 71.8 | 0.5 | 33.1 | 0.23 |
| 2 | 53.1 | 0.37 | 27.3 | 0.19 |
| H=30 | | | | |
| 4 | 71. | 0.5 | 41.56 | 0.3 |
| 3 | 71.3 | 0.5 | 26.8 | 0.2 |
| 2 | 59.3 | 0.42 | 23.25 | 0.16 |

Table 6-1: Maximum , minimum and ration of these two values to the tank radius

The results reveal an interesting feature. The apex radii from mode 3 through mode 6 are almost equal to half of the tank radius. For a given mode, the apexes are equidistantly located. Thus, the angle between the apexes decreased from 120° for mode three to 60° for mode six. The present results show that irrespective of the number of apexes and their corresponding angular difference, all the apexes are locked on the same circumference whose radius is about half that of the tank. This indicates that whenever a mode is established, the apex location remains constant but the base location changes to satisfy the equilibrium condition. Havelock (1931) theoretically derived the stability conditions for the system of point vortices equally distributed on a circumference. He found that a system with more than six point vortices is unstable. He also concluded that in the presence of external boundaries and a central vortex, for the system of point vortices to be stable, the point vortices must be located on a circumference with the radius equal to about half the radius of the boundary. In the flow configuration for the present study, a satellite vortex is located at each apex. Although the present images do not explicitly show the presence of the satellite vortices, inspection during the experimental trials confirmed their presence. The images in Jansson et al. (2006) also show the presence of satellite vortices at the apexes of the polygonal patterns. Thus, the present results, for the first time, confirm Havelock's (1931) stability conditions. By analyzing the images of Jansson et al. (2006), who used different tank and disk sizes, one finds the apex radius to indeed be about half of the tank radius, which further confirms the present findings.

Vatistas et al (1994) derived the dispersion relation for the swirling potential flow in a confined geometry. Their expression for the theoretical radius of the unperturbed core is the root of the following equation,

$$\left(\frac{a}{R_t}\right)^2 \cdot \left( \frac{2.R_t^2.g.h_0}{\frac{\omega^2}{a^4}} + 1 - 2.\ln\left(\frac{a}{R_t}\right) \right) - 1 = 0$$

Where, $\omega$ is the angular velocity of the unperturbed core and $a$ is the unperturbed core radius. For the present case, $\omega$ is equivalent to the disk speed, and $a$ is equivalent to the mean radius of the pattern, ($a = \frac{R_{\max} + R_{\min}}{2}$). The values of $a$, estimated from the present experimental conditions, are also given in Table 6-2 and are found to be in good agreement with the mean radius of the patterns, given in Vatistas et al (1994). This conformity is not surprising since in the present experiments, water was used as the working fluid and the flow under given conditions can be considered weak viscous flow. In our calculations, we assumed $\omega$ to be equal to the angular speed of the disc. This is a fairly good approximation, since the ratio between the fluid velocity to rotating speed of the disc, measured with a L.D.A technique, approaches 1(one) in a similar experiment, see Poncet and chauve (2007). The dispersion equation given above is solved numerically and the values for the radius of the unperturbed core $a$ are calculated and given in the table 6-2.

| H=20 | Mean Radius a | R=a/rt | |
|---|---|---|---|
| | | theory | Experimental |
| N=3 | 50.73 | 0.34 | 0.35 |
| N=4 | 52.74 | 0.4 | 0.371 |
| N=5 | 57.84 | 0.49 | 0.41 |
| N=6 | 62.69 | 0.55 | 0.44 |
| H=25 | | | |
| N=2 | 38.85 | 0.20 | 0.27 |
| N=3 | 50.34 | 0.38 | 0.35 |
| N=4 | 55.12 | 0.47 | 0.39 |
| N=5 | 58.53 | 0.53 | 0.41 |
| | | | |
| H=30 | | | |
| N=2 | 39.47 | 0.21 | 0.27 |
| N=3 | 45.28 | 0.36 | 0.32 |
| N=4 | 54.59 | 0.48 | 0.38 |

Table 6-2: Comparison between the experimental and the theoretical results.

The observation described above confirms that the calculations conducted by Vatistas et. al (1994), based on the potential vortex, are in accordance with our observations. It is worth noticing that the stream lines induced by potential vortices equally distributed on a circle form similar polygonal shapes observed in these experiments. The geometric analysis of the fully established patterns, along with an examination of the spatial power spectrum of the polygonal patterns, follows. The patterns in binary images, their unwinding contours, and the associated power spectrum are shown in figure 6-6. The power spectrum indicates that when the patterns are stable and well established there are no other modes than the fundamental with its harmonic amplitude modulating the basic wave. As it will be argued below, the polygonal character of the vortex core is due to the presence of satellite vortices on a circular ring which rotates at constant frequency but lower than

the frequency of the disc. The presence of these satellite vortices at the apexes is clearly shown in figure 6-1, taken from (Jansson et al (2006)). Their equidistance on a constant radius explains the regular polygonal formations. Indeed, the vortices around the apexes create a depression at their center, which repels the free surface and gives to the core a polygonal shape. Therefore, the polygonal shapes of the vortex core can be seen as a system of rotating arrays of vortices equally distributed on a circle with a radius of about half the radius of the tank.

In what follows, for patterns ranging from triangular to hexagonal, attention is focused on the flow dynamics around the apexes and troughs using power spectrum analysis. To facilitate the analysis, this phenomenon is investigated in a relative frame of reference rotating with the pattern. In order to achieve this, we bring back each contour with its respective rotation angle and superpose it on the initial pattern, as illustrated in figure 6-7. The power spectrums at the apexes and the troughs are, respectively, similar; therefore the analysis is performed on the average of the power spectra over the apexes and troughs. We start the analysis by inspection of the power spectrum where the frequency normalized with the pattern frequency of the triangular pattern shown in figure 6-8.

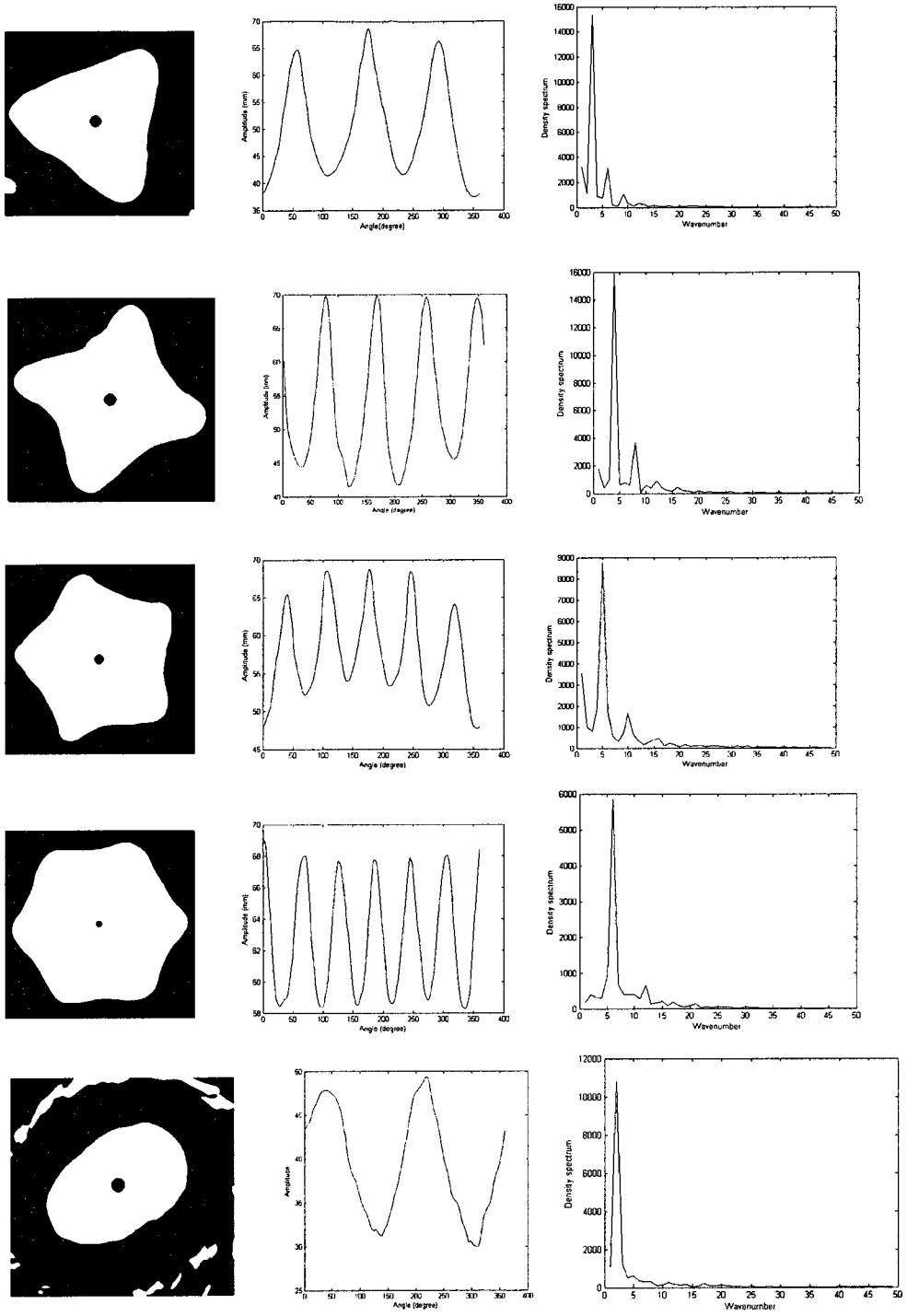


(a) (b) (c)

Figure 6-6: a) binary image of the rotating wave b) Winded up contour of the patterns c) Density spectrum giving a wave number

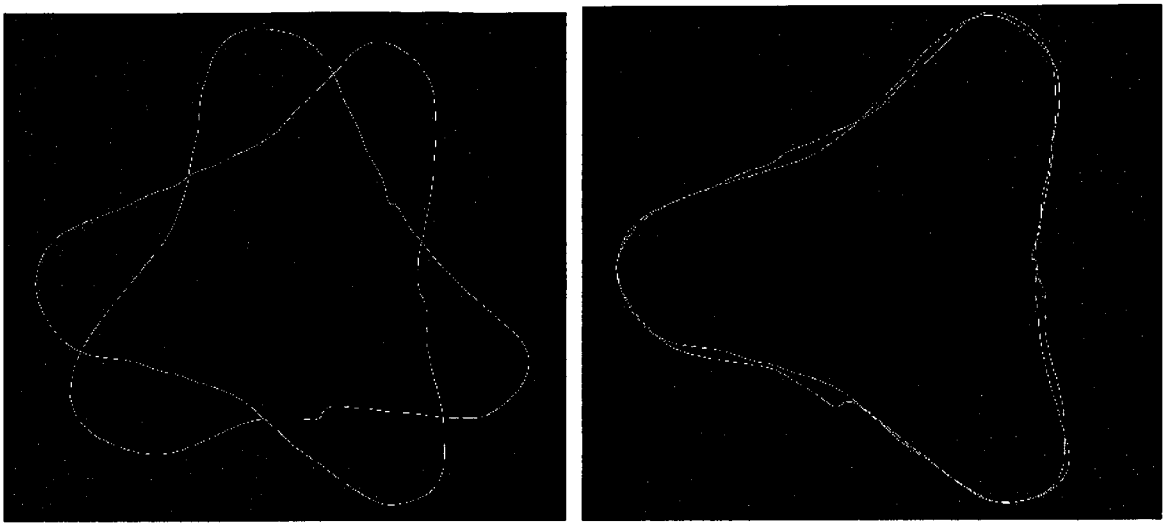

Figure 6-7 pattern superpositions

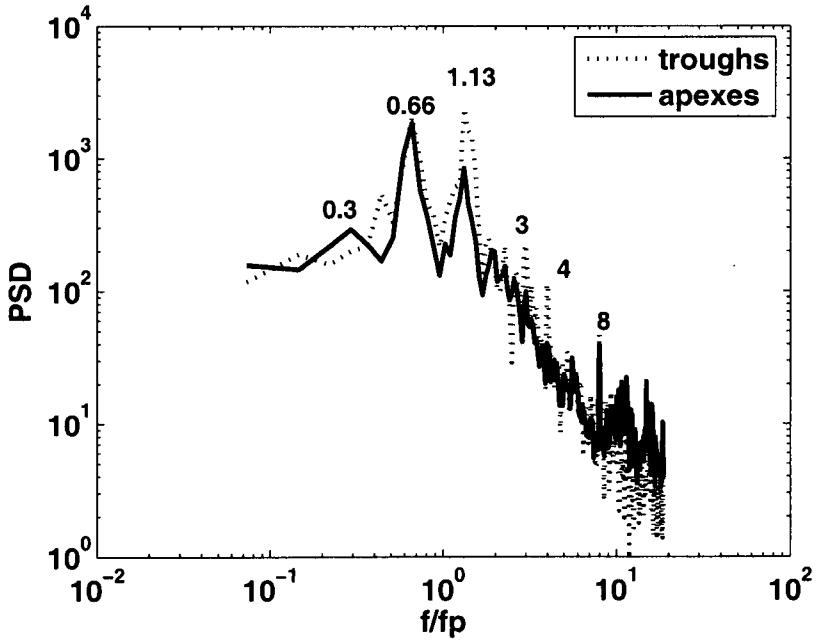


Figure 6-8: Flow dynamics around the apexes and the trough of the triangular pattern

Figure 6-8 shows that both troughs and apexes are under almost similar dynamic qualities. A close analysis, however, reveals that there are two types of processes involved. The first occurs at low frequencies within the interval 0.07 to 0.4, while the second happens between 0.4 and 18. The power spectra at the apexes and troughs ranging from 0.07 to 0.4 were found to be slightly deferent. Although the wave amplitude is relatively small, figure 6-8 discloses that at a frequency of $0.3f_p$ (which is sufficiently close to one third the rotational speed of the pattern). The apexes are under the influence of a different dynamic condition than that occurring at the troughs. This particular frequency differentiates the dynamic manifestations that take place on the apexes and the troughs, while the other parts of the power spectrums are similar. The power spectrum also shows the prevalence towards a frequency close to two thirds ($\frac{2}{3}f_p$), and its harmonics followed by continuous decrease in power. This decrease is similar to that observed in *Kolmogorov's spectrum for turbulent flows*. Some peaks are more evident at the troughs; having the values 3, 4, and 8 Hz respectively. The relative high magnitude of power at frequency ($\frac{2}{3}f_p$) and its harmonics should correspond to the small amplitude traveling around the pattern, while the power cascade with the distinct peaks should be associated with the complex flow dynamics surrounding the triangular pattern. The relevant peaks at the trough might explain the sporadic bursting observed during the tests.

The distinct dynamic behavior at the apexes with a frequency of about 0,3 times the frequency of the pattern should be related to presence of

satellite vortices on the apexes. Therefore, the dynamics associated with this secondary instability is ultimately characterized by a frequency which is close to one third the frequency of the pattern. This is an interesting feature which deserves to be reported because it looks like a cascade of period tripling. Indeed, the frequency of the pattern (primary instability) induced by the rotating disk is approximately one third of the disk (the pattern period is three times the period of the disk). Subsequently the secondary instability (satellite vortex) around the apex has a period around three times the period of the pattern. As it will be confirmed below this tripling cascade seems to be robust and exists for all the observed patterns.

Increasing the speed of the disk, the triangular pattern undergoes a bifurcation into a square polygonal pattern. Similarly to the triangular pattern, the power spectra, figure 6-9, suggests that there is a wave which moves around the apexes of the square polygonal pattern with a frequency of one third the frequency of the pattern. Since this frequency does not appear in the power spectrum of the troughs it must be a localized phenomenon affecting only the apexes. This observation fortifies our conjecture that a frequency which is around one third the frequency of the pattern characterizes a distinct flow dynamic event at the apexes.

The power spectrum of the N = 4 pattern is distinguished by fundamental frequencies of $0.318 f_p$ and $0.5 f_p$ at the apexes. The power spectrum also shows the attendance of the main frequency $f = f_p$ and its harmonics at the troughs. Increasing further the speed of the disk, the

square polygonal pattern undergoes a bifurcation and becomes a pentagon. Similar to the triangular and the square polygonal patterns, the power spectrums of the pentagonal pattern, in figure 6-10, also show wave activity at about one third the frequency of the pattern.

The power spectrum at the apexes resembles the one of quasi periodic regime, whereas the flow dynamics at the trough looks like the one of turbulent flow. Further increasing the speed of the disk causes the pentagonal pattern to bifurcate into a hexagonal pattern, which is the last observed pattern before the hollow core becomes circular and its diameter enlarges with the disk speed, while the flow around it becomes chaotic. Here the closeness of the troughs and the apexes make the dynamics at the two particular points of the hexagonal pattern alike. Again the flow at both the apexes and at the troughs is characterized by the frequency which is one third the frequency of the pattern.

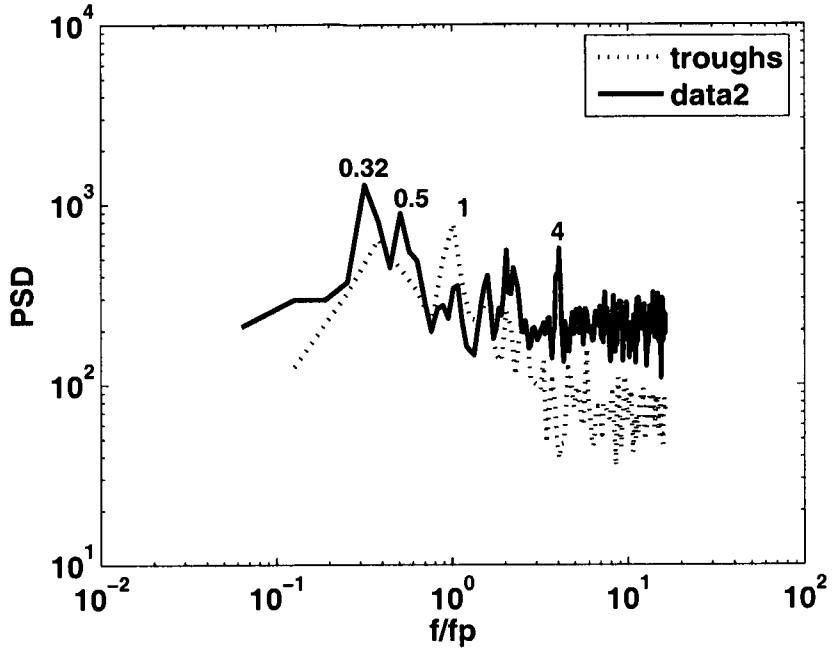


Figure 6-9: Flow dynamics around the apexes and the trough of the square pattern

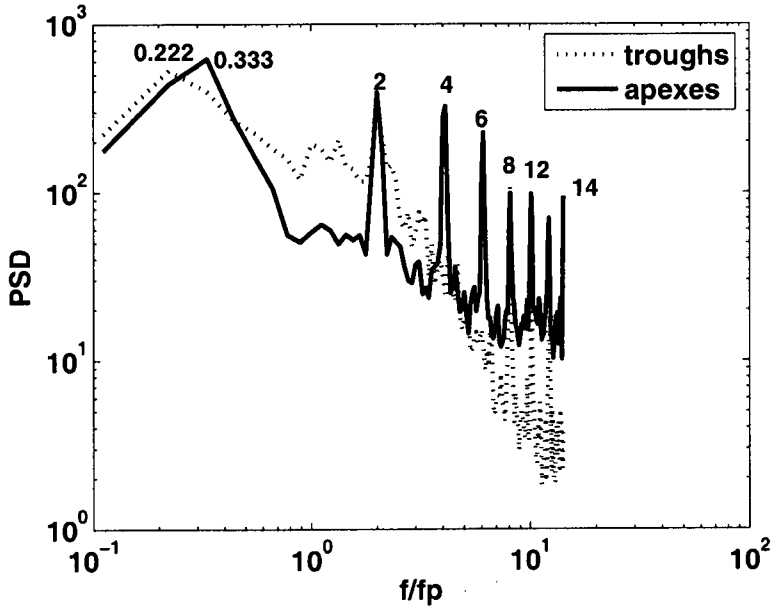


Figure 6-10: Flow dynamics around the apexes and the trough of the pentagon pattern

From the results of the flow dynamics at the troughs and the apexes we can infer that the increase in intensity of the secondary flow at the apexes enhance the role of nonlinear effects (characterized by the increase in the intensity of harmonics) which trigger the destabilization of the pattern.

In figure 6-11, we show the average power spectrum over 360 point of the displacement of the contour with respect to the mean contour. Here, we notice that the frequency around one third dominates the power spectrum for N=4 to N=6 . This observation arises a fundamental question: whether or not the one third cascade is particular for swirling flows. Indeed as pointed out above, the frequencies of the patterns are locked at one third the frequencies of the rotating disk and now we notice that the secondary flow has a frequency close to one third the frequency of the rotating polygonal patterns. Then, similarly to the sub-harmonic or the periodic doubling cascade which was intriguing at the beginning before it was established as one of the routes to chaos or turbulence in fluid mechanics; is one third cascades a route to turbulence in swirling flows? The fact that this one third frequency locking in swirling flow is reported elsewhere enforces the consistency of the hypothesis. Still, the question needs more investigations.

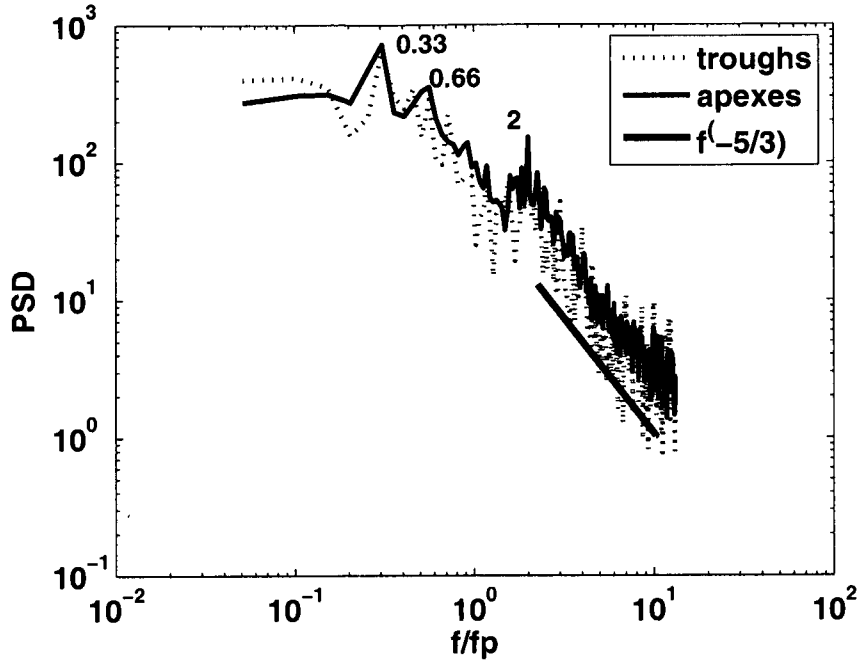


Figure 6-11: Flow dynamics around the apexes and the trough of the hexagonal pattern

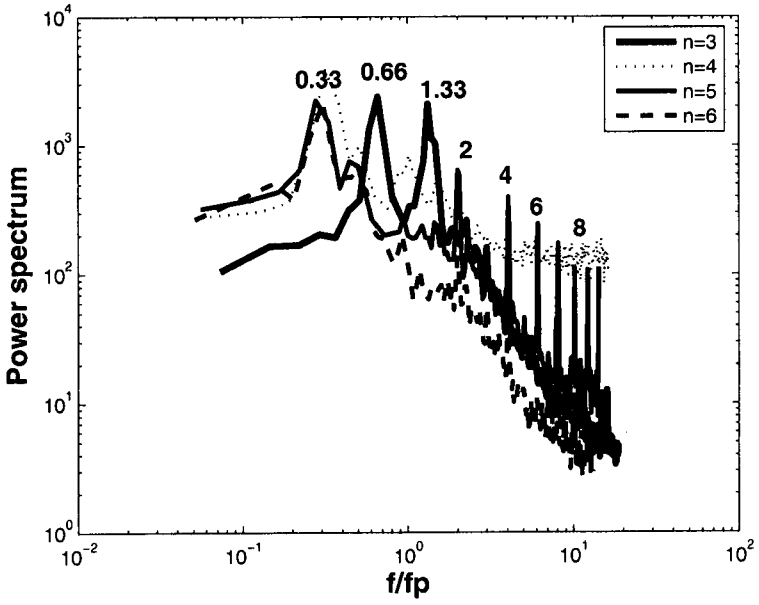


Figure 6-12: Flow dynamics around the apexes of observed patterns

# 4. Conclusion.

The results described in this chapter are novel and fundamental. For the first time the stability conditions of Havelock (1931) and J.J Thomson (1897) are confirmed. The last author proved that the maximum polygonal pattern or the maximum satellite vortices on a circular ring is six. Moreover, for the system of satellite vortices surrounded with circular boundaries to be stable they should be located on a circular ring of radius equal to half of the containing wall. For the first time, the frequency locking between the pattern and disk frequencies is determined. In the shallow water condition, this frequency locking is around one third (1/3). Furthermore, for the first time the flow dynamics around the apexes and troughs are described. The apexes host satellite vortices which can be considered as secondary instabilities. This secondary flow around the apexes is characterized by a frequency which is around one third the pattern's frequencies. This experimental evidence provoked the question concerning the one third cascades in swirling flows in shallow water conditions.

# Chapter 7: Transition between Kelvin's equilibria

## 1. Introduction

### 1.1 Outline

All the theoretical and experimental work on the polygonal patterns dealt with their stability. However none of them elaborated on how different stationary configurations evolve from a given equilibrium (mode) to the next one. Vatistas (1990) and Vatistas et al (2008), observed that the transition from one equilibrium mode to the next occurs through mixed modes, and that the bandwidth of the transition interval shrinks with the increase in mode number. However, no systematic investigation into the transition was reported. Hence, the underlying physical mechanism(s) that leads to the transition from one stable state to the subsequent remained unknown. The present work is the first in this subject.

### 1.2 Bifurcations in swirling flows

As pointed out in chapter 2, several swirling flows found in nature and industry can be reproduced at a laboratory scale in a closed or open stationary cylindrical container by rotating one endwall, both of its endwalls or the rotating disc. These swirling flows, produced in this simple geometry are found to exhibit rich and complex bifurcation scenarios, Hopf, double Hopf, Naimark-Sacker and tangent double Hopf bifurcations. For instance, Lopez and Marques (2004) numerically analyzed the case where both endwalls are co-rotating. The basic state that enjoys the invariance to

rotations about the axis and symmetry reflection undergoes a primary instability, and induces non-axisymmetric rotating waves that may or may not be reflection symmetric. They showed that when the aspect ratio (ratio of height of the working fluid to radii of the container) is higher than one the primary instability preserves the reflective symmetry. However, when the aspect ration is less than one the symmetry reflection breaks down. They also showed that when the aspect ratio is almost one, there is mode competition between symmetry reflection preserving and symmetry refection breaking and the pure rotating wave modes are unstable; the only stable mode is the mixed mode. More complex, modes competition between rotating waves of azimuthal wave numbers $N$ and $N+1$ are obtained through numerical simulation when the aspect ratio is equal to 0.5 and the endwalls are counter-rotating, see Marques et al (2003).

All the works devoted to the instabilities in confined swirling flows show that the aspect ratio, Reynolds number and ratio of rotating frequency of the endwalls are the fundamental bifurcation parameters that control symmetry breakings of the swirling flow. All the studies dealing with symmetry breaking in swirling flow considered flooded vortex cores, but none of them dealt with hollow vortex cores. Despite the extensive numerical and experimental work a convincing explanation of the symmetry breaking and its mechanism remains to be found. Moreover, the problem becomes more complex when the vertical cylindrical container is open, i.e the free surface is presence. In most of the numerical studies on confined swirling flows with

free surfaces, this last is considered flat with zero shear stress; see Lopez et al (2004). However, the flat free surface hypothesis is found invalid under shallow water conditions. All of the studies on the stability of swirling flow were restricted to the investigation of the influence of the control parameters on the bifurcation scenarios. Hence, bifurcation diagrams were given and the location of Hopf, double Hopf, Naimark-Sacker and tangent double Hopf bifurcations, in parameter space as well as modes competition, are indicated. However, no explanation of the mechanisms leading from a given mode to another has been tackled. This can be explained by the fact that all studies conducted until today are either numerical or experimental; using the DPIV technique which we believe cannot adequately handle this complicated problem. However the present experimental set up and visualization technique allows the investigation of the transition. Due to the resemblance between the present experiments and those conducted in flooded vortex core (where the rotating patterns are hidden), the present experiment can be used as a paradigm for the investigation of the instabilities in swirling flow.

# 2. Experimental setup and measurement technique

## 2. 1 Experimental setup

The present experiments were conducted in the apparatus shown schematically in Figure 6-2 which consists of a Plexiglass stationary cylindrical tank of a 284 mm inner diameter, with a flat disk revolving in the

counter-clockwise direction near the tank bottom. The experiments were conducted with disks of two different diameters, 252 and 270 mm, and at two different initial water heights ($h_0$) of 30 and 40 mm. The disk speed ($f_d$) was varied from 1.9 to 4.28 Hz, the corresponding Froude number ranged from 3.2 to 4.5. The Froude number is defined as $Fr = R_d f_d / 2\pi\sqrt{gh_0}$ where, $f_d$ , $R_d$ and $g$ are the disk frequency, disk radius and gravity, respectively.

When the swirl is imparted to a thin liquid layer confined in a stationary cylinder, by rotating a disc near the bottom of the cylindrical, the centrifugal force due to the rotary motion of the liquid along with the gravity causes the free surface to form an inverted bell shape. Its central depression grows deeper as the disk speed increases. Eventually, the receding liquid exposes part of the disk's central surface to air, whereby, the line of intersection between the surfaces of the disk, liquid, and air outlines the core shape. With the increase of the disk speed, the circular shape of the core first become elliptical and then acquire different polygonal equilibrium patterns the so called Kelvin's stationary equilibria.

### 2.2 Measurement technique

In the present experiments, in order to enhance the signature of the patterns, blue water-soluble dye was mixed with water prior to experimentation. A two megapixel CCD camera (JAI CV-M2) was placed above the cylinder to collect images of the core patterns formed on the disk

(see Figure 6-2). The camera was connected to a PC equipped with a digital frame grabber that acquires 8-bit images at a rate of 30 frames per second. A circular neon lamp surrounding the cylindrical tank is used to ensure the uniformity of light.

It was observed that the Froude number range, over which the transition occurs from one mode ($N$) to the next, and also the mode stability range decreases with an increase in $N$. Thus, for the transition from $N = 4$ to $N = 5$ and from $N = 5$ to $N = 6$, the Froude number range was very narrow and it was difficult to accurately capture the transitional modes. Therefore, the experiments were conduction for the transition from $N = 2$ through $N = 4$. The first set of experiments was conducted with 252 mm diameter disk and at the initial water height of 30 mm. In this set of experiments, the transition from mode $N = 2$ to $N = 3$ was investigated. The second set of experiments was conducted with 270 mm diameter disk and at the initial water height of 40 mm. In this set of experiments, the transition from mode $N = 3$ to $N = 4$ was investigated. For each experimental run in a given set of experiments, 1000 images were acquired. An image processing algorithm has been developed in order to accurately detect the edges of the patterns in each image. A sample image at $N = 4$ state is shown in Figure 7-1. The pattern contour, detected through the image processing algorithm, is superimposed on the image for comparison.

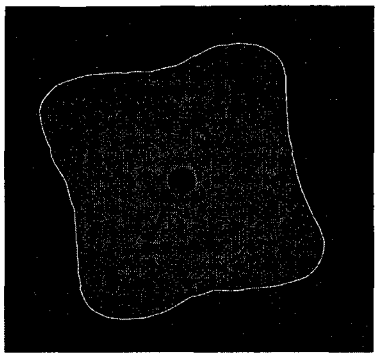

Figure 7-1: Pattern contour

# 3. Results and discussion

## 3.1 Transition in laboratory frame of reference

A detailed investigation of the transition process was conducted through spectral analysis. The frequency spectra of the patterns for different cases were computed from the corresponding sequences of the detected contours. To compute the frequency spectrum, time series of the radial distance of the pattern edge from the disk center was extracted at each value of $\theta$ (i.e. $\theta = 0^\circ$ to $360^\circ$). The spectrum was computed for each time series and then averaged for each experimental run. During the experiments, more transition states were captured from $N = 3$ to $N = 4$ compared to that from $N = 2$ to $N = 3$. Therefore, the detailed description of the transition mechanism is presented for the transition from $N = 3$ to $N = 4$. Subsequently, it is further elaborated for the transition at other modes to establish the generality of the transition mechanism. The shapes of the hollow-core patterns that evolve during the transition from $N = 3$ to $N = 4$ are depicted in Figures. 3-2-3-4 (a), 3-5 (a-c) and 3-6-3-7 (a). Figure 7-2(a) shows the

image of the pattern at $N$ = 3 equilibrium state, obtained at $F_r$ = 3.37 ($f_d$ =3.20 Hz). At this state, the pattern takes the form of a trefoil. As the Froude number is increased, the pattern starts to expand from the troughs, while the apexes remain at the same radial distance from the center (see Figures. 7-3a and 7-4a). Eventually, the pattern acquires quasi-triangular form. Once the critical Froude number is reached, the quasi-triangular pattern transforms gradually into a quasi-square form (see Figure 7-5 a-c). It is observed that at the critical Froude number, the transition from quasi-triangular to quasi-square form takes approximately 20 seconds. With a further increase in the Froude number, the pattern at the mode $N$ = 4, starts to stabilize and the troughs recede. The pattern after reaching the equilibrium state at the mode $N$ = 4 is shown in Fig.7-7 (a). It should be noted that the radial distance of the apexes from the center remains the same from one equilibrium state through transition to the next equilibrium state. The underlying physical mechanism for the transition is investigated through spectral analysis and discussed below. The frequency spectrum at $N$ = 3 equilibrium state is shown in Figure 7-2 (b). The plot shows several spectral peaks. The most energetic peak ($f_m$) occurred at a frequency of 3.22 Hz. Three harmonics of $f_m$ at 6.44 Hz, 9.66 Hz and 12.9 Hz are also visible in the spectrum. For a given mode, the most energetic peak is related to the frequency of the pattern ($f_p$) as,

$f_p = \frac{f_m}{N}$ where, $N$ is the number of apexes of the given polygonal pattern. At the $N$ = 3 mode, $f_p$ = 1.07 Hz. The plot also shows a less energetic peak at a frequency of 4.86 Hz. Hereinafter, this modulation is referred to as growing

frequency ( $f_g$ ) as will be shown later, this modulation plays a significant role in the transition. Although at the $N$ = 3 equilibrium state, the amplitude of this modulation is several orders of magnitude less than $f_m$ and its harmonics. This modulation interacts with $f_m$ and their interaction is evident in the spectral peaks at 1.6 Hz and 8.08 Hz, where, 1.6 Hz correspond to $f_g - f_m$ and 8.08 Hz correspond to $f_g + f_m$. Hereinafter, these frequencies are referred to as $f_b$ and $f_s$, respectively.

As the disk speed is increased, the $N$ = 3 equilibrium state is distorted due to the increase in the modulation amplitude associated with $f_g$. This behavior is clearly visible in the spectra shown in Figures. 7-3 (b) and 7-4 (b). The plot in Figure 7-3 (b) shows that as the disk frequency increased from 3.2 to 3.33 Hz, the modulation amplitude is increased by almost two orders of magnitude and its frequency is shifted to $f_g$ = 4.98 Hz. The frequencies associated with $f_m$ , $f_b$ and $f_s$ are also shifted. The plot also shows that the amplitude at $f_b$ and $f_s$ also increased by more than an order of magnitude which is likely due to the increase in the modulation amplitude at $f_g$. The spectrum in Figure 7-4 (b) also shows similar behavior with a further shift in the frequency due to the increase in the disk frequency ( $f_m$ = 3.4 Hz, $f_g$ = 5.1 Hz). It should be noted that $f_m$ , related to the rotating pattern, is slightly lower than the disk frequency, as the corresponding images show, the pattern mode is still three.

As the disk frequency is further increased, it approaches the critical value, the transformation from mode $N$ = 3 to $N$ = 4 occurred. This transformation process is depicted in Figures 7-5 (a-c). The corresponding frequency spectra are plotted in Figures 7-5(d-f), respectively. The spectrum in Figure 7-5 (d) shows the trend similar to that in Figures 7-3 (b) and 7-4 (b) as the fundamental mode is still three. The spectrum in Figures 7-5 (e) corresponds to the situation when the transformation is underway. The spectrum shows that the amplitude of $f_g$ is increasing while the amplitude of $f_m$ is decreasing. The spectrum in Figure 7-5 (f) represents the behavior after the transformation is completed and it shows that the amplitude of $f_g$ is further increased and becomes comparable to that of $f_m$ before the transformation. At this state, the amplitude of $f_m$ is reduced by one order of magnitude. No frequency shift occurred at the transformation stage. With a further increase in the disk frequency, the pattern at $N$ = 4 reached the equilibrium state. The spectrum at this state is shown in Figure 7-6-7-7 (b). The modulation originating in the mode $N$ = 3 (i.e. $f_g$) is now the dominant frequency at mode $N$ = 4. The higher harmonic corresponding to this frequency is also prominent in the spectrum.

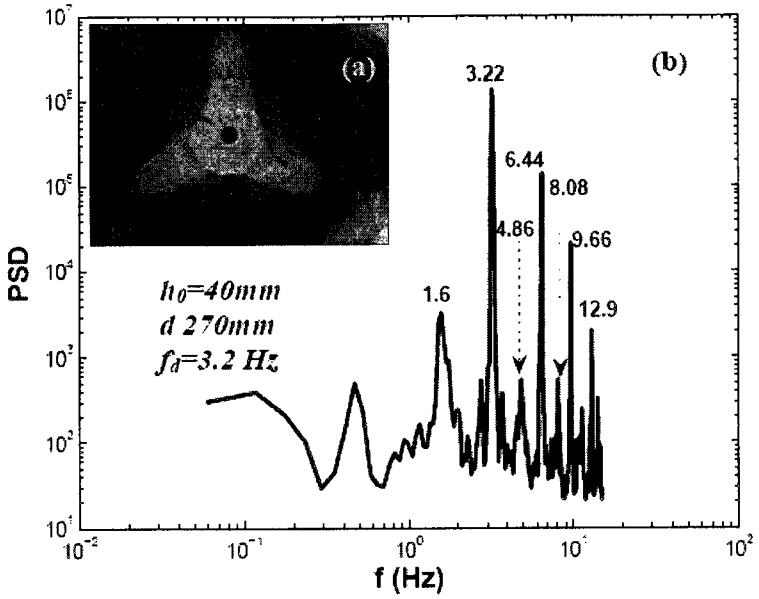


Figure 7- 2: a) Image of the pattern b) Power spectrum

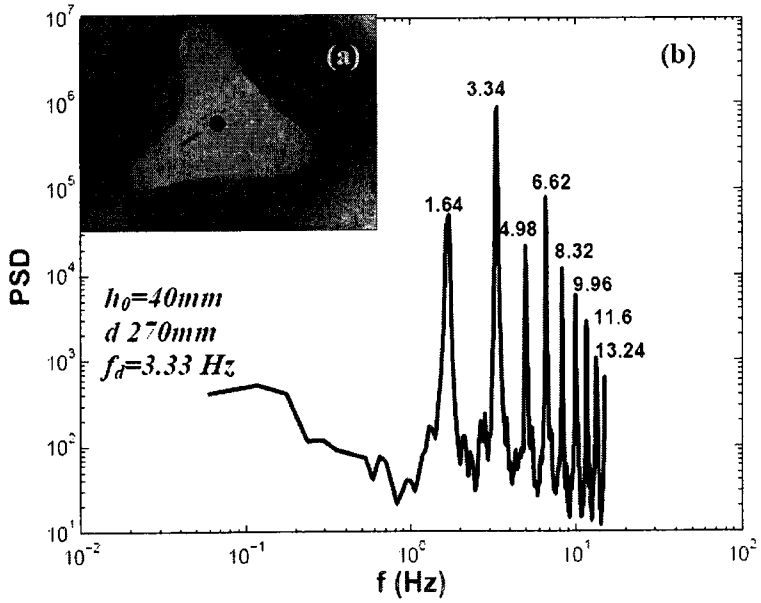


Figure 7-3: a) Image of the pattern b) power spectrum

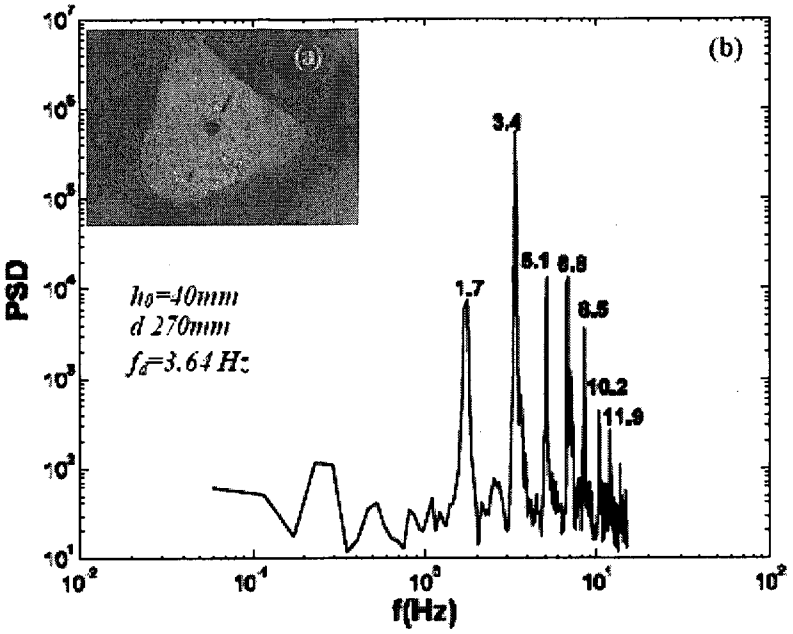


Figure 7-4: a) Image of the pattern b) power spectrum

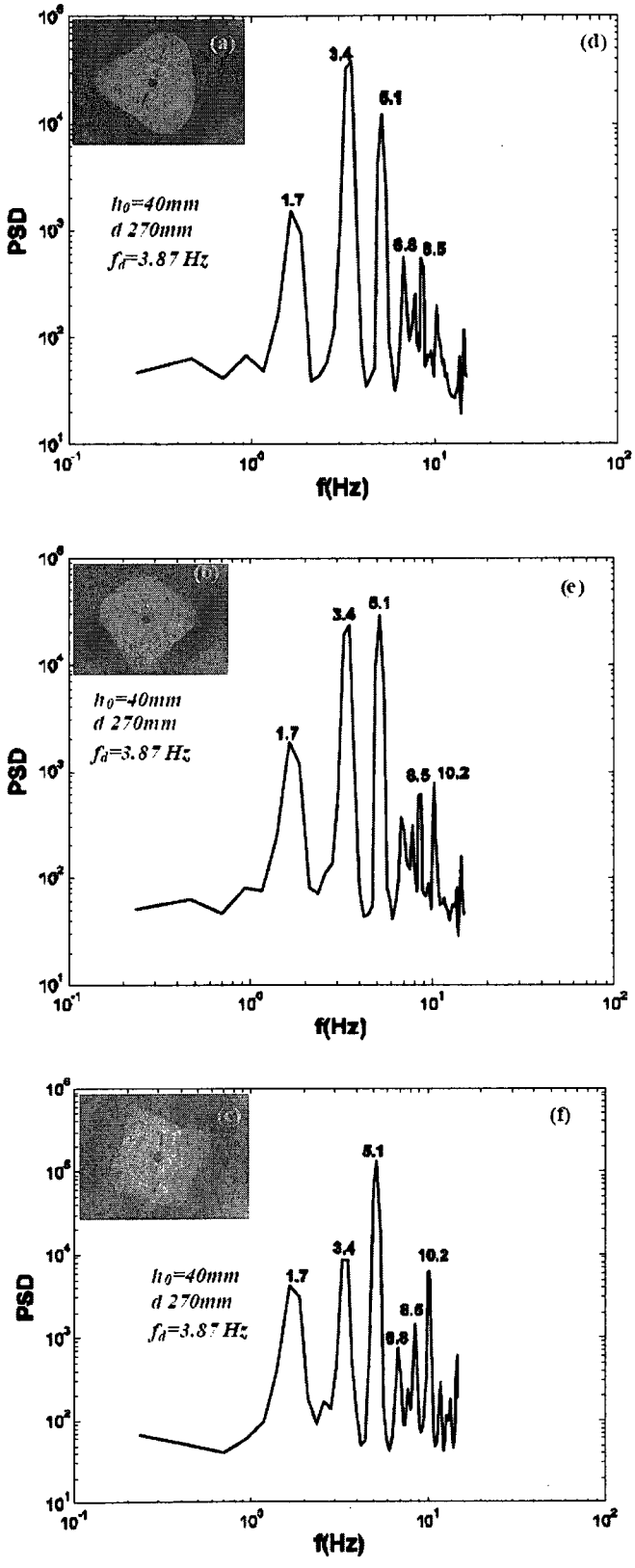


Figure 7-5: a,b,c images of the pattern during the transition d,e,f Power spectrums

A careful inspection of the spectra in Figures 7-2–7-6 shows that $\frac{f_g}{f_m}$ is almost 3/2. This frequency locking is very crucial in explaining the transition mechanism. Theoretical analysis of dynamic systems has shown that in a coupled oscillating systems with distinct frequencies $f_1$ and $f_2$ (bi-periodic state), if the ratio between the two frequencies become rational, the bi-periodic state looses its stability and becomes periodic with respect to one frequency, while the other frequency disappears (Berger et al. 1984) . Using this analogy for the present case, the transition mechanism from mode *N* to *N + 1* can be explained as follows. At a given equilibrium state, as the disk speed (or the Froude number) increases, a higher frequency modulation ( $f_g$ ) is induced and is locked with the dominant frequency associated with the equilibrium mode ( $f_m$ ). Initially, the ratio ( $\frac{f_g}{f_m}$ ) is close to rational (Figures. 7-2 and 7-3) and then becomes rational (Figure 7-4 and 7-5), while the amplitude of the growing mode continues to increase. As the ratio becomes rational and the amplitude of the growing mode become comparable to the existing equilibrium mode, the transition occurs and the hollow-core vortex transforms from triangular to square shaped. At the disk speed where the transition occurred, the frequency of the patterns at *N* = 3 and *N* = 4 are $f_m$ = 3.4 Hz and $f_g$ = 5.1 Hz. This ratio is 3/2 which correspond to the ratio *N/(N-1),* where *N* is the mode at the initial equilibrium state (*N* = 3 for the given case). The fact that it change from a triangle to the square, when the

ratio $\frac{f_g}{f_m}$ becomes rational, is consistent with the theory on the structural stability of the biperiodic regimes. The theory stipulates that the only way a biperiodic regime looses it stability is through synchronization, see Berger et al (1984).

Further increasing the disk frequency, after the transition, causes the amplitude at the frequency, corresponding to the previous mode ( $f_m$ ), to decrease and with a further increase in the disk frequency, the amplitude at $f_m$ becomes very small and the ratio $\frac{f_g}{f_m}$ becomes irrational again. After transition, the only dominant mode is the one that corresponds to $f_g$, which for the transition to the next mode ($N$ = 5) acts as $f_m$ (see Figures 7-6 and 7-7). The spectra in Figures 7-2-7-6 also shows a low frequency peak which is equal to $f_b = f_g - f_m$. This frequency corresponds to a wave traveling along the pattern contour which is caused by the interaction of $f_m$ and $f_g$. The frequency of this wave is higher than the frequency of the pattern and thus, this wave causes the alternative fattening of the apexes (also see images in Figures. 7-2-7-6).

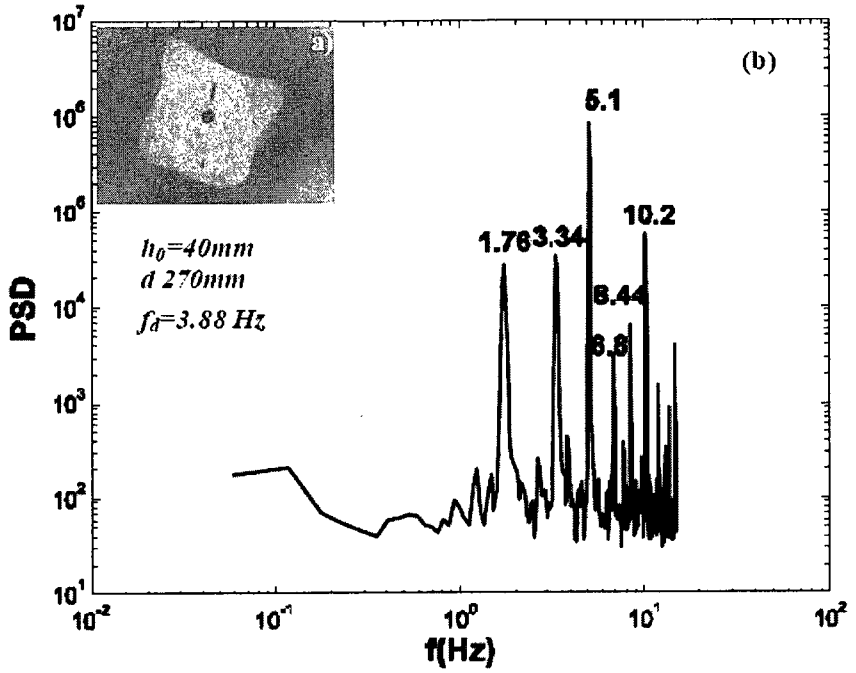


Figure 7-6: a) Image of the pattern b) power spectrum

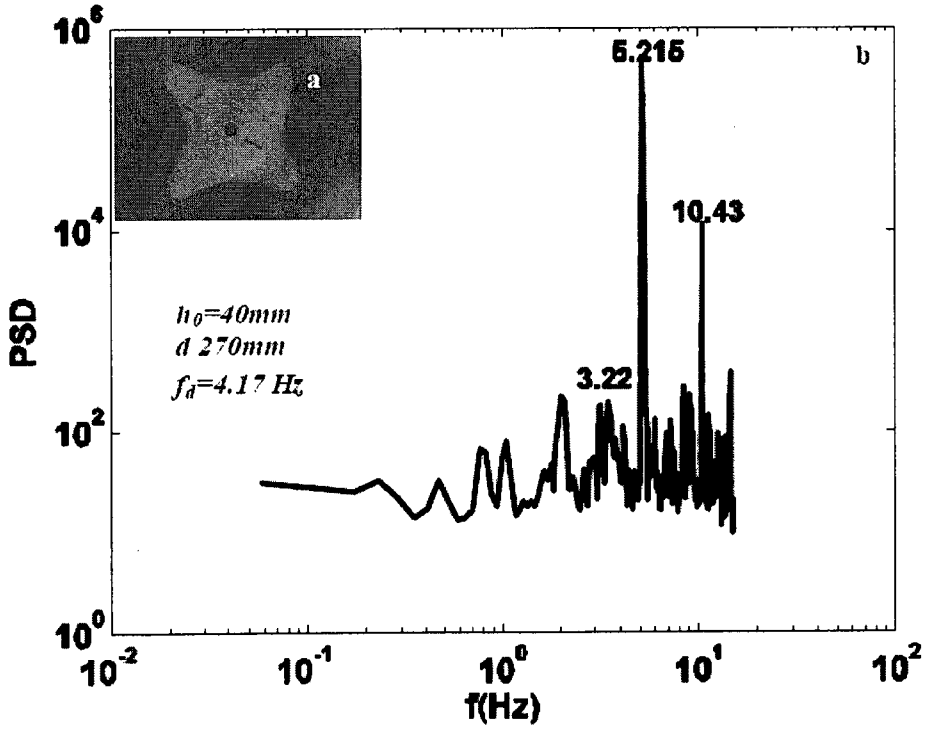


Figure 7-7: a) Image of the pattern b) power spectrum

Previously, we have described the transition process based on the experimental results for the transition from the modes $N$ = 3 to $N$ = 4. In the following we have demonstrated that the observed process is not specific to these modes but it is a general phenomenon also present in the transition at other modes. The images and the corresponding spectra at the transition phase from $N$ = 2 to $N$ = 3 are shown in Figures. 7-8, 7-9, and 7-10. Figure 3-9 shows that at the $N$ = 2 equilibrium state, the dominant mode occurred at $f_m$ = 1.406 Hz.

The growing modulation that led to the transition to the $N$ = 3 mode is also present at $f_g$ = 2.871 Hz and $\frac{f_g}{f_m}$ = 2.04 which is still irrational. The rational value of the ratio $\frac{f_g}{f_m}$ at which transition should occur is 2/1. During the experiments we were not able to accurately capture the locking mode of the frequencies, i.e. the rational value $\frac{f_g}{f_m}$ = 2, because we passes the critical speed at which the transition occurs, i.e the disk speed at which a synchronization between modulating wave ($f_g$) and the dominate mode ($f_m$) occurs. The $\frac{f_g}{f_m}$ has decreased and become irrational ($\frac{f_g}{f_m}$ =1.97). Hence, it is easy to infer that, similar to the transition from $N$=3 to $N$=4, the transition from $N$=2 to $N$=3 occurs when $\frac{f_g}{f_m}$ =2/1.

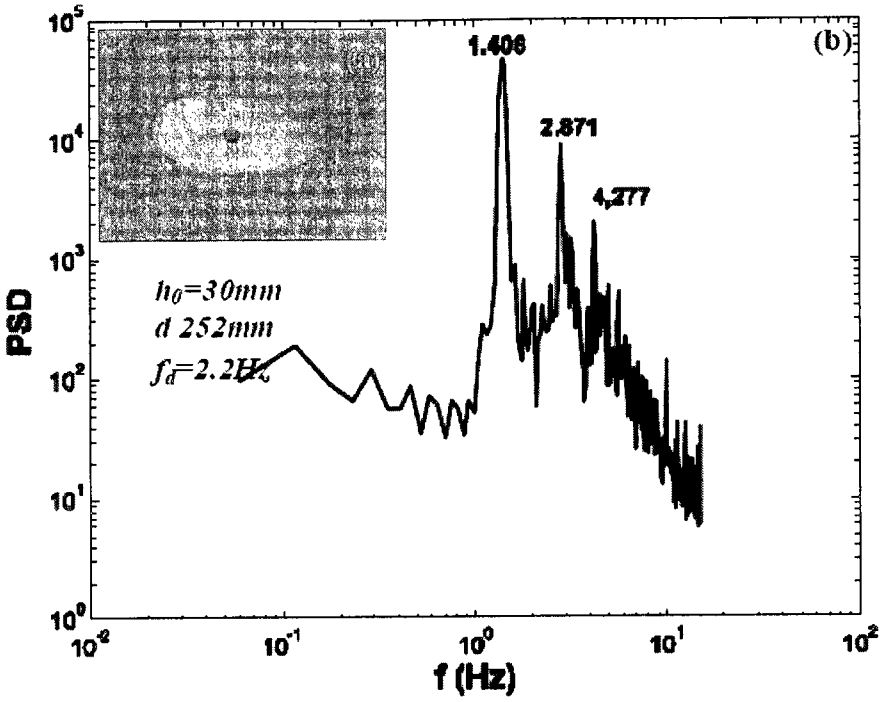


Figure 7-8 a) Image of the pattern b) Power spectrum

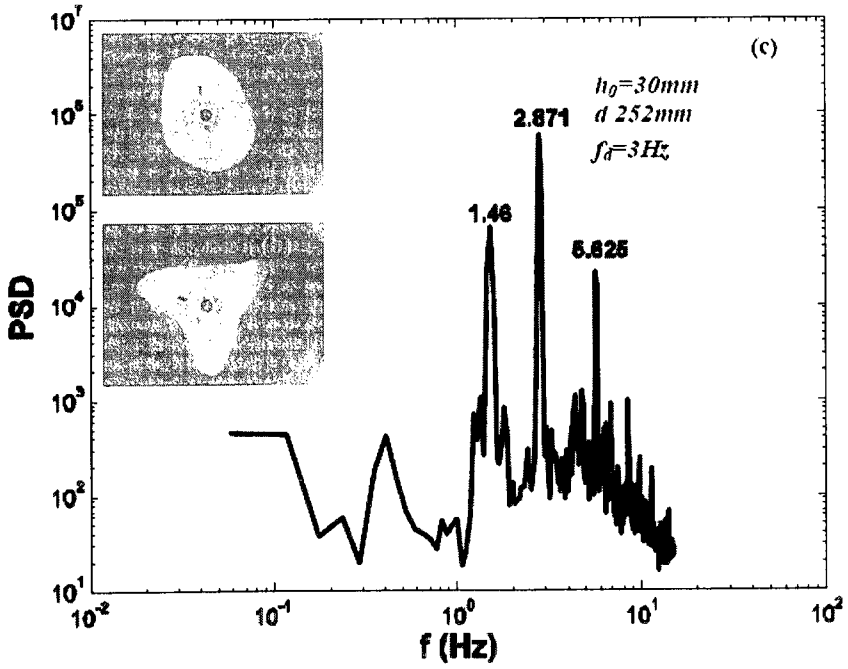


Figure 7-9: a,b) Image of the pattern during the transition c) power spectrum

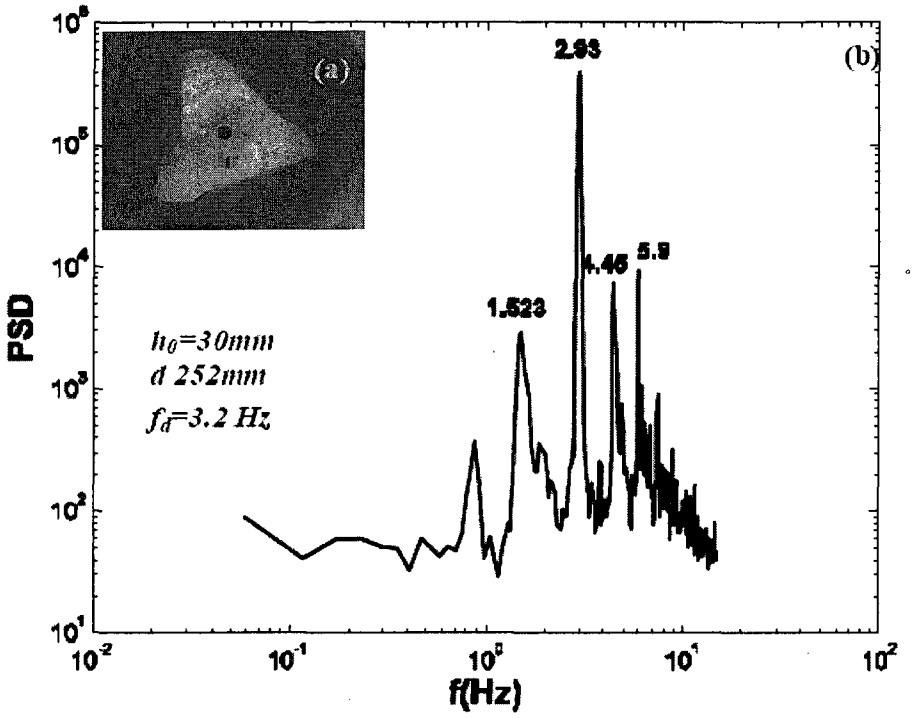


Figure 7-10:a) Image of the pattern b) power spectrum

The pattern contour and the corresponding frequency spectrum just after the transition to $N$ = 3 are presented in Figure 7-10. As expected, the amplitude of $f_m$ decreased and the amplitude of $f_g$ increased. At this state the ratio $\frac{f_g}{f_m}$ becomes irrational again ($\frac{f_g}{f_m}$=1.924). The growing mode that leads to the transition to the $N$ = 4 mode also appeared in the spectrum at a frequency of 4.45 Hz. However, the ratio between the two frequencies responsible for the transition from $N$ = 3 to $N$ = 4 is still irrational and equal to 1.512, close to 3/2 found above.

Although the description of the transition mechanism is based on the two transitions, i.e. $N$ = 2 to $N$ = 3 and $N$ = 3 to $N$ = 4, the spectra at the equilibrium modes $N$ = 5 and $N$ = 6 shown in Figure 7-11 confirmed that the transition should follow the same route as the transition at these modes. For the transition from the $N$ =5 equilibrium the transition should occur at, $\frac{f_g}{f_m}$ = 5/4 = 1/25. The spectrum in Figure 7-11a shows that $\frac{f_g}{f_m}$ = 1.267, which is still irrational as expected and close to the rational value of 1.25. As for the transition from the $N$ = 6 equilibrium state, it should occur when $\frac{f_g}{f_m}$ = 6/5 = 1/2. The spectrum in Figure 7-11b shows that $\frac{f_g}{f_m}$ = 1.222 which is still irrational as expected and close to the rational value of 1.2.

Based on the above results the transition mechanism can be described as follows. At the equilibrium state of a given pattern, $N$, the dominant mode is characterized by a frequency, $f_m$. A wave modulation is induced in the flow at a frequency that corresponds to the mode $N+1$ ( $f_g$ ). As the Froude number increases, the amplitude of $f_g$ increases. The transition occurs when the ratio $\frac{f_g}{f_m}$ = $N/(N-1)$, which is rational. The ratio $\frac{f_g}{f_m}$ remains irrational but close to $N/(N-1)$ before and after the transition. Hence, the transition between two subsequent patterns occurs in two steps.

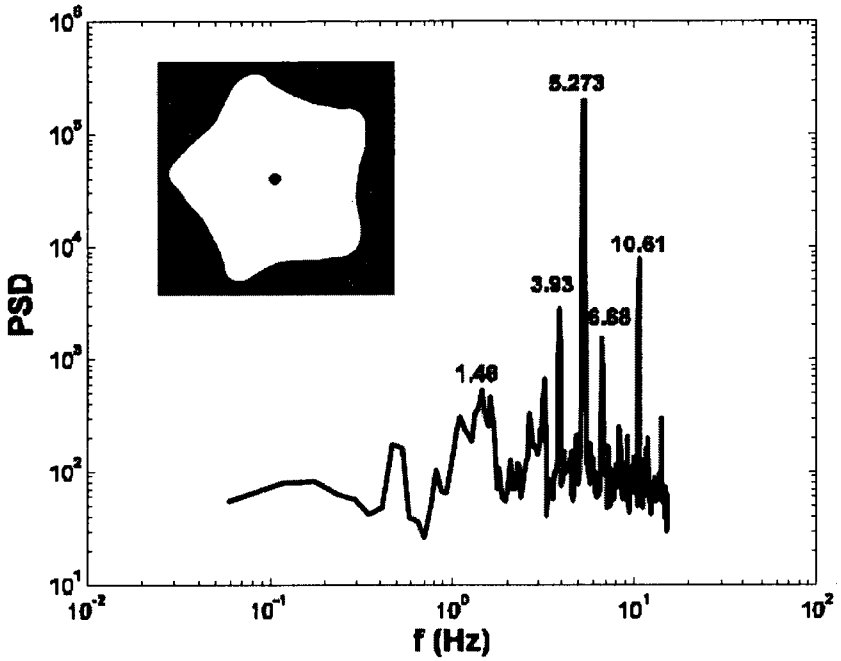


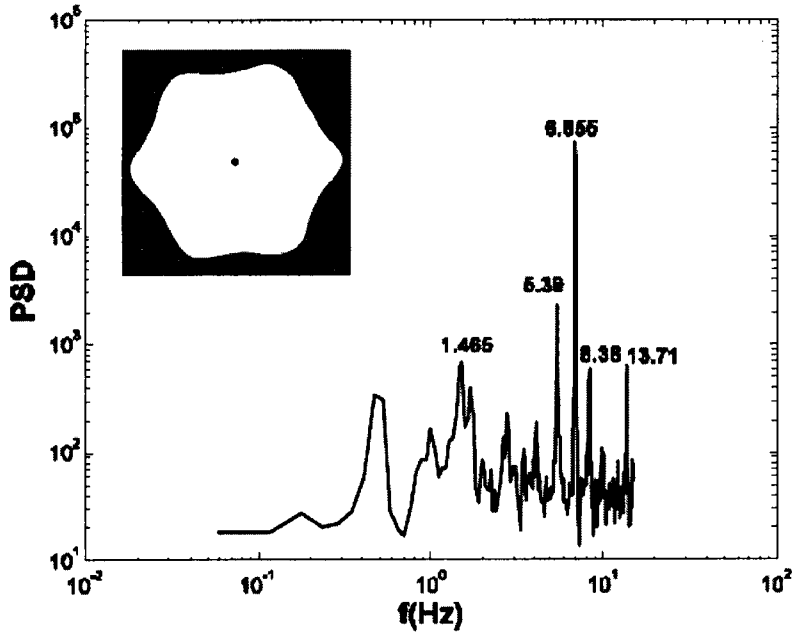


Figure 7-11: Power spectrum of the patterns 5,and 6 for $h_0$=20mm for different $f_d$ disk diameter is 252mm

First, for a given pattern (first oscillators with frequency $f_m$), a growing mode (second oscillators with frequency $f_g$) modulating a pattern arises. The ratio between the frequencies $f_g$ and $f_m$ is an irrational number but close to a rational one; therefore the route to the transition is first biperiodic. Indeed, the corresponding power spectrums are not dense and they include peaks corresponding to $f_g - f_m$ and $f_g + f_m$. As we approach the critical condition the amplitude modulating mode increases and its frequency become locked to the frequency of the pattern; this synchronization between the dynamics of the pattern and the growing mode causes a transformation in the pattern from *N* into *N+1*. This funding is consistent with a theory which stipulates that the synchronization is the only route to produce a topological change in a biperiodic regime. According to our findings, the transition from *N*=2 through *N*=6 should follow the devil's staircase scenario where the stairs corresponds to the synchronization at $\frac{f_g}{f_m}$ = *N/(N-1)*. A transition from *N*=2 to *N*=3 occurs at $\frac{f_g}{f_m}$=2, from *N*=3 to *N*=4 at $\frac{f_g}{f_m}$=3/2, from *N*=4 to *N*=5 at $\frac{f_g}{f_m}$= 4/3, from *N*=5 to *N*=6 at $\frac{f_g}{f_m}$ = 5/4.and from *N*=6 to *N*=infinity occurs at $\frac{f_g}{f_m}$=6/5.

### 3.2 Transition in frame of reference moving with the patterns.

In the present subsection we investigate the transition from the triangular to the square pattern, discussed above in frame of the reference moving with the patterns. Similar to the above, a power spectrum analysis was used. The average power time series and the spectrums over 360 points on the pattern's contour are shown in figure 7-13-7-16. At the beginning the pattern is a trefoil, see Figure 7-3a; and the corresponding time series and power spectrum are shown in Figure 7-13. The time series in Figure 7-13a-b shows a fast wave train with frequency, $f_2$=4.4 Hz, embedded within another one having a frequency, $f_1$=0.58 Hz.

Increasing the disk speed to 3.64 Hz, the pattern remains triangular but more open and its lobes become fatter successively. The sequential fattening is due to a wave interaction between the parent wave ($N$=3) and the growing mode ($N$=4). This interaction takes the form of a beating wave rotating around the pattern (with a wave number $N+1$-$N$=1 and frequency $f_{N+1} - f_N$) behaving like a soliton. The power spectrum displayed in figure 7-13 indicate that the amplitude of the growing mode has increased, which is in accordance with the observations in the absolute frame of reference, see figure 7-5.

Since the two frequencies $f_1$ and $f_2$ are not locked and the amplitude of the growing mode had been increased, an observer traveling with the

pattern will simultaneously observe a growing mode ($N$=4) at frequency $f_2 = 4.4Hz$ and a rotating beating wave at frequency $f_1$=0.58 Hz. The effect of the growing mode is embedded within a beating wave or rotating soliton-like crest. Then the phenomenon can be interpreted as a soliton carrying a growing mode. Therefore the actual frequency of the growing mode in the relative frame of reference is $f_3 = f_2 - f_1$ =3.96 Hz which corresponds to the frequency of the growing mode in the absolute frame of reference ($f_g$ =5.1= $f_3 + f_p$), where $f_p = \frac{f_m}{3}$ =3.4/3=1.13Hz.

A further increase in disk speed to 3.87 Hz leads to a transition from triangular to square. This changeover is displayed in figure 7-14 in term of the evolution of the time series and its corresponding power spectrum. The time series shows that the amplitude in the relative frame of reference becomes smooth at the end of the transition (when the pattern reaches a square form). This interesting phenomenon can be interpreted as energy release or energy transfer from one mode to another.

Increasing slightly the disk frequency to 4.17Hz, the pattern completes its transition and the sides of the polygon (square) curve in. As shown in the figure 7-15b there is no soliton rotating around the square pattern which is under equilibrium conditions.

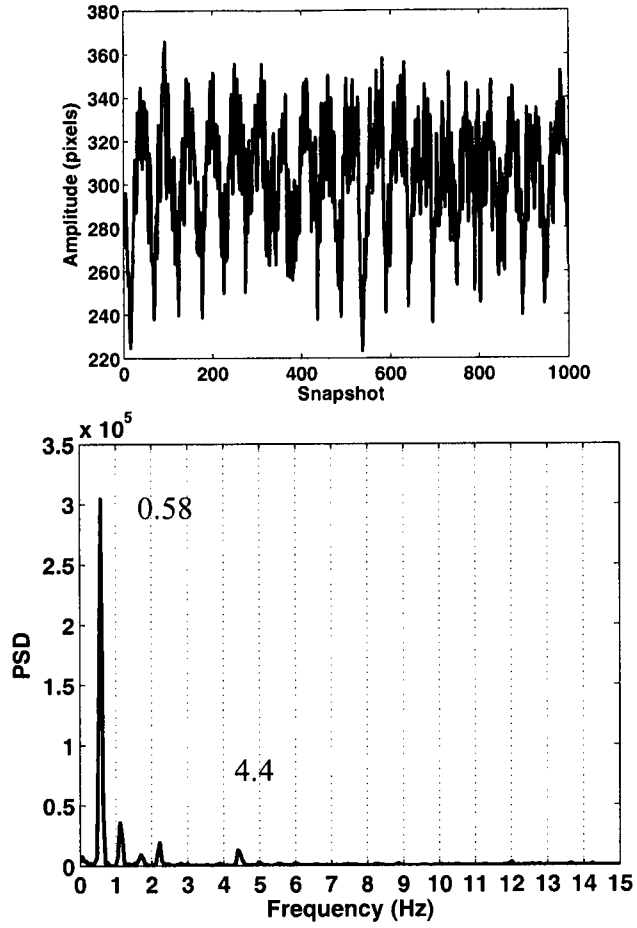


Figure 7-12 a) Average time series b) Average power spectrum

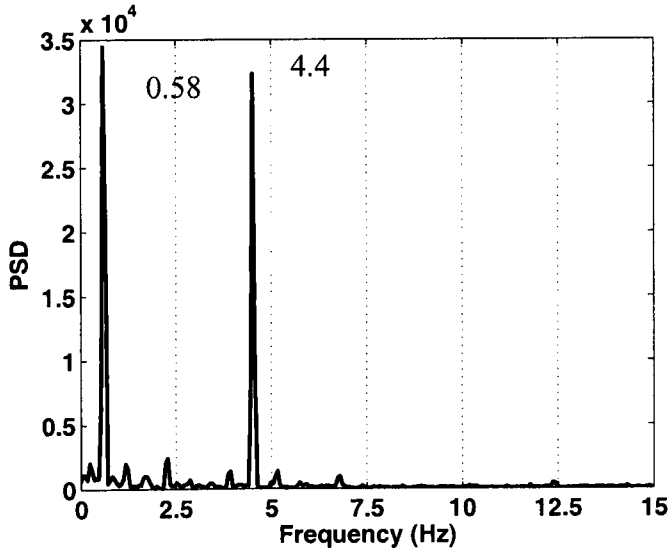


Figure 7-13 power spectrum

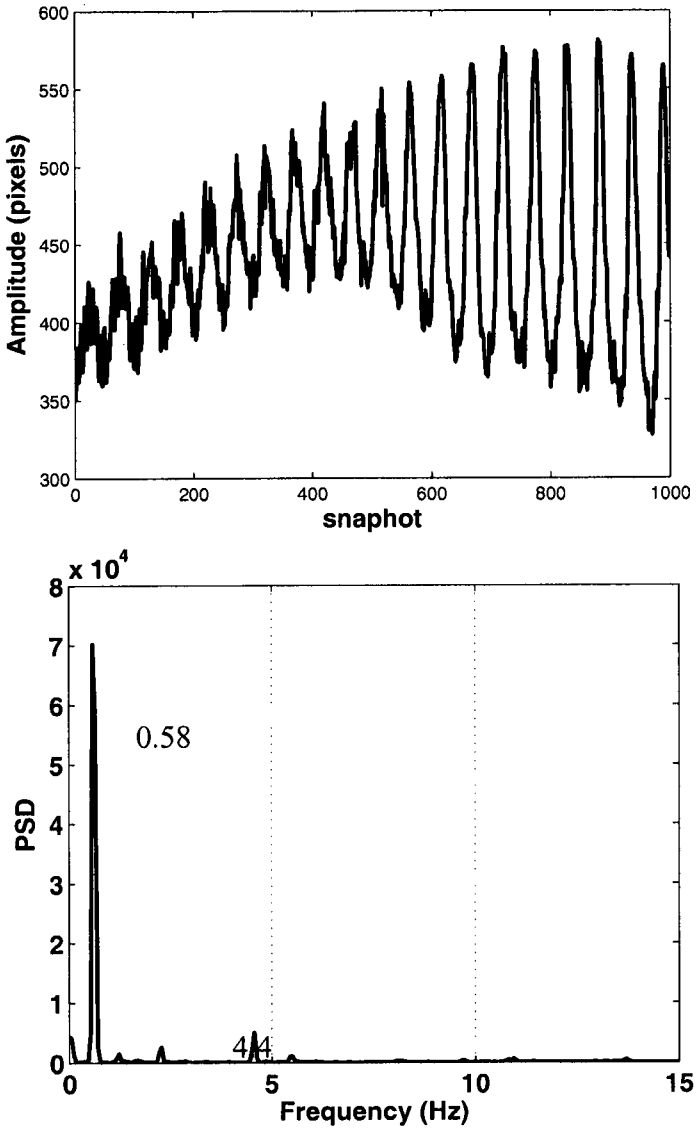


Figure 7-14 a) time series b) power spectrum

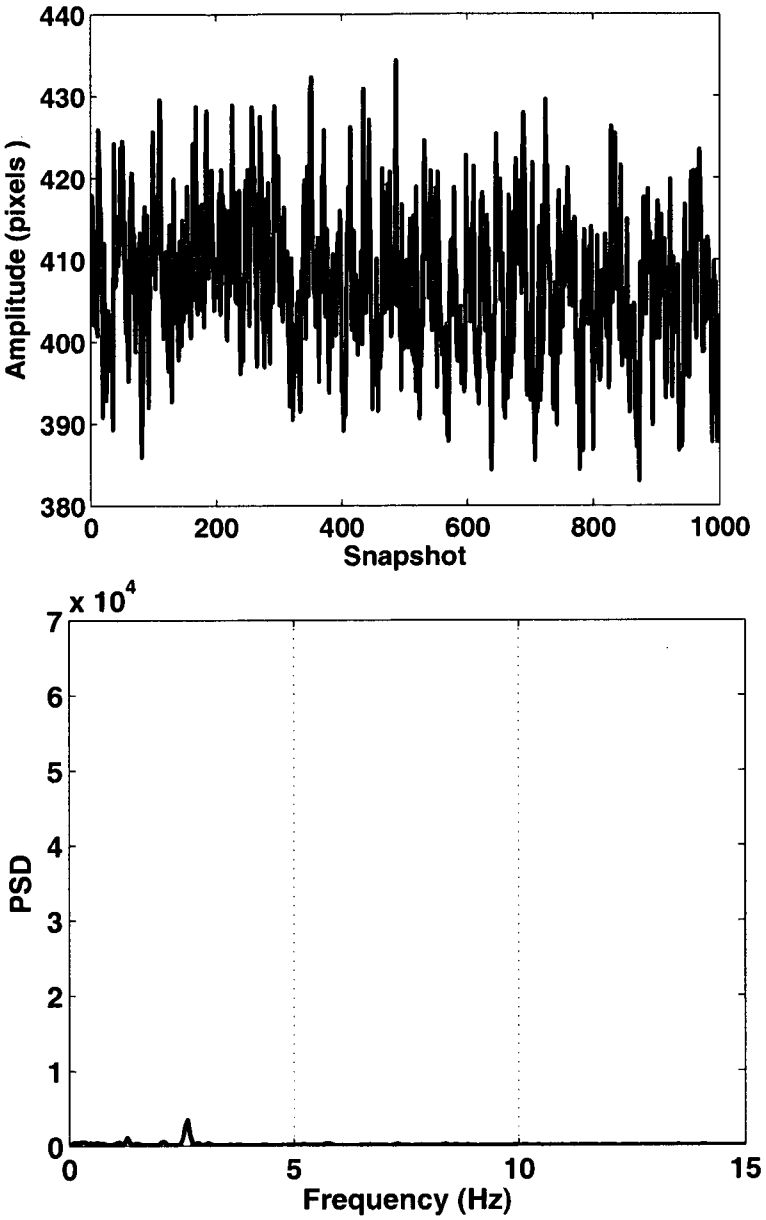


Figure 7-15: a) time series b) power spectrum

### 3.3 Transition in terms of pattern's area

The transition can be also depicted as the evolution of the dry area inside the vortex core. The unwind pattern contours are shown in figure 7-16. The area of the vortex core corresponds to the area underneath the curve; which is evaluated numerically.

Subsequently, we follow the evolution of the vortex core as the pattern approaches the next equilibrium. At the beginning, the pattern was a trefoil, Figure 7-3a with an average area of 1.2937e+005 (pixels X degrees). As the disk speed increases the trefoil pattern opens up and the area of the vortex core increases. Indeed, at the disk frequency of $f_d$ =3.64 Hz, shown in figure 7-4a, the area of the vortex core increases to 1.5797e+005 (pixels X degrees). The area continues to grow as a critical speed ( $f_d$ =3.87 Hz) is approached whereby the triangular pattern transforms into a square. This transformation is illustrated in Figure 7-17, which clearly shows that the vortex core area augments, reaching a maximum before it starts to decrease to minimal area when the square pattern appears. These features can be attributed to the limited energy that can be stored in a ring with three satellite vortices. This means that the system will absorb the excess energy by reorganizing itself by increasing in "vibration mode" or introducing an additional vortex into the ensemble. A further increment in speed will result in smaller areas until the transition is completed, whereby, the area reaches its minimum value.

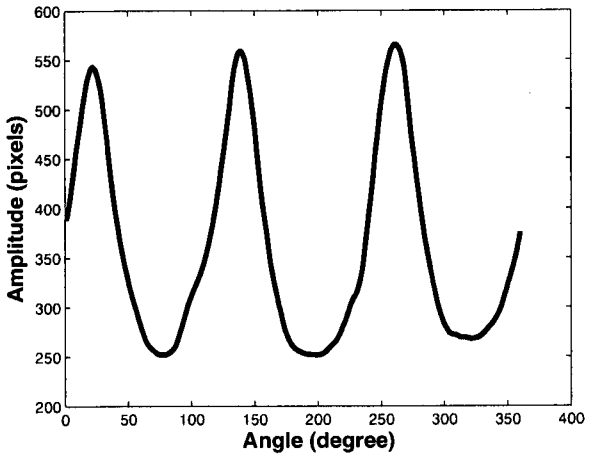


Figure 7-16 Triangular pattern unwinding

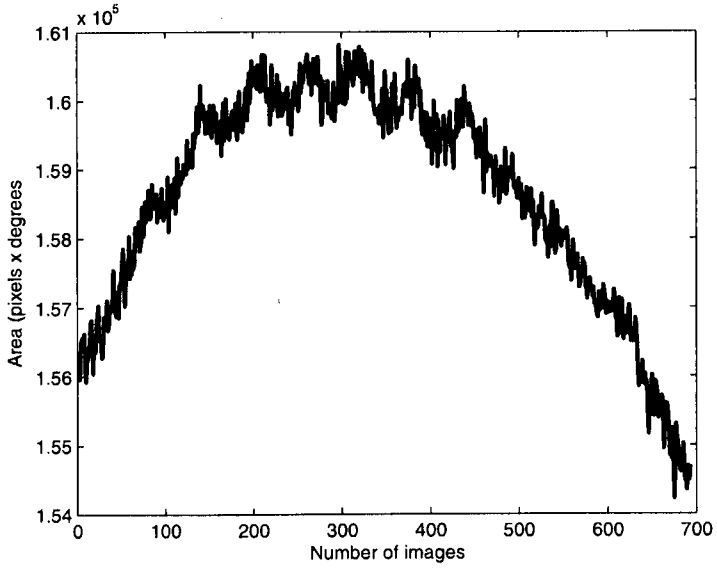


Figure 7-17 evolution of pattern area during the transition

# 4. Concluding Remarks

The present chapter was devoted to the transition from one pattern to another. This transition was investigated in two frames of reference. The investigations of the transition, in an absolute frame of reference, shows that the transition from one pattern to another is, at first, a biperiodic regime before it becomes periodic when the two frequencies lock. The transitions follow a "devil staircase" route, to which the staircases represent the location where the ratio of the two frequencies become rational. The investigation of the transition in a relative frame of reference shows that the transition can be interpreted also as an energy transfer from one mode to another. The changeover mechanism is also depicted as a vortex-core area variation. This investigation shows that the wave dynamics of the vortex core should reorganize itself to absorb the excess energy fed by the disc. The results of the present study are relevant to several fields of physics, plasma, superfluidity, and optics. Moreover, the present experiment can be considered a paradigm to investigate planetary vortices.

# General Conclusion

In this thesis we have tackled, analytically and experimentally, two problems that are among the oldest in fluid mechanics. The first deals with a film of fluid flowing down an inclined plane, and the second with the equilibrium of a system of point vortices arranged symmetrically around a circular ring. The first problem dates back to Nusselts (1916) and is still the subject of interest of many researchers for its applications and theoretical interests. In the present thesis this problem was approached analytically. In part I (chapter 2), we have proposed four- and three- equation models. In comparison with models of the same dimensions found in the literature, these two models involve only the flow parameters namely the flow rate, film thickness, shear stress and velocity at the free surface (for the four equation-model). The linear stability and instability conducted with these two models is accurate in comparison with those obtained with other four equation models and with more involved numerical work. However, they present a challenging problem for the nonlinear stability analysis; this is due to the presence of cross derivatives (time and space). In order to get more insight on the film fluid dynamics, a lower dimension model is need; hence, a two-equation model is proposed. The two-equation model involves only a flow rate and film thickness, and is an improvement of an existing model. Indeed, examining an existing model (Usha and Uma (2004)), we remarked that one of the boundary condition (tangential component of the dynamical condition at the free surface) is not satisfied at the claimed second order with respect to the

long wave parameter. This flaw comes from their choice of velocity field. Hence, a correction is introduced to their velocity profile which consists of the inclusion of the shear stress at the free surface in order to ensure the consistency of the boundary condition for the desired accuracy. We have shown that the correction is relevant because it induces significant differences in the occurring condition of the bifurcations scenarios. Moreover, we have shown also that the wave profiles issued from the bifurcation are different.

The extensive modeling effort conducted with ordinary fluid is also conducted with electrically conducting fluid flowing down an inclined plane under the influence of electrical and magnetic fields. Here we have proposed an improved model for higher Reynolds number. Indeed, the model proposed for this problem by Korsunky (1999) is very similar to the Shkadov (1968) model for ordinary fluid. The Korsunsky model does not predict a Hopf bifurcation while we have shown that our model predicts this major scenario.

In the second part of this these we have tackled, experimentally, the problem of a system of point vortices equally distributed on circular ring. The outcomes of the present research are important. First, we have confirmed for the first time the theories, of Kelvin (1867) and Haveloch (1931), on the equilibria conditions of a system of point vortices. Moreover, we have also investigated for the first time the dynamics of the point vortices system. We found that a system of point vortices rotate at one third the frequency of the rotating disk which is almost equal to the frequency of the parent vortex. The

point vortices, which are located at the apexes of the polygonal pattern, can be considered a manifestation of a secondary flow characterized by a frequency which is around one third the frequency of the pattern. This mimics the question of whether or not a period tripling is a route, leading such swirling flow to chaos; all the more reason why Marques et al (2003) have shown that a rotating wave following a Hopf bifurcation rotates at one third the frequency of the rotating lateral wall, in similar configuration. Another fundamental result is the one which deals with the transition from the elliptical vortex core form to the heptagonal one. We found that this transition follows a "devil staircase" route. The transition between two subsequent patterns starts first as a biperiodic regime before the two frequencies becomes synchronic. In topological terms, the transition is a destruction of torus into a limit cycle when the two frequencies are locked or synchronic. We found that the staircases occur when the ratio of the two frequencies is rational at N-1/N, where N is the number of the apexes of the polygonal pattern. Furthermore, a transition from a mode N=3 to N=4 is investigated in a frame of reference moving with the pattern. This study reveals that the transition can be thought of as energy transfer. Indeed, as the value of the control parameter is increased energy embedded in the beating waves is released at the transition stage. Since the transition from one mode to another, investigated in absolute frame of reference, shows that it follows a same route and the transition in the frame of reference moving with the pattern should also follow the same route. Hence, we can infer that as the control parameter is increased it triggers a wave dynamics N+1, which

interacts with the parent mode N (vortex-core pattern) to produce a beating wave. This beating wave envelopes another growing wave dynamics where its energy is transferred to the parent mode to force the parent mode to rotate at the same frequency of N+1.

As shown through this manuscript our contributions to the modeling of the falling film fluid and to the understanding of the polygonal patterns, exhibited by a hollow vortex core, are significant. At the same time several fundamental questions arise, each of them can constitute a research question. In the case of the problem of falling film, improving its modeling remains an open question. As shown, the problem involves at least four parameters, but most of the studies devoted to dynamics of falling film were restricted to the variation of one parameter, keeping the others constant. We believe it is time to conduct a deep comparison between all of the existing models using a continuation method which allows the variation of more than one control parameter and also allows us to investigate the persistence of the bifurcation scenarios predicted by the models found in literature. In light of this investigation, a new experiment should be conducted to validate or reject the conclusion of the investigation with the continuation method. Investigation of the problem in a magnetohydrodynamics frame remains an interesting open research question for its promising applications in metallurgy and nuclear energy.

As shown, our contribution to the investigation of the pattern of the hollow-core vortex is original and pushes the limits of our knowledge further. At the same time several question arise. The first is the investigation of the velocity field and its modifications with the variation of the control parameter. In this thesis we have investigated the transition of the pattern in one direction (the control parameter is increasing), however does the transition from higher mode to lower modes follows the "devil staircases" or energy transfer? Another question arises, would the observation depicted and the conclusions drawn in this thesis hold, if the rotating disk is in clock direction? Through this thesis we have used water as a working fluid, however, as shown in Vatistas (1990) higher viscosity fluid, such as oil, produce interesting behaviors. Hence, revisiting this work using the image processing technique, as used in this thesis, will be interesting and prospective work.

# References


Aitov, T.N. Kirillina, E.M. and Tananaev, A.V. (1988). Stability of the flow of a thin layer of liquid metal in a coplanar magnetic field, Magnetohydrodynamics 24, pp. 5-10.

Allison, M.Godfrey, D. A. and Beebe, R. F. (1990) A wave dynamical interpretation of Saturn's Polar hexagon. *Science*, 247(4946) 1061-1063.

Amaouche,M. Mehidi, N. Amatousse, N. (2005) An accurate modeling of thin film flows down an incline for inertia dominated regimes. EJMB/Fuids 24, pp. 49-70.

Aref, H. (1983) Integrable, chaotic, and turbulent vortex motion in two dimensional flows. *Annu. Rev. of Fluid Mech.*, 15, 345-389.

Aref, H, Rott, N, and Thomann, H. (1992) Gröbli's solution of the three-vortex problem *Annu. Rev Fluid Mech*. 24, 1-20.

Armstrong and Brown (1994). Traveling waves on vertical films: numerical analysis using finite element method, Physics of fluids, 6, 6, pp. 2202-2220

Bach and Villadsen (1984). Simulation of the vertical flow of a thin, wavy film using a finite-element method International journal of heat and mass transfer , 27, 6, pp. 815-827

Benjamin, T. B. (1957). Wave formation in laminar flow down an inclined plane. Fluid Mech. 2, pp. 554-574.

Benny, J. (1966). Long waves on liquid film. J. Math. Phys. 45, pp. 150-155.

Bluestein, H. B. and Pazmany A. L. (2000).Observations of tornadoes and other convective phenomena. *Bulletin of the American Meteorological Society*, 81, (12),2939- 2952

Burbea, J. and Landau, M. (1982) The Kelvin waves in vortex dynamics and their stability. **J.** *Comput. Phys.* 45, 127-156.

Brauner, N., and Maron, D. M. (1982). Characteristics of Inclined Thin Films, Waviness and the Associated Mass Transfer. Int. J. Heat Mass Transfer 25, 1, pp. 99-109.

Brevdo, L. Laure, P. Dias, F. Bridges, T.J. (1999). Linear pulse structure and signaling in a film fows on an inclined plane. J. Fluid Mech. 396, pp. 37-71.

Chang, H. C. Demikhin, E. A. (2002). Complex wave dynamics on thin films .Elsevier.

Chang, H. C. (1994). Wave evolution on a falling film. Ann. Rev. Fluid Mech 26, pp. 103-136.

Curtis, J. E. and Grier, D. G. (2003a) Structure of optical vortices. *Phys. Rev. Lett,* 90(13), 133901.

Curtis, J. E. and Grier, D. G. (2003b) Modulated optical vortices. *Optics Letters* 28,872- 874.

Davies-Jones, R. P. Tornado dynamics. (1986). In *Thunderstorm Morphology and Dynamics*, 2nd ed., edited by E. Kessler, University of Oklahoma Press, Norman, OK, 197-236

DeBruin, G. J. (1974). Stability of a layer of liquid flowing down an inclined plane J. Eng. Math. 8, pp. 259-270.

Daube, O. & Sorensen, J. N. (1989) Simulation numerique de l' ecoulement periodique axisymetrique dans une cavite cylindrique. *C. R. Acad. Sci.* 308 *(II b)*, 463-469.

Dhanak, M. R. (1992) Stability of a regular polygon of finite vortices. *J. Fluid Mech.* 234, 297-316.

Dritschel, D. G. (1985) The stability and energetics of corotating uniform vortices. *J.Fluid Mech.* 157, 95-134.

Durkin, D. and Fajans, J. (2000) Experiments on two-dimensional vortex patterns *Phys.Fluids*, 12, (2) 289-293.
Driscoll, C. F. and Fine, K. S. 1990 Experiments on vortex dynamics in pure electron plasmas *Phys. Fluids* B 2, 1359.

Elmegreen, B. G., Meloy Elmegreen, D., and Montenegro, L. (1991) Optical traces of spiral wave resonances in galaxieas, ii. Hidden three-arm spirals in a sample of 18 galaxies. *The astrophysical Journal-suppliment series*, **79** 37-48.

Enauss, J (1987) swirling flow problems at in takes *A.A.Balkema* ,165.

Escudier, M. P. (1984) Observations of the flow produced in a cylindrical container by a rotating endwall. *Exps. Fluids* **2**, 189–196.

Escudier, M.P (1987) Confined vortices in flow machinery. *Ann.Rev Mech.* 19,27-52.

Feng-Chen Li, and Akimi Serizawa (2004). Experimental study on flow characteristics of a vertically fallingfilm flow of liquid metal NaK in a transverse magnetic field, Fusion Engineering and Design 70185–199

Fine, K., Cass, A., Flynn, W. and Driscoll, C. (1995), Relaxation of 2D Turbulence to Vortex Crystals, *Phys. Rev. Lett.* 75(18), 3277.

Fridman A. M., Morozov A. G., Nezlin M. V., and Snezhkin E. N. (1985) Centrifugal instability in rotating shallow water and the problem of the spiral structure in galaxies. *Physics Letters*, 109A (5), 228-231.

Floryan, J. M., Davis, S. H. and Kelly, R. E. (1987). Instabilities of a liquid film flowing down a slightly inclined plane Phys. Fluids 30, pp. 983
Ganesh, R. and Lee, J. K (2002) Formation of quasistationary vortex and transient hole patterns through vortex merger. *Phys. Plasm.* 9(11), 4551-4559.

Godfrey, A. D. (1988) Hexagonal feature around Saturn's north pole. *Icarus*, 6(2), November, 335-356.

Gonzales,R.C and Wood, R.E. (2004) *Digital image processing using MATLAB 7 edition Prentice Hall*

Gregory, N., Stuart, J. T., Walker, W. S. (1955) On the stability of three-dimensional boundary layers with application to the flow due to a rotating disk. *Phil. Trans. Roy. Soc. London Ser.* A 248, 155 - 199.

Groöbli, W. (1877) Specielle Probleme über die Bewegung geradliniger paralleler Wirbelfäden. Zürcher und Furrer, Zürich. Republished in Vierteljahrschrift der naturforschenden Gesellschaft in Zürich, 22, 37-81, 129-167.

Helmholtz, (1858): "Ueber Integrale der hydrodynamischen Gleichungen, welche denWirbelbewegung entsprechen", *Journal für die Reine und Angewandte Mathematik* 55, pp. 25–55.

Hirsa, A. H., Lopez, J. M. & Miraghaie, R. (2002) Symmetry breaking to a rotating wave in a lid-driven cylinder with a free surface: Experimental observation. *Phys. Fluids* 14, L29–L32.

Hollerbach, R. (1996) Magnetohydrodynamic shear layers in a rapidly rotating plane layer. *Geophys.Astrophys. Fluid Dyn.* 82, 237-253.

Hsieh, D.Y. (1965). Stability of a conducting liquid flowing down an inclined plane in a magnetic field, Phys. Fluids 8, pp. 1785-1792.
Havelock, T. H. (1931) The stability of motion of rectilinear vortices in ring formation. *Philosophical Magazine* 11(7), 617-633.

Jansson R. N., Haspang, M. PJensen, . K. H. Hersen P., and Bohr T., (2006). Polygons on a Rotating Fluid Surface *Phys. Rev. Lett.*, 96, 174502

Jansson R. N., Haspang, M. PJensen, . K. H. Hersen P., and Bohr T.(2007) *Phys. Rev. Lett.* 96, 174502 (2006). Erratum *Phys. Rev. Lett.* 98, 049901

Jones L. O. and Whitaker. S (1966.An experimental study of falling liquid films AIChE J. 12, pp. 525

Einstein, A (1905) Zur Elektrodynamik bewegter korper *Ann. Phys.*, Lpz. 17 891–921.

Kapitza P.L and. Kapitza S.P(1949). Wave flow of thin layers of viscous fluid. Zh. Eksp.Teor.Fiz. 19, pp. 105

Kheshgi & Scriven (1987). Disturbed film flow on a vertical plate, Physics of fluids, 30, 4, pp. 990-997.

Keller, J. J. & Escudier, M. P. (1980) Theory and observations of waves on hollow-core vortices. *J. Fluid Mech.* 99, 495-511

Kelvin (Lord) (1867): "On Vortex Atoms", *Philosophical Magazine* 34, 15–24.

Kelvin (Lord) (1878) Mathematical and Physical Papers, iv. *Cambridge University Press*.

Kelvin (Lord) (1880) On the vibrations of a columnar vortex. *Philos. Mag.* 5(10), 155-168.

Kirchhoff, G. (1877) Vorlesungen über mathematische Physik. Mechanik Teubner,Leipzig.

Korsunsky, (1999). Long waves on a film layer of conducting fluid film flowing down inclined plane in an electromagnetic field. Eur J.Mech. B/fluids 18 2, pp. 295-313.

Kurakin, L. G. and Yudovich, V. I. (2002) The stability of stationary rotation of a regular vortex polygon. *Chaos*, 12 (3), 574-595.

Mason, B. J. (1971) Global atmospheric research programme. *Nature*, 233, 382-388.

Ladikov Yu P (1966). Flow stability of a conducting liquid flowing down inclined plane in the presence of a magnetic field, Fluid Dynamics 1,1-4.

Lauer, T. R., et al. (1993) Planetary camera observations of the double nucleus of M31.*The Astronomical Journal*, 106(4), 1436-1447.

Lee J.J and Mei,C.C (1996). Stationary waves on an inclined sheet of viscous fluid at high Reynolds number and moderate Weber numbers. J. Fluid. Mech .30, pp. 191-229.

Lewis B.M. and Hawkins, H.F. (1982) Polygonal eye walls and rainbands in hurricane", *Bull. Amer. Meteor. Soc.*, 63 (11) November, 1294 -1301.

Liu, J. and Gollub, J. P. (1994). Solitary wave dynamics of film fows. Phys.Fluids. 6, pp. 1702-1712.

Liu, J. Paul, J. D. and Gollub, J. P. (1993). Measurements of the primary instabilities of film flows. J. Fluid Mech. 250, pp. 69-101

McIntyre, M (1989) on the Antarctic ozone hole *J.Atmos.Terr.Phys*.51,19 (1989).

Landau, L. D. and Lifshitz, E. M. (1987). " Fluid Mechanics" . Second Edition, *Pargamon Press, Oxford*.

Lopez.J.M, Marques.F,Hirsa.H. and Mirghaie.R. (2004) Symmetry breaking in free surface flows. *J.Fluid .Mech* . 502, 99-126

Löfgren H.B., and Åkerstedt, H.O(1998). Electromagnetic braking of the flow of a liquid metal with a free surface, Fluid Dynam. Res. 23, pp. 1–25.

Marques.F Gelfgat A. Yu. Lopez. J.M 2003 Tangent double Hopf bifurcation in a differentially rotating cylinder flow *Physical Review E*. 68.

Mayer, A. M. (1878): "Floating Magnets", *Nature* 17, pp. 487–488.

Maxworthy, T. A (1972).vorticity dource for large dust devils and other comments on naturally occurring columnar vortices. *J. Atmos. Sci*. 30, 1717-1722

Miraghaie, R., Lopez, J. M. and Hirsa, A. H. (2003) Flow induced patterning at the air–water interface. *Phys. Fluids* 15(6), L45-L48.

Mitchell, T.B. and Driscoll, C.F. (1994) Symmetrization of 2D vortices by beat-wave damping. *Phys. Rev. Lett.* 73(16), 2196-2199

Morley. N.B, Smolentsev. S, Munipalli.R., Ni, M.-J. Gao. D., Abdou. M,(2004). Progress on the modeling of liquid metal, free surface,MHD flows for fusion liquid walls, Fusion Engineering and Design 72, pp. 3–34

Narula.M.,Ying.A, and Abdou.M.A. (2005). A study of liquid metal film flow under fusion relevant Magnetic fields, Fusion Science and Technology 47, pp. 564-568

Nguyen, L.T. and Balakotaiah, V. (2000). Modeling and experimental studies of wave evolution on free falling viscous films. Phys. Fluids. 12, pp. 2236-2256.

Nusselt, W. (1916). Die obser.achenkondensation des wasserdampfes. Z. VerDtsch. Ing. 60, pp. 541-552.

Ooshida, T. (1999). Surface equation of falling film flows with moderate Reynolds number and large but finite Weber number. Phys. Fluids.11, pp. 3247
O'Caroll, S. M and. Gutro, R. J (2002).``The Antarctic Ozone Hole," Poster paper, American Geophysical Union Meeting in the Moscone Convention Center, December

Peurrung, A.J., and Fajans, J. (1993). A limitation to the analogy between pure electron plasmas and two-dimensional inviscid fluids *Phys. Fluids B*, 5, 4285

Peurrung, A.J., and Fajans, J. (1993) Experimental dynamics of an annulus of vorticity in a pure electron plasma *Phys. Fluids A* **5**, 493

Poincare. H. (1893) Theorie des tourbillons, Leçons professées pendant le deuxième semestre 1891-92, *Cours de la faculte des sciences de Paris*, 205 p.

Poncet S., Chauve M.-P. (2007) , Shear-layer instability in a rotating system, *J. Flow Visualization & Image Processing*, 14 (1), p.85-105

Polvani, L. M and Dritschel, D. G. (1993) Wave and vortex dynamics on the surface of a sphere. *J. Fluid Mech*. 255, 35-64.

Panga M.K.R and Balakotaiah (2003). V.low-Dimentional model for vertically Falling Viscous Film, Phys. Rev. lett 90, pp. 151501

Prokopiou, T. Cheng, M. and Chang, H. C. (1991) Long waves on inclined films at high Reynolds number. J. Fluid Mech. 222, pp. 665-691.

Ruelle, D. and Takens, F. (1971). On the nature of turbulence. Communications in Mathematical Physics, 20, pp. 167–192.

Ruyer-Quil, C. and Manneville, P. (1998). Modeling film flows down an inclined plane. Eur. Phys. J. B. 6, pp. 277-292.

Ruyer-Quil, C. and Manneville, P. (2000). Improved modeling of flows down inclined planes. Eur. Phys. J. B. 15, pp. 357-369.

Ruyer-Quil, C. and Manneville, P. ( 2002). Further accuracy and convergence results on the modeling of .ows down inlined planes by weighted residual approxi-mation. Phys. Fluids 14, pp. 170-183.

Ruyer and Manneville (2004). Comment on "low-Dimensional model for vertically Falling Viscous Film," Phys. Rev. lett 93, pp. 199401 .

Stainthorp F. P. and Allen, J. M. (1965). The development of ripples on the surface of liquid film flowing inside a vertical tube Trans. Am. Inst. Chem. Eng. 43, pp. 85.

Strobel W. J. and Whitaker S. (1969). The effect of surfactants on the flow characteristics of falling liquid films AIChE J. 15, pp. 527.

Sivashinsky, G. I. and Michelson, D. M. (1980). On Irregular Wavy Flow of a Liquid Film Down a Vertical Plane Prog. Theor. Phys. 63, pp. 2112.155

Shkadov, V. Ya. (1968). Theory of wave .ow of thin layer of a viscous liquid. Izv. Akad. Nauk SSSR. Mekh. Zhidk. Gaza 2, 20.

Takahama, H. and Kato, S., (1980). Longitudinal flow characteristics of vertically falling liquid films without concurrent gas flow. International Journal of Multiphase Flow. 6, pp. 203-215.

Tailby S. R. and Portalsky S (1962). On Irregular Wavy Flow of a Liquid Film Down a Vertical Plane , Trans. Inst. Chem. Engr. 40, pp.114.
Taylor, F. W. (2006). Venus before Venus Express. *Planetary and Space Science*, 54(13-14), 1249-1262

Thomson J. J.( 1897) "Cathode Rays", *Philosophical Magazine* 44, pp. 293–316

Thomson, J.J. (1883) Treatise on Vortex Rings. Macmillan, London, 1883.

Vatistas G. H. (1989) Analysis of fine particle concentrations in a combined vortex Analyse des concentrations en fines particules dans un vortex forcé *Journal of Hydraulic Research* , vol. 27, n°3, pp. 417-427

Vatistas, G.H. "A note on liquid vortex sloshing and Kelvin's equilibria". *Journal of Fluid Mechanics*, (1990), vol. 217, 241-248.

Vatistas G. H. Wang J. Lin S. (1992) Experiments on waves induced in the hollow core of vortices *Experiments in fluids*, vol. 13, n°6, pp. 377-385

Vatistas G. H. ; Wang J. ; Lin S (1994) ; Recent findings on Kelvin's equilibria , *Acta mechanica* , vol. 103, n°1-4, pp. 89-102

Vatistas, G.H., Esmail, N., and Ravanis, C. (2001),Wave Development in Disk-Like Nearly Inviscid Liquid Vortices, 39th AIAA Aerospace Sciences Meeting and Exhibit. Paper no. AIAA 2001-0168, 8-11 Reno, NV.

Vatistas,G.H Ait Abderrahmane H Siddiqui.K. . (2008) , An experimental confirmation of Kelvin's equilibria, *Phys Rev. Lett.* 100, 174503.

Vettin, F. (1857). Über den aufsteigenden luftstrom, die entstebung des hagels und der wirbel-stürme. *Ann. Phys. Und Chem. (2) Leipzig* ,102, p. 246.

Vogel, H. U. (1968): Experimentelle Ergebnisse über die laminare Strömung in einem zylindrischen Gehäuse mit darin rotierender Scheibe. *MPI Bericht* 6

Williams, P. D. (2003b) Nonlinear interactions of fast and slow modes in rotating stratified fluid flows. Ph.D. *Thesis, Department of Physics,University of Oxford*.

Williams, P. D. (2004) Storm in a teacup. *Weather*, 59(2), 96-98.

Yarmchuk, E.J., M.J.V. Gordon, and R.E. Packard. (1979) Observation of stationary vortex arrays in rotating superfluid helium. *Phys. Rev. Lett.*, 43, 214-217.

UshaR. and Uma B., (2004). Modelling of stationary waves on a thin viscous film down an inclined plane at high Reynolds numbers and moderate Weber numbers using energy integral method Phys. Fluid,16, pp. 2679.

Yih, C. -S. (1955). Stability of two-dimensional parallel flows for three-dimensional disturbances. Quart. Appl. Math. 12, pp. 434.

# Appendix A

$$\frac{\partial q(x,t)}{\partial x}+\frac{\partial h(x,t)}{\partial t}=0$$

$$-h_{xxx}h^3We\varepsilon^3+\left(\frac{3h^2h_{xx}s}{R}+\frac{2h^2h_xs_x}{R}-\frac{h^3s_x^2}{R}-\frac{3h^2q_{xx}}{R}\right)\varepsilon^2+\frac{\tau 0h^2}{R}-\frac{3h^3}{R}+$$
$$\left(\begin{array}{l}\left(\frac{1}{210}\tau 0^2h^4+\frac{8}{35}h^2s^2-\frac{10}{7}q^2-\frac{2}{105}\tau 0h^3s-\frac{1}{42}\tau 0h^2q+\frac{3\cot\theta h^3}{R}\right)h_x+\left(-\frac{1}{42}\tau 0h^3+\frac{20}{7}qh-\frac{10}{7}h^2s\right)q_x\\ +\left(-\frac{1}{105}\tau 0h^4-\frac{3}{7}qh^2+\frac{16}{35}h^3s\right)s_x+\left(\frac{-1}{42}qh^3-\frac{1}{105}h^4s+\frac{1}{315}\tau 0h^5\right)\tau 0_x+h^2q_t-h^2h_ts\end{array}\right)\varepsilon=0$$

$$\frac{1}{2}h_{xxx}h^3We\varepsilon^3+\left(\begin{array}{l}\left(-\frac{8}{5}\frac{hs}{R}-\frac{1}{10}\frac{\tau 0h^2}{R}\right)h_x^2+\left(-\frac{6}{5}\frac{h^2s_x}{R}-\frac{1}{10}\frac{h^3\tau 0_x}{R}+\frac{2hq_x}{R}\right)h_x+\left(\frac{hq}{R}-\frac{13h^2s}{5R}-\frac{h^3\tau 0}{20R}\right)h_{xx}+\\ \frac{7}{10}\frac{h^3s_{xx}}{R}-\frac{1}{60}\frac{h^4\tau 0_{xx}}{R}+\frac{2h^2q_{xx}}{R}\end{array}\right)\varepsilon^2$$
$$+\left(\begin{array}{l}\left(-\frac{1}{560}\tau 0^2h^4-\frac{1}{6}h^2s^2-\frac{3\cot\theta h^3}{R}+\frac{11}{84}hsq+\frac{19}{1680}\tau 0h^3s+\frac{5}{7}q^2\right)h_x+\left(\frac{1}{28}\tau 0h^3+\frac{83}{84}h^2s-\frac{27}{14}qh\right)q_x+\\ +\left(-\frac{1}{3}h^3s+\frac{1}{4}qh^2+\frac{1}{560}\tau 0h^4\right)s_x+\left(-\frac{1}{840}\tau 0h^5+\frac{1}{144}h^4s+\frac{1}{84}qh^3\right)\tau 0_x+\left(\frac{1}{40}\tau 0h^3+\frac{4}{5}h^2s-\frac{1}{2}qh\right)h_t\\ -\frac{1}{10}h^3s_t-\frac{1}{2}h^2q_t+\frac{1}{120}\tau 0_th^4\end{array}\right)\varepsilon$$
$$+\frac{3h^3}{2R}-\frac{hs}{R}=0$$

$$\frac{1}{3}h_{xxx}h^4We\varepsilon^3+\left(\begin{array}{l}\left(\frac{88}{35}\frac{h^2s}{R}+\frac{6}{35}\frac{h^3\tau 0}{R}-\frac{8hq}{7R}\right)q_x^2+\left(-\frac{16}{7}\frac{h^2q_x}{R}+\frac{18}{35}\frac{h^3s_x}{R}+\frac{4}{35}\frac{h^4\tau 0_x}{R}\right)h_x+\left(\frac{79}{35}\frac{h^3s}{R}-\frac{8}{7}\frac{h^2q}{R}+\frac{2}{35}\frac{h^4\tau 0}{R}\right)h_{xx}\\ -\frac{61}{105}\frac{h^4s_{xx}}{R}-\frac{11}{7}\frac{h^3q_{xx}}{R}+\frac{h^5\tau 0_{xx}}{70R}\end{array}\right)\varepsilon^2$$
$$+\left(\begin{array}{l}\left(\frac{47}{385}h^3s^2+\frac{1}{1320}h^5\tau 0^2+\frac{h^4\cot\theta}{3R}+\frac{h^3\tau 0q}{231}-\frac{23}{154}h^2sq-\frac{30}{77}hq^2-\frac{179h^4\tau 0s}{27720}\right)hx+\left(-\frac{279}{385}h^3s+\frac{641}{462}qh^2-\frac{961\tau 0h^4}{27720}\right)q_x+\\ \left(\frac{13}{27720}\tau 0h^5+\frac{898}{3465}h^4s-\frac{73}{462}qh^3\right)s_x+\left(\frac{1}{1848}h^6\tau 0-\frac{47h^5s}{9240}-\frac{h^4q}{154}\right)\tau 0_x+\left(\frac{4qh^2}{7}-\frac{22h^3s}{35}-\frac{\tau 0h^4}{35}\right)h_t+\frac{13h^4s_t}{105}+\frac{2}{7}h^3q_t-\frac{h^5\tau 0_t}{140}\end{array}\right)\varepsilon+$$
$$-\frac{2hq}{R}+\frac{2h^2S}{R}-\frac{h^4}{R}=0$$

# Appendix B

$$501760\ WeR\,k^8+\left(492800WeR^2+752640\right)I\,k^7+\left(1505280\cot\theta+30105600WeR-1827840R-121800WeR^3-\left(501760WeR^2+564480\right)Ic\right)k^6$$
$$+\left(\left(15993600WeR^2-814464R^2+1478400R\cot\theta+82790400\right)I+3958080cR+246400WeR^3c\right)k^5$$
$$+\left(\begin{matrix}-1850240.c^2R+47088R+90316800\cot\theta-93623040R+263424000WeR-365400\cot\theta R^2-125440WeR^3c^2\\+\left(-1505280\cot\theta\,cR+2841300cR^2-60211200.c-15052800WeR^2c\right)I\end{matrix}\right)k^4+$$
$$\left(+\left(-16941960R^2-3079440c^2R^2+2167603200+4790800\cot\theta R\right)I+739200\cot\theta R^2-345312cR^3+206713920cR\right)k^3+$$
$$\left(\begin{matrix}672840c^2R^3+790272000\cot\theta-96902400c^2R-550368000R-376320\cot\theta\,c^2R^2+\left(\begin{matrix}1034880c^3R^2+57539160cR^2-15128006400c\\-45158400\cot\theta cR\end{matrix}\right)I\end{matrix}\right)k^2+$$
$$\left(\left(2370816000-56434560c^2R^2\right)I-497280c^3R^3+951148800cR\right)$$
$$k+\left(16934400c^3R^2-790272000c\right)I-361267200c^2R+125440c^4R^3=0$$

# Appendix C

$$q_x+h_t=0$$

$$-\frac{1}{3}h_{xxx}.We.\varepsilon^3+\left(-\frac{51}{49}\frac{q}{h^2}+\frac{39}{490}\tau0\right).\varepsilon.h_t-\frac{3.h^2R}{1960}\varepsilon^2\tau0_t h_t+\left(-\frac{3}{5}\frac{\tau0}{h.R}-\frac{4}{7}\frac{q}{h^3.R}\right)\varepsilon^2\left(h_x\right)^2+\frac{32}{245.R}\varepsilon^2\tau0_x.h_x+\frac{124}{49.h^2.R}\varepsilon^2q_xh_x+$$
$$\left(\frac{\cot(\theta)}{R}-\frac{3775}{3773}\frac{q^2}{h^3}-\frac{1285}{22638}\frac{q.\tau0}{h}+\frac{295}{15092}.h.\tau0^2\right)\varepsilon.h_x+R\left(\frac{817.h.q}{135828}-\frac{1937.h^3\tau0}{1164240}\right).\varepsilon^2\tau0_t.h_x+\left(\frac{3095}{30184}q+\frac{2027}{150920}\tau0.h^2-\frac{1307}{3622080}h^4\tau0_t.R\right).\varepsilon^2\tau0_t$$
$$-\frac{1369}{1358280}.h^2.R.\varepsilon^2\tau0_tq_x+\left(\frac{89}{33957}\tau0+\frac{7765}{11319}\frac{q}{h^2}\right)\varepsilon.q_x+\frac{13}{17640}.h^3.R.\varepsilon^2\tau0_{tt}+\frac{212}{49}\varepsilon^2\frac{h_xq}{h^2.R}+\frac{169}{1470}\varepsilon^2\frac{h\tau0_{xx}}{R}-\frac{2137}{6519744}.h^4.R\varepsilon^2\tau0.\tau0_{xt}+$$
$$+\frac{1285}{543312}.h^2.R.q.\varepsilon^2\tau_{xt}-\frac{16}{735}.h.\varepsilon.\tau_t-\frac{3}{7}\frac{\tau0}{h.R}-\frac{124}{49}.\varepsilon^2\frac{q_{xx}}{h.R}+\frac{27}{49}\varepsilon^2\frac{q_t}{h}-\frac{59}{245}\varepsilon^2\frac{\tau_0h_{xx}}{R}+\frac{16}{7}\frac{q}{h^3.R}-\frac{1}{R}=0$$

$$\frac{1}{2}h_{xxx}.We\varepsilon^3-\frac{4}{49}\frac{1}{R}\varepsilon^2h_x\tau0_x+\left(\frac{99}{784}q-\frac{9}{490}\tau0.h^2\right)\varepsilon\tau0_x+\frac{79}{169344}\tau0_t.h^4.R\varepsilon^2\tau0_x+\left(\frac{135}{49}\frac{q}{h^3.R}+\frac{55}{98}\frac{\tau0}{h.R}\right).\varepsilon^2h_x^2+\left(\frac{157}{70560}h^3.R.\tau0-\frac{53}{7056}.h.R.q\right)\varepsilon^2\tau0_t.h_t$$
$$\left(-\frac{205}{49}\frac{1}{h^2.R}q_x-\frac{3}{2}\frac{\cot(\theta)}{R}+\frac{60}{49}\frac{q^2}{h^3}-\frac{27}{980}.h.\tau0^2+\frac{9}{98}.\frac{\tau0q}{h}\right)\varepsilon.h_x+\frac{1}{42}.h\varepsilon\tau0_t+\frac{1}{336}h^2.R.\varepsilon^2h_t\tau0_t+\frac{23}{14112}.h^2.R.\varepsilon^2q_x\tau0_t+\left(-\frac{15}{784}\tau0.-\frac{79}{98}\frac{q.}{h^2}\right)\varepsilon.q_x+$$
$$\left(\frac{10}{7}\frac{q}{h^2}-\frac{1}{8}\tau0\right)\varepsilon.h_t+\left(-\frac{565}{98}\frac{q}{h^2.R}+\frac{16}{49.R}\tau0\right)\varepsilon^2.h_{xx}+\frac{41}{94080}.h^4.R.\varepsilon^2.\tau0\tau0_{xt}-\frac{13}{4704}.h^2.R.q.\varepsilon^2\tau0_{xt}-\varepsilon^2\frac{h^3.R.\tau0_{tt}}{1680}+\frac{3}{14}\frac{\tau0}{h.R}-\frac{5}{7.h}\varepsilon.q_t$$
$$-\frac{13}{84}\frac{1}{R}.h.\varepsilon^2.\tau0_{xx}+\frac{47}{14}\varepsilon^2.\frac{q_{xx}}{h.R}+\frac{3}{2.R}-\frac{15}{7}\frac{q}{h^3.R}=0$$

# Appendix D

$$
\begin{aligned}
&78274560\,i\,We\,R\,k^6 + (100638720 - 2728320\,i\,We\,R^3\,c - 98219520\,We\,R^2)\,k^5 + (-75479040\,c \\
&\quad + 1896652800\,i\,We\,R + 18117504\,R^2\,c + 234823680\,i\,\mathrm{cotg}(\theta) + 39137280\,We\,R^2\,c + 2257920\,i\,We\,R^3\,c^2 \\
&\quad - 416102400\,i\,R)\,k^4 + (94566528\,R^2 + 479404800\,i\,c\,R + 3734640\,i\,R^3\,c - 31006272\,R^2\,c^2 \\
&\quad - 14360371200 - 8184960\,i\,\mathrm{cotg}(\theta)\,R^2\,c - 294658560\,\mathrm{cotg}(\theta)\,R)\,k^3 + (-128378880\,i\,c^2\,R \\
&\quad + 10476748800\,c + 12848640\,R^2\,c^3 + 117411840\,\mathrm{cotg}(\theta)\,c\,R - 219663360\,R^2\,c - 3810240000\,i\,R \\
&\quad + 5689958400\,i\,\mathrm{cotg}(\theta) - 10636920\,i\,R^3\,c^2 + 6773760\,i\,\mathrm{cotg}(\theta)\,R^2\,c^2)\,k^2 \\
&\quad + (9386496\,i\,c^3\,R^3 + 6174282240\,i\,c\,R - 17069875200 + 143095680\,R^2\,c^2)\,k + 5689958400\,c \\
&\quad - 2393395200\,i\,c^2\,R - 29352960\,R^2\,c^3 - 2634240\,i\,c^4\,R^3 = 0
\end{aligned}
$$